DIFFRACTION STUDIES OF

MOLECULAR CRYSTALS

Thesis

Submitted by

J.S.W. OVERELL

for the degree of

DOCTOR OF PHILOSOPHY

University of Edinburgh

September, 1981.

TABLE OF CONTENTS[†]

†
Each chapter is presented such that the references are
given at the end of each and where a section of another
chapter is referenced, the chapter number is also given,
otherwise only the section number is given.
Publications are listed at the end of this thesis.

DECLARATION

The research described in this thesis is the
unaided work of the author, and where research
has been carried out in collaboration with
other people, a significant contribution was
made by the author.

ACKNOWLEDGEMENTS

"The Road goes ever on and on

Down from the door where it began.

Now far ahead the Road has gone,

And I must follow, if I can,

Pursuing it with weary feet,

Until it joins some larger way,

Where many paths and errands meet.

And whither then? I cannot say."

by Bilbo Baggins,

an extract from "Lord of the
Rings" by J.R.R. Tolkien.

ABSTRACT

The contents of this work are concerned with studies of some molecular crystals, mainly members of the aromatic benzene family. The techniques of investigation used are X-ray diffraction, Raman light scattering and neutron powder diffraction, although some single crystal neutron diffractometry has also been done. These subjects appear in the above order through this work.

The experimental technique of X-ray diffraction has been used successfully to solve the structure of the 280K phase of the 1:1 molecular complex system deutero-benzene hexafluorobenzene $(C_6D_6 \cdot C_6F_6)$. This particular system has been the subject of much work, both here and by previous authors and it has several phase transitions on varying the temperature.

Raman light scattering has been used to probe the above molecular complex system and a structural phase transition was reported. Preliminary data have also been collected at high pressure for this system and these are also presented.

Neutron powder diffraction has been used to refine the crystal structure of carbonyl sulphide, as a preliminary to doing phonon studies on a single crystal of this material. The $C_6D_6 \cdot C_6F_6$ system has also been studied using this technique, although the low temperature unit cell and crystal structure of this complex has yet to be solved.

The quasi-crystalline incommensurate phase is reviewed and several examples are taken from the literature and discussed at some length. Several experimental data sets are presented, with a view to explaining quasi-elastic neutron and diffuse X-ray scattering phenomena observed in the $p-C_6F_4Br_2$ system at temperatures between 4.2K and 300K. Future experiments are suggested in this connection.

GENERAL INTRODUCTION

The research described in this thesis is to be concerned with studies of molecular crystals using mainly diffraction techniques. A molecular crystal is one in which the basis of the crystal structure is constituted of molecules, rather than single atoms. The molecules in such crystals usually behave as if they are rigid units and the assumption that this is the case is called the rigid body approximation, although by no means all molecular crystals may be thus approximated.

The current areas of interest concerning molecular crystals include structural analysis and molecular lattice dynamics, both of which are greatly simplified by assuming the molecules to be rigid. In the former we may use a known molecular geometry in order to reduce the number of unknowns in the analysis and in the latter we achieve separation of the intermolecular and intramolecular vibration frequencies. There are many molecular crystals whose constituent molecules cannot be considered as being rigid (e.g. anthracene, polyphenyls) and these must be treated with a more complex physical model.

It is quite common for molecular crystals to display structural phase transitions of various types, including displacive, order-disorder and incommensurate transitions. In recent years interest has grown in this aspect of molecular crystals, especially in the incommensurate phases that are exhibited by some systems. It follows that studying molecular crystals with phase transitions may be very fruitful with respect to elucidating the different types of intermolecular forces that may be present and the competition between them.

The particular molecular-crystal systems studied in this work, and the reasons for choosing them, are as follows:

(i)   the existence of the 1:1 deuterobenzene hexafluorobenzene molecular complex has been known for some time and a great deal of previous work has been done on this system. However, the crystal structure of this complex was not known at any temperature and this prompted the structural studies that we have performed. The previous work of other authors had shown that this system undergoes several phase transitions on varying the temperature, and this led to the present experimental studies of the temperature dependence of the molecular lattice dynamics by light scattering techniques.

(ii)   The choice of carbonyl sulphide for structural refinement, as a preliminary to future inelastic neutron scattering studies, was based on two main factors. First, the number of degrees of freedom of this system is small, so that the molecular lattice dynamics will be relatively simple and ab initio calculations may be done, as have been done for deuterium cyanide (DCN) previously. Secondly, the electric dipole moment of the molecule is important, thus making the study of the lattice vibrations in this system of further interest.

(iii)   The reason for studying the molecular system para-dibromo-tetrafluorobenzene is that the isomorphous system para-diiodotetra-fluorobenzene and the closely related structure of para-dichloro-benzene both display interesting phase transitions. It might therefore be expected that this system may also show similar phenomena.

The experimental techniques used in this work are single crystal X-ray diffraction , Raman light scattering, neutron powder diffraction and quasi-elastic neutron scattering. Here we outline some of the potential uses of each technique with regard to molecular crystals. X-ray diffraction has been commonly used for structural analysis,

amongst other things, of a wide variety of systems including molecular crystals. The general availability of X-ray sources and the wide choice of experimental conditions, makes this method extremely con-venient if suitable single crystals are available. However, for systems that contain hydrogen (or deuterium) X-ray diffraction is a relatively insensitive method for finding accurate hydrogen nuclei positions and this may be one reason to opt for neutron diffraction instead. If, also, single crystals are not available - and this is common in the case of molecular crystals - then neutron powder diffrac-tion has proved a very useful alternative in structural analyses of molecular systems. The Raman scattering of light by any system (in the form of a single crystal or a powder) gives information con-cerning the dynamics of that system. For the specific case of molecular crystals with phase transitions Raman scattering can be a very powerful probe with regard to monitoring the behaviour of the dynamics of the system through a phase transition. If the rigid body approximation is valid for the molecules in the system then the intramolecular (internal) and intermolecular (external) vibrational frequencies are usually well separated, the latter having the lower frequencies. The corresponding Raman spectra are then more easily interpreted. However, if the rigid body approximation is not valid, then the internal and external modes of vibration may well become coupled, with their frequencies of the same order. Coupled modes give rise to asymmetric Raman line shapes in the scattered spectra and these may be analysed to find the nature of the coupling forces between the different modes.

The thesis presented here is organised such that each of the first three chapters covers one experimental technique - first reviewing

the technique and then giving an account of its application to one
(or more) of the molecular crystal systems discussed above. The
first chapter, covering X-ray diffraction, describes the deter-
mination of the crystal structure of the benzene-d_6 hexafluorobenzene
complex at 280K using single-crystal X-ray diffraction data.
Chapter 2 deals with Raman light scattering, where the above molecular
system is again studied with a view to finding a structural phase
transition on varying the temperature. Some high pressure data are
also presented for the same system. In Chapter 3 attention is turned
to the technique of neutron powder diffraction, and crystal structure
studies are presented for the carbonyl sulphide and the benzene-d_6
hexafluorobenzene systems. The experimental studies of the para-
dibromotetrafluorobenzene system, using the techniques of X-ray
diffraction, Raman light scattering and quasi-elastic neutron
scattering, have been drawn together into a separate chapter,
Chapter 4, because of the discovery of evidence for an incom-
mensurate phase in this system. Incommensurate phases attract a
great deal of current interest, as reviewed in the first half of
the chapter.

§1   Introduction

The processes concerning X-ray diffraction from small single crystals is considered, and the theoretical discussion is given from first principles leading to the integrated intensity expression for a Bragg reflection. The case of polycrystalline samples is not specifically discussed, since no X-ray powder diffraction work has been done. The extension to the expressions for X-ray diffraction maxima from powdered samples is very similar to that given for neutrons in Chapter 3, with the difference that the line shape for the former is not usually Gaussian, and X-ray scattering factors must also be included.

The order in which quantities are discussed is as follows. We first derive the electric field intensity at a point of observation at some distance away from the crystal. This leads to the introduction of the X-ray structure factor amplitude and this is given next, along with the functional form of the X-ray atomic scattering factor which is included in the above amplitude.

Temperature effects on the diffracted intensity are discussed and then we give the derivation of the experimentally measured quantity, the integrated intensity of a Bragg reflection. The processes of absorption and extinction that are always present in X-ray diffraction studies are discussed briefly also, and this is followed by an account of the double Bragg scattering process. This sub-section concludes §2.

Section §3 gives experimental results and a full analysis of a particular diffraction study, a précis of which is given in the publication at the end of this work. Conclusions to be drawn are given at the end of this last section.

X-ray photographic work has also been done and some of these results are presented in Chapter 4, §5 with respect to a possible incommensurate

phase of the system $p\text{-}C_6F_4Br_2$.

§2   General Theory

2.1   Intensity diffracted from a small crystal

The following discussion is based upon that given by Warren[1] and by James[4].

We consider an unpolarised, monochromatic beam of X-rays impinging upon a perfect single crystal that is small enough such that the incident beam may be considered as a plane wave, of wavelength λ and intensity I_o. The wavevector of the incident beam is denoted by $\underline{k}$.

The position vector of the nth atom in the cell $m_1 m_2 m_3$ with respect to some origin is given by

1.(1) $\underline{R}_m^n = m_1 \underline{a} + m_2 \underline{b} + m_3 \underline{c} + \underline{r}_n$,

where $\underline{a}$, $\underline{b}$, $\underline{c}$ are the direct lattice vectors and $\underline{r}_n$ is the position vector of the nth atom within the cell $m_1 m_2 m_3$. We consider the scattered beam, of wavevector $\underline{k}'$, at a point P, distance R from the crystal; for scattering diagrams see Figures 1.1a, b.

The total distance the wavefront must travel from the origin O to the point of observation P is $x_1 + x_2$, so that the electric field at P, due to the unmodified (elastic) scattering is

1.(2) $\varepsilon_p = \dfrac{\varepsilon_o e^2}{mc^2 R} f_n \cos 2\pi [\nu t - \frac{1}{\lambda} (x_1 + x_2)]$,

where ε_o is the electric field amplitude at the origin, e and m are the electron charge and mass respectively and c is the speed of light. ν and λ are, respectively, the frequency (Hz units) and wavelength of the electric field, and f_n is the scattering factor of the nth atom. This last quantity will be discussed in more detail in §2.2.

Figures 1.1a, b: Figure 1.1a shows the scattering geometry

of the incident and diffracted beams, the

nth atom (A) in the cell $m_1m_2m_3$ (see text)

and the point of observation (P). Quantities

used in the text are given in the diagram.

The wavefronts are denoted by dashed lines

perpendicular to $\underline{k}$ and $\underline{k}'$, the incident

and diffracted beam wavevectors respectively.

Figure 1.1b shows the relation of the in-

cident $(\underline{k})$, diffracted $(\underline{k}')$ and scattering

$(\underline{K}_s)$ wavevectors for the process in Figure

1.1a. 2θ is the scattering angle in both

figures.

FIG.1·1a,b

a

$\underline{k}$

O

θ'

2θ

x_1

$\underline{R}_m^n$

y

A

x_2

OP = R = x_2'

OA = $\left| \underline{R}_m^n \right|$

AP = x_2

x_1 = OA cos θ'

x_2'

$\underline{k}'$

x_2

P

b

$\underline{k}$

2θ

$\underline{k}'$

$\underline{K}_s$
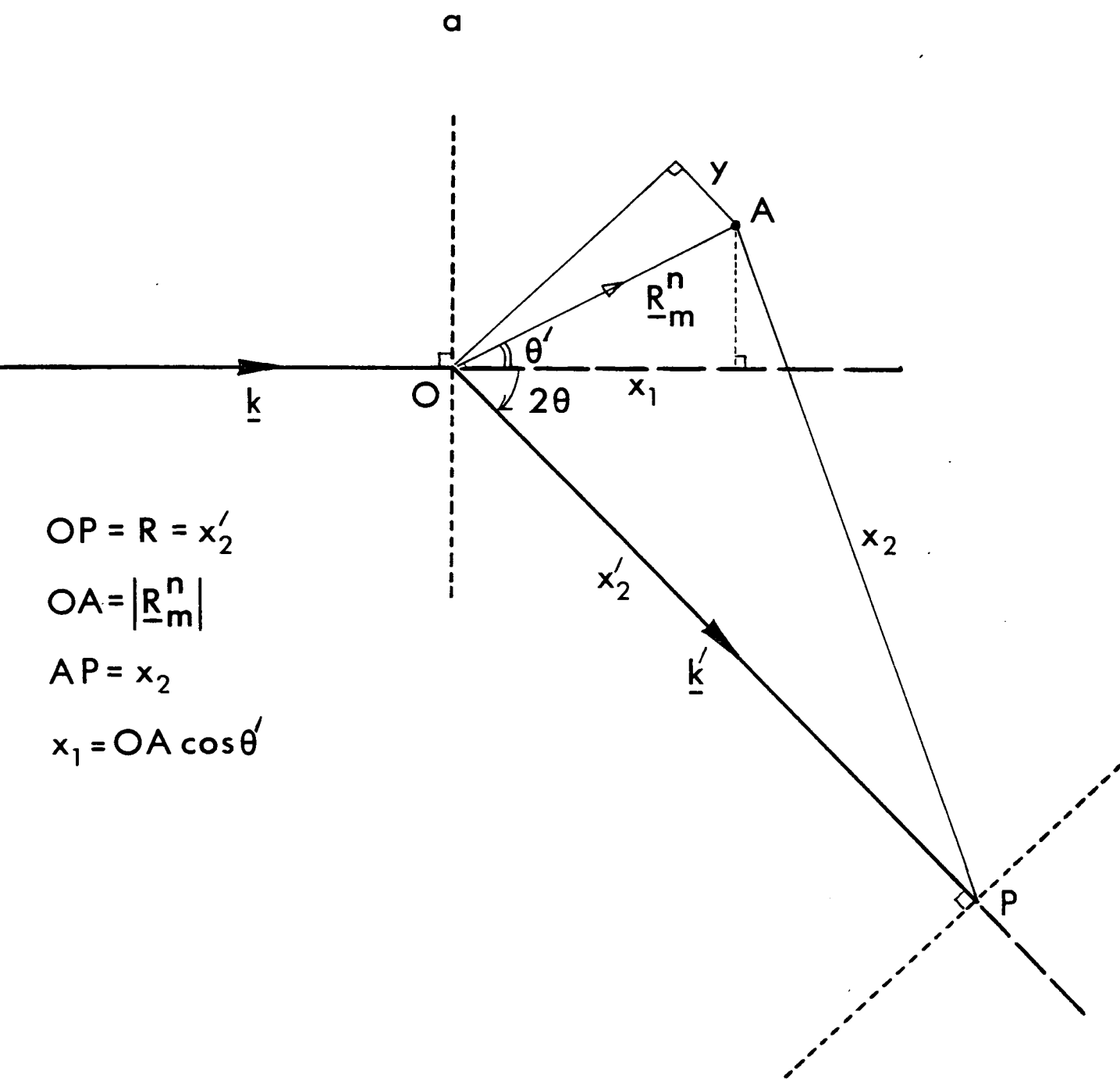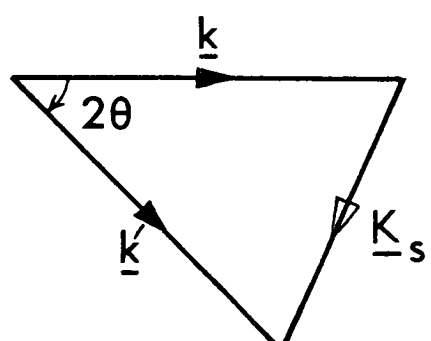
We now make the approximation that the wave at P is a plane wave, so that $x_2 \sim x_2'$. Therefore we require an expression for $(x_1 + x_2')$ in terms of $\underline{R}_m^n$ and of the wavevectors $\underline{k}, \underline{k}'$. From Figure 1.1a we see that $\underline{k}.\underline{R}_m^n = x_1 k$ and that $\underline{k}'.\underline{R}_m^n = yk' = yk$ so that, if $x_2 \sim R-y$, then we have the required distance travelled by the beam as $R - (\underline{k}' - \underline{k}).\underline{R}_m^n$, where we have chosen the reciprocal constant that relates λ to $|\underline{k}|$ such that $|\underline{k}| = 1$. Hence the electric field at P may be written in the complex form

$$1.(3) \quad \epsilon_p = \frac{\tilde{\epsilon}_o e^2}{mc^2 R} f_n \exp 2\pi i (\nu t - \frac{1}{\lambda} [R - (\underline{k}'-\underline{k}).\underline{R}_m^n]) .$$

The total electric field due to the whole crystal is obtained by summing over all the n atoms and over all the cells $m_1 m_2 m_3$. Without loss of generality, we assume the crystal has the shape of a parallelepiped, of sides $N_1 a, N_2 b, N_3 c$, so that the total field due to the whole crystal is divided into four summations, the first of which is (for the n atoms in a cell)

$$1.(4) \quad \sum_n f_n \exp(\frac{2\pi i}{\lambda} (\underline{k}' - \underline{k}).\underline{r}_n)$$

and the other three are of the form

$$1.(5) \quad \sum_{m_1=0}^{N_1-1} \exp(\frac{2\pi i}{\lambda} (\underline{k}' - \underline{k}).m_1 \underline{a})$$

where we have replaced $\underline{R}_m^n$ using 1.(1).

These last three summations in m_1, m_2, m_3 are of the form

$$\ell + \sum_{m_i=0}^{N-1} a \, r^{m_i} = \ell + \frac{a(r^N - 1)}{(r - 1)} .$$

Hence, evaluating ϵ_p and putting

1.(6) $\quad Q(N_1\underline{a}) = \dfrac{\exp(\frac{2\pi i}{\lambda}(\underline{k}' - \underline{k}).N_1\underline{a})}{\exp(\frac{2\pi i}{\lambda}(\underline{k}' - \underline{k}).\underline{a})} \qquad$ etc.,

we have

1.(7) $\quad \varepsilon_p = \dfrac{\varepsilon_o e^2}{mc^2R} \cdot \exp\left[2\pi i(\nu t - \frac{R}{\lambda})\right].F.Q(N_1\underline{a})Q(N_2\underline{b})Q(N_3\underline{c}) \qquad$,

where

1.(8) $\quad F = \sum\limits_{n} f_n \exp(\frac{2\pi i}{\lambda} (\underline{k}' - \underline{k}).\underline{r}_n) \quad$.

Equation 1.(8) is the structure factor amplitude and is discussed in §2.2. A similar equation for $\varepsilon_p^{\;*}$, the complex conjugate of ε_p, may be written and we must form the product $\varepsilon_p \varepsilon_p^{\;*}(^c/8\pi)$ in order to find the scattering intensity at the point P. This product will have quantities of the form

$$\left(\frac{e^{iNx} - 1}{e^{ix} - 1}\right) \cdot \left(\frac{e^{-iNx} - 1}{e^{-ix} - 1}\right) = \frac{\sin^2(Nx/2)}{\sin^2(x/2)} \quad ,$$

hence the scattered intensity at P, I_p is given by

1.(9) $\quad I_p = \dfrac{c}{8\pi} \left(\dfrac{\varepsilon_o e^4}{m^2c^4R^2}\right) F\ F^{*}\ S(N_1\ \underline{a})S(N_2\underline{b})S(N_3\underline{c}),$

where the function $S(N_1\underline{a})$ is defined by

1.(10) $\quad S(N_1\underline{a}) = \dfrac{\sin^2(\frac{\pi}{\lambda} N_1(\underline{k}' - \underline{k}).\underline{a})}{\sin^2(\frac{\pi}{\lambda} (\underline{k}' - \underline{k}).\underline{a})}$

and $S(N_2\underline{b})$, $S(N_3\underline{c})$ are similarly defined. In the case of an un-polarised incident beam of X-rays, it is necessary to resolve the electric vector into two components that form a mutually orthogonal set of axes with the incident wavevector $\underline{k}$. We then average the value of the amplitude of the electric field vector at P, thereby introducing a factor of $\frac{1}{2}(1 + \cos^2 2\theta)$, where 2θ is defined in

Figure 1.1b.

Therefore, for an unpolarised incident beam of intensity I_o $(= \frac{c}{8\pi} \epsilon_o{}^2)$, the intensity I_p $(= \frac{c}{8\pi} \epsilon_p{}^2)$ scattered from a small parallelepiped crystal is given by

1.(11) $I_p = I_e |F|^2 \, S(N_1\underline{a}) S(N_2\underline{b}) S(N_3\underline{c})$,

where we have put

1.(12) $I_e = (\dfrac{I_o e^4}{2m^2c^4R^2}) (1 + \cos^2 2\theta)$ and $|F|^2 = F \, F^*$.

Clearly, the intensity I_p is seen to be strongly dependent upon the functions S defined in equation 1.(10), since where the denominator is zero then these functions have very sharp maxima. This particular condition, in the case of $S(N_1\underline{a})$, is expressed by

1.(13) $(\underline{k}' - \underline{k}) . \underline{a} = \lambda h$,   h integral.

Similar equations hold for $S(N_2\underline{b})$ and $S(N_3\underline{c})$ and these are just the familiar Laue equations which must be satisfied if there is to be any diffracted beam and therefore they must be equivalent to the Bragg law. For completeness we now verify this last relation.

Let any arbitrary reciprocal space vector, $\underline{r}^*$, be represented by the expression

1.(14) $\underline{r}^* = p_1\underline{a}^* + p_2\underline{b}^* + p_3\underline{c}^*$,

where $\underline{a}^*, \underline{b}^*, \underline{c}^*$ are the reciprocal lattice vectors and the $\{p_i\}$ are numerical coefficients.

Now, since products of the form $\underline{a}.\underline{b}^* = 0$ and $\underline{a}.\underline{a}^* = $ constant, then 1.(14) may be written as (choosing $\underline{a}^*.\underline{a} = 1$, etc.)

1.(15) $\underline{r}^* = (\underline{r}^*.\underline{a})\underline{a}^* + (\underline{r}^*.\underline{b})\underline{b}^* + (\underline{r}^*.\underline{c})\underline{c}^*$.

Since $\underline{r}^*$ is arbitrary, then we may choose $\underline{r}^* = \underline{k}' - \underline{k}$, so that

$$\underline{k}' - \underline{k} = [(\underline{k}' - \underline{k}).\underline{a}]\,\underline{a}^* + [(\underline{k}' - \underline{k}).\underline{b}]\,\underline{b}^* + [(\underline{k}' - \underline{k})]\underline{c}^*$$

(1.(16) $= \lambda h\,\underline{a}^* + \lambda k\,\underline{b}^* + \lambda\ell\,\underline{c}^*$

from equation 1.(13). Hence we have

1.(17) $\underline{k}' - \underline{k} = \lambda\underline{G}_{hk\ell}$,

implying that the (hkℓ) of 1.(16) are the Miller indices of a reflection whose corresponding reciprocal lattice vector is $\underline{G}_{hk\ell}$.

Equation 1.(17) is just the Bragg equation, since the scattering vector $\underline{K}_s = \underline{k}' - \underline{k}$ is a reciprocal lattice vector (aside from the factor of λ which may be scaled arbitrarily by setting $|\underline{k}| = 1$), and so equation 1.(13) must be equivalent to the Bragg law.

2.2   X-ray structure factor amplitude

The structure factor, F, is a quantity used above in equation 1.(11), in the derivation of the diffracted intensity from a small perfect single crystal and it depends upon the atomic coordinates within the unit cell. These are represented by the position vector $\underline{r}_n$, in equation 1.(11) and it is convenient to express $\underline{r}_n$ in terms of the fractional coordinates of the nth atom within the cell, (x_n, y_n, z_n), in the following way:

1.(18) $\underline{r}_n = x_n\underline{a} + y_n\underline{b} + z_n\underline{c}$.

From the definition of F, 1.(8), we have

$$F = \sum_n f_n \exp\left(\frac{2\pi i}{\lambda} (\underline{k}' - \underline{k}) \cdot \underline{r}_n\right)$$

$$= \sum_n f_n \exp\left(\frac{2\pi i}{\lambda}(h\underline{a}^* + k\underline{b}^* + \ell\underline{c}^*) \cdot (x_n\underline{a} + y_n\underline{b} + z_n\underline{c})\right)$$

and this is

$$1.(19) \qquad F_h = \sum_n f_n \exp\left[2\pi i(hx_n + ky_n + \ell z_n)\right] \quad .$$

This is the simplest and most useful form of the structure factor

for the reflection whose indices are (hkℓ), denoted by

subscript h.

The quantities f_n are the X-ray atomic form or scattering

factors and they represent the relative scattering power of an atom.

In contrast to neutrons, where the f_n would be the scattering

angle independent coherent scattering lengths, the case for X-rays

is more complicated. In this latter case the atomic scattering

factor depends upon the scattering angle, 2θ, and reference (2)

contains their functional form and tables of numerical values for

their evaluation.

Briefly, however, the approximate expression used for the f_n

for X-rays is:

$$1.(20) \qquad f_n = C_n + \sum_{i=1}^{4} D_{n_i} \exp\left[-E_{n_i} \left(\frac{\sin \theta}{\lambda}\right)^2\right] ,$$

where the constants C_n, D_{n_i}, E_{n_i} (9 in total) are different for

different atom types.

2.3 Temperature effects on diffracted intensity

Equation 1.(11) gives the diffracted intensity from a small single crystal at some point of observation, distance R from the crystal. This expression was derived on the assumption that the atoms occupied definite sites on the crystal lattice. This is not realistic, however, since the atoms are possessed of thermal energy and therefore the crystal lattice sites are only average positions due to atomic thermal vibrations.

We consider now the effect of thermal motion of the atoms on the scattered intensity. Consider the jth atom which is situated at the average position whose vector is $\underline{r}_j$, where for brevity we have replaced the previous $m_1 m_2 m_3$ and n suffices by the suffix j. At any instant the jth atom has the position vector $\underline{r}'_j$ given by

$$L.(21) \qquad \underline{r}'_j = \underline{r}_j + \underline{u}_j \quad ,$$

where $\underline{u}_j$ is the instantaneous displacement vector from the average position. By repeating the previous derivation and omitting terms that disappear on multiplying by their complex conjugates, the intensity is obtained by summing over all the atoms' complex amplitudes of vibration and multiplying by their complex conjugates, which gives

$$
\begin{aligned}
I \;=\;& I_e \sum_j f_j \exp\left[\frac{2\pi i}{\lambda}(\underline{k}'-\underline{k})\cdot(\underline{r}_j + \underline{u}_j)\right] \\
& \times \sum_{j'} f_{j'}^{*} \exp\left[\frac{2\pi i}{\lambda}(\underline{k}-\underline{k}')\cdot(\underline{r}_{j'} + \underline{u}_{j'})\right] \\
=\;& I_e \sum_j \sum_{j'} f_j f_{j'}^{*} \exp\left[\frac{2\pi i}{\lambda}(\underline{k}'-\underline{k})\cdot(\underline{r}_j - \underline{r}_{j'} + \underline{u}_j - \underline{u}_{j'})\right] .
\end{aligned}
$$

1.(22)

However, we require the time average of this since this is the quantity that is measured experimentally. This is

$$<I> = I_e \sum_{jj'} \{f_j f_{j'}^* \exp\left[\frac{2\pi i}{\lambda} (\underline{k}' - \underline{k}) \cdot (\underline{r}_j - \underline{r}_{j'})\right]$$

1.(23)
$$\times <\exp(\frac{2\pi i}{\lambda} (\underline{k}' - \underline{k}) \cdot (\underline{u}_j - \underline{u}_{j'}))>\} \quad .$$

Putting $\frac{2\pi}{\lambda}(\underline{k}' - \underline{k}) = \frac{2\pi}{\lambda} \underline{K}_s = \underline{K}$, where $\underline{K}$ is a scaled scattering vector, then the time averaged exponential factor in 1.(23) becomes

$$<\exp(i \underline{K} \cdot (\underline{u}_j - \underline{u}_{j'}))> \quad .$$

This expression may be reduced further if the following relation is noted. If a quantity x is small and equally likely to be positive or negative, then the average $<e^{ix}>$ may be evaluated since odd powers of x average to zero and terms higher than x^2 are negligible, therefore $<e^{ix}> = e^{-\frac{1}{2}<x^2>}$. This result is stated as exact if x follows a Gaussian distribution. Hence if $(\underline{K} \cdot (\underline{u}_j - \underline{u}_{j'}))$ is small or follows a Gaussian distribution, which is not unreasonable, then

$$<\exp(i\underline{K} \cdot (\underline{u}_j - \underline{u}_{j'}))> = \exp -\frac{1}{2}<K^2(\underline{u}_j - \underline{u}_{j'})^2>$$
1.(24)
$$= \exp(-\frac{1}{2}K^2<u_j^2>) \exp(-\frac{1}{2}K^2<u_{j'}^2>) \exp(K^2<\underline{u}_j \cdot \underline{u}_{j'}>)$$

and introducing the abbreviations

1.(25) $\quad M_j = \frac{1}{2}K^2<u_j^2>, \quad M_{j'} = \frac{1}{2}K^2<u_{j'}^2>$

and writing

$$\exp(K^2<\underline{u}_j \cdot \underline{u}_{j'}>) = 1 + (\exp(K^2<\underline{u}_j \cdot \underline{u}_{j'}>) - 1),$$

then the intensity at the point of observation P becomes

$$I = I_e \sum_{jj'} f_j f_{j'}^* \exp(i\underline{K}.(\underline{r}_j - \underline{r}_{j'}))e^{-M_j}e^{-M_{j'}}$$

1.(26)
$$+ \left\{ I_e \sum_{jj'} f_j f_{j'}^* \exp(i\underline{K}.(\underline{r}_j - \underline{r}_{j'}))e^{-M_j}e^{-M_{j'}} \right.$$

$$\left. \left[\exp(K^2 \langle \underline{u}_j.\underline{u}_{j'} \rangle) - 1 \right] \right\} \quad .$$

The first term in this expression gives the sharp maxima we expect when the Bragg law is satisfied, attenuated by the factor $\exp(-(M_j + M_{j'}))$. This latter exponential is the Debye-Waller factor that accounts for the thermal vibration of the atoms, where M_j is defined in 1.(25) in terms of the mean-square displacement of atom j, $\langle u_j^2 \rangle$.

Atoms that are vibrating in a crystal lattice will usually only affect nearest neighbours, so that the displacements $\underline{u}_j$ and $\underline{u}_{j'}$ may be correlated to some extent and $\langle \underline{u}_j.\underline{u}_{j'} \rangle$ will therefore be non-zero if atoms j and j' are close together. If, however, the atoms j and j' are widely separated(further than third nearest neighbours, say), then $\underline{u}_j$ and $\underline{u}_{j'}$ may usually be considered as uncorrelated and the average $\langle \underline{u}_j.\underline{u}_{j'} \rangle$ is therefore zero. Hence the second term in equation 1.(26) will not give rise to maxima of diffracted intensity for large values of the separation $|\underline{r}_j - \underline{r}_{j'}|$. Instead, it represents a diffuse contribution to the diffracted intensity which is the temperature diffuse scattering of a thermally agitated crystal lattice.

Different atomic species will have amplitudes of thermal motion that increase as their mass decreases and so the exponential factor e^{-M_j} in 1.(26) is usually included in the summation for the structure factor. Thus the structure factor, including temperature effects, becomes

$$1.(27) \quad F = \sum_j f_j \, e^{-M_j} \exp(2\pi i(hx_j + ky_j + \ell y_j)),$$

where $M_j = \frac{1}{2}K^2\langle u_j\rangle$ and u_j is the magnitude of the displacement of the jth atom from its average position. From the definition of $\underline{K}$ below equation 1.(23), and from the scattering diagram Fig. 1.1b, we see that

$$\frac{1}{2}K^2 = 8\pi^2 \, \frac{\sin^2\theta}{\lambda^2}$$

by choosing $|\underline{k}| = 1$ arbitrarily, thence M_j may be written in terms of the scattering angle 2θ as

$$M_j = 8\pi^2 \left(\frac{\sin\theta}{\lambda}\right)^2 \langle u_j^2\rangle$$

1.(28)

$$= B_j \left(\frac{\sin\theta}{\lambda}\right)^2 ,$$

defining the atomic isotropic temperature parameter B_j as

$$1.(29) \quad B_j = 8\pi^2\langle u_j^2\rangle .$$

Thus it is clear that the reduction in diffracted intensity becomes more pronounced for reflections with large $\left(\frac{\sin\theta}{\lambda}\right)$ and for large atomic mean squared displacements $\langle u_j^2\rangle$.

The discussion of anisotropic temperature parameters is not given here since this is presented in Chapter 3 with regard to thermal neutron scattering, but the essential features are exactly the same for X-rays.

2.4   Integrated intensity of a reflection

The result of the previous discussion gives equation 1.(26), which is the diffracted intensity of a reflection from a small, perfect crystal, when all the necessary conditions of orientation

are satisfied. Equation 1.(26) also includes the temperature dependence due to atomic thermal motion within the crystal. However, this derivation leads to the diffracted energy of a reflection at a single point of observation. Since a Bragg reflection will have finite width due to the imperfections in the real crystal and due to the beam collimation used, the intensity observed at the point P (in Figure 1.1a) is not that which we would measure experimentally. The finite width of the Bragg reflections means that the intensity profile must be measured at several different points in the scattering angle P, P', P" etc., and the integrated intensity is therefore the summed intensity under the profile of the reflection.

At the present, only a simplified treatment is given for the integrated intensity, and later, the interpretation of experimental results and the discussion of various problems which arise from these interpretations is given.

In order to find the integrated intensity of a Bragg reflection, we consider a roughly collimated primary beam impinging upon a small crystal that is in approximately the correct Bragg orientation to diffract the beam from the (hkℓ) crystal planes. The crystal will be rotated throughout the measurement at a constant angular velocity, ω, about an axis normal to the incident beam direction and parallel to the (hkℓ) crystal planes. The angular range through which the crystal will be rotated will be sufficiently large such that diffracted intensity is collected from all parts of the crystal which may contribute to the reflection under measurement. This range is usually of the order of one or two degrees in scattering angle, allowance having been made for an estimate of the background on either side of the reflection. The detector will also rotate, at an angular velocity of 2ω and will

have an aperture wide enough to collect all the diffracted intensity from the reflection. Therefore, we actually measure the total diffracted energy, rather than the intensity for the (hkℓ) reflection, from all parts of the crystal.

Consider the (hkℓ) crystal planes as being vertical and the incident and scattered wavevectors, $\underline{k}$ and $\underline{k}'$ respectively, as lying in the horizontal plane, this geometry being shown in Figure 1.2. The scattering vector, $\underline{K}_s$, for the process $\underline{k} \rightarrow \underline{k}'$ is then $\underline{K}_s = \underline{k}' - \underline{k}$ and this vector also lies in the horizontal plane. The diffracted beam is detected at O' in Figure 1.2. If now the incident beam is $\underline{k}_1$ at some angle α, in the scattering plane, to $\underline{k}$ then the diffracted beam direction may be given by $\underline{k}_1'$, at angles β, γ to the original scattered wavevector $\underline{k}'$. The angles γ and β are, respectively, parallel and perpendicular to the plane defined by $\underline{k}$ and $\underline{k}'$. The diffracted beam is then detected at O" and the scattering vector for the process $\underline{k}_1 \rightarrow \underline{k}_1'$ is $\underline{K}_{S1} = \underline{k}_1' - \underline{k}_1$. This also is shown in Figure 1.2. The vector $\underline{\Delta S}$ is defined as

1.(30) $\underline{\Delta S} = (\underline{k}_1' - \underline{k}_1) - (\underline{k}' - \underline{k}) = \underline{K}_{S1} - \underline{K}_s$.

The total diffracted energy is obtained by integrating the scattered intensity over both the total receiving area of the detector and time. This is

1.(31) $E_{Tot.} = \iint I_p \, dt \, dA = \iiint I_p \, dt \, d\gamma \, d\beta \, R^2$,

where we have replaced the integration over the receiving area by that over the angles β and γ, the detector at O' being distance R from the crystal at O.

The crystal is rotating during the measurement and its angular

Figure 1.2:   Measurement of the total diffracted energy of a Bragg

reflection. The vector $\underline{k}_1$ makes angle α with $\underline{k}$,

in the scattering plane defined by $\underline{k}$ and $\underline{k}'$. The

angles β and γ are perpendicular and parallel to

the $\underline{k}$, $\underline{k}'$ scattering plane respectively, and the

changes produced in $\underline{\Delta S}$ by the changes in α, β

and γ are shown in the inset of the figure. The

crystal is at O, O' and O'' being the detector

positions for the $\underline{k} \rightarrow \underline{k}'$ and $\underline{k}_1 \rightarrow \underline{k}_1'$ scattering

processes respectively. The crystal to detector

distance OO' is R.

FIG.1·2
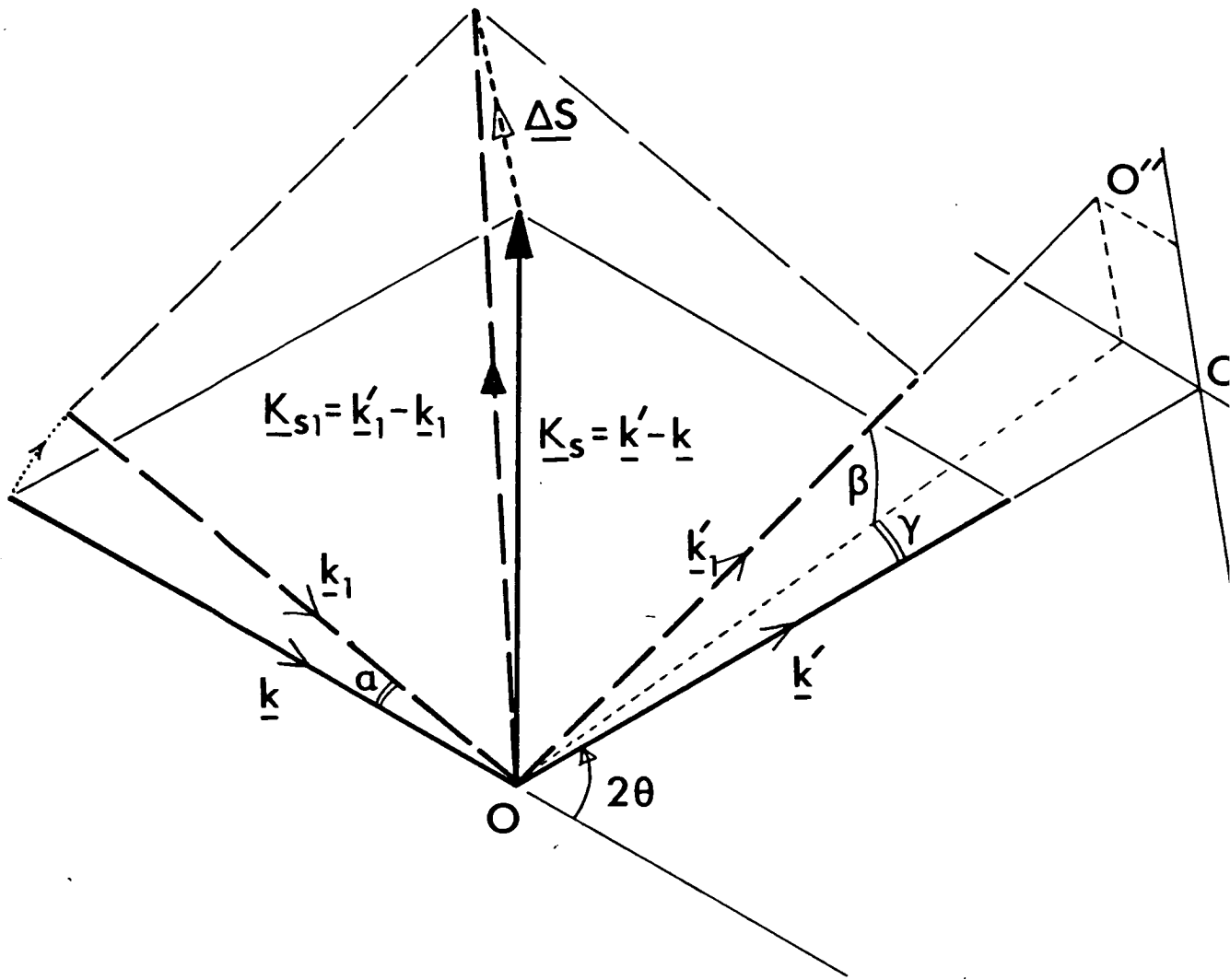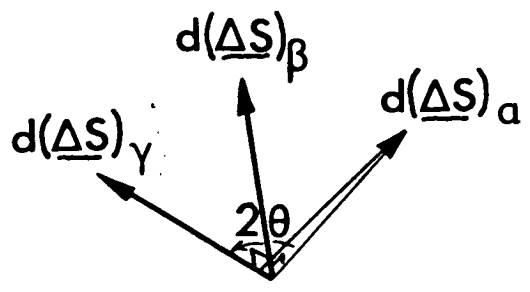
velocity is ω. For convenience we may consider the incident beam as moving in the opposite sense with the same angular velocity. Therefore, if the instantaneous position of the incident beam makes angle α with $\underline{k}$, i.e. it has wavevector $\underline{k}_1$, then the time that the beam spends between the angles α and α + dα is $dt = \dfrac{d\alpha}{\omega}$. This means the total diffracted energy may be written

$$1.(32) \qquad E_{Tot} \quad = \quad \iiint I_p \frac{R^2}{\omega} \, d\alpha \, d\beta \, d\gamma \quad .$$

Since $\underline{\Delta S} = \underline{K}_{S1} - \underline{K}_S$ and by definition $\underline{K}_S = \lambda \underline{G}_{hk\ell}$, where $\underline{G}_{hk\ell}$ is the reciprocal lattice vector for the (hkℓ) reflection, then considering one of the sine functions $S(N_1\underline{a})$, in 1.(9), with $\underline{K}_{S1} = \underline{\Delta S} + \lambda \underline{G}_{hk\ell}$ we have

$$\sin^2\left(\frac{\pi}{\lambda} \, (\underline{k}_1' - \underline{k}_1) \cdot N_1\underline{a}\right) \quad = \quad \sin^2\left(\frac{\pi}{\lambda}(\underline{\Delta S} + \lambda \underline{G}_{hk\ell}) \cdot N_1\underline{a}\right)$$

$$= \quad \sin^2\frac{\pi}{\lambda}(N_1\underline{a} \cdot \underline{\Delta S}) \quad .$$

Now let $\underline{\Delta S}$ be expressed in terms of the reciprocal lattice vectors $(\underline{a}^*, \underline{b}^*, \underline{c}^*)$ thus:

$$1.(34) \qquad \underline{\Delta S} \quad = \quad (p_1\underline{a}^* + p_2\underline{b}^* + p_3\underline{c}^*) \quad ,$$

where the $\{p_i\}$ are again numerical coefficients. Equation 1.(33) becomes, on using 1.(34),

$$1.(35) \qquad \sin^2\left[\frac{\pi}{\lambda} \, N_1\lambda(p_1\underline{a}^* + p_2\underline{b}^* + p_3\underline{c}^*) \cdot \underline{a}\right] \quad = \quad \sin^2(\pi N_1 p_1) \quad ,$$

and so the total diffracted energy, $E_{Tot.}$ is found by substituting 1.(11) and 1.(35) into 1.(32) to obtain

$$1.(36) \qquad E_{Tot.} \quad = \quad \frac{I_e R^2 F^2}{\omega} \iiint \prod_{i=1}^{3} \frac{\sin^2(N_i p_i \pi)}{\sin^2(p_i \pi)} \, d\alpha \, d\beta \, d\gamma \quad ,$$

where the 'Π' notation is the product of the terms i = 1, 2 and 3 in the { } brackets.

The changes dα, dβ, dγ produce corresponding changes in k and k', dα being perpendicular to k and dβ, dγ perpendicular to k'. There are also changes produced in ΔS as a result and these are shown in the inset of Figure 1.2. These changes are given by

$$\left| d(\underline{\Delta S})_\alpha \right| = d\alpha, \quad \left| d(\underline{\Delta S})_\beta \right| = d\beta, \quad \left| d(\underline{\Delta S})_\gamma \right| = d\gamma \quad .$$

The end point of the vector ΔS therefore traces out a volume in reciprocal space as a result of the changes dα, dβ, dγ and this is given by

$$1.(37) \quad dV = d(\underline{\Delta S})_\beta \cdot d(\underline{\Delta S})_\alpha \times d(\underline{\Delta S})_\gamma$$

$$= \sin 2\theta \, d\alpha \, d\beta \, d\gamma \quad .$$

Hence the total diffracted energy is

$$1.(38) \quad E_{Tot.} = \frac{I_e F^2 R^2}{\omega \sin 2\theta} \int_V \prod_{i=1}^{3} \left(\frac{\sin^2(N_i p_i \pi)}{\sin^2(p_i \pi)} \right) dV \quad .$$

Since no restriction has been placed on the volume element dV in this integral, we are at liberty to choose a convenient volume and thus we may write

$$dV = (\lambda \underline{a}^* dp_1) \cdot (\lambda \underline{b}^* dp_2) \times (\lambda \underline{c}^* dp_3)$$

$$= \frac{\lambda^3}{v_a} \, dp_1 \, dp_2 \, dp_3 \quad ,$$

where v_a is the volume of the direct lattice unit cell. Since the Bragg condition for the reflection with indices (hkℓ) is expressed as $\underline{K}_S = \lambda \underline{G}_{hk\ell}$, then we require the vector ΔS to be the zero vector and so we are only interested in very small values of

P_1, P_2, P_3 close to zero, so that $\sin^2 \pi p_i \sim (\pi p_i)^2$. Therefore, on using 1.(39), the integral in 1.(38) may be extended to $\pm \infty$ since there is only one Bragg peak and the coherent diffraction of energy decreases rapidly once we move away from the strict Bragg condition. Therefore, equation 1.(38) becomes

$$1.(40) \quad E_{Tot.} = \frac{I_e F^2 R^2}{\omega \sin 2\theta} (\frac{\lambda^3}{v_a}) \prod_{i=1}^{3} (\int_{-\infty}^{+\infty} \frac{\sin^2 \pi N_i p_i}{(\pi p_i)} dp_i)$$

and each of the three integrals just gives the number of unit cells along the corresponding direct lattice direction. Hence, putting $N_1 N_2 N_3 = N$, equation 1.(40) becomes

$$1.(41) \quad E_{Tot.} = \frac{I_e F^2 R^2 \lambda^3 N}{\omega v_a \sin 2\theta} .$$

By introducing the volume of the small crystal $\delta V = N v_a$, and by substituting the expression for I_e (viz. equation 1.(12)) we have for the total diffracted energy of a Bragg peak

$$1.(42) \quad E_{Tot.} = (\frac{I_o F^2 \lambda^3 e^4}{\omega v_a^2 m^2 c^4}) \delta V \{\frac{1 + \cos^2 2\theta}{2 \sin 2\theta}\} .$$

This last equation depends only on δV, the volume of the crystal, for a given reflection and experimental arrangement. The angle dependent factor in 1.(42) is the Lorentz polarisation correction for a single crystal in an unpolarised X-ray beam, for scattering angle 2θ. The numerator in this factor arises because of the averaging of the electric field amplitude at the point of observation and the denominator appears because of the changes in the incident and diffracted wave-vectors indicated in Figure 1.2.

The dependence of the total diffracted energy upon the volume of the crystal is only valid when the crystal is small, as we assumed

above.   The above result is invalid for larger crystals, the reason
being that we have neglected processes that remove energy from the beam
other than   Bragg scattering.   These processes include absorp-
tion and extinction, which are discussed in the next section, §2.5.

2.5   Absorption and Extinction

In the previous derivation of the integrated intensity of a Bragg
reflection, using the moving crystal - moving detector arrangement, the
processes of absorption and extinction have been ignored.   This is
justified for a very small crystal or a weak Bragg reflection.   A very
strong Bragg reflection results in the diffraction of a large amount
of energy out of the incident beam, and therefore it is possible that
not all parts of the crystal will diffract the incident beam.   There-
fore corrections are usually made, where possible, to account for these
effects.   To form a qualitative picture of the extinction and absorp-
tion processes it is necessary to consider the real nature of a crystal.

In the previous sections we assumed that the sample was a perfect
single crystal.   However, a real crystal is usually highly imperfect
and in fact is constituted of a very large number of small, individually
perfect, crystallites which are slightly misoriented from their neigh-
bours.   This spread of orientation of the microscopic components of a
crystal is called the mosaic spread and results in the Bragg reflections
having finite width.   Hence, the more perfect a crystal, the smaller is
the spread of orientation of the individual crystallites and the re-
sulting mosaic spread and Bragg reflection width are less.

The first of the two processes to be discussed is absorption and
this is treated qualitatively.   When a beam of X-rays passes through a

crystal, energy will be removed from the beam and converted into thermal energy, either in ejecting an electron from an atom and giving it kinetic energy, or by giving the atoms extra thermal energy. The greater the number of electrons in an atom, then the more likely it is that the atom will remove energy from the incident beam via the first of the two channels described above. Therefore, absorption of X-rays in matter increases as the atomic number of the atom increases.

It is also noted that the absorption of X-rays varies with their incident wavelength. If the energy of the X-ray quantum is just insufficient to eject an electron from an atom then the absorption will be much less than when this energy is great enough to completely remove the electron. Therefore on varying the wavelength of incident X-rays on a crystal of an element and monitoring the absorption, several well defined peaks will be observed due to the removal of electrons in various atomic energy states. These peaks are the absorption edges of the atom and, of course, the wavelengths for which these peaks occur differs for differing elements.

It is seen that this absorption process is completely independent of any diffraction of the incident beam, and it is usually treated as a linear effect. This is done by assuming that the incident intensity, I_o, is reduced by the factor $e^{-\mu t}$, where t is the total path length in the crystal and μ is the linear absorption coefficient of the crystal. This coefficient may easily be calculated with a knowledge of the absorbing power of the atoms that constitute the crystal structure. The International Tables for X-ray Crystallography[2] contains the numerical values of the mass and atomic absorption coefficients for all the elements for a variety of wavelengths. The linear absorption coefficient is evaluated using the expression

1.(43) $$\mu = (\frac{1}{v_a}) \sum_i n_i \sigma_i \quad ,$$

where v_a is defined as before and n_i is the number of atoms of one species within this volume, each having an atomic absorption coefficient of σ_i. The unit of μ is inverse length.

There has been much work done on the absorption of X-rays by crystals in relation to evaluating the corrections that are required in order to find the true integrated intensities of reflections, see for example, references (4, 12-15).

It is usually the case that the absorption correction relevant to a particular experimental arrangement can be exactly calculated for only a very few cases. Some such cases are for perfect spherical crystals (of radius R) in the forward and backscattering directions ($2\theta = 0°$ and $2\theta = 180°$ respectively). For other values of the scattering angle the absorption factor must be calculated numerically for different values of μR. It can be shown that the absorption factor varies rapidly with μR[15], especially at low scattering angles, and therefore any deviation from the ideal spherical shape will cause an appreciable uncertainty in the absorption correction and so relatively large errors are introduced in the integrated intensities, of the order of a few percent or more. Since the real crystal used in an X-ray experiment is very rarely a perfect sphere, the absorption-corrected integrated intensities of reflections are difficult to obtain to an accuracy of better than a few percent.

In contrast to the process of absorption, which is not connected with the diffraction of the X-ray beam, is extinction. This phenomenon is due to energy being diffracted out of the incident beam when the specimen is oriented as for the Bragg condition. There are

two types of extinction and they are briefly described below.

Primary extinction is caused by the individually perfect mosaic crystallites reflecting the incident beam more than once within their own volume. Each reflection of the incident X-rays from a set of lattice planes introduces a phase lag of $\pi/2$ radians relative to the incident beam, so that after two such reflections the reflected beam is out of phase with the incident beam. Therefore destructive interference will take place and this reduces the amplitude and hence the intensity of the incident beam. This is a diffraction process and should not be confused with ordinary absorption.

The other extinction process is named secondary because it involves not only one mosaic crystallite, but many. If the crystal is roughly oriented to reflect from a particular set of lattice planes, then for one particular setting of the crystal a fraction of the mosaic crystallites will reflect the incident beam because of their small, relative misorientation with respect to their neighbours. This means that the intensity of the incident beam is diminished and so the mosaic crystallites having a greater depth within the crystal do not receive the full incident beam intensity. Instead, as the beam penetrates the crystal it is reduced in intensity by the diffraction from other crystallites at that particular Bragg setting, as well as by absorption and primary extinction. The two extinction processes are represented schematically in Figures 1.3a,b.

The subject of extinction has produced a large amount of work, see for example references (5) - (11). The integrated intensities that have been measured by the author were not corrected for either absorption or extinction. The reason for this was that the crystals used were usually highly imperfect and also of cylindrical shape.

Figures 1.3a,b: Schematic representation of (a) primary

and (b) secondary extinction. Diagram (a)

represents a single, perfect mosaic crystallite

in a Bragg reflecting position, whilst the

bottom diagram shows a collection of such

crystallites (some of which are oriented as

in (a), these being hatched) that would con-

stitute part of the real crystal.

FIG. 1·3a,b

a

I_o $\underline{k}$

lattice planes

$I' < I_o$

I'

b

I_o $\underline{k}$

$\underline{k}'$
I_1

I_2

I_3
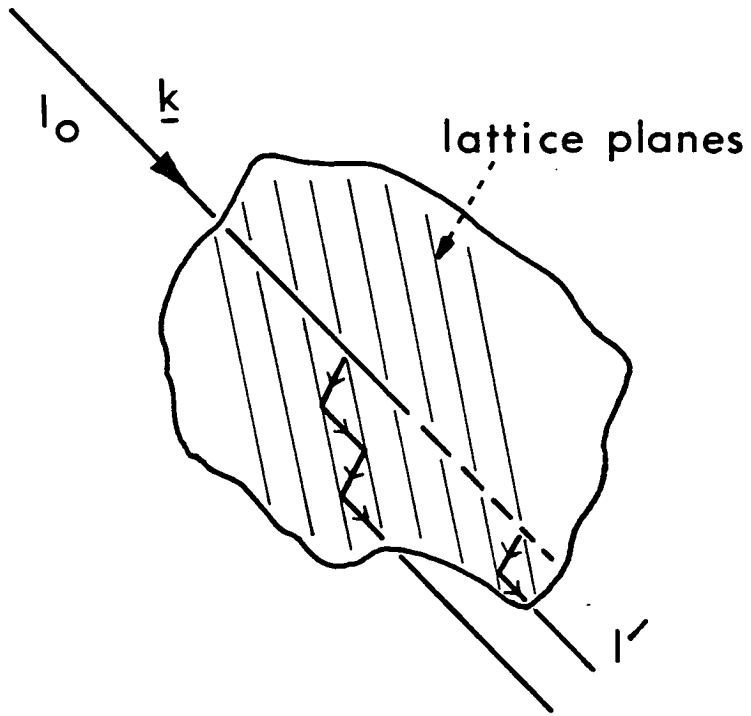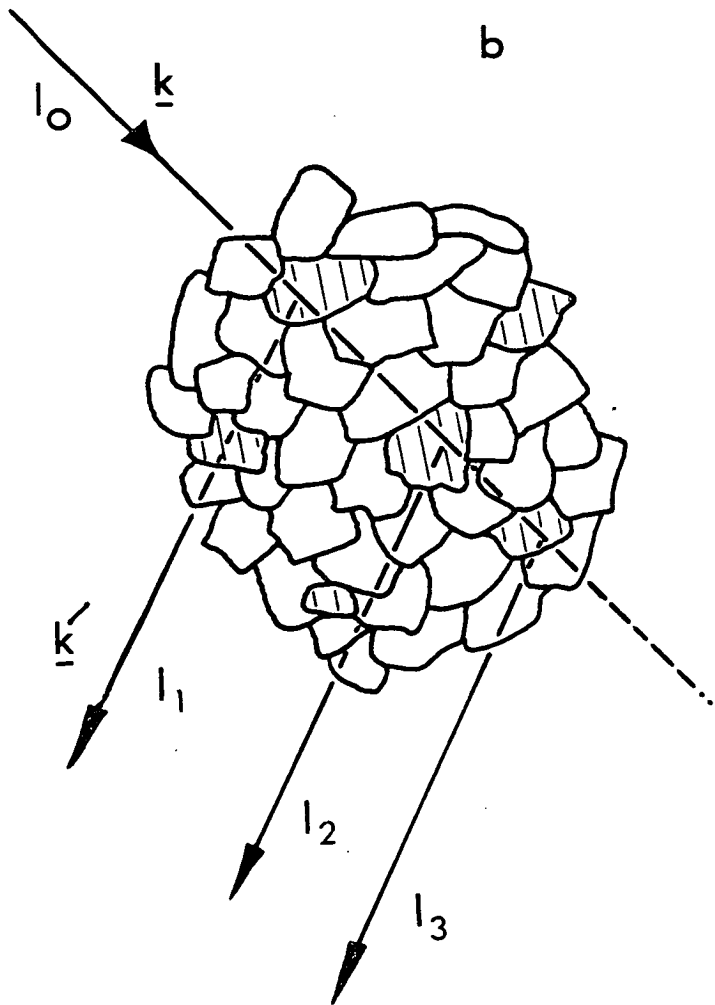
$I_1 > I_2 > I_3$

Therefore, the high imperfection of crystals makes extinction negligible and the shape of the crystals makes any absorption correction extremely complicated. Extinction corrections in simple cases of orientation settings for cylindrical crystals have been given by Hamilton[6,7]. Also given in the same references are extinction corrections for crystals of more general shapes in general orientations, but no attempt is made to reproduce those results here.

Despite the inherent difficulties of corrections for absorption and extinction for cylindrical crystals, such a shaped sample has been used without applying these corrections to successfully solve a crystal structure.

This is presented in section §3 and in the publication at the end of this work.

2.6   Double Bragg Scattering

This section is included since the process described here was encountered in the analysis of the structure presented in §3. Double Bragg scattering is therefore briefly discussed with the aid of a diagram.

From equation 1.(17) it is seen that Bragg scattering may only take place when the scattering vector for the process is identically a reciprocal lattice vector. Thus:

$$1.(17) \qquad \underline{K}_s \;=\; \underline{k}' - \underline{k} \;=\; \lambda \underline{G}_{hk\ell}$$

for the reflection whose indices are (hkℓ). Since the scattering is strictly elastic, the moduli of $\underline{k}$ and $\underline{k}'$ are equal, $|\underline{k}| = |\underline{k}'| = k$, say. Therefore, the two wavevectors $\underline{k}$ and $\underline{k}'$

must terminate at reciprocal lattice points that lie on a sphere (3 dimensions) or on a circle (2 dimensions). This construction is due to Ewald[16] and is the most instructive geometrical interpretation of the Bragg equation. Figure 1.4 shows part of a reciprocal lattice of an appropriately oriented crystal, the incident beam wavevector is $\underline{k}$. The circle is the section of the reflection or Ewald sphere in the plane of the figure.

Consider the reciprocal lattice points O and P_1. Since they both lie on the Ewald sphere, diffraction may take place with a scattering vector of $\underline{K}_{S1} = \underline{k}_1' - \underline{k}$ and scattering angle $2\theta_1$. We suppose that this Bragg reflection is very intense. The scattered beam of wavevector $\underline{k}_1'$ will pass through P_1 and so we may now consider this point as the new origin. Since P_2 also lies on the Ewald sphere scattering may again take place, but now with scattering vector

$$\underline{h} = \underline{k}_2' - \underline{k}_1' \text{ and Bragg angle } 2\theta_2.$$

If the detector is set at scattering angle $2\theta_1$, then the intense reflection whose reciprocal lattice vector is $\underline{K}_{S1}$ will be recorded. However, if we consider the detector as being situated at scattering angle $(2\theta_1 + 2\theta_2)$ then the ordinary Bragg process $\underline{k} \rightarrow \underline{k}_2$, of scattering vector $\underline{K}_{s2}$, will take place, as well as the two successive processes $\underline{k} \rightarrow \underline{k}_1'$, $\underline{k}_1' \rightarrow \underline{k}_2'$.

If both of these last two processes involve intense Bragg reflections then the ordinary single scattering event $\underline{k} \rightarrow \underline{k}_2'$ will be enhanced by the double scattering event described above.

It is seen that this description may be extended easily to the case of multiple scattering where more than two successive events are involved.

Figure 1.4:   Ewald diagram representing the process of double Bragg scattering. $\underline{k}$ is the incident beam wavevector and $\underline{k}_1'$, $\underline{k}_2'$ are diffracted beam wavevectors. $\underline{K}_{S1}$, $\underline{h}$ and $\underline{K}_{S2}$ are scattering vectors such that $\underline{K}_{S2} = \underline{K}_{S1} + \underline{h}$, and the circle and square points are the reflecting sphere section and reciprocal lattice points respectively.

FIG. I·4
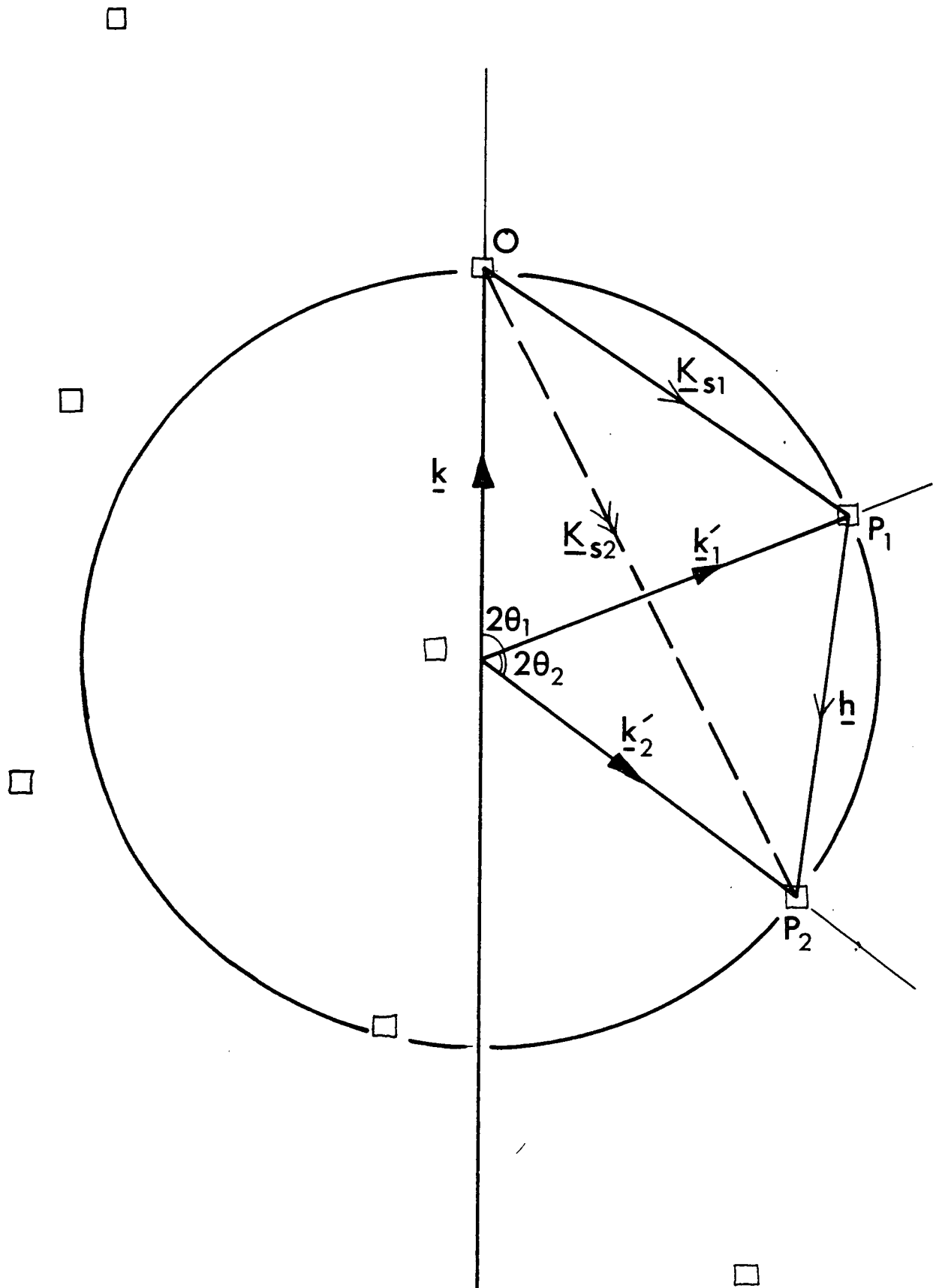
§3   Experimental Results

3.1   Introduction to §3

We present in this section a full analysis and description of the crystal structure at 279K of the molecular complex system deutero-benzene-hexafluorobenzene, $C_6D_6 \cdot C_6F_6$. An introduction to this system is given in §3.2 and experimental considerations are outlined in §3.3.

The structure of this system has been determined for the first time as rhombohedral, space group R3m, and of unit cell dimensions $a = 7.310(19)\overset{o}{A}$ and $\alpha = 109.67(43)^{o}$, giving a unit cell volume of $299(5)\overset{o}{A}{}^{3}$. There is one molecule of each species within the unit cell and they are alternately arranged in infinite stacks along the unique [111] crystallographic direction, the molecular planes being perpendicular to this direction.

Both constrained and unconstrained refinements have been done and the results of both are presented in §3.4. The constraints consisted of rigidly fixing the bond lengths and geometry of the molecules such that the resulting hexad symmetry axis was coincident with the unique axis of the structure. The unconstrained model relaxes the fixed bond lengths but the hexad symmetry is retained.

The crystal structure and molecular packing are discussed in §3.5 with respect to the constrained refinement results, which suggest that the different molecular species are rotationally staggered by 30° about the unique axis, and that the structure is in fact pairs of molecules along the stack direction. The inter- and intra-pair separations are found to be $\sim 3.72\overset{o}{A}$ and $\sim 3.52\overset{o}{A}$ respectively. Conclusions to be drawn are presented in §3.6.

3.2   Introduction to the $C_6D_6 \cdot C_6F_6$ system

Considerable interest was generated by the report by Patrick et al.[17] of the existence of several molecular complexes between hexafluoro-benzene (HFB) and various aromatic hydrocarbons. A great variety of studies of these complex systems using different experimental techniques have been performed and an account of some of that work is reviewed here.

Thermodynamic measurements by Duncan et al.[18,19] were done in order to establish the phase diagrams, amongst other properties, of several molecular complexes involving HFB, including HFB-benzene. Gilson et al.[20] have made nuclear magnetic resonance (NMR) measurements on the HFB-benzene system, and reported line width and second moment transitions at about 90K on cooling. They conclude that these transitions are probably caused by reorientations about the six fold axis of the molecules. Spectroscopic[21] and dipole[22] measurements of complexes containing HFB do not show any evidence of charge transfer between the different species of molecules as was first assumed by Patrick et al.[17] This led to the X-ray diffraction studies of Dahl[23,24,25] performed to gain information concerning the inter-molecular forces present in the two complexes HFB-mesitylene and HFB-hexamethylbenzene. Dahl[23,24,25] concludes that the possibility of forces stronger than the van der Waals type should not be ignored in these systems.

The differential scanning calorimetry measurements done by Brennan et al.[26] on the HFB-benzene system demonstrated a thermal anomaly at 249K on warming and at 246K on cooling. However, the work done by Gilson et al.[20] showed no unusual NMR behaviour at $\sim$ 250K.

More recently Potenza et al.[27] have determined the crystal

structure of the closely related complex system naphthalene-octa-
fluoronaphthalene. The molecules were found to be arranged in infinite
stacks, alternating in the two species, and where the differing
species are laterally displaced, relative to each other, by about 1.4Å.

Further calorimetric and NMR experiments on the HFB-benzene-d_6
system have been done by Ripmeester et al.[28] and they observed a
number of transition phenomena at temperatures of 199K, 247.5K and
272K on warming. They also propose that the HFB molecule is rotational-
ly disordered to some extent in the temperature range 100K to 300K
in accord with the observations of Gilson et al.[20] The transition at
247.5K is in agreement with the calorimetric work of Brennan et al.[26]
Recently the Raman light scattering technique was used in order to
probe the temperature dependence of the dynamics of the HFB-benzene
system[29]. This work is described in detail in §4, Chapter 2.
Polycrystalline samples, both protonated and deuterated, were studied
in this work in the temperature range 4.2K to 300K, and a structural
phase transition was reported at ∿ 170K on cooling and ∿ 200K on
warming. This will be related to the thermal anomaly at 199K reported
by Ripmeester et al.[28] Since the crystal structure was unknown at any
temperature, this prompted the present X-ray diffraction study of a
small single crystal of the 1:1 molar complex HFB-benzene-d_6 at
just below room temperature. Previously, Small[30] had reported a very
weak X-ray diffraction pattern for this system at room temperature.

3.3 Experimental considerations

Constituent chemicals were obtained from the Imperial Smelting Co.
(C_6F_6, stated purity 99.95%) and Fluka Chemicals (C_6D_6, stated
purity 99.6% at.) and were used without further purification. The
mixture used was prepared by using a titration burette which could
measure volume to an accuracy of ∿ 0.05 cm^3. Approximately 20 cm^3 of

mixture was prepared and this was equimolar in the two constituents to ∿ 0.3%.

A sample was prepared by sealing some of the frozen, polycrystal-line, mixture in a Lindemann capillary tube of diameter 0.5 mm and approximate length 4 mm. To avoid any combustion, and hence contamina-tion from the combustion products, that would result by sealing the ends of the tube by melting the glass, the sample tube was sealed with glue, and then attached directly to the goniometer head. This gonio-meter arrangement was then mounted on an Enraf-Nonius CAD-4 4-circle diffractometer.

The zone refining technique was used to grow the crystal on the diffractometer, using a fine wire, of diameter ∿ 0.5 mm, as the heater. Since the materials used were impure before mixing, this crystal growing technique would aid in the partial purification of the mixture. Several attempts at growing the crystal resulted in a single crystal specimen ∿ 2 mm in length, and nitrogen gas cooling apparatus was used to maintain the crystal at a temperature of about 280K, well below its melting point of about 297K. Great care had to be taken when growing the crystal to ensure that the temperature of the cold nitrogen stream was above 272K, where the constituent chemicals tended to supercool and then solidify below their natural individual freezing points of about 279K. If a crystal was grown below 273K then it was found to be a mixed crystal of the required molecular complex and one of the constituents.

The crystal gave a distinct diffraction pattern and it was also observed that considerable diffuse scattering was present underneath the Bragg reflections, but this has not been measured and analysed. Undoubtedly this diffuse scattering is related to the dynamical dis-order reported by Ripmeester et al.[28].

The data were collected using a CAD4 diffractometer operating with filtered CuKα radiation of wavelength $\lambda = 1.5405\overset{o}{A}$. 1487 reflections were measured in concentric shells out to $(\sin\theta)/\lambda = 0.532\overset{o-1}{A}$ in reciprocal space (corresponding to a maximum scattering angle of $2\theta = 110^{o}$), with three control reflections being measured once each every hour for $2\theta \lesssim 60^{o}$ and every 2 hr. for $2\theta \gtrsim 60^{o}$. The average sample temperature throughout the experiment was 279(1)K. The beam width used was 0.4 mm at the sample, this value being taken from the collimator specifications. The shape of the crystal relative to the incident beam is not the optimum spherical shape that would normally be chosen, had the choice been available. This problem was partially overcome in the analysis by applying a rudimentary volume correction to the measured integrated intensities, the form of which will be given in the next section.

3.4   Results and analysis

The raw data consisted of 1487 integrated intensities grouped over 150 symmetry independent reflections, both the reflection and its Friedel pair having been measured. The time variation of the integrated intensities of the three control reflections throughout the experiment has been plotted and the result is shown in Figure 1.5. This figure shows that these variations were less than 4% from the corresponding mean integrated intensities, indicating that the experimental conditions under which the data were measured were satisfactorily stable. The linear absorption coefficient was calculated as 14.14 cm^{-1}, which gives a reduction in intensity of the beam of ∿ 49% for a path length of 0.5 mm in the crystal. However, no corrections were applied to account for any possible variation

Figure 1.5:   The variation of the control reflections

throughout the experiment. The intensity

of the (200), (11$\bar{1}$) and (1$\bar{2}$0) reflec-

tions are plotted against the Nth control

count. Up to a control count of 40 the

control reflections are monitored hourly,

thereafter two hourly. Full lines are a

guide to the eye only.
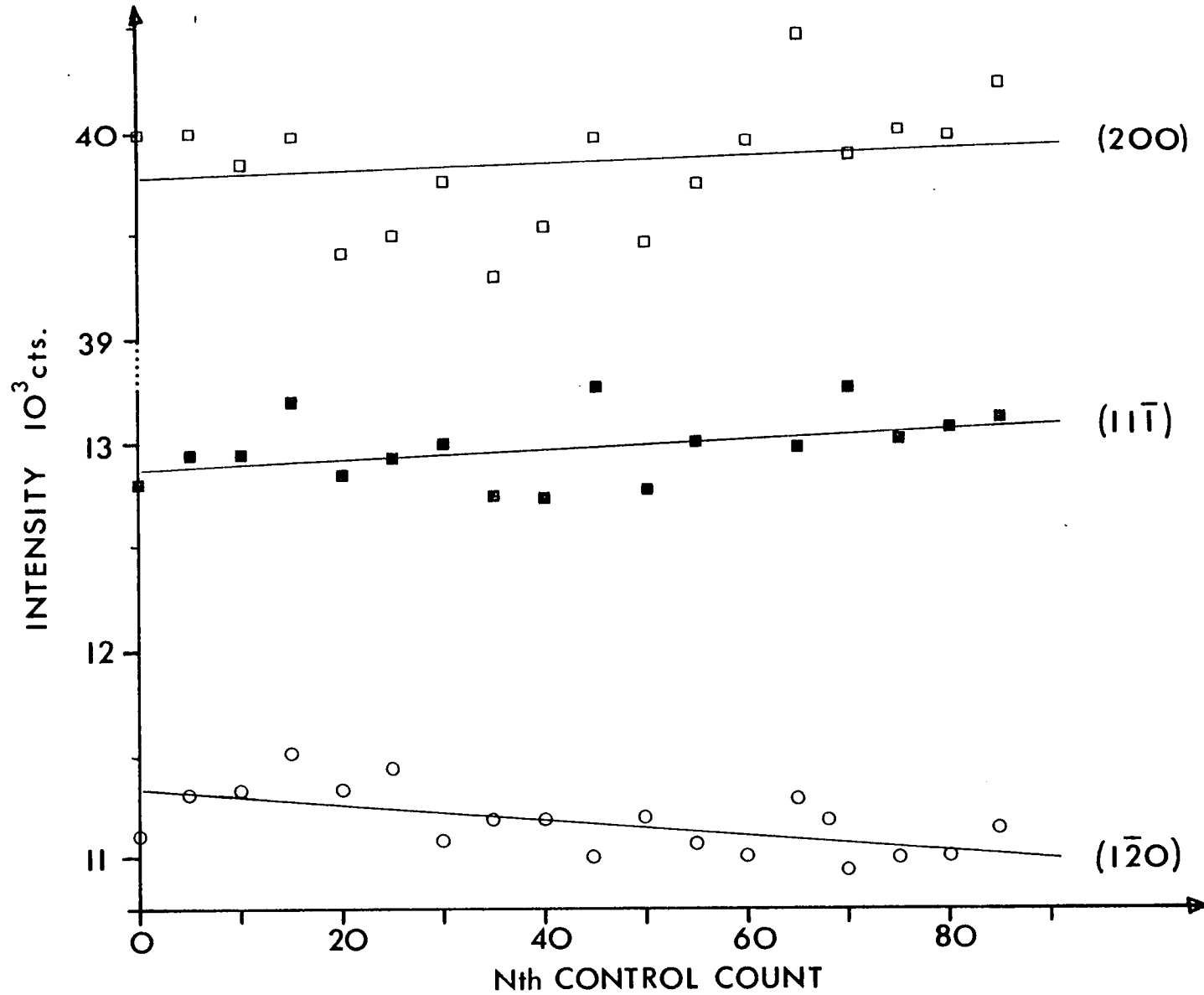
FIG. 1·5

in the diffracted beam intensity caused by the absorption process.
This was justified in terms of the asymmetrical crystal shape relative
to the incident and diffracted beams. The process of extinction (see
section §2.5) becomes important only when crystals of very high per-
fection are used, and therefore in the present study this process is
ignored. From hereon in this chapter we use the word intensity to
imply integrated intensity.

From an initial analysis of the reflection intensities it was
seen that about 30 were spuriously high in intensity relative to the
other reflections in the same proposed symmetry related group. The Miller
indices of these reflections were analysed with a knowledge of the indices
of the 9 reflections whose intensity exceeded 5×10^5 counts, and it
was found that all of the spurious intensities could be explained as
being double Bragg scattering processes (§2.6). The most pronounced
case of this double scattering process was the $(\overline{5}13)$ reflection
(and its Friedel pair), whose intensity was approximately twenty
times that of the average intensity taken over the other reflections
in the same group. The $(\overline{5}13)$ reflection indices are equivalent to
the $(\overline{3}03) + (\overline{2}10)$ indices. These 30 spurious intensities were there-
fore removed from the data set, making a reduced total of 1457 re-
flections.

The correction to be applied that accounts approximately for the
volume variation of the crystal in the incident beam is of the form
$I = I_o \cosec \delta$, where I_o and I are measured and corrected inten-
sities respectively. The angle δ is that between the incident beam
direction and the axis of the cylindrical tube in which the crystal
is contained. With a knowledge of the four orientation angles
$(\theta, \phi, \omega, \kappa)$ the angle δ may be found by setting up the crystal
orientation matrix equations in the four angles above. The angle δ

follows from taking the dot product between the vector along the axis
of the sample tube and that describing the incident beam direction.
The result is that

$$1.(44) \qquad \cos\delta \quad = \cos\omega\sin\varepsilon\cos\varepsilon(1 - \cos\kappa) + \sin\varepsilon\sin\omega\sin\kappa \quad ,$$

where the angle ε is a fixed parameter of the instrument, and is equal
to 50°. From equation 1.(44) $\cosec \delta$ is easily found and this quan-
tity was calculated for each individual reflection. It is convenient
at this point to introduce an overall consistency factor in order to
test whether or not the above correction makes an improvement on the
data. This quantity will be defined as

$$1.(45) \qquad R_{overall} \quad = \quad \left| \frac{\sum_{j} (\sum_{i} |\bar{I}_j - I_{ij}|)}{\sum_{j} (\sum_{i} I_{ij})} \right| \quad ,$$

where the sum over i is for a proposed individual symmetry group
of reflections of intensities I_{ij} and mean intensity $\bar{I}_j$, and the
sum over j runs over the 150 symmetry independent groups. $R_{overall}$
had the value ~ 12.0 for the raw data and ~ 8.5 for the volume cor-
rected intensities. This indicates a considerable overall improve-
ment in the data, and therefore the corrected intensities are used
in the refinements.

A similar consistency factor defined by

$$1.(46) \qquad R_{internal} \quad = \quad \frac{\sum_{i} |\bar{I} - I_i|}{\sum_{i} I_i}$$

was calculated for each symmetry independent group of reflections.
For the most intense 51 groups, the average of this internal con-
sistency factor was 0.055, which gives an indication of the quality
of the data. In this case, the value of $R_{internal}$ means that the

data is not of the highest quality, but it must be remembered that the shape of the crystal is non-uniform with respect to the incident and diffracted beams and that no account has been made for the absorption or extinction processes.

Of the different rhombohedral space groups only two, $R\bar{3}m$ and R3m, were found to be consistent with the groupings of the indices of the reflections. There are statistical ways of determining whether or not a centre of symmetry is present, such as Wilson's test[31], but it is not possible to determine this given only a reflection and its Friedel pair.

The crystal symmetry of the two possible space groups means that the molecular planes are necessarily aligned perpendicular to the unique axis of the structure but there are four possible relative orientations of the two species of molecule about this axis. We choose to set the benzene molecule at the origin and the HFB at the body centre position. These four distinct possibilities arise since an atom must either lie on a mirror plane or midway between a pair of such planes. In order to distinguish easily between these various structural models in the text that follows, abbreviations are introduced where 'D' indicates the carbon-deuterium pair in the benzene molecule and 'F' the corresponding pair in the HFB molecule. The abbreviations used are:

DOM   only 'D' on mirror planes.

FOM   "   'F'   "   "   "

AOM   all atoms on mirror planes

NOM   no   "   "   "   "   .

For atoms that lie on a symmetry plane in this structure the possibility of 'puckering' of the molecules is allowed as there is no molecular hexad symmetry axis. This has not been included in the

calculations but the structural models that would allow this molecular distortion, along with the relations between the fractional coordinates and the anisotropic temperature parameters, are indicated in Table 1.1. Also given in Table 1.1 for each model is an indication of the possibility of one of the molecules being displaced from its centre of symmetry, thereby reducing the space group symmetry. This last aspect of the analysis is given in greater depth later, the purpose of Table 1.1 is merely to give a clear indication of the molecular distortions and translations allowed by each structural model within the space groups considered in the absence of any constraint on the molecular geometry.

The constraints that are used fix the molecular geometry to be planar, and to have a hexad symmetry axis that is parallel to the unique axis of the structure. This means that the puckering of the molecules mentioned above is not allowed in this regime of constraints. The bond lengths are also fixed and their values are $C-C = 1.38\text{Å}$ [34], $C-F = 1.34\text{Å}$ [35] and $C-D = 1.08\text{Å}$. The unconstrained models retain the hexad molecular symmetry but relax the fixed bond lengths with the exception of the $C-D$ bond which is held fixed, and the initial values for these bonds in the unconstrained refinements are taken from those of the constrained refinement results.

The data comprising the symmetry related groups of reflections was then reduced by statistical averaging to a single value of the intensity for each group. There were 19 groups that were considered unobserved and they were left in the data set.

The refinement program is based on the familiar ORFLS[32] program but differs in that it has the facility of adding constraints in the orthogonal coordinate system[33]. The structure refinements were

TABLE 1.1:   Molecular distortions and translations

allowed by the various structural models cited

in the text within the space groups considered

in the absence of hexad symmetry of the mole-

cules. Also given are the relationships[3] of

the fractional coordinates and anisotropic

temperature parameters for atoms on (a) and midway

(b) between symmetry planes.

Space group: R$\bar{3}$m

Model	Puckering allowed in absence of hexad axis	Translation along unique axis
DOM	C–D only	
FOM	C–F only	Not allowed in R$\bar{3}$m
AOM	C–D, C–F	
NOM	None	

Space group: R3m

Model	Puckering allowed in absence of hexad axis	Translation along unique axis
DOM	C–D only	
FOM	C–F only	Allowed for all models in R3m
AOM	C–D, C–F	
NOM	None	

	x_f	y_f	z_f	β_{11}	β_{22}	β_{33}	β_{23}	β_{31}	β_{12}
(a)	x	x	-2x	A	A	C	D	D	E
(b)	x	-x	z	A	A	C	D	-D	E

TABLE 1.1

started using an overall scale factor and an overall isotropic tempera-
ture parameter, with extra isotropic thermal motion allowed for the
fluorine atoms. Both the constrained and unconstrained calculations
were done and the philosophical justification for performing the
constrained refinements is given later in the discussion of the
analyses in section 3.5 and more fully in Chapter 3, §3.5. The
molecules are forced to have a hexad symmetry axis and so in the case
of the unconstrained refinements one molecule is specified by one
coordinate for each of two atoms. This means that the number of para-
meters in the initial refinements is three in the constrained case and
six in the unconstrained case.

The results of the initial refinements are given in Tables 1.2a
and 1.2b for the constrained and unconstrained cases respectively,
and are labelled as rows I. These tables give, in the first two
columns, the model abbreviation and the R factor defined by

$$1.(47) \qquad R \quad = \quad \frac{\sum\limits_{j} w_j \left| I_j^{calc.} - I_j^{obs.} \right|}{\sum\limits_{j} I_j^{obs.}} \quad ,$$

where the j labels the intensity of the jth observed $(I_j^{obs.})$ and
calculated $(I_j^{calc.})$ symmetry independent reflection. The weight
associated with the jth reflection is w_j, and unit weights were used
throughout. The function that is minimised in all refinements is

$$1.(48) \qquad R_W \quad = \quad \sum\limits_{j} w_j (I_j^{calc.} - I_j^{obs.})^2$$

and the value of this is given in column 3 of Tables 2a and 2b. The
corresponding refined parameters are given in the other columns, along
with their respective standard deviations in parentheses and where
appropriate, isotropic temperature parameters are given.

TABLES 1.2a, 1.2b: Salient results from the constrained

(Table 1.2a) and unconstrained (Table 1.2b)

refinements. All bonds and the shift para-

meter are in $\overset{\text{o}}{A}$ and the isotropic tempera-

ture parameters ($TO_{C,D}$ for carbons and

deuteriums, TO_F for the fluorines) are

in genuine $\overset{\text{o}2}{A}$ units. The rows labelled

I, II, III and IV are as follows:

I   Isotropic refinements in $R\bar{3}m$

II   Isotropic refinements in R3m with the

shift parameters refined

III Anisotropic refinements in $R\bar{3}m$

IV as III but using the strongest 51

reflections.

TABLE 1.2a

Model	R	R_W $(\times 10^{12})$	$TO_{C,D}$	TO_F	Shift	
NOM	0.174	1.40	0.19(4)	0.27(5)	-	
DOM	0.182	1.36	0.18(4)	0.28(5)	-	I
AOM	0.442	5.57	0.20(8)	0.36(14)	-	
FOM	0.393	5.12	0.17(7)	0.40(13)	-	
NOM[††]	0.174	1.40	0.19(3)	0.27(-)	0.034(46)	
DOM[††]	0.179	1.32	0.18(3)	0.28(-)	0.096(22)	
AOM[*]	0.443	5.51	0.18(7)	0.35(-)	0.155(32)	II
FOM[*]	0.397	4.88	0.16(6)	0.38(-)	0.215(21)	
NOM	0.184	0.684	-	-	-	
DOM[†]	0.167	0.676	-	-	-	III
NOM	0.160	0.628	-	-	-	
DOM	0.138	0.624	-	-	-	IV

[*] These refinements had an initial shift of 0.01 Å

[†] A full parameter set is given in Table 1.3.

[††] These refinements had an initial shift of $\sim$ 1.02 Å

TABLE 1.2b

Model	R	R_W (×10^{12})	C-C	C-C	C-F	$TO_{C,D}$	TO_F	Shift	
NOM	0.134	0.611	1.20(4)	1.33(3)	1.35(3)	0.19(3)	0.23(3)	-	
DOM	0.133	0.643	1.21(3)	1.34(3)	1.33(3)	0.18(3)	0.24(4)	-	I
NOM[††]	0.135	0.614	1.21(5)	1.33(4)	1.34(4)	0.19(2)	0.23(-)	0.015(22)	
DOM[††]	0.133	0.643	1.21(4)	1.34(4)	1.32(4)	0.18(3)	0.23(-)	0.015(32)	II
NOM	0.098	0.154	1.20(3)	1.38(3)	1.33(3)	-	-	-	
DOM	0.104	0.159	1.16(3)	1.31(4)	1.42(3)	-	-	-	III
NOM	0.080	0.137	1.19(5)	1.39(6)	1.31(5)	-	-	-	IV

[††] These refinements had an initial shift of $\sim$ 1.02 $\overset{o}{A}$.

It is apparent on studying Table 1.2a that the structural models that place the fluorine atoms on the symmetry planes (models FOM and AOM) give a considerably poorer fit to the data than do the models that put these atoms midway between these planes. This means that the structural models that would allow a puckering distortion of the HFB molecule in the absence of any molecular constraint give the poorest fit to the data, and for this reason the constraints on the bond lengths are not lifted for models FOM and AOM.

The above refinements have been done for the space group $R\bar{3}m$, the highest symmetry consistent with the data. However, the other possibility, R3m, must also be considered. In order to reduce the symmetry we must introduce a further parameter into the refinement in the form of a shift of one of the molecules, chosen arbitrarily to be the HFB, along the unique axis of the unit cell. This corresponds to a dimerisation of the molecules and we call this the shift parameter   ,the variation of which alters the separation of the molecules along the unique axis.

Further refinements were done using the overall scale factor and the overall isotropic temperature parameter for the constrained molecules, with the addition of atomic coordinates in the unconstrained case, as well as the shift parameter described above. The shift parameter was found to be very highly correlated with the extra thermal motion parameter for the fluorine atoms. The latter was therefore fixed in these refinements. The sense of the shift parameters is unimportant since the reflection intensities are invariant under a change of sign of this new parameter. As a result of this invariance, if the refinement is initiated with zero shift then the parameter changes calculated by the refinement will be arbitrary and the result indeterminate, and this means that the refinement cannot

converge to the minimum in parameter space. Therefore, it is necessary

to initiate the refinement with a small non-zero shift in order to

obtain an interpretable result. Several such starting values were

tried, with the initial values of the other parameters the same for

each refinement, and all parameters were refined. This was done for

both the constrained and unconstrained cases for models NOM and DOM

and some of the results are given in Table 1.2a, 1.2b rows II. The

results for all four models in the constrained case are presented,

but for the unconstrained case, the models AOM and FOM were unstable

and so their results are not tabulated. That this instability exists

is probably because these unconstrained models are far enough from

the minimum that the refinement cannot converge.

The constrained models that give the best results for the above

refinements are DOM and NOM, and a diagram for each model illus-

trating all of these results is displayed as Figures 1.6a and 1.6b

respectively. These figures show the R factor for the initial

conditions described above versus the initial shift and the inset

shows the final R factor to which the refinement converges when

all parameters are refined, such that a parameter set describing a

point on the initial R factor curve refines to a corresponding

parameter set in the inset. These points are labelled 1, 2, 3, ...

Also given in these figures are points corresponding to parameter

sets to which the refinement converges if the shift parameter is held

fixed at non-zero values whilst all other parameters are refined.

The discussion and interpretation of these results and figures

is postponed until §3.5, the purpose at present being to give the

results of the analyses.

We now introduce anisotropic thermal parameters, β_{ij}, for the

best models NOM and DOM, for both constrained and unconstrained cases.

Figures 1.6a, b: Plots for models DOM and NOM

(respectively 1a, 1b) showing the

variation of:

(i)   initial R factor against initial

shift (●)

(ii)   final R factor against the initial

shift when all parameters except the
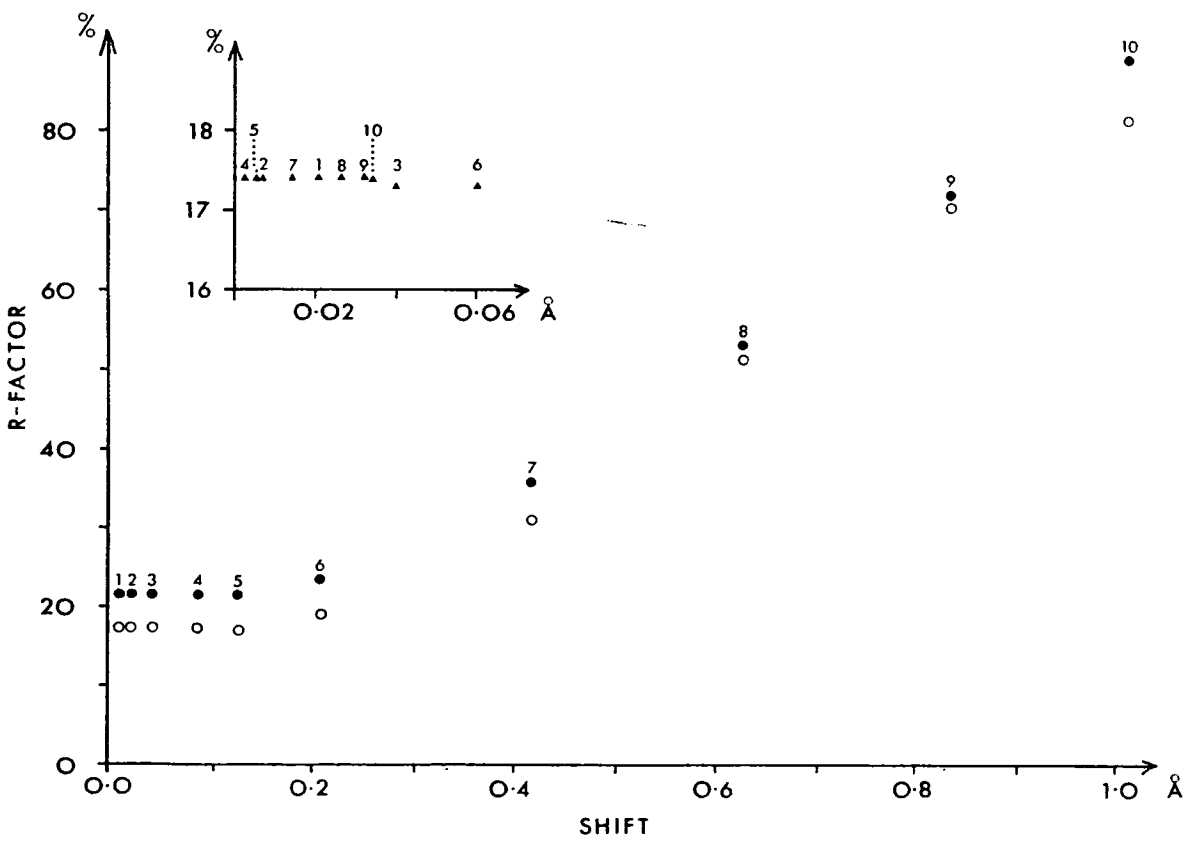
shift are refined (O).

The inset shows the variation of the final R

factor against the refined shift, when all

parameters are refined (▲).

R factors are given in % and shifts in $\overset{o}{A}$.
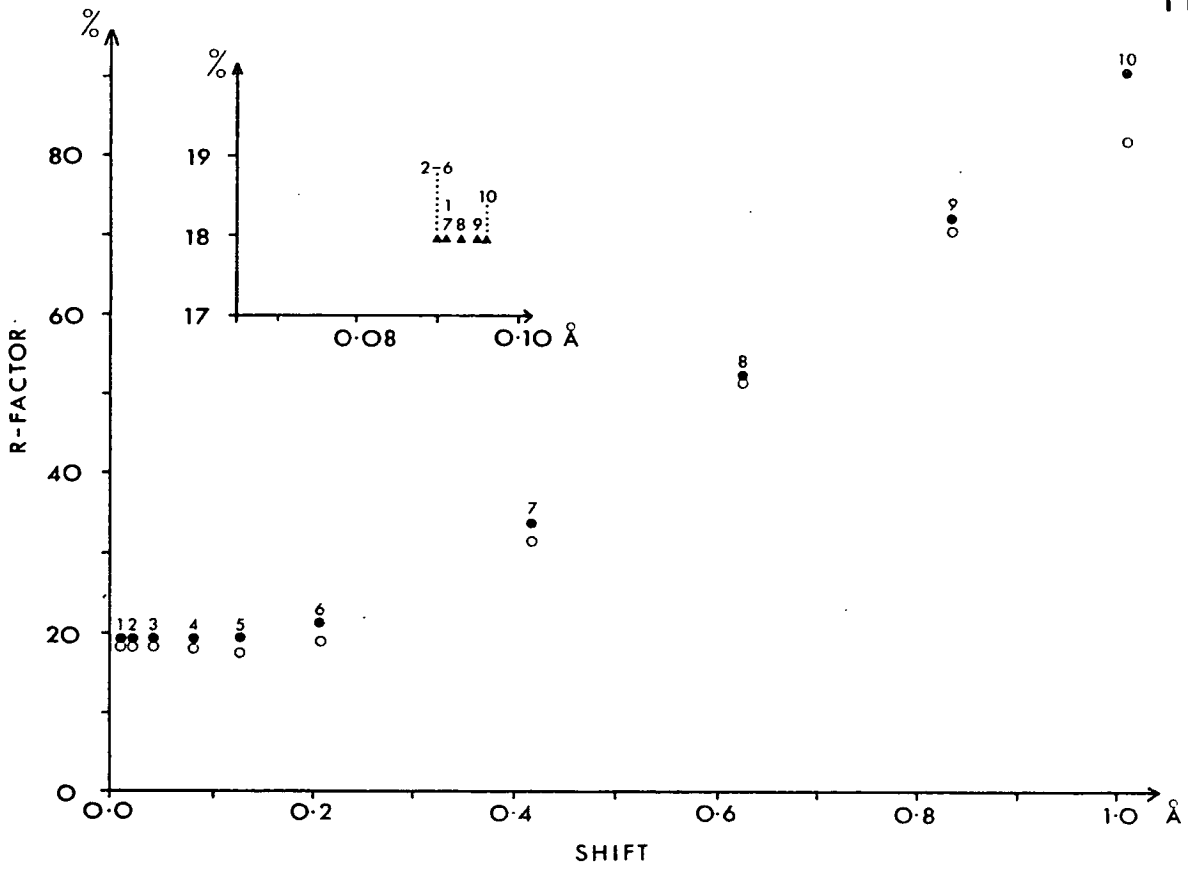
FIG.1·6a,b

The definition of these parameters is given in Table 1.3. The justification for introducing more parameters into the refinement is based upon the value calculated for the internal consistency factor. Experience shows that the expected best R factor is somewhat greater than this internal consistency factor, but possibly as low as 0.08. The best R factors obtained have been 0.174 and 0.133 for the constrained and unconstrained refinements, so that it should be possible to reduce this value further, and the only course open is to introduce the β_{ij}.

Mention must be made at this point of the correlation between the β_{ij} and the shift parameter. The use of anisotropic thermal parameters implies that the atoms move in such a way that the so-called surfaces of constant probability are ellipsoids. Consider, then, the HFB molecule at the body centre of the unit cell undergoing isotropic thermal motion. The shift parameter is then varied, and since the sign of the shift is either positive or negative with equal weight, we may think of the isotropic, spherical surface of constant probability being elongated along the direction of shift. If now the isotropic thermal motion is replaced by anisotropic parameters and the shift parameter is again varied, the latter variable elongates the already ellipsoid shape of the constant probability surface. This leads to two sets of parameters performing much the same role in the refinement and hence ill conditioning of the least squares matrix results. We therefore set the shift parameter to zero and fix it throughout the remainder of the calculations described. The crystal symmetry is therefore increased to $R\bar{3}m$ again, the symmetry of the structure of the initial isotropic refinements.

It has already been pointed out that the atomic coordinates, and

also the β_{ij}'s, are interrelated and these relationships have been given in Table 1.1. The result is that one coordinate and four independent β_{ij}'s are necessary to describe an atom. Some of the β_{ij}'s for different atoms were found to be highly correlated and were therefore removed from the variable list. This meant that, in the case of constraints, of the 13 possible parameters only 12 for DOM and NOM were varied, whereas in the unconstrained case, of the 16 possible parameters only 13 for NOM and 14 for DOM were varied. Where a parameter is held fixed, the tabulated standard deviation is left blank. These results are given in Tables 1.2a, 1.2b in rows III. From these tables it is seen that the constrained and unconstrained 'best fits' occur for different structural models. The minimum value of R_W is obtained with model DOM for constrained refinements and model NOM for unconstrained refinements and the implications of this are discussed shortly. The final R factor for the constrained and unconstrained cases are 0.167 and 0.098 respectively and the final parameter set values are given for the constrained model DOM in Table 1.3, with standard deviations where applicable, and a list containing observed and calculated intensities is given in Table 1.4. The R factor was further reduced to 0.138 and 0.080, for the respective constrained and unconstrained refinements, by repeating the above anisotropic thermal parameter calculation but using a reduced data set consisting of the strongest 51 reflections whose intensities exceeded 4000 counts. The unconstrained refinement R factor of 0.080 is consistent with the limit set by the previously calculated internal consistency factor. No further reduction of the R factor is expected and the results of these refinements are given in the final rows (IV) in Tables 1.2a and 1.2b.

TABLE 1.3: Full parameter set for the anisotropic constrained refinements of model DOM. The temperature parameters β_{ij}, are defined by $\exp - [\beta_{ij} h_i h_j]$ $i,j = 1,2,3$ using the summation convention. All coordinates and bond lengths in orthogonal $\overset{\circ}{A}$ units, temperature parameters in genuine $\overset{\circ}{A}^2$ units.

TABLE 1.3

par. atom	x	y	z	β_{11}	β_{22}	β_{33}	β_{23}	β_{31}	β_{12}
C	0.5636	0.5636	-1.1272	0.232(95)	0.232(95)	0.445(153)	-0.041(55)	-0.041(55)	-0.025(69)
D	1.0048	1.0048	-2.0096	0.232(95)	0.232(95)	0.445(153)	-0.041(55)	-0.041(55)	-0.025(69)
C	1.1149	3.0651	2.0900	1.092(280)	1.092(280)	0.588(223)	-0.182(-)	0.182(-)	0.417(185)
F	0.1705	4.0095	2.0900	0.487(57)	0.487(57)	0.211(33)	0.018(58)	-0.018(58)	-0.327(25)

TABLE 1.4:   Reflection indices with their corresponding

observed and calculated integrated intensities

for the final constrained refinement in model

DOM, row III in Table 1.2a. They are tabulated

in order of increasing 2θ.

It will be noted that some observed intensities

are negative. This arises because of the

background subtraction technique in evaluating

the measured integrated intensity of a

reflection.

H	K	L	I(OBS)	I(CALC)	I(SIG)
-1	0	1	2514086	2501874	50065
0	-1	0	1662983	1683445	22456
-1	1	1	787535	649549	8620
-2	1	1	143407	229548	2678
-1	2	0	883706	836476	7405
0	-1	-1	8289119	8280386	148781
-2	0	2	1327530	1426976	15400
0	-2	0	211877	90106	3511
-2	2	1	93085	10139	691
-1	2	1	214436	253119	1881
-1	3	-1	1111665	1181017	19132
-1	-1	-1	1140344	1047699	25540
-3	1	2	16794	1999	650
-2	3	0	8477	162372	112
-1	3	0	52167	57	1582
0	-2	-1	38945	351547	508
-2	2	2	70730	152923	1444
-3	0	3	589090	23397	13370
-3	2	2	272682	350190	3838
-2	3	1	258037	202148	3052
-1	2	2	330	153970	41
0	-3	0	192	28155	49
-3	3	1	33069	25702	396
-1	3	1	18069	152543	263
-2	4	-1	141	29084	33
-1	4	-1	16629	29278	275
-1	-2	-1	830919	571319	24901
-4	2	2	26229	14113	648
-2	4	0	132067	24141	1484
0	-2	-2	54123	2853	975
-4	1	3	72156	28633	871
-3	4	0	33293	3745	467
-3	3	2	17389	448	265
-2	3	2	23866	37935	307
-1	4	0	24710	35776	314
0	-3	-1	1970	21459	90
-4	2	3	22212	3182	307
-3	4	1	50438	2339	649
-2	4	1	16785	6643	208
-1	3	2	10588	2866	165
-4	0	4	1404	19204	97
0	-4	0	279	31460	44
-4	4	1	419	2834	37
-5	2	2	6101	38575	97
-2	5	-1	6887	3300	141
-1	4	1	33307	21804	463
-1	-2	-2	2203	3047	51
-3	5	-1	800	5724	40
-3	3	3	913	31152	44
-1	5	-1	1126	32816	44

H	K	L	I(OBS)	I(CALC)	I(SIG)
-1	-3	-1	589	25766	47
-5	2	3	4997	307	231
-4	3	3	139	12220	117
-3	5	0	48	253	35
-3	4	2	2508	8611	68
-2	5	0	2958	1802	63
-2	3	3	1582	13655	140
0	-3	-2	770	6231	33
-4	4	2	1	4816	32
-2	4	2	14184	6711	269
-5	1	4	4874	31	94
-4	5	0	6652	118	95
-1	5	0	3368	976	76
0	-4	-1	73	239	41
-5	3	3	4488	10869	118
-3	5	1	529	9	35
-1	3	3	810	35812	56
-5	2	4	940	2550	54
-4	5	1	3586	2572	136
-2	5	1	4087	217	84
-1	4	2	380	2487	129
-2	6	-2	10407	342	264
-2	-2	-2	54477	78620	3350
-5	0	5	553	887	54
-6	2	3	4567	525	64
-3	6	-1	2889	1885	74
-4	4	3	65	113	39
-2	6	-1	484	1129	44
-3	4	3	-35	96	46
0	0	-5	10	7070	82
-1	-3	-2	9411	114	130
-5	5	1	-39	29	35
-1	5	1	214	11	38
-6	3	3	9484	1033	182
-5	4	3	5246	5	118
-4	6	-1	22	127	39
-4	5	2	68	462	44
-3	6	0	81	290	36
-3	5	2	15	52	35
-1	6	-1	722	11	53
-2	4	3	-28	353	35
0	-3	-3	-3	760	52
-1	-4	-1	-66	706	52
-6	2	4	1279	1092	48
-4	6	0	69	382	37
-2	6	0	137	985	36
0	-4	-2	1011	4478	38
-5	5	2	192	34	45
-2	5	2	43	78	35
-6	3	4	506	60	39

H	K	L	I(OBS)	I(CALC)	I(SIG)
-6	1	5	376	98	34
-5	6	0	638	34	50
-4	6	1	24	42	33
-3	6	1	50	430	33
-1	6	0	16	360	42
-1	4	3	1057	0	55
0	-5	-1	930	21	48
-4	4	4	1221	1474	119
-6	2	5	59	16	34
-5	6	1	251	40	33
-3	7	-2	538	5	44
-5	4	4	463	1057	101
-2	7	-2	789	568	57
-4	5	3	313	399	44
-3	4	4	-17	1059	65
-2	6	1	-42	27	32
-1	5	2	880	255	41
-2	-3	-2	0	168	48
-7	3	3	176	355	47
-5	5	3	31	251	35
-3	7	-1	44	59	35
-3	5	3	-49	732	46
-1	-3	-3	-106	31	62
7	-2	-4	-61	88	31
-4	7	-1	0	13	32
-2	7	-1	598	36	31
-1	-4	-2	19	524	29
-6	0	6	211	5	37
-6	4	4	184	331	38
-4	6	2	9	69	34
-2	4	4	-7	718	45
0	-6	0	-28	4	36
-7	3	4	-85	0	25
-6	1	6	110	0	24
-6	5	3	54	138	25
-5	6	2	50	4	26
-4	7	0	49	0	26
-3	7	0	8	0	31
-3	6	2	38	0	25
-2	5	3	38	179	28
-1	6	1	-8	105	25
0	-4	-3	-0	98	25
-5	-1	7	29	2	24
-1	7	-1	167	277	39
-1	-5	-1	-72	391	34
-7	2	5	-7	11	23
-5	7	0	61	7	25
-2	7	0	20	13	26
0	-5	-2	-1	42	24
-6	6	2	-7	3	24

REFLECTION INDICES , OBSERVED , CALCULATED AND THE OBSERVED
STANDARD DEVIATION INTENSITIES FOR THE C6D6.C6F6 SYSTEM AT 280K.

Table 1.4

-41a-

3.5   Discussion of results and analyses

The isotropic refinements give values of the temperature parameters that are large, especially for the C-F pair in HFB. This is in accord with the observation of Ripmeester et al.[28] that the HFB molecule is to some extent dynamically disordered in the temperature range 100K to 300K. These large amplitudes of thermal motion are undoubtedly connected with the presence of thermal diffuse scattering observed in unpublished X-ray photographic work, done by the author, on single crystals of the same complex system.

The introduction of anisotropic thermal parameters into the refinement procedure was justified in terms of the internal consistency factor. Their subsequent refinement shows that the principal temperature parameters (β_{ii}) have large values, and this is again in qualitative agreement with the observations of disorder by Ripmeester et al.[28] A structural model for the possible disorder of the HFB molecule was not explicitly included in the refinements that have been presented, but the values of the thermal vibration parameters do suggest that large amplitudes of thermal motion are present in this structure, in fact far larger than those present in the benzene crystal where the largest anisotropic mean square displacement has a value $\sim 0.09 \ \overset{\circ}{A}{}^{2}$ [34]. In the present structure we have a largest value of $\sim 1.1 \ \overset{\circ}{A}{}^{2}$.

The results for the unconstrained models, given in Table 1.2b, give a refined C-C bond length of $\sim 1.20 \ \overset{\circ}{A}$ in all cases, and this is not a satisfactory result. This is an example of where the unconstrained model gives a better R-factor and fit to the data than does the constrained model, but where certain refined parameter values do not correspond to those which are generally accepted. In this

case, it is known that a C-C bond of $\sim$ 1.20 Å is too short by about 13%, so any comparison between the structural models DOM, NOM, ... etc. must be made using the constrained model results. The philosophy of constraints is described in Chapter 3, §3.5. However, the basic tenet is that it is always better to include parameter values in the refinement that are known more accurately than the measured data could possibly determine, thereby increasing the reliability of the other variables that are refined. Therefore, the comparison of the different structural models, NOM and DOM, with respect to the shift parameter will be based upon the constrained results obtained for these models.

The introduction of the shift parameter reduced the symmetry of the structure used in the initial refinements to R3m by removing the $\bar{1}$ centre. It has been said that the sense of the shift is unimportant since the diffracted intensities are invariant under the change of sign of the shift parameter. Refinements were done with this parameter varied and the results have been given in Figures 1.6a, 1.6b for the best constrained models. These results indicate that for model DOM the refined shift parameter is confined to values of 0.096 Å with standard deviations approximately 0.02 Å, giving a distribution of values between 0.08 Å and 0.12 Å. However it is seen from Figure 1.6b that model NOM gives results that suggest that the refined shift parameter has a value of $\sim$ 0.03 Å with error $\sim$ 0.05 Å, so that it is not possible to say whether or not the shift is non-zero in model NOM. The results of model DOM are therefore tentatively taken as evidence that the HFB molecule is not situated at the body centre of the unit cell, and that therefore the space group symmetry is R3m. This distortion that breaks the centre of symmetry in R$\bar{3}$m will not alter the intensity distribution by an amount that would make

statistical tests, such as that due to Wilson[31], effective. It is
therefore believed that such tests can not be used in cases where
crystal pseudo-symmetry exists.

The differences between models DOM and NOM are twofold. The
former model has the molecules eclipsed as viewed down the unique
axis, whereas in the latter the molecules are staggered. Therefore
in the absence of hexad symmetry, in model DOM the possibility of
puckering of the benzene-d_6 molecule is realised whereas in model
NOM this is prohibited by crystal symmetry. Secondly, and probably
most importantly, model DOM gives a small shift of the HFB molecule,
and this gives rise to the structure being made up of pairs of
molecules rather than the molecules of different species being
equally spaced along the unique axis. This molecular pairing means
that there are a great variety of possible stacking faults that
would cause the calculated structure (with no faults) to be only a
moderately good fit to the true, faulted structure. An example
of such a faulted structure might be ... AB AB A BA BA B AB AB ...,
where A and B represent the different molecular species within
one infinite stack. Clearly, as mentioned above, the number of such
faults that are possible is very great. This would partially account
for the seemingly poor quality of the data and the relatively high
R factor obtained in the final cycles of the constrained refinement.

The work of Dahl[23,24,25] has shown that in some HFB complexes,
forces stronger than van der Waals may be present and in the present
case the intermolecular separations are calculated to see whether
or not this is true in this system. These results are tabulated
in Table 1.5, along with the relevant van der Waals radii and separa-
tions. For Model DOM with a shift of $\sim$ 0.10 Å the nearest neigh-
bour, intrastack C...F separation observed in this system is $\sim$ 3.90 Å

TABLE 1.5:   Intermolecular distances for models NOM
              and DOM with a shift of 0.10 $\overset{o}{A}$.   Van der
              Waals radii and separations are also shown.
              All values in $\overset{o}{A}$ units.

TABLE 1.5

	radii		separations	
C	1.55	C-F	2.90
F	1.35	F-D	2.55
D	1.20	C-D	2.75

Model		Shift	C-C	C-F	F-D	C-D
NOM	intra-stack	0	3.62	3.86	3.63	3.78
NOM	inter-stack	0	-	-	2.69	-
DOM	intra-stack	0	3.69	3.99	3.87	3.90
DOM	intra-stack	0.10	3.60	3.91	3.78	3.81
DOM	inter-stack	0	-	-	2.76	-
DOM	inter-stack	0.10	-	-	2.72	-

Figure 1.7:   Projection of part of the structure in space

group   R3m,   along the unique axis.   Heights

of molecules are given in fractions of the body

diagonal.   The symmetry planes are vertical and

coincident with the rhombohedral axes shown.

Some separations are also shown (in $\overset{o}{A}$).

$\bigcirc$ ....:...   fluorine atom

$\bullet$ ....   carbon atom

$\bullet$ ....   deuterium atom.

FIG. I·7

½-SHIFT

⅓

⅔

2·72

2·80
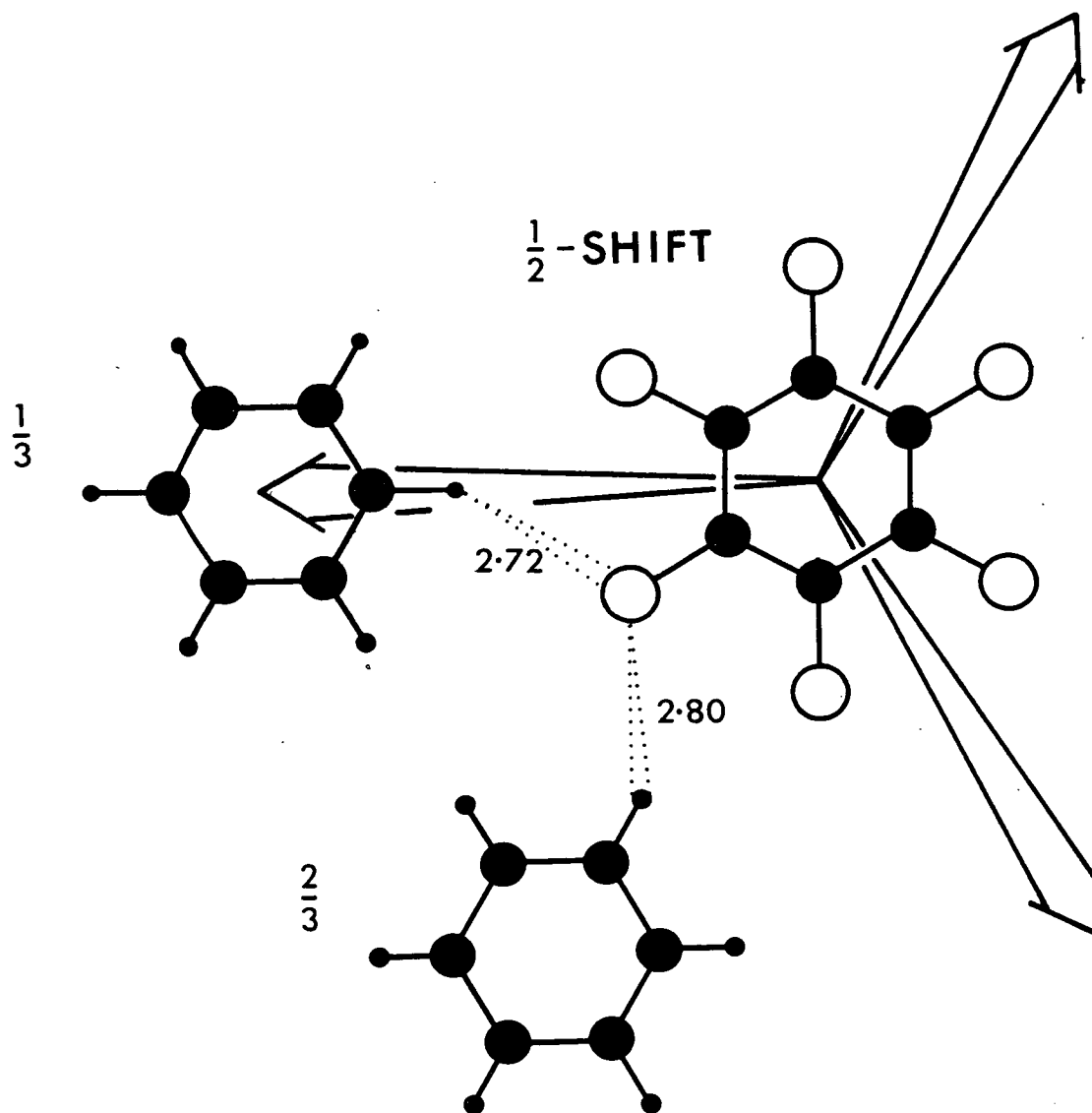
and this is about 1 Å larger than that expected from purely van der Waals interactions. Part of the rhombohedral structure is shown in Figure 1.7, and the nearest neighbour, interstack F...D separations are shown as 2.72 Å and 2.80 Å. Again, these intermolecular separations are somewhat larger than those expected from van der Waals interactions alone. These observations are not inconcistent with the evidence[21,22] that this complex does not display any charge transfer characteristics. Also, theoretical work concerning molecular com-plexes[36,37] indicates that even in strongly charge transfer systems, the stability of the complex may involve forces other than those of charge transfer. The pairing of the molecules found in the present work is therefore not inconsistent with the fact that this system is not of the charge transfer type.

Following the proposal, given by Ripmeester et al.,[28] of a degree of dynamic rotational disorder of the HFB molecule, the closest inter-stack F...D approach when the benzene-d_6 molecule is stationary whilst the HFB is rotationally disordered about the unique axis is calculated as 2.04 Å. This value is considerably less than the van der Waals separation of 2.55 Å, so it is possible that forces of a different type may be involved if the HFB molecule is disordered in the manner considered above.

Further evidence for disorder of the HFB molecule is furnished by the unit cell volume, which is observed to be 299(5)Å^3, about 13(2)% larger than that given by the sum of the two molecular volumes, ∿ 265 Å^3, calculated from the separate structures.

Before we draw conclusions from the above discussion, it is interesting to note that the rhombohedral cell that has been described may be transformed to several pseudo-structures in different crystal systems. These transformations are described by a (3 × 3) matrix, $\underline{T}$,

such that

1.(49) $\quad \underline{x}_{\text{pseudo.}} \quad = \quad \underline{\underline{T}} \cdot \underline{x}_{\text{rhomb.}}$,

where $\underline{x}_{\text{pseudo.}}$ and $\underline{x}_{\text{rhomb.}}$ are position vectors in the pseudo-
and rhombohedral unit cells respectively. We may obtain a pseudo-
monoclinic cell by the matrix $\underline{\underline{T}}$ given by

1.(50) $\qquad \underline{\underline{T}} \quad = \quad \begin{pmatrix} 0 & 1 & 1 \\ 2 & 1 & 1 \\ 0 & -1 & 0 \end{pmatrix}$

and this results in a cell of dimensions

$$a = 8.433 \text{ Å}, \quad b = 11.829 \text{ Å}, \quad c = 7.312 \text{ Å}$$

$$\alpha = 89.63^{\circ}, \quad \beta = 125.22^{\circ}, \quad \gamma = 90.71^{\circ}.$$

Similar transformations $\underline{\underline{T}}'$, $\underline{\underline{T}}''$ given by

1.(51) $\quad \underline{\underline{T}}' = \begin{pmatrix} 0 & 0 & 1 \\ 1 & 1 & 0 \\ \frac{1}{2} & -\frac{1}{2} & -\frac{1}{2} \end{pmatrix}$ and $\underline{\underline{T}}'' = \begin{pmatrix} 0 & 0 & 1 \\ 0 & 1 & 0 \\ \frac{1}{2} & 0 & -\frac{1}{2} \end{pmatrix}$

give a pseudo-body centred cubic cell of dimensions

$$a = 8.402 \text{ Å}, \quad b = 8.409 \text{ Å}, \quad c = 8.433 \text{ Å}$$

$$\alpha = 90.49^{\circ} \quad \beta = 90.5^{\circ} \quad \gamma = 90.56^{\circ}$$

and a pseudo-face centred tetragonal cell of dimensions

$$a = 11.945 \text{ Å}, \quad b = 11.829 \text{ Å}, \quad c = 8.433 \text{ Å}$$

$$\alpha = 90.71^{\circ} \quad \beta = 90.01^{\circ} \quad \gamma = 90.05^{\circ}$$

respectively.

The molecular dimer unit described in the preceding discussion
has dimensions approximately 3.5 Å in length and 5.4 Å in diameter.

This may be roughly approximated by a sphere of radius ~ 3.2 $\overset{o}{A}$ and

so it might be expected that the intermolecular forces would attempt

to arrange the molecules in a pseudo-cubic structure. Alternatively,

if the molecular unit could be very well described by a spherical

shape, then the structure may have been hexagonal close packed or

face centred cubic.

3.6 Conclusions

The organic molecular complex that has been described in this study

is of particular interest since it consists of two species of molecule

that are of the simplest aromatic form. The analyses were performed

with and without constraints on the bond lengths, which, in the case

of one of the C-C bonds, showed that the comparison of the various

structural models had to be based upon the constrained refinement

results.

These results have been fully discussed and it is believed that

the data, although not of the highest quality, are good enough to be

able to draw a tentative conclusion relating to the pairing of the

different species of molecules in model DOM. In order to be able to

arrive at a more conclusive result it would be necessary to collect

intensities of higher angle reflections than was done in the present

study. This may be achieved by using a shorter wavelength of

radiation, preferably neutrons. The preference for using neutron

radiation rather than X-radiation is that the Bragg scattering of

neutrons is governed by the relevant coherent scattering length

which is angle independent. However, the X-ray scattering factors

are heavily suppressed at high values of $(\sin\theta)/\lambda$ which means that

the Bragg reflections with large indices would be more readily

observed with neutrons than with X-rays. Therefore, if greater
resolution is required, then a shorter wavelength must be used, of
the order of $\lambda \lesssim 0.5$ Å, in order to probe out to ~ 2 Å^{-1} in
reciprocal space, for a maximum scattering angle of $2\theta \sim 110°$ as
we have in the present study. Neutron wavelengths of this order
are not easily available on conventional diffractometers, but the
spallation neutron source (SNS) will be able to produce such wavelengths
with ease. Therefore, it would be worthwhile to use the SNS for in-
vestigating this system further. Neutron powder diffraction could
be used initially in order to see if the high angle reflections
needed are in fact observable, and then single crystal diffracto-
metry would follow. In the present case, of the highest angle re-
flections, for which $2\theta \sim 100°$, there are several that have in-
tensities of several hundred counts. These reflections would there-
fore be more intense with neutrons and thus more easily measurable.

The discussion of packing considerations indicated that the
interstack F....D separations are larger than the van der Waals
separations, but if rotational disorder of the HFB is allowed then
this separation may become much less, as little as 2.04 Å. This
latter distance is smaller than the separation required for hydrogen
bond formation, which is ~ 2.35 Å, but this type of bond has not
been discussed with respect to this system before and it is not known
whether or not hydrogen bonds occur. Since this complex is not of
the charge transfer type and therefore has no regions in the molecules
that have a localised high charge density, it seems unlikely that
hydrogen bonds would form.

It is therefore concluded that the intermolecular forces acting
within a stack have a lesser effect on the molecular binding to form
the crystal, than do the corresponding forces between molecules in

different stacks. This leads to the belief that the interstack

F....D interaction plays a relatively important role in the formation

of the crystal.

Finally it is noted that the transition phenomenon observed by
Ripmeester et al.[28] at 272 K is probably related to a structural phase

transition, since unpublished neutron powder diffraction data in-

dicates that at 250 K the structure is possibly monoclinic, different

from the rhombohedral structure presented here. This is also sup-

ported by the fact that when the present diffraction study was

finished, the crystal was cooled very slowly by several degrees,

whereupon it shattered. This would indicate that a transition has

taken place, otherwise this molecular system could easily accommodate

the removal of thermal energy by reducing the very large mean square

amplitudes of vibration that are present at $\sim$ 280 K. Further, it is

already known that a structural phase transition takes place at

$\sim$ 200 K[29] on warming, and other neutron powder diffraction scans

at 5 K suggests an even more complicated crystal structure than at

250 K. Clearly, a great deal more work must be done in order to

fully elucidate the various structural transitions that take place

in this system.

The unpublished data mentioned above is the subject of further

analysis in this work, and this is given in Chapter 3, §5.2.

REFERENCES FOR CHAPTER 1

(1) Warren, B.E., "X-ray Diffraction" (1969) Addison-Wesley.

(2) International Tables for X-ray Crystallography, Vol. II, p. 71 and 99-101, p. 166-7.

(3) Idem., Vol. I, p. 272, Vol. IV, p. 327-8.

(4) James, R.W., "The Optical Principles of the Diffraction of X-rays" (1950), London: Bell.

(5) Bacon, G.E., Lowde, R.D., Acta Cryst. (1948), 1, 303.

(6) Hamilton, W.C., Acta Cryst. (1957), 10, 629.

(7) Ibid., Idem. (1963), 16, 609.

(8) Chandrasekhar, S., Adv. in Physics (GB) (1960) 9, 363.

(9) Ibid., Acta Cryst. (1960), 13(8), 588.

(10) Chandrasekhar, S., Phillips, D.C., Nature (1961) 190, 1164.

(11) Kuznetsov, A.V., Terminasov, Yu.S., Zh. Tekh. Fiz. (USSR) (1961), 31(3), 383 (Russian).

(12) Paalman, H.H., Pings, C.J., J. Appl. Phys. (1962), 33(8), 2635.

(13) Ferrari, A., Braibanti, A., Tiripicchio, A., Acta Cryst. (1961) 14(10), 1089.

(14) Ibid., Ricerca, Sci. II A (Italy), 3(1), 55. (Italian).

(15) Jeffrey, J.W., Rose, K.M., Acta Cryst. (1964), A17, 343.

(16) Ewald, P.P., Zeit. fur Krist. (1921), 56, 129.

(17) Patrick and Prosser, Nature (1960), 187, 1021.

(18) Duncan, W.A., Swinton, F.L., Trans. Farad. Soc. (1966), 62, 1082.

(19) Duncan, W.A., Sheridan, J.P., Swinton, F.L., Trans. Farad. Soc. (1966), 62, 1090.

(20) Gilson, D.F.R., McDowell, C.A., Canad. J. Chem. (1966), 44, 945.

(21) Beaumont, T.G., David, K.M.C., J. Chem. Soc. (B) (1967), 1131.

(22) Bauer, M.E., Knobler, C.M., Horsma, D.A., Perez, P., J. Phys. Chem. (1970), 74, 4594.

REFERENCES FOR CHAPTER 1 (Contd.)

(23) Dahl, T., Acta Chem. Scand. (1971), 25, 1031.

(24) Dahl, T., Acta Chem. Scand. (1972), 26, 1569.

(25) Dahl, T., Acta Chem. Scand. (1973), 27, 995.

(26) Brennan, J.S., Brown, N.M.D., Swinton, F.L., J. Chem. Soc.
      Farad. I (1974), 70, 1965.

(27) Potenza, J., Mastropaolo, D., Acta Cryst. (1975), B31, 2527.

(28) Ripmeester, J.A., Wright, D.A., Fyfe, C.A., Boyd, R.K.,
      J. Chem. Soc. Farad. Trans. II (1978), 74 (7), 1164.

(29) Mackenzie, G.A., Overell, J.S.W., Pawley, G.S., Solid State
      Commun. (1979), 31, 431.

(30) Small, R.W.H., Private Communication, (1979).

(31) Wilson, A.J.C., Acta Cryst. (1949), 2, 318.

(32) Busing, W.R., Martin, K.O., Levy, H.A., (1962) ORFLS Report
      ORNL-TM-305, Oak Ridge Nat. Labs., Tennessee.

(33) Pawley, G.S., (1972), "Advances in Structure Research by
      Diffraction Methods", p. 1-64, ed. Hope, W., Mason, R.;
      Pergamon Press, London.

(34) Cox, E.G., Cruickshank, D.W.J., Smith, J.A.S., Proc. Roy. Soc.
      (1958), 247, 1.

(35) Boden, N., Davis, P.P., Stam, C.H., Wesselink, G.A., Molecular
      Physics (1973), 25, 81-86.

(36) Hanna, M.W., J. Amer. Chem. Soc. (1968), 90, 285.

(37) Lippert, J.C., Hanna, M.W., Trotter, P.J., Ibid., (1969), 91, 4035.

CHAPTER 2   RAMAN SCATTERING

§1. Introduction

The Raman effect is the inelastic scattering of electromagnetic radiation by matter. The scattered radiation is altered in frequency from the incident radiation, and it is these frequency shifts, along with other measured quantities, that give an insight into some of the aspects of the dynamical nature of matter. This type of scattering may take place from any of the three phases of matter, the degree to which it may be observed varying for different materials.

The phenomenon was discovered by C.V. Raman in 1921 when he was involved in a series of experiments dealing with the scattering of light by all kinds of transparent media. It was found that some radiation, now known as Raman scattering, was altered in frequency from the exciting radiation[1], which was at that time usually un-filtered sunlight. This new type of radiation, distinct from fluorescence because of the time scales involved, was also noted to be strongly polarised[2], and was observed from crystals and glasses[3], as well as from liquids, this last group of materials being the first medium in which the new effect was experimentally observed.

The quantities of interest concerning the Raman scattered radiation are the frequency shifts and line widths, the polarisation and the intensity of each Raman line. Further discussion of these observables will be given later. The frequency shifts are usually measured in wavenumbers (cm^{-1}) and this is the unit of Raman shift used throughout.

The remainder of this chapter will be devoted to the Raman spectra of polycrystalline samples, although some preliminary

Raman studies have also been done on an unoriented single crystal. These last data are not presented in this chapter, rather they are given in Chapter 4 where other experimental data are given in connection with the incommensurate phase. Therefore, all the data presented in this chapter are taken from polycrystalline samples.

General experimental considerations are given in §2, and for experiments performed by the author the relevant conditions are given with the data that is presented.

The analysis of the polycrystalline sample Raman spectra are limited and any theoretical models that are used for such calculations are described and justified in section 3. In this last section we present the formalism of crystal lattice normal modes and only the basic ideas of Raman scattering theory, for a more detailed and comprehensive account the reader is referred to the large amount of work that has been done on this subject and related topics (see for example, (9), (13) and (17)).

The experimental spectra that have been measured with temperature and pressure as the variables, and any relevant conclusions to be drawn from these results are given in section 4.

§2   <u>Experimental Considerations</u>

In order to derive criteria by which a Raman scattering experiment may be performed, it is necessary to consider, qualitatively, the process of inelastic scattering of light quanta by some medium, which will be crystalline in the present work.

Raman scattering in crystalline systems is very weak, the ratio of the incident to scattered photon flux being of the order of 10^9, and the resulting frequency shifts are small compared to that of the incident radiation, which is usually in the visible spectrum. Due to

the weak nature of the scattering, the scattered intensity is usually collected at 90° or 180° to the incident radiation in order to avoid the intense forward scattering. With these observations in mind, it is therefore necessary to have a very intense, coherent source of radiation that is well collimated and is of sufficiently narrow bandwidth so as not to interfere with the measured spectrum. Even with a very intense source of exciting radiation, the Raman scattering is very weak, so that in order to disperse and detect this radiation we require a device of very high resolving and dispersing power coupled with a highly efficient, sensitive detection system.

The advent of the laser[4] and its subsequent development has meant that we have a source of exciting radiation that is entirely consistent with our experimental needs. Here we will only be concerned with one or two of the many lasers available, these being an argon or krypton ion laser (Spectra Physics model 165).

As is common in lasers, these particular two have several different exciting lines and this may be of added advantage when, for instance, at high pressure the emission due to fluorescence from the sample may become so great as to completely swamp the Raman spectrum. This may occur when using one of the laser exciting lines whereas another in the same laser may not produce as much fluorescence in the sample, hence the option of being able to change exciting lines with no great difficulty is a very great advantage over a single mode laser, where only one exciting line is available.

A triple grating monochromator, such as that shown in Figure 2.1, is an excellent device for the analysis of the scattered radiation and for the detection of the scattered photons, a very low noise photo-multiplier tube, with the appropriate frequency response is used. The above apparati are coupled with the computer that controls the whole

Figure 2.1:   Schematic representation of the triple grating

monochromator and computer interface used for

performing Raman experiments, after Arthur[5].

'G' denotes a grating, 'S' a slit, 'L' a

lens and 'M' a mirror. The flow of infor-

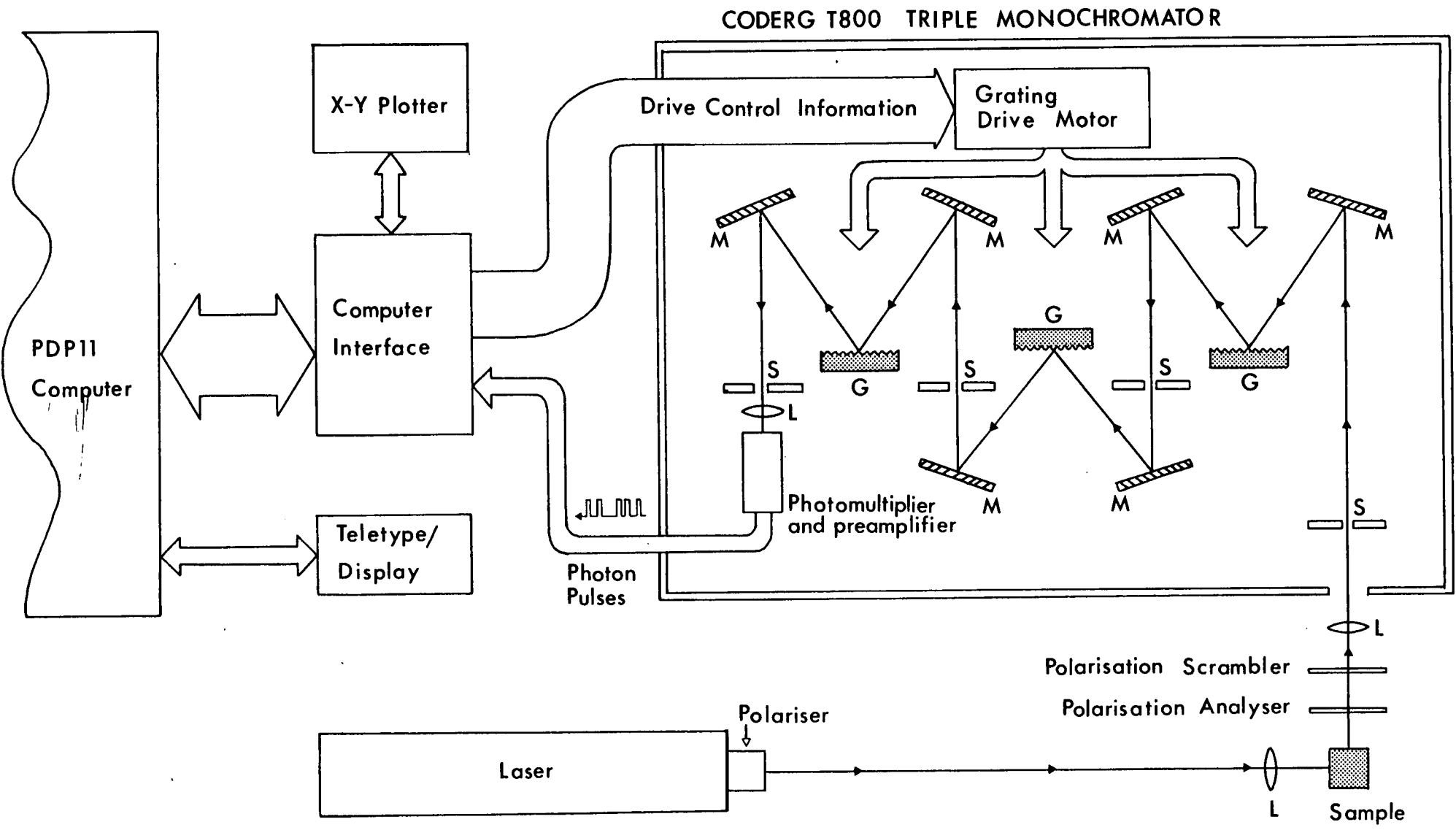mation is also represented schematically.

CODERG T800 TRIPLE MONOCHROMATOR

FIG. 2·1

system and this serves to complete the apparatus used for Raman experiments. This system is shown schematically in Figure 2.1 and cryogenic or high pressure apparatus is described separately and is omitted from the figure.

With such an experimental arrangement as is briefly described above, due to Arthur[5], it is possible to measure Raman spectra in a relatively short time, compared to other experimental techniques, such as neutron of X-ray scattering. A Raman spectrum may be measured in a matter of minutes, whereas the latter techniques usually require hours or days to perform. Therefore, it is essential that the experimental arrangement used for the Raman scattering technique is capable of handling large amounts of data quickly and in a consistently repeatable manner. Such a system is fully described by Arthur[5] and the essential features have been shown in Figure 2.1.

With regard to the pieces of apparatus involving the actual sample, both low temperature and high pressure cells have been used. For low temperature measurements, the cooling apparatus used was a standard Thor Cryogenics cryostat in which the sample is mounted, and a Thor 3010 temperature controller coupled with a GaAs diode for the temperature sensing. The necessary control heater is placed close to the sample, both of these being mounted on a copper block for efficient heat transfer and reliable temperature equilibrium. The cryostat used allows a cooling flow of either nitrogen or helium gas depending upon the temperature range required for the experiment.

The high pressure cell used is shown in Figure 2.2, and is used in a backscattering geometry. The cell consists of two anvils, one of which is rigidly fixed and the other is caused to move against the first using a lever principle, an incompressible hydraulic fluid being the medium that transmits the applied pressure. In each of the

Figure 2.2:   The essential features of the high pressure cell

mentioned in the text, in the backscattering

geometry. Labels are keyed below:

D1, D2   diamonds

A2   moving anvil

A1   rigidly fixed anvil

G   metallic gasket

M   mirror

S   sample chamber

FIG. 2·2

SCATTERED
BEAM

INCIDENT
BEAM

M

D1

S   G

D2

A1   A2
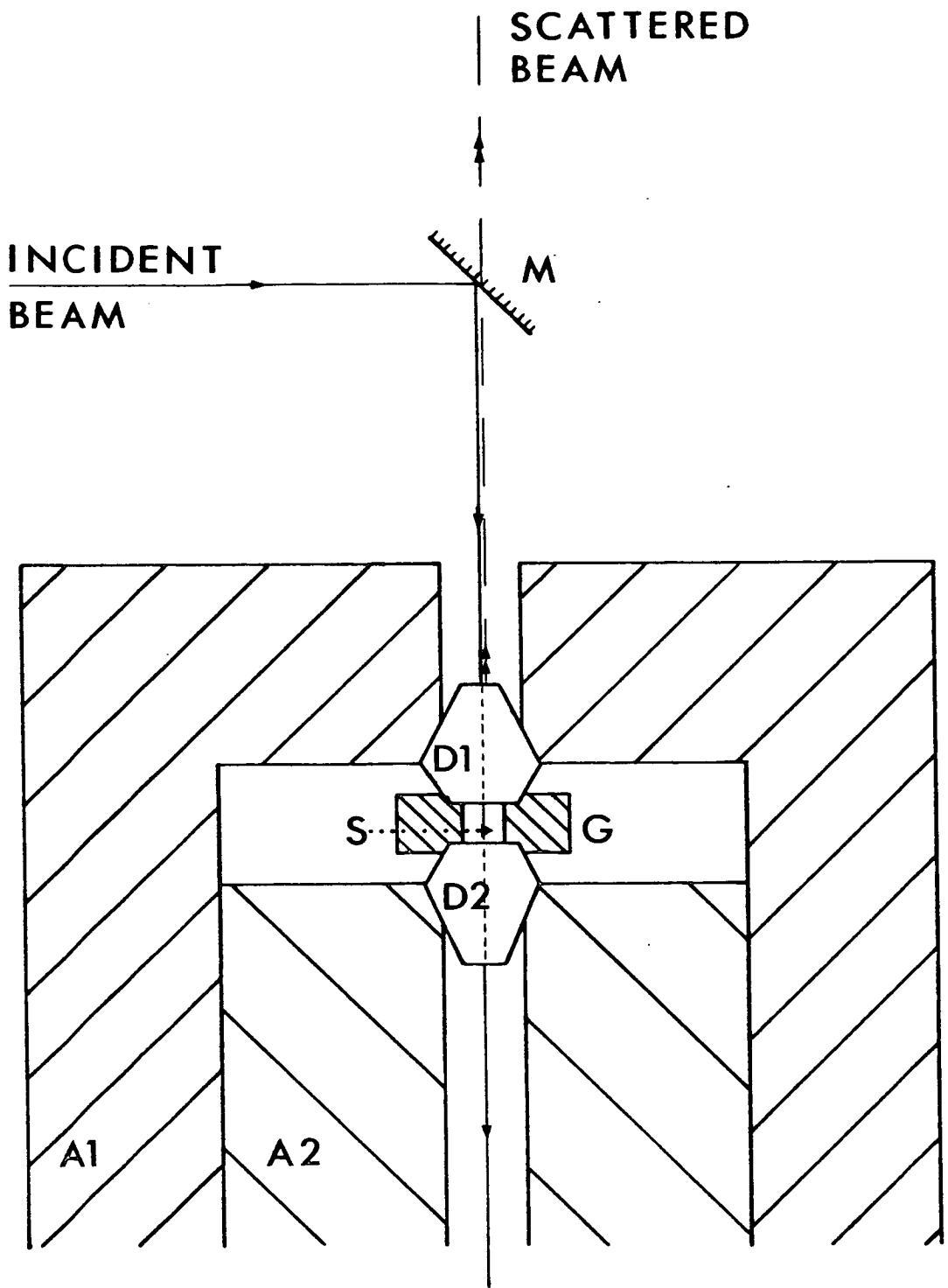
anvils is set a small diamond of high quality and it is between the
two highly parallel faces of the diamonds in close contact that high
pressure is attained. The total area over which uniform pressure is
applied is   of the order of ~ 0.04 mm^2. The theoretical maximum
pressure is about 200 kbar, but the maximum pressure obtained during
an experiment did not exceed 25 kbar. In order to be able to use this
high pressure cell, it is necessary to enclose the sample within the
centre of a very thin annular metallic gasket that flows smoothly
under high pressure. This ensures that the sample is contained
within a small volume and gives a uniform hydrostatic high pressure
throughout the sample chamber. The mass of sample usually used is
about 0.01 mg. Figure 2.2 shows the cell in back scattering
geometry, but the passage of the scattered beam does not actually
pass through the mirror as shown. The intensity that is exactly back
scattered retraces the path of the incident beam, but the rest of the
back scattered light falls on a cone that has the mirror on its
principle axis so that the spectrometer sees a cone of radiation
and the assumption is made that the spectra do not vary appreciably over the
solid angle ($\sim 5.10^{-3}$ steradians) of this cone of scattered intensity. However,
we continue to refer to this as 'back scattering geometry' for brevity.

The calibration of the pressure is achieved by enclosing a very
fine piece of some substance within the sample chamber, whose Raman
shift variation with pressure is accurately known. Such a compound
is highly pure, natural ruby, a form of alumina, whose Raman spectra
increases in wavenumber almost exactly linearly with increasing pressure.
This makes it the most common calibration compound used in high pressure
Raman scattering work.

It is unfortunate, however, that the pressure cell available

cannot also accommodate temperature variation. Ideally, we would be able to vary the temperature and pressure of the sample simultaneously in order, for instance, to establish the phase diagram of a system with respect to both these variables. However, the technical problems of combining temperature variations and the high precision manufacture of the pressure cell have not yet been solved comprehensively.

§3   Theoretical Aspects of Raman Scattering

3.1   Introduction

In this section we present the qualitative theory of Raman scattering. Since no polarisation studies were done, the corresponding theoretical aspects required for Group Theoretical Analyses of Raman spectra are not given, rather the reader is referred to some of the various works on the subject and also to the general, more detailed theory of Raman scattering (see, for example, (6) - (11)).

In §3.2 the formalism of the normal modes of a crystal are presented, leading to the concept of the phonon as the quantum of lattice vibrational energy. In §3.3 a simple qualitative outlook on the theory of Raman scattering is discussed. The reason for the inclusion of §3.2 is that oscillator models used in §3.4 in the discussion of Raman lineshapes requires the understanding of uncoupled phonon modes in a crystal. Hence, section §3.2 is included for completeness and the discussion follows reference (13).

The results of lineshape analyses on measured spectra and the spectra themselves are presented in §4, followed by the relevant discussion and conclusions.

3.2   Normal modes of a crystal lattice

The following discussion may be found in more detail in reference (13), the purpose of this section being merely to show how, within a harmonic approximation, the lattice vibrations of a crystal may be reduced to a set of uncoupled simple harmonic oscillators.

We start by writing the Hamiltonian of the crystal, in the harmonic approximation, in terms of the displacements, $\{q_i\}$, and momenta, $\{p_i\}$, of the N atoms in the crystal as

$$2.(1) \quad H = \sum_{i=1}^{N} (p_i^2/2m_i) + \tfrac{1}{2} \sum_{i,j=1}^{N} q_i \cdot \phi_{ij} \cdot q_j \;,$$

where the $\{\phi_{ij}\}$ are the interatomic force constants between atoms i and j in the crystal. Rescaling the $\{q_i\}$ and $\{\phi_{ij}\}$ by

$$2.(2) \quad W_i = q_i \sqrt{m_i} \quad \text{and} \quad \phi_{ij} = \phi_{ij}/\sqrt{m_i \, m_j}$$

and using the canonical equation[14]

$$2.(3) \quad \dot{p}_{i\ell} = -\frac{\partial H}{\partial q_{i\ell}} \;,$$

the equation of motion is given by

$$2.(4) \quad \ddot{W}_{i\ell} = -\sum_{jm} \phi_{i\ell jm} \, W_{jm} \;,$$

(ℓ, m are Cartesian labels, whereas i, j refer to atoms) where $\underline{\phi}$ is called the dynamical matrix, of elements $\phi_{i\ell jm}$, which contains all the information concerning interatomic forces. This matrix will usually have non-zero off-diagonal elements but it may be diagonalised by using 'normal coordinates' and thus the crystal oscillations become decoupled.

In order to show this, we define Fourier coordinates $\{Q_{ki\ell}\}$

such that

$$2.(5) \qquad Q_{\underline{k}i\ell} = \frac{1}{\sqrt{N}} \sum_{\underline{I}} W_{\underline{I}i\ell} \exp(-i \, \underline{k} \cdot \underline{I})$$

and the inverse relation is

$$2.(6) \qquad W_{\underline{I}i\ell} = \frac{1}{\sqrt{N}} \sum_{\underline{k}} Q_{\underline{k}i\ell} \exp(i \, \underline{k} \cdot \underline{I}) \quad .$$

The quantity $W_{\underline{I}i\ell}$ is now the mass weighted displacement of the ith atom in the unit cell of origin $\underline{I}$. Using these definitions and rewriting equation 2.(4) as

$$2.(7) \qquad \overset{\shortmid\shortmid}{W}_{\underline{I}i\ell} = - \sum_{jm} \phi_{\underline{I}i\ell\underline{J}jm} W_{\underline{J}jm}$$

we find that, on choosing a particular $\underline{I} = \underline{I}'$,

$$\overset{\shortmid\shortmid}{Q}_{\underline{k}i\ell} = - \sum_{jm} \phi_{\underline{I}'i\ell \, \underline{J}jm} \sum_{\underline{J}} Q_{\underline{k}jm} \exp(i\underline{k} \cdot (\underline{J}-\underline{I}'))$$

$$= - \sum_{jm} \sum_{\underline{J}} \phi_{\underline{I}'i\ell \, \underline{J}jm} Q_{\underline{k}jm} \exp(i\underline{k} \cdot (\underline{J}-\underline{I}'))$$

$$2.(8) \qquad \qquad = - \sum_{jm} D_{i\ell jm}(\underline{k}) Q_{\underline{k}jm} \quad ,$$

where we have defined

$$2.(9) \qquad D_{i\ell jm}(\underline{k}) = \sum_{\underline{J}} \phi_{\underline{I}'i\ell\underline{J}jm} \exp(i\underline{k} \cdot (\underline{J}-\underline{I}')) \quad .$$

From the last equation, we see that the matrix $\underline{\phi}$ has been block-diagonalised into a set of Hermitian matrices $\underline{\underline{D}}$, which are $3r \times 3r$, where r is the number of atoms in the primitive cell. The Hermitian matrix $\underline{\underline{D}}$ has a set of orthonormal complex eigenvectors $\{\underline{e}_c\}$ with

corresponding real eigenvalues $\{\omega_c^2\}$:

$$2.(10) \qquad \sum_{jm} D_{i\ell jm}(\underline{k}) e_c(jm\underline{k}) = +\omega_c^2(\underline{k}) e_c(i\ell\underline{k}) \quad .$$

If we now define complex normal coordinates from the Fourier coordinates $\{Q_{\underline{k}i\ell}\}$ by the equation,

$$2.(11) \qquad Q_{\underline{k}c} = \sum_{i\ell} e_c^*(i\ell\underline{k}) Q_{\underline{k}i\ell} \quad ,$$

and similarly for the inverse relationship,

$$2.(12) \qquad Q_{\underline{k}i\ell} = \sum_c e_c(i\ell\underline{k}) Q_{\underline{k}c} \quad ,$$

then equation 2.(8) becomes

$$2.(13) \qquad \ddot{Q}_{\underline{k}c} = -\omega_c^2(\underline{k}) Q_{\underline{k}c} \quad .$$

This is the equation of motion for the displacement from equilibrium of a simple harmonic oscillator of frequency $\omega_c(\underline{k})$. Equation 2.(4) describes a set of 3N coupled oscillators, which have now been decoupled to equation 2.(13) describing 3N uncoupled simple, harmonic oscillators. The discussion leading to equation 2.(13) has been purely classical, but in order to transform to the quantum mechanical notation we rewrite the normal coordinate $Q_{\underline{k}c}$ as a Hermitian operator $\hat{Q}_{\underline{k}c}$ and introduce the operators $\hat{b}_{\underline{k}c}$ and $\hat{b}_{-\underline{k}c}^\dagger$ (where the superscript '†' denotes Hermitian conjugation) defined by [15]

$$2.(14a) \qquad \hat{Q}_{\underline{k}c} = \left(\frac{\hbar}{2\omega_c(\underline{k})}\right)^{\frac{1}{2}} (\hat{b}_{\underline{k}c} + \hat{b}_{-\underline{k}c}^\dagger)$$

$$2.(14b) \qquad \hat{P}_{\underline{k}c} = i\left(\frac{\hbar\omega_c(\underline{k})}{2}\right)^{\frac{1}{2}} (\hat{b}_{\underline{k}c} - \hat{b}_{-\underline{k}c}^\dagger)$$

where $\hat{P}_{\underline{k}c}$ is the conjugate momentum to $\hat{Q}_{\underline{k}c}$. From classical Poisson brackets[20]

$$2.(15a) \qquad \{\hat{Q}_{\underline{k}c}, \hat{P}_{\underline{k}'d}\} \equiv \delta(\underline{k}-\underline{k}')\delta_{cd}$$

$$2.(15b) \qquad \{\hat{Q}_{\underline{k},c}, \hat{Q}_{\underline{k}',d}\} \equiv 0$$

the operators $\hat{b}$ and $\hat{b}^{\dagger}$ may be shown to have the commutation relations

$$2.(16a) \qquad \left[\hat{b}_{\underline{k}c}, \hat{b}^{\dagger}_{\underline{k}'d}\right] = \delta(\underline{k}-\underline{k}')\delta_{cd}$$

$$2.(16b) \qquad \left[\hat{b}_{\underline{k}c}, \hat{b}_{\underline{k}'d}\right] = \left[\hat{b}^{\dagger}_{\underline{k}c}, \hat{b}^{\dagger}_{\underline{k}'d}\right] \equiv 0$$

and therefore $\hat{b}$ and $\hat{b}^{\dagger}$ are boson creation and annihilation operators respectively. The bosons that these operators refer to are the quanta of the crystal lattice vibrations and these are called 'phonons'. These quanta are respectively created or destroyed in the Stokes or Anti-Stokes Raman scattering processes.


3.3   Basic theoretical considerations

The Raman effect is the inelastic scattering of light by some medium, therefore the scattered radiation is changed in frequency from that of the incident radiation, which is usually an excitation line of a laser. There are in fact many different sources of this kind of inelastic scattering, some of these being the rotational, vibrational and electronic properties of atoms and molecules. Scattering of light by quanta such as phonons also occurs for magnons, plasmons, and polaritons. These processes may all be described as light scattering by quasi-particles and the geometry of these various inter-actions is represented in Figure 2.3. Energy and wavevector conservation

Figure 2.3:   Conservation of momentum in any light - quasi

particle scattering process. $\underline{k}_\ell$, $\underline{k}_s$ and $\underline{k}_p$

are respectively the wavevectors of the in-

cident photon, the scattered photon and that

for the quasi-particle. 2θ is the

scattering angle for the Raman effect

$|\underline{k}_s| \neq |\underline{k}_\ell|$.

FIG. 2·3
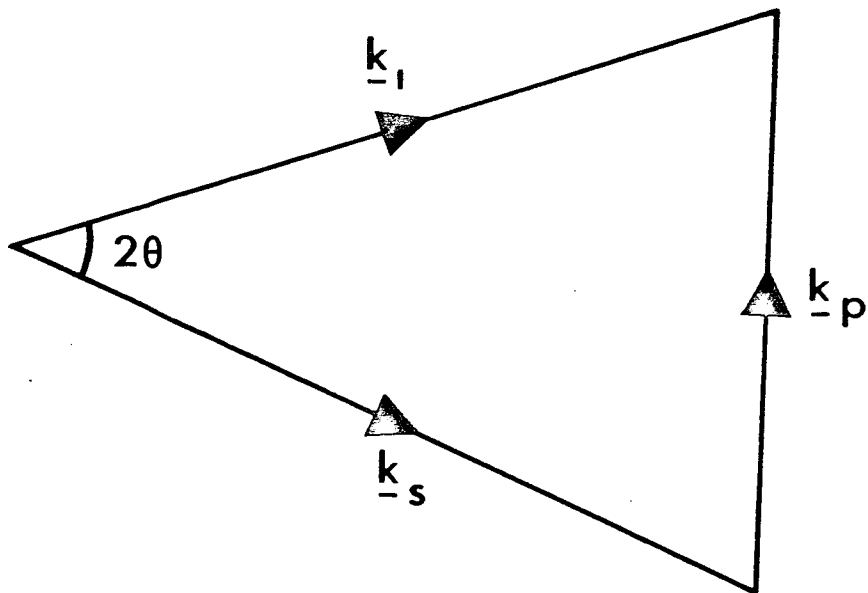
is represented by the equations

2.(17) $E_\ell = E_s \pm E_p$ and $\underline{k}_\ell = \underline{k}_s \pm \underline{k}_p$,

where the suffices ℓ, p, and s refer to incident light, quasi-particle and scattered light respectively and the + and - represent incident photon energy gain and loss respectively. This means either the annihilation or creation of a quasi-particle respectively. For further references on these specific cases the reader is referred to (12).

The classical theory of light scattering is based on the assumption that an incident electromagnetic wave induces an oscillating dipole moment in the scattering medium. Let the incident wave have frequency ω rads.sec^{-1}, and if the electric field vector is expressed by

2.(18) $\underline{E} = \underline{E}_o \cos \omega t$,

where $|\underline{E}_o|$ is the maximum value of $|\underline{E}|$, then the induced dipole moment $\underline{M}$ will have the same frequency as the incident wave and thus

2.(19)
$$\underline{M} = [\alpha]\, \underline{E}$$
$$\underline{M} = [\alpha]\, \underline{E}_o \cos \omega t \ .$$

The quantity $[\alpha]$ is the polarisability tensor of the medium, and it describes the manner in which the medium reacts to an applied electromagnetic field, in this case $\underline{E}$. However, if now the atoms or molecules are vibrating with frequency ω_c, then the polarisability will also vary with frequency ω_c. This means that

2.(20) $[\alpha] = \alpha_o + \alpha_c \cos \omega_c t$.

Therefore, combining equations 2.(18), 2.(20) we obtain the induced oscillating dipole moment $\underline{M}$ when the atoms or molecules are vibrating with frequency ω_c, as

2.(21) $\quad \underline{M} = \{\alpha_o + \alpha_c \cos \omega_c t\}\underline{E}_o\{\cos \omega t\}$

which may be written

2.(22) $\quad \underline{M} = \alpha_o\underline{E}_o \cos \omega t + \tfrac{1}{2}\alpha_c\underline{E}_o\{\cos(\omega+\omega_c) + \cos(\omega-\omega_c)\}.$

From this very simple approach we have derived the essential inelastic nature of Raman scattering. We see that the induced dipole moment $\underline{M}$ may be replaced by three oscillating dipole moments of frequencies ω, $\omega \pm \omega_c$ respectively. Therefore, in scattering the incident light, these dipoles will radiate at these frequencies and we obtain the unmodified Rayleigh scattering of frequency ω, and the two extra terms, of frequencies $\omega \pm \omega_c$, due to the vibrations of the atoms or molecules. These two terms are the Stokes, anti-Stokes Raman scattering of frequencies $\omega - \omega_c$ and $\omega + \omega_c$ respectively.

It is easily seen that the Stokes, anti-Stokes scattering processes correspond respectively to the photons of incident light giving up energy to or receiving energy from the motion of the atoms or molecules in the scattering medium. Therefore it is clear in this discussion, that although the Rayleigh scattering is derived from the static polarisability, α_o, of the system, the changes in the polarisability caused by atomic or molecular motions, gives rise to the Raman effect.

From equation 2.(22) it is also clear that at each vibrational (or rotational) frequency, corresponding to a particular normal mode in the medium, a corresponding Raman shift might be expected. The

normal modes of a crystalline system were briefly discussed in the previous section and so each normal mode (of frequency ω_c) may give rise to two Raman lines of frequencies $\omega \pm \omega_c$ in the scattered spectra of the system. However, there are other considerations to be taken into account when observing a Raman spectrum. If the molecules vibrate in such a manner that the scattered light is completely polarised in a particular plane, then in performing a polarisation analysis on the Raman scattered radiation, it is possible to exclude the scattered intensity from a particular normal mode of vibration by choosing the appropriate analyser polaroid orientation. The different polarisations of the various Raman lines due to different normal modes is a direct consequence of the point symmetry of the crystal and therefore it is possible to select a normal mode by polarisation analysis of the Raman spectra. The symmetry classification of normal modes of crystals for the various point group symmetries is the subject of Group Theory[8-11].

For the present work, the samples used were mostly polycrystalline and so any polarisation analysis is very limited. It may be shown that only two different spectra exist for a polycrystalline sample, these being due to the diagonal and off-diagonal elements of the polarisability tensor. However, no such analysis was done and it was not possible to distinguish normal modes of different symmetry.

3.4 Lineshape analysis of measured Raman spectra

In §3.2 the formalism for the normal modes of vibration of a crystal were discussed in the harmonic approximation. This led to equation 2.(13) which described the motion of 3N decoupled simple harmonic oscillators, each with frequency $\omega_c(\underline{k})$, where $c = 1, 2, \ldots, 3N$.

It is clear that such a simple description is not adequate for a real crystal since energy dissipation processes, such as damping, will always be present.

In order to explicitly include the dissipative process of damping it is necessary to add another term into equation 2.(13) which is proportional to the instantaneous velocity of the oscillator. This term would be of the form $\gamma_c \dot{Q}_{\underline{k}c}$, where γ_c is a damping constant and determines the frequency response of the oscillator to the driving field, in this case the laser radiation. For a large damping constant γ_c, the energy supplied by the source of the forcing frequency is rapidly dissipated and the amplitude of vibration of the driven oscillator will quickly disappear. The exponential decrease of the oscillator amplitude disappears less rapidly for a smaller damping constant.

It may easily be shown that if an oscillatory solution is assumed for the damped simple harmonic oscillator equation of motion with a forcing frequency of ω, then the resulting amplitude of vibration, $Q_{\underline{k}c}$, will be out of phase with the driving amplitude and will also have frequency ω. $Q_{\underline{k}c}$ will be proportional to the function

$$\Omega(\omega) \quad = \quad \left[(\omega^2(\underline{k}) - \omega^2)^2 + \gamma_c^2 \omega^2 \right]^{-1}$$

and the phase lag between the forcing and driven amplitudes will be given by

$$\varepsilon \quad = \quad \sin^{-1}\{\gamma_c \omega \Omega(\omega)\} \quad .$$

In the case of the undamped oscillator the frequency response of the amplitude $Q_{\underline{k}c}$ is singular at $\omega = \omega_c(\underline{k})$ and the amplitude goes to infinity, whereas for $\omega \neq \omega_c(k)$ the response is zero. When damping is introduced the amplitude $Q_{\underline{k}c}$ will have a maximum at

$\omega = \omega_c(\underline{k})$ but will be finite in magnitude. The response is therefore not singular but damped, and the width of the resulting amplitude – driving frequency relation is given by γ_c.

Since lattice vibrations are quantised and are bosons the temperature of the system (T) is an important factor in determining the number, $(n(\omega) + 1)$, of bosons that may have frequency ω at temperature T. This temperature dependence is introduced via the Bose factor[18] and is given by

$$\left[1 - \exp\left(- \frac{\hbar\omega}{k_B T}\right)\right]^{-1} \quad ,$$

where k_B is the Boltzmann constant.

Using the previous discussion the Raman spectra profiles were fitted using expressions of the form

$$2.(23) \qquad S \quad = \quad P_1 P_2 P_3 \{(\omega^2 - P_2)^2 + P_3 \omega^2\}^{-1} \quad ,$$

where one expression describes one Raman line. The quantities P_1 and P_3 are respectively the strength (in counts. cm.) and the squared width (in cm^{-2}) of the Raman line. The strength of a line is discussed below. The parameter P_2 is the squared oscillator frequency, and in the underdamped limit, where $P_3 \ll P_2$ or $\gamma_c^2 \ll \omega_c^2(\underline{k})$, then P_2 is the peak frequency squared. The exact expression for the peak frequency is obtained by maximising S in equation 2.(23), and the result is

$$\omega_{peak} \quad = \quad \left(P_2 - \frac{P_3}{2} \right)^{\frac{1}{2}} \quad ,$$

from which $\omega_{peak}^2 \sim P_2$ if $P_3 \ll P_2$ follows immediately.

We have already seen in §3.3 that the Raman effect is derived from the changes in the polarisability of the crystal, so that a normal mode of vibration that alters the polarisability by a large amount may give rise

to correspondingly strong Raman scattering. The integrated intensity of a Raman line is proportional to the strength of that line and, therefore, also to the way in which the corresponding mode of vibration changes the polarisability of the whole crystal. We therefore take the parameter P_1 as a measure of the integrated intensity of Raman lines in measured spectra.

The results obtained from the fitting procedure described above should be interpreted with caution because of the inherent limitations of the method. This is so because, given a Raman spectrum, it must be decided how many modes there might be and then an attempt is made to fit the measured profile with that number of modes only. It is always true that the introduction of more parameters into the fitting procedure will not decrease the quality of fit, usually the fit will become better, but the interpretation of the resulting fitted parameters becomes more unreliable as the number of variables increases. No provision is made in the procedure that is used for the introduction of a new Raman line whilst the fitting process runs; if more modes are added, this requires a separate run of the program.

Therefore, in the text that follows where experimental spectra, fitted curves and parameters are presented the interpretation of the fitted parameters is given with caution bearing in mind the limitations of the fitting method used.

Wherever the fitted parameters are plotted against the absolute temperature, this is done such that time progresses from left to right in all cases except for Figure 2.8.

§4 Experimental Measurements

4.1 The benzene-hexafluorobenzene system.

The Raman spectra of the molecular complex systems $C_6D_6 \cdot C_6F_6$ and $C_6H_6 \cdot C_6F_6$ are examined for evidence of structural phase transitions. The temperature range studied lies between that of liquid helium, at 4.2K, and melting of the specimens at 297K.

A full description of some of the work that has been done on these systems has already been given in Chapter 1, §3, where the room temperature crystal structure of the $C_6D_6 \cdot C_6F_6$ system is discussed. Therefore we only present a brief resumé of the relevant parts of the work mentioned above.

The existence of a 1:1 molecular complex of benzene and hexa-fluorobenzene was reported by Patrick et al.[19], and subsequently several experimental techniques have been used to probe this system. Differential scanning calorimetry measurements made by Brennan et al.[20] showed a thermal anomaly at 249K on warming. This anomaly was observed for all of the samples they used. Two more anomalies were also observed on warming, before melting took place at 297K, but these were not reliably reproducible, and were attributed to the melting of pockets of eutectic mixtures which occur at molar ratios of approximately 86/14 and 14/86. There is no doubt that the work of Brennan et al.[20] shows a transition at 249K on warming and 246K on cooling.

Nuclear magnetic resonance (NMR) measurements taken by Gilson et al.[21] on the same material as was studied by Brennan et al.[20] show no unusual NMR line behaviour in the region of the thermal anomaly at ∿247K. However, in the temperature range 150K to 90K the NMR line broadens on cooling, but this behaviour is not uncommon at a temperature

where no thermal anomaly exists, and therefore is not taken as evidence of a transition.

Further calorimetric measurements by Ripmeester et al.[22] show several thermal anomalies on warming from 170K to 300K. These occur at temperatures of 199K, ∿247K and 272K, and that at ∿247K is in agreement with the results of Brennan et al.[20] NMR measurements also done by Ripmeester et al.[22] show the presence of in-plane re-orientations of both types of molecules in the temperature range 100K to 300K, indicating that a plastic crystalline phase may exist for this system.

The samples used in the present work were prepared by mixing equal molar quantities of the two constituents, and although this was done before sealing the mixture in the specimen tube, this will not appreciably affect the molar ratio since the vapour pressures of the two constituents are almost identical at room temperature. The mixtures were then transferred to tubes about 11 mm long and 0.9 mm in diameter, which could be mounted in a Thor Cryogenics cryostat. Cooling of the sample was achieved by either a flow of helium or nitrogen gas, depending upon the temperature range studied. The temperature of the sample was measured using a GaAs diode and controlled by a Thor 3010 temperature controller which was connected to a heater adjacent to the sample.

The Raman spectra were excited using the 6766 Å line of a krypton ion laser and measured on the computer controlled spectrometer system which was briefly described in §2. The incident laser beam was focussed on the sample and the light scattered at 90° was collected in the spectrometer. No polarisation analysis of the spectra was possible since the sample was polycrystalline.

On freezing the mixture of constituent liquids a polycrystalline sample results, but the orientation distribution of the individual

crystallites is not necessarily random. Any preferred orientation direction will cause spectra of a particular polarisation to be scattered more intensely than when the distribution of orientations of the crystallites is random.

It was found on melting and re-freezing the sample that the relative intensities in the spectrum may change for a particular temperature of measurement. This is a result of a change in the arrangement of the crystallites comprising the sample, but since the spectra were recorded using the same powder in each case the effects of pre-ferred orientation and polarisation are assumed the same in each case.

In order to look for evidence of the transition reported by Brennan et al.[20] at 249K on warming, the sample was cooled to below 215K and then warmed from 215K to 285K using 10K steps, and scans were made from 18 cm^{-1} to 113 cm^{-1} at each temperature. The results of these scans are shown in Figure 2.4, along with the curve obtained by fitting the experimental data with an expression of the form of 2.(23) for each mode. The fitted parameters, three for each Raman line, are tabulated in Table 2.1 and each of the three parameters are plotted separately against the absolute temperature in Figure 2.5. Only results for the deuterated sample will be shown since those for a protonated sample are essentially the same in general appearance.

From Figure 2.4 it is clear that no sharp transition takes place, the peaks at $\sim$35 cm^{-1} and $\sim$77 cm^{-1} decrease in intensity whilst broadening and shifting to slightly lower frequencies as the tempera-ture is raised. The scattering about the exciting line also broadens but increases in intensity as the temperature is increased. The plots displayed in Figure 2.5 show these general trends, but since no account could be taken of the intense scattering about the exciting line, the

Figure 2.4.   External mode scans made on warming from 215K
              to 285K for a deuterated sample of $C_6D_6 \cdot C_6F_6$.
              The open circles are experimental measurements
              and the full line the fitted curve. Each scan
              is raised by 1000 counts from the preceding one.

Figure 2.5.   Parameters from Table 2.1 plotted against the
              absolute temperature. Uncertainties in the
              parameters are mostly of an order less than
              the size of the symbols used in the figure.

              Similar symbols in each plot of this figure represent
              one mode in the Raman spectrum, and these are keyed
              in Table 2.1.
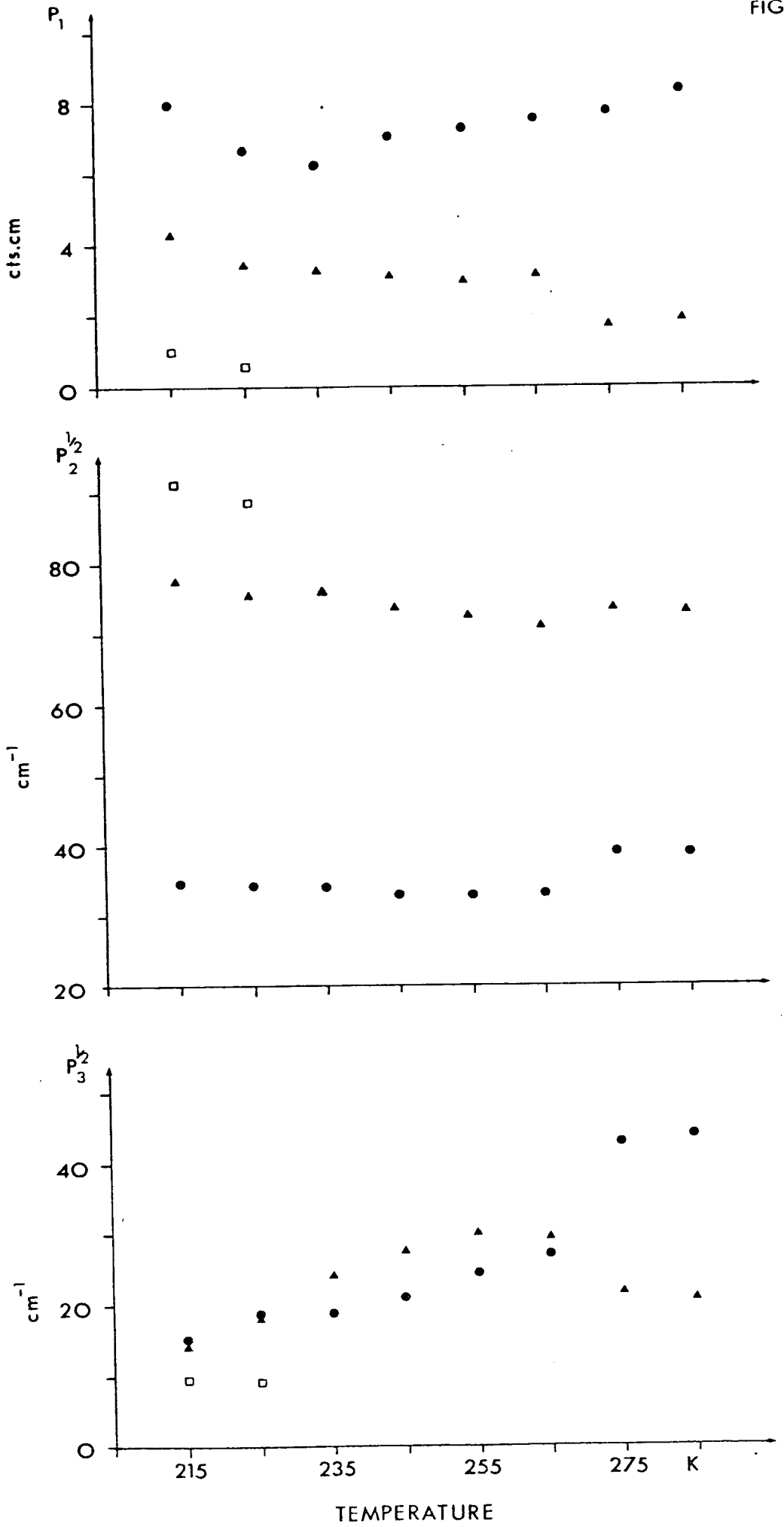
FIG. 2·4

FIG. 2·5
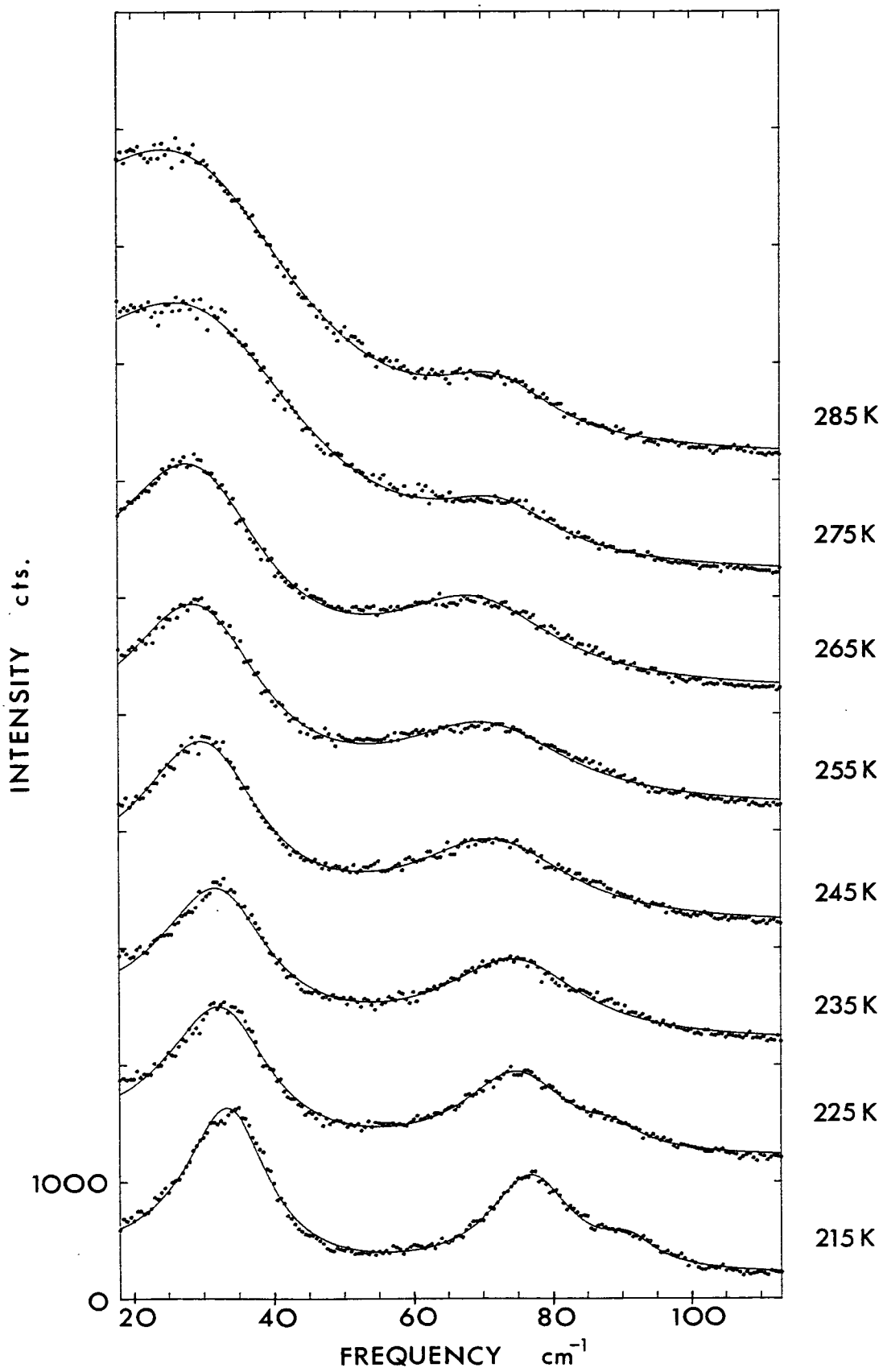
TABLE 2.1

Fitted parameters for the curves shown in Figure 2.4. The
definitions are given in the text. Uncertainties are given
in parentheses. Similar definitions are used in Tables 2.2 and 2.3.

T (K)	P_1 (cts. cm)	$\sqrt{P_2}$ (cm^{-1})	$\sqrt{P_3}$ (cm^{-1})	symbol
215	8.0(0)	34.7(1)	14.4(1)	●
	4.3(0)	77.4(0)	14.7(1)	▲
	1.0(0)	91.1(1)	9.3(3)	◻
225	6.7(0)	34.4(0)	18.1(0)	●
	3.5(0)	75.7(1)	18.9(0)	▲
	0.6(0)	88.9(1)	9.1(1)	◻
235	6.3(1)	34.1(1)	18.9(2)	●
	3.3(0)	76.0(0)	24.2(0)	▲
245	7.1(1)	32.9(1)	21.0(3)	●
	5.2(0)	73.5(1)	27.5(3)	▲
255	7.3(1)	33.0(1)	24.4(4)	●
	3.0(0)	72.9(2)	30.2(5)	▲
265	7.6(1)	33.3(1)	27.0(4)	●
	3.2(0)	71.3(1)	29.6(4)	▲
275	7.8(1)	39.2(2)	42.9(7)	●
	1.8(0)	73.7(1)	21.7(7)	▲
285	8.4(1)	38.8(1)	43.7(8)	●
	1.9(0)	73.2(2)	20.8(6)	▲

parameters P_1 and $\sqrt{P_2}$ show increases in places, especially for the 35 cm^{-1} line, due to the increase in this intense background scattering. The parameter $\sqrt{P_3}$, the line width, shows an increase at temperatures between 260K and 275K and this may also be due to the intense background at low frequencies. However, it is possible that this increase in the line widths represents a real broadening of the Raman lines, and this would imply that the normal modes that give rise to these spectral lines are becoming more highly damped at $\sim$ 270K, so the corresponding phonons have shorter lifetimes. The Raman spectra of the liquids are featureless and show no evidence of the peaks found below 285K and they have been omitted.

On cooling this system the external mode spectrum changes substantially in appearance. Part of this spectrum, from 55 cm^{-1} to 103 cm^{-1}, is displayed in Figure 2.6 for several temperatures from 210K to 90K. Fitted curves are also shown, the parameters for which are tabulated in Table 2.2 and plotted in Figure 2.7. The changes that take place are the appearance of several new Raman modes, one of which has a frequency of 61.8 cm^{-1} at 170K, and this mode may be used as an indication of these changes.

Figure 2.8 displays the strength, P_1, of the line at 61.8 cm^{-1} as a variable with temperature, the values plotted being taken from the results of the fitting procedure. From this figure it is seen that the intensity of this new mode increases as the temperature is reduced below $\sim$ 170K and this is shown as the lower curve in Figure 2.8. Extrapolation to $P_1 = 0$ gives 175K for the transition temperature on cooling. This result is a good estimate since this particular mode is well resolved even at a temperature of 160K, so that the fitted parameters are reliably estimated. However, although the transition takes place at 175K on cooling, Figure 2.8 shows that

Figure 2.6:   External mode scans made on cooling from 210K

to 90K for $C_6D_c.C_6F_6$. Open circles are experi-

mental data and the full line is the fitted

curve. Each scan is raised by 5000 counts from

the preceding one.

Table 2.2 :   Fitted parameters for the curves shown in

Figure 2.6. Uncertainties are shown in

parentheses.

Figure 2.7:   Parameters from Table 2.2 plotted against

the absolute temperature.

Similar symbols in each plot of this figure represent

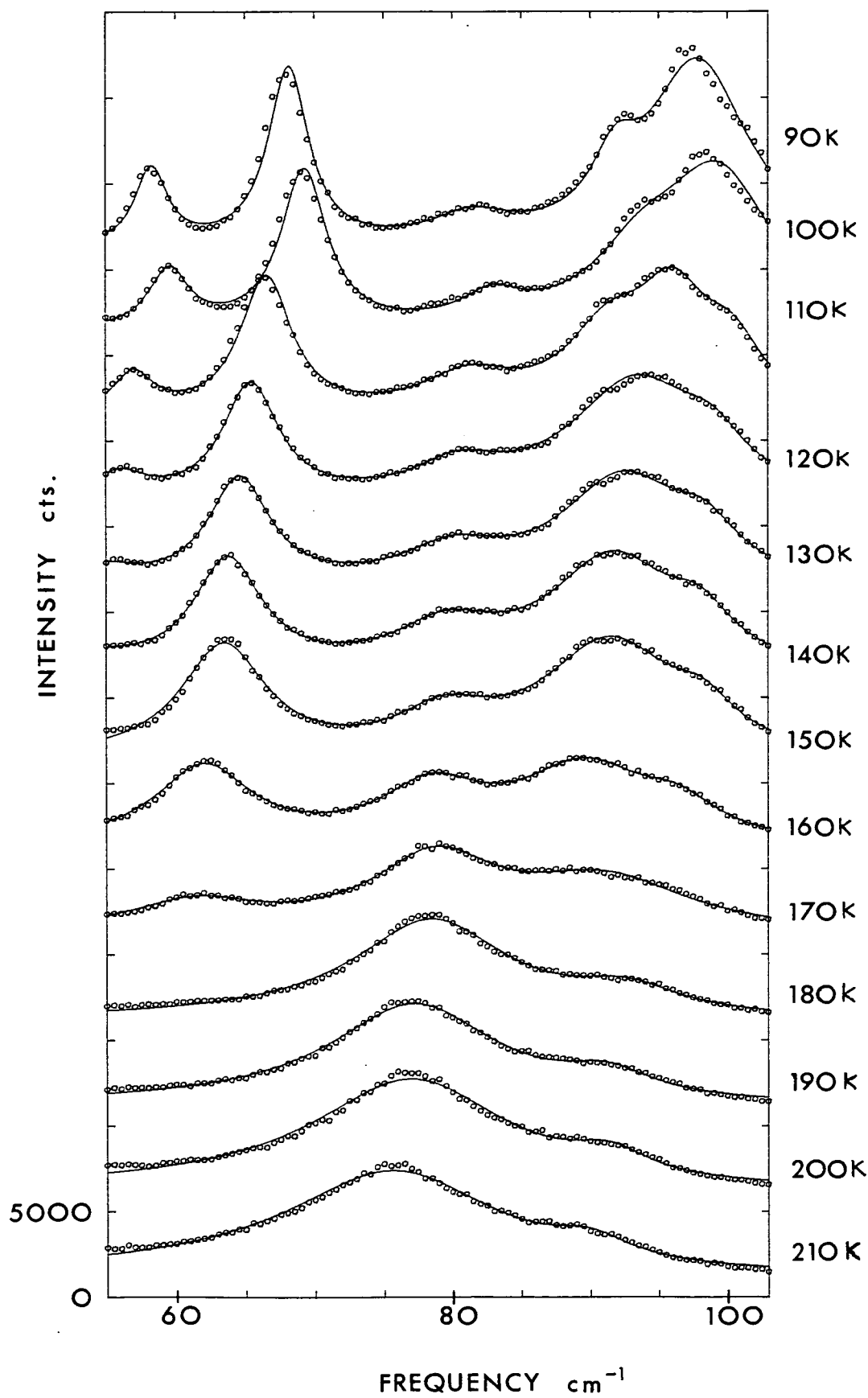one mode in the Raman spectrum, and these are keyed

in Table 2.2.

FIG.2·6

TABLE 2.2

T (K)	P_1 (cts. cm)	$\sqrt{P_2}$ (cm^{-1})	symbol	$\sqrt{P_3}$ (cm^{-1})
210	26.1(1)	76.6(1)	▲	19.2(2)
	4.7(1)	90.0(1)	●	7.0(3)
200	28.4(1)	77.8(0)	▲	17.6(1)
	5.6(1)	91.5(1)	●	6.9(2)
190	26.7(1)	77.7(1)	▲	15.0(0)
	6.1(1)	91.4(0)	●	8.2(2)
180	27.2(1)	78.9(0)	▲	13.8(1)
	6.7(1)	92.8(1)	●	9.7(3)
170	8.4(6)	61.8(1)	▫	11.2(1)
	20.4(1)	79.0(0)	▲	11.0(1)
	14.3(1)	91.6(0)	●	15.2(1)
160	24.8(2)	62.2(0)	▫	8.5(2)
	15.8(3)	78.7(0)	▲	9.2(2)
	22.0(4)	89.9(1)	●	11.8(4)
	8.2(5)	96.5(1)	△	7.1(4)
150	37.4(2)	63.6(0)	▫	7.5(1)
	11.8(3)	79.5(1)	▲	8.4(3)
	34.6(4)	91.7(1)	●	12.0(4)
	9.6(7)	98.2(1)	△	5.9(5)
140	5.1(1)	54.3(1)	○	7.5(5)
	39.0(2)	63.9(0)	▫	6.1(1)
	13.5(2)	79.7(1)	▲	9.4(2)
	35.0(2)	91.8(1)	●	11.2(1)
	12.5(3)	98.0(1)	△	6.1(1)
130	6.9(0)	55.0(0)	○	6.2(0)
	39.5(1)	64.7(0)	▫	5.5(0)
	11.4(1)	80.2(0)	▲	8.8(1)
	34.7(0)	92.6(0)	●	11.1(0)
	13.1(1)	98.4(0)	△	6.2(0)
120	10.6(2)	56.0(1)	○	4.9(2)
	44.5(3)	65.5(0)	▫	4.9(1)
	10.9(3)	80.6(1)	▲	7.9(3)
	39.9(8)	93.5(2)	●	11.6(3)
	13.0(1)	99.0(1)	△	6.2(5)

TABLE 2.2 (Contd.)

T	P_1	$\sqrt{P_2}$	symbol	$\sqrt{P_3}$
110	17.6(3)	56.8(0)	◯	3.6(1)
	56.1(3)	66.4(0)	▢	4.6(0)
	13.9(2)	81.2(0)	▲	8.5(2)
	26.1(4)	91.2(1)	■	7.6(1)
	36.1(4)	95.9(1)	●	6.5(1)
	19.8(4)	100.2(1)	△	5.7(2)
100	26.5(4)	59.4(0)	◯	3.5(0)
	67.2(3)	59.1(0)	▢	4.1(0)
	10.4(2)	82.8(0)	▲	5.2(1)
	20.2(3)	93.6(1)	■	8.3(1)
	50.4(3)	99.3(0)	●	9.9(1)
	1.4(1)	104.6(9)	△	10.1(3)
90	41.9(6)	58.7(0)	◯	2.8(0)
	87.7(5)	68.5(0)	▢	3.7(0)
	13.2(2)	81.8(1)	▲	8.6(0)
	38.5(5)	92.7(0)	■	6.2(1)
	59.6(9)	97.6(0)	●	4.7(1)
	34.1(6)	101.6(0)	△	7.0(1)

FIG.29
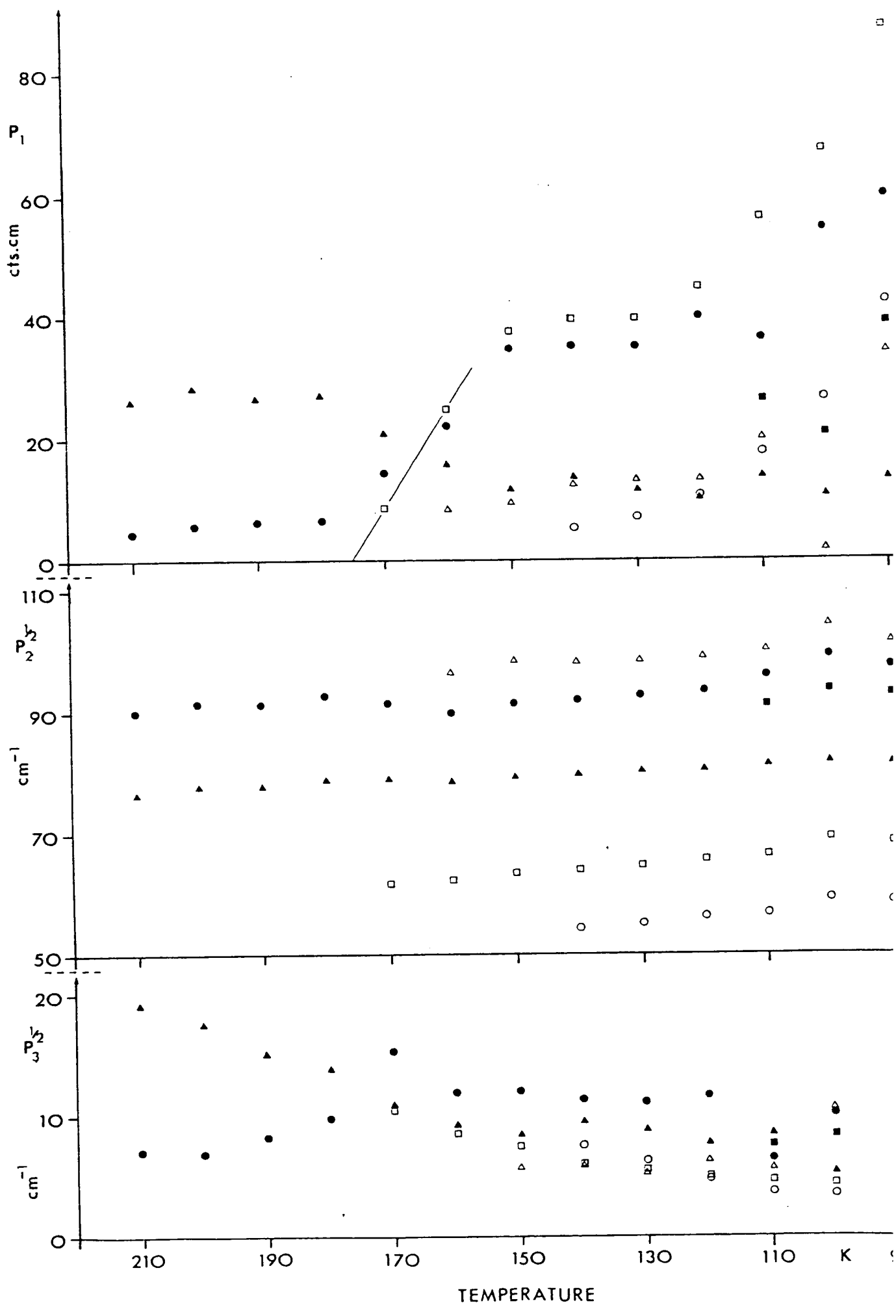
Figure 2.8:   The strength of the Raman line of frequency

61.8 cm^{-1} plotted for warming and cooling,

the progression of time throughout the

experiment being indicated by the arrows.
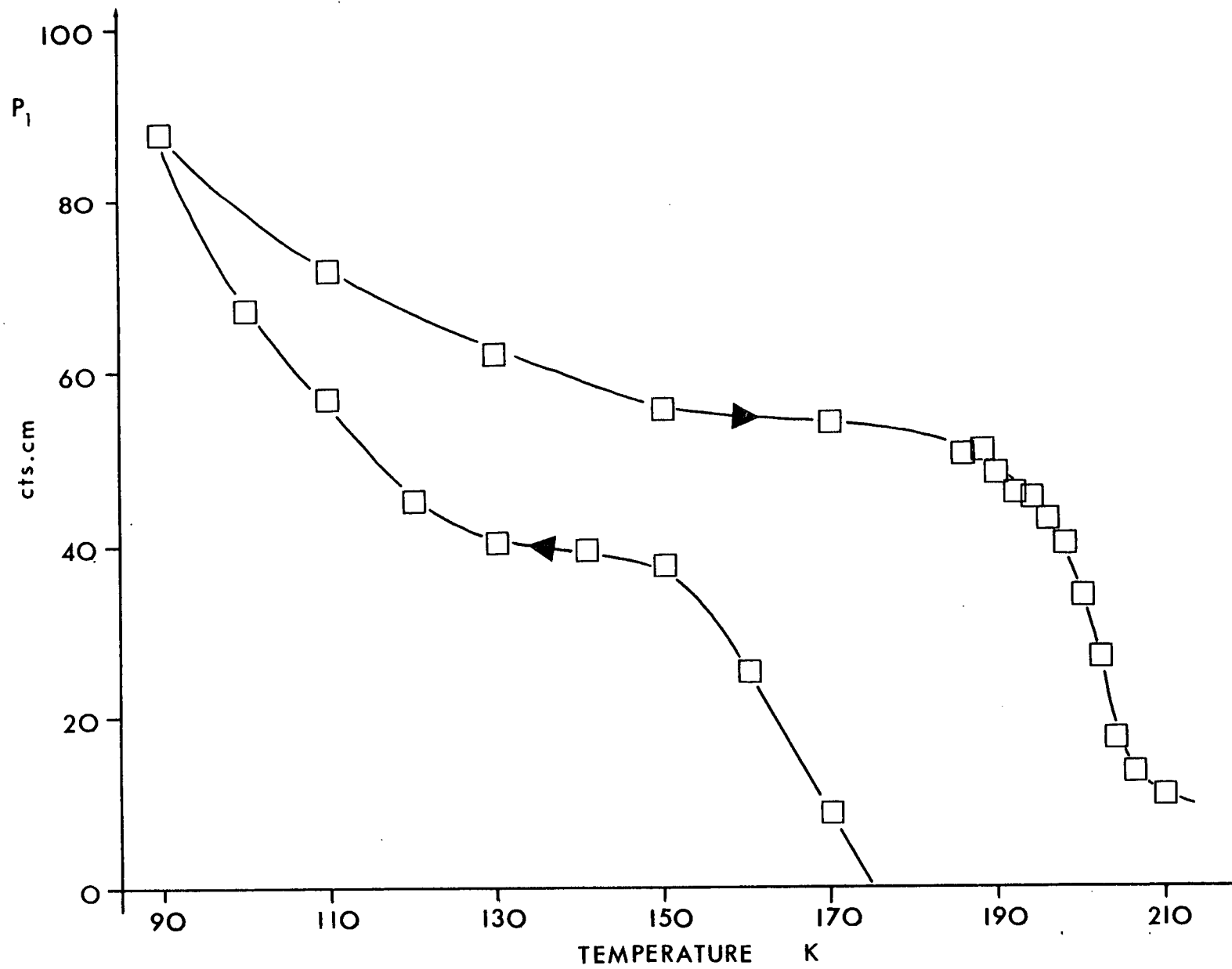
FIG. 2·8

it is not complete until at least 100K, since the intensity of the
new mode is still increasing as the temperature is further reduced.

The variations of the parameters P_1, $P_2^{\frac{1}{2}}$, $P_3^{\frac{1}{2}}$ with temperature
have been given in Table 2.2 and Figure 2.7. The frequencies ($P_2^{\frac{1}{2}}$)
of the modes increase steadily with decreasing temperature and this
is as expected, although at 160K the mode of frequency 90 cm^{-1} shows
a slight deviation from this behaviour. Whether this is due to the
transition or whether it is related to the addition of the extra
mode at $\sim$ 96 cm^{-1} into the fitting procedure is not known. It is
highly likely that the mode at $\sim$ 96 cm^{-1} is in fact scattering at
temperatures higher than 160K, but since it cannot be resolved it
is introduced into the fitting procedure only when the spectrum
profile at $\sim$ 90 cm^{-1} cannot be accounted for by one mode alone.

All of the modes show a slight deviation in linear frequency
variation at 100K, but the cause of this is not known. Some of
the modes also show an increase in their widths at 100K, and these
are probably linked with the increase in frequencies. This would
mean that these effects may be due to the fitting procedure.

Each measurement in Figure 2.8 was taken about 5 minutes after
the thermocouple adjacent to the sample indicated stability and the
changes in intensity were rapid in following those in the tempera-
ture. In a few cases where the scan was repeated after an extra
equilibration time of about 10 minutes, no subsequent changes in
the spectrum were apparent. It is clear from Figure 2.8 that the
state of the sample on cooling was not equilibrium, as a comparison
with results taken on warming over the same temperature range shows.
These latter results are the upper curve in Figure 2.8 and the same
part of the external mode spectrum as was shown in Figure 2.6 for
cooling, is shown in Figure 2.9 for warming. The fitted curves are

also given and the corresponding parameters are tabulated in Table 2.3 and plotted in Figure 2.10.

The results of the fitting procedure plotted in Figure 2.10 show some unusual features. The mode at 61.8 cm^{-1} has already been discussed and its strength has been plotted in Figure 2.8. However, it is noted that the frequency and width also show unusually large changes at the transition on warming. Since the strength of this mode is decreasing rapidly on approaching the transition temperature, the fitting procedure might attempt to counteract this by altering the width and frequency of the mode. This might have been avoided by fixing both the frequency and line width to values obtained for a temperature of $\sim$ 200K. However, it is possible that the line width variation is real, and this then means that the mode becomes highly damped at the transition, with the peak frequency $((P_2 - \frac{1}{2}P_3)^{\frac{1}{2}})$ and the line width $(P_3^{\frac{1}{2}})$ being of the same order.

A more conclusive result regarding the damping of modes near the transition would of course be obtainable by performing the same measurements on a single crystal sample and using a polarisation analysis to filter out a particular Raman mode, but since the sample was polycrystalline this was not possible.

The other dramatic change in the fitted parameters plotted in Figure 2.10 is the line width of the mode of frequency 81.5 cm^{-1}. The very sudden increase of the line width parameter $(P_3^{\frac{1}{2}})$ of this mode at 170K is not accompanied by large changes in any of the other fitted parameters in the whole scan. This being the case, it is therefore tentatively concluded that this is a real effect corresponding to a large increase in the damping forces affecting this mode of vibration at 170K. No previous work done on this system suggests a transition at this temperature on warming, so that an alternative explanation should be sought. However, at present this is not discussed further.

Figure 2.9:   External mode scans made on warming from 90K

               to 210K. Open circles are the experimental

               data and the full line the fitted curve.

               Each scan is raised by 5000 counts from the

               one preceding it.

Figure 2.10:   Plots of parameters in Table 2.3 against

               absolute temperature.

               Similar symbols in each plot of this figure represent one
               mode in the Raman spectrum, and these are keyed in Table 2.3.

 Table 2.3 :   Fitted parameters for curves in Figure 2.9.
               The absolute temperature is also shown.   Uncer-
               tainties are given in parentheses.

FIG. 2·9a

INTENSITY   cts.

192K

190K

188K

186K

170K

150K

130K

110K

90K

5000

0

60

80

100

FREQUENCY   cm⁻¹

FIG. 2·9b

FIG. 2·9b
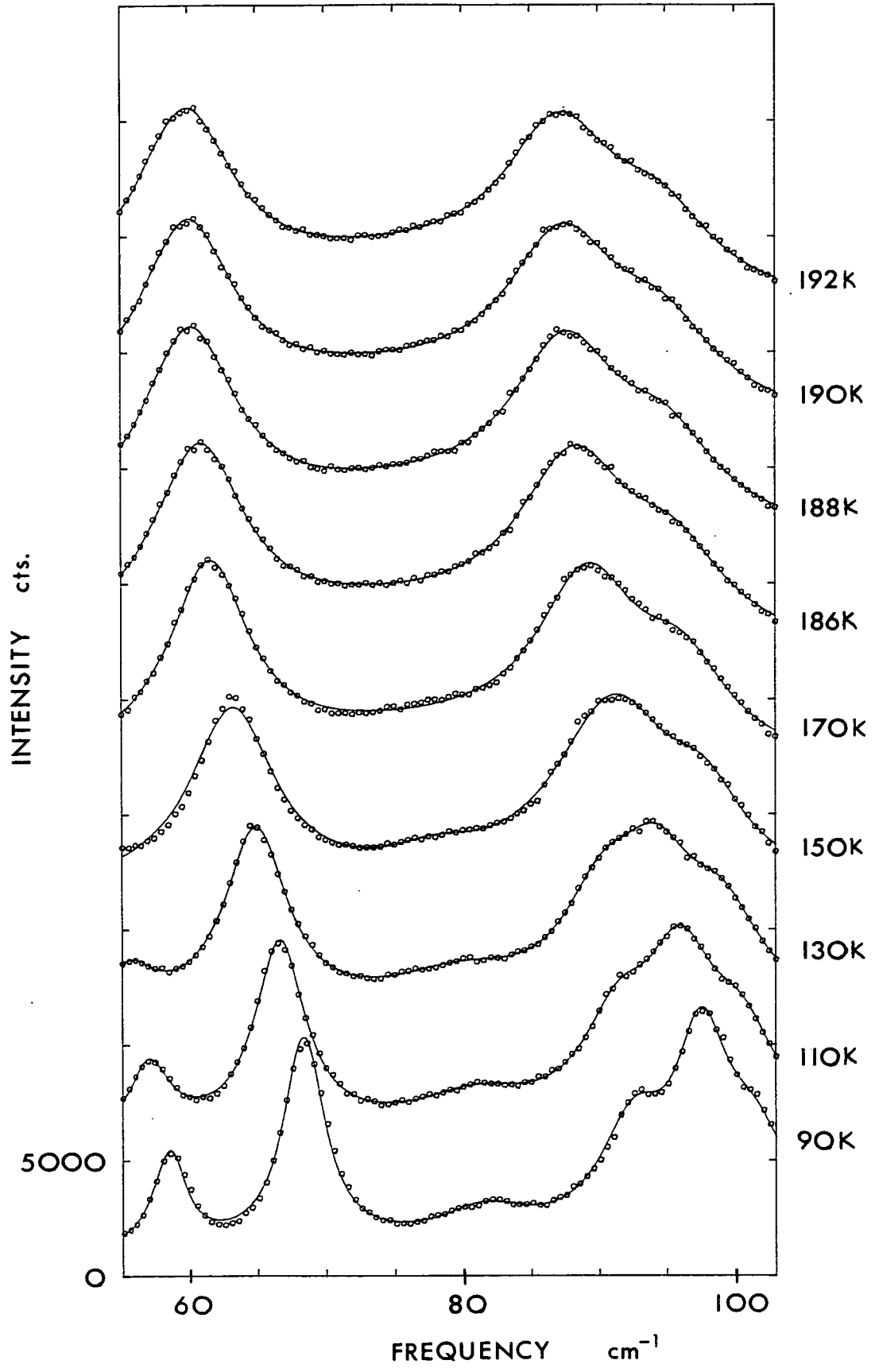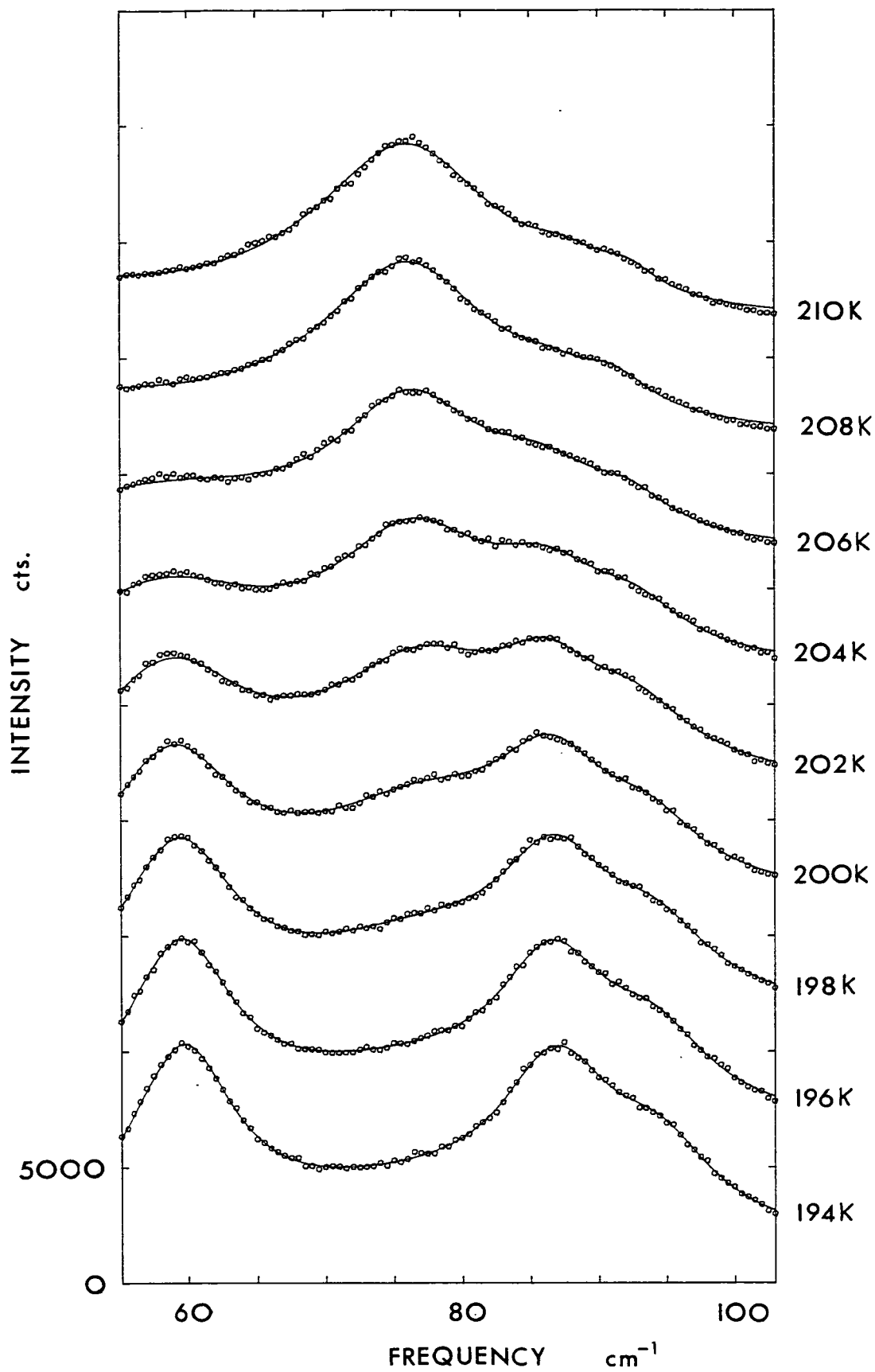
FIG. 2·10
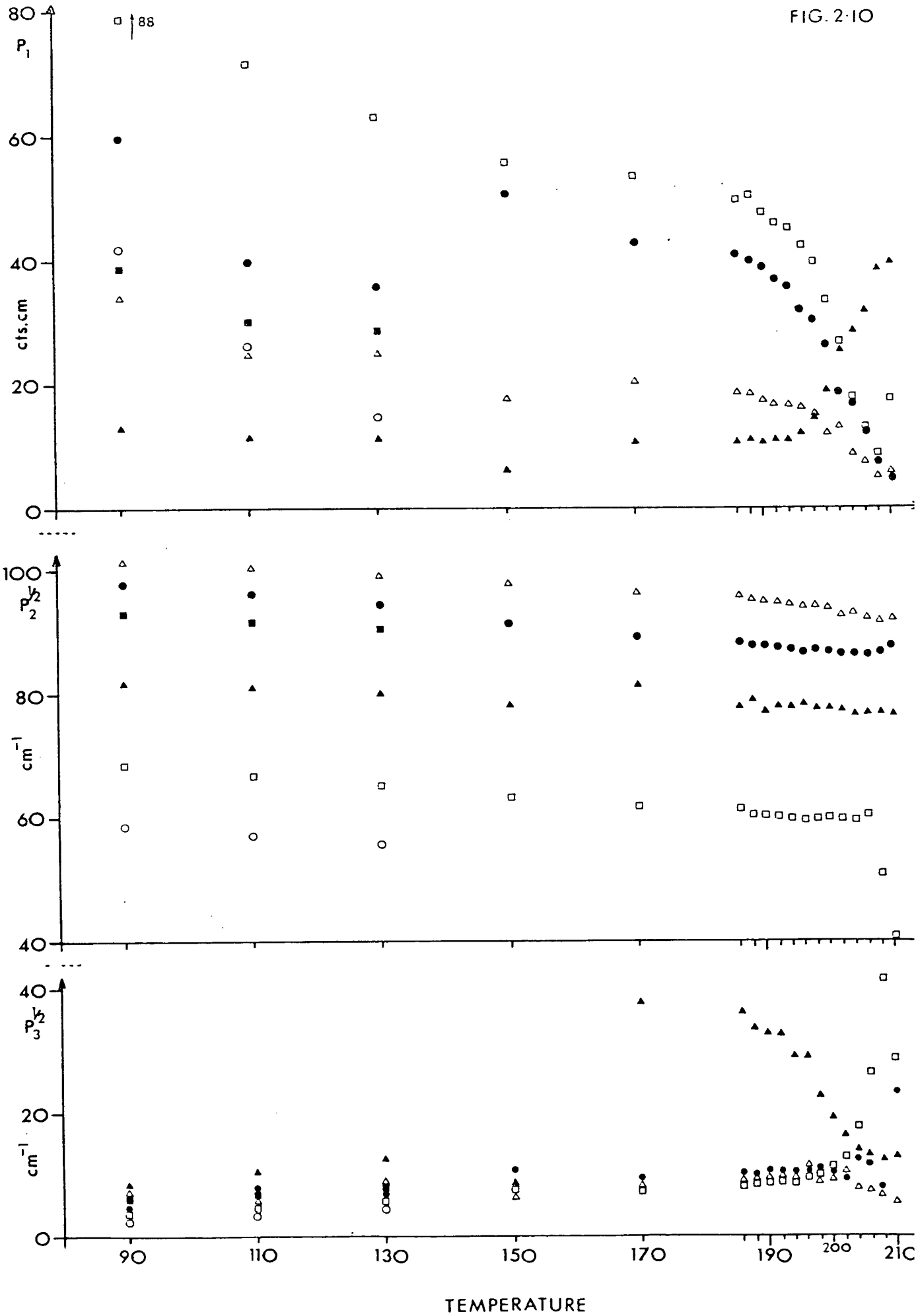
TABLE 2.3

T (K)	P_1 (cts. cm.)	$\sqrt{P_2}$ (cm^{-1})	$\sqrt{P_3}$ (cm^{-1})	symbol
90	41.9(6)	58.7(0)	2.8(0)	○
	87.7(5)	68.5(0)	3.7(0)	▢
	13.2(2)	81.8(1)	8.6(0)	▲
	38.5(5)	92.7(0)	6.2(1)	
	59.6(9)	97.6(0)	4.7(1)	
	34.1(6)	101.6(0)	7.0(1)	△
110	26.1(2)	57.1(0)	3.7(0)	○
	71.3(2)	66.7(0)	4.5(0)	▢
	11.4(1)	81.0(0)	10.6(1)	▲
	29.9(2)	91.5(0)	6.5(1)	
	49.5(2)	96.1(0)	6.5(0)	●
	24.9(2)	100.6(0)	6.2(1)	△
130	14.7(2)	55.7(0)	4.4(1)	○
	62.7(3)	65.0(0)	5.6(0)	▢
	11.3(1)	80.0(1)	12.8(2)	▲
	28.6(4)	90.4(0)	7.2(1)	
	35.5(4)	94.3(1)	7.1(0)	
	25.1(3)	99.2(0)	7.3(1)	△
150	55.6(1)	63.4(0)	7.5(0)	▢
	6.2(1)	78.1(0)	8.2(2)	▲
	50.5(1)	91.3(0)	10.8(1)	
	17.8(1)	97.9(0)	7.0(1)	△
170	53.8(3)	61.7(0)	7.1(1)	▢
	10.4(2)	81.3(7)	37.7(7)	▲
	42.3(5)	89.4(0)	9.2(1)	●
	20.2(4)	96.3(1)	8.2(2)	△
186	49.4(3)	61.1(0)	8.1(1)	▢
	10.3(3)	78.0(1.0)	35.9(1.1)	▲
	40.6(8)	88.4(1)	10.1(3)	
	18.2(6)	95.8(1)	9.4(3)	△
188	50.1(2)	60.4(0)	8.3(1)	▢
	10.7(1)	78.9(3)	33.6(6)	▲
	39.4(3)	87.8(0)	9.9(1)	
	18.1(2)	95.1(2)	9.3(2)	△

TABLE 2.3 (Contd.)

T	P_1	$\sqrt{P_2}$	$\sqrt{P_3}$	symbol
190	47.1(0)	60.3(0)	8.4(0)	□
	10.3(0)	76.9(0)	33.0(0)	▲
	38.5(0)	87.7(0)	10.4(0)	
	17.2(0)	95.0(0)	9.5(0)	△
192	45.9(3)	60.1(0)	8.7(1)	□
	10.6(4)	77.8(9)	32.4(1.4)	▲
	36.4(8)	87.4(0)	10.1(3)	
	16.8(6)	94.8(1)	9.7(3)	△
194	44.9(4)	59.9(8)	29.0(1.6)	□
	35.4(8)	87.1(1)	10.2(3)	▲
	16.5(6)	94.6(2)	9.9(3)	△
196	42.0(3)	59.8(0)	9.3(1)	□
	11.7(5)	78.6(7)	29.1(1.5)	▲
	31.5(9)	86.8(1)	9.7(4)	●
	16.1(7)	94.2(1)	10.1(4)	△
198	39.2(3)	59.7(0)	10.0(2)	□
	14.1(7)	77.9(5)	21.4(1.3)	▲
	30.0(1.0)	87.0(0)	10.2(5)	
	14.2(7)	94.4(1)	9.9(4)	△
200	33.1(3)	59.4(0)	11.0(1)	□
	18.9(8)	77.7(3)	18.9(9)	▲
	26.0(1.0)	86.8(1)	10.4(6)	
	11.8(8)	93.9(2)	9.6(4)	△
202	26.1(1)	59.4(0)	12.8(1)	□
	25.3(1)	77.5(0)	15.7(0)	▲
	18.2(1)	86.4(0)	9.4(0)	
	12.9(1)	92.9(0)	10.5(1)	△
204	17.6(1)	59.5(0)	17.3(2)	□
	28.2(2)	76.8(1)	13.8(1)	▲
	16.5(2)	86.5(1)	11.2(2)	
	8.4(2)	93.0(1)	8.7(2)	△
206	12.5(1)	60.2(1)	25.7(5)	□
	31.6(2)	76.7(1)	13.5(1)	▲
	12.3(2)	86.1(1)	10.8(2)	
	7.2(2)	92.4(1)	7.9(2)	△

TABLE 2.3 (Contd.)

T	P_1	$\sqrt{P_2}$	$\sqrt{P_3}$	symbol
208	8.6(3)	50.6(8)	44.1(2.2)	◻
	38.1(2)	76.7(0)	15.6(1)	▲
	4.8(3)	86.4(3)	7.4(5)	
	7.2(3)	91.2(2)	7.1(2)	△
210	17.1(1)	40.1(1)	29.3(4)	◻
	39.3(1)	76.7(0)	16.4(0)	▲
	5.8(1)	87.7(1)	23.7(0)	
	5.0(1)	92.2(1)	5.5(1)	△

The upper curve of Figure 2.8 shows a transition centred on 201K. Figure 2.11a demonstrates clearly the changes that have taken place in the external mode spectrum on warming through this transition and Figure 2.11b shows scans that have been constructed from those at 198K (B) and 206K (T) in Figure 2.11a. From top to bottom in Figure 2.11b, these are T, $\frac{1}{4}$(3T+B), $\frac{1}{2}$(T+B), $\frac{1}{4}$(T+3B) and B, and since they correspond very closely to those in Figure 2.11a the proportions of each phase present at each temperature may be directly deduced.

The hysterisis found by Brennan et al.[20] for the transition at 249K was 3K, whereas in the present discussion we see, from Figure 2.8, a hysterisis of about 25K, and this is consistent with the conclusion that the different experimental techniques are sensing different types of transitions. This would also account for the lack of evidence of a transition at ∿ 250K on warming in the Raman data presented here.

The cause of the discrepancy of results on cooling and warming is not known but it is possible that pockets of eutectic mixtures that are frozen into the sample do not transform until 100K. There is a small deuteration effect, the results using protonated samples give transition temperatures about 4K higher and a similar hysterisis effect was also found.

The work of Gilson et al.[21] showed that in the temperature range 150K to 90K, on cooling, the NMR linewidth broadened. However, no major changes in the Raman spectrum are seen between 150K and 90K on cooling, although it is pointed out that this temperature range is probably that in which the transition at 175K saturates. This might suggest a relation between the NMR measurements and the saturation of the transition observed here, but this is doubtful since, on warming to 150K, the NMR line has sharpened, whereas the

Figures 2.11a, b: (a) shows the scans (taken from Figure

2.9) on warming from 198K to 206K, in 2K

steps, each scan raised by 5000 counts

from the preceding one.

(b) shows the same frequency range but

constructed from scans at 206K (T) and

198K (B) in (a), and from top to bottom,

these are T, $\frac{1}{4}$(3T+B), $\frac{1}{2}$(T+B), $\frac{1}{4}$(T+3B), B.

FIG. 2·11a,b
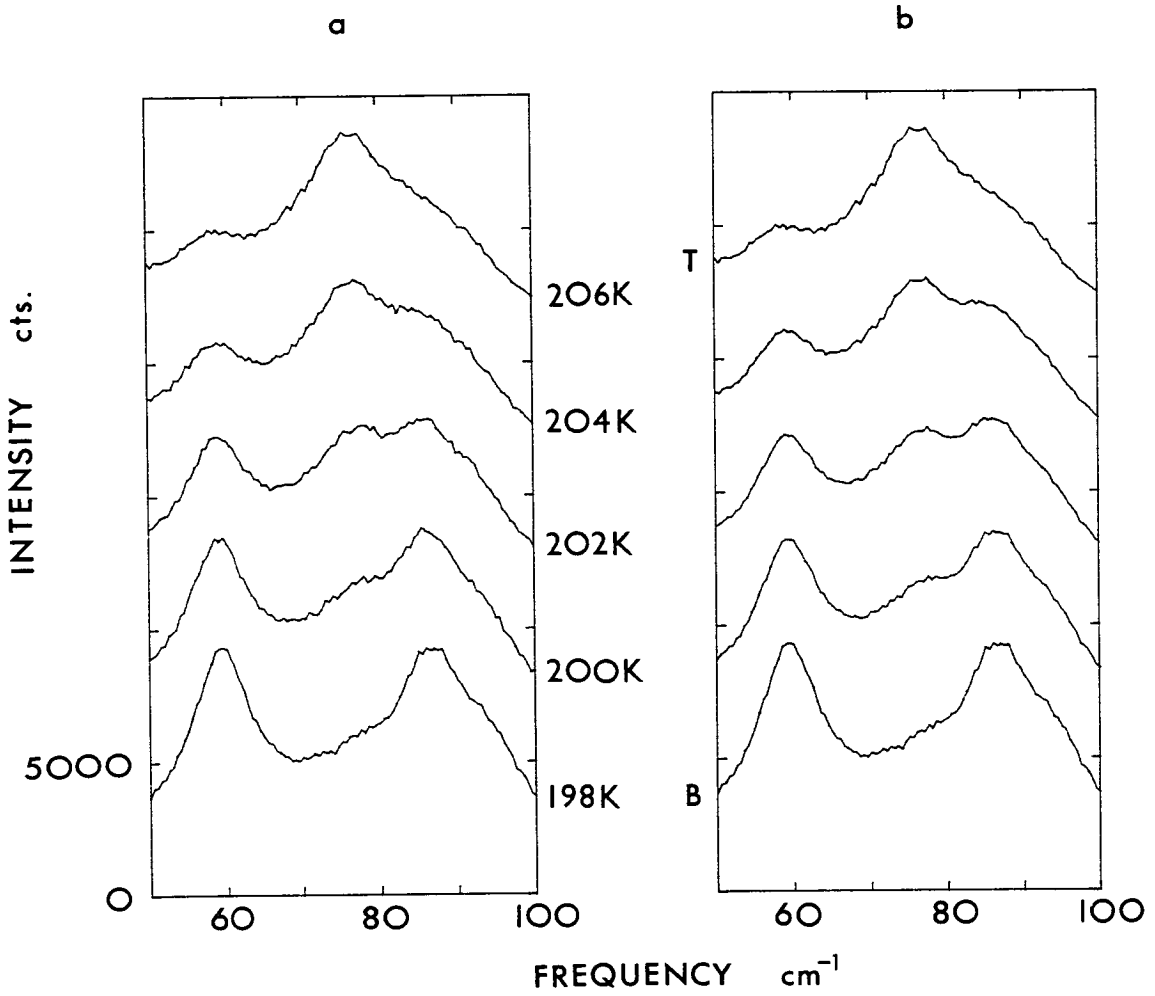
the Raman data shows no evidence of a transition until about 198K, after Fig. 2.11a (B).

As the temperature is reduced to 4.2K the Raman spectrum changes continuously, the external modes becoming sharper and better resolved than at higher temperatures. The external mode spectrum of a deuterated specimen of this system is given in Figure 2.12 and on a peak and shoulder count it displays about 13 modes, indicating that the crystal structure at 4.2K is considerably complex.

Further evidence of this complexity was sought by making high resolution measurements over the internal modes of this system. It might be expected that these peaks would show a change in structure over the transition, since this would be caused by a change in the Davydov splitting which may alter in a phase change.

In all cases the structure of these internal modes became better resolved at lower temperatures, and this is shown by Figure 2.13 where the temperatures of measurement were 215K and 4.2K. However, no change in the structure of the internal modes was apparent, and the only deduction to be made is that if there is a phase transition to a more complex structure at low temperatures, then the inter-molecular forces are so weak as to leave the Davydov splitting un-altered.

The preceding discussion has shown that several transitions take place in this system on varying the temperature. The crystal structure of the $C_6D_6 \cdot C_6F_6$ system at 280K has been presented in Chapter 1, §3, where the experimental technique used was X-ray diffractometry and this revealed a very simple rhombohedral structure at just below room temperature. From the external Raman spectrum given in Figure 2.12 it is obvious that the crystal structure at 4.2K is very complex. Unpublished neutron powder diffraction data also suggests a considerably

Figure 2.12:   External mode spectrum for $C_6D_6 \cdot C_6F_6$

at 4.2K in the frequency range

20 cm^{-1} to 120 cm^{-1}.

Figure 2.13:   Internal mode spectra for $C_6D_6 \cdot C_6F_6$

around 560 cm^{-1} at 215K and 4.2K.
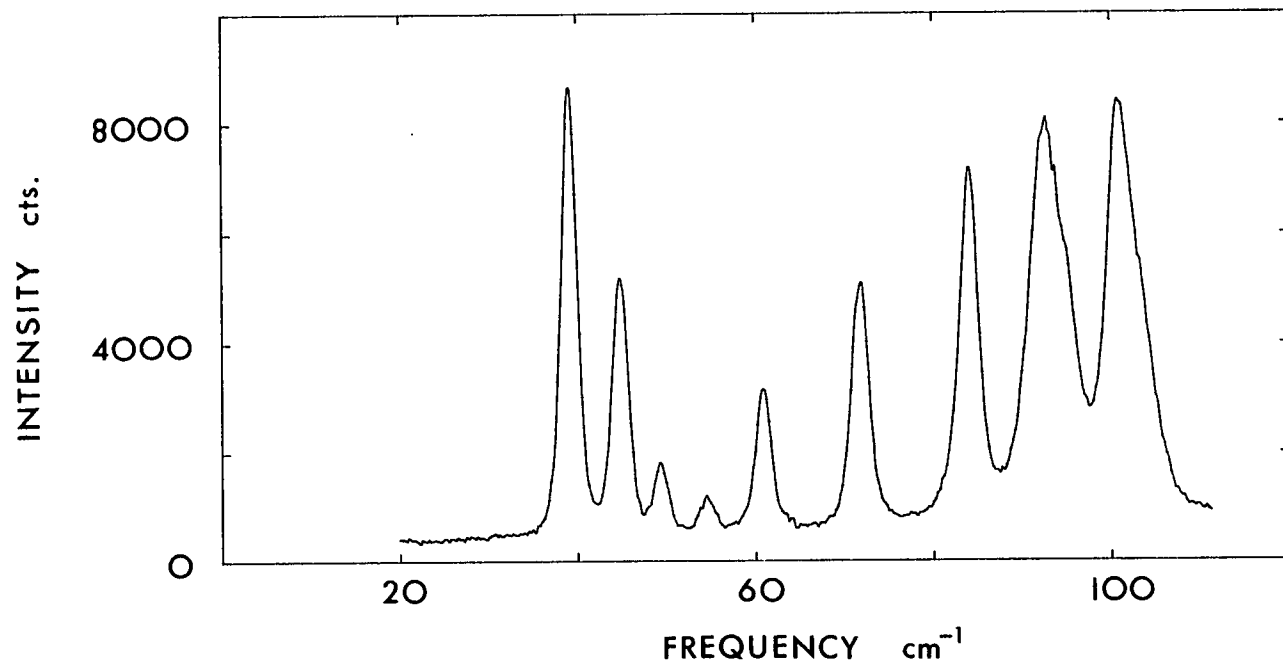
FIG.2·12

FIG. 2·13
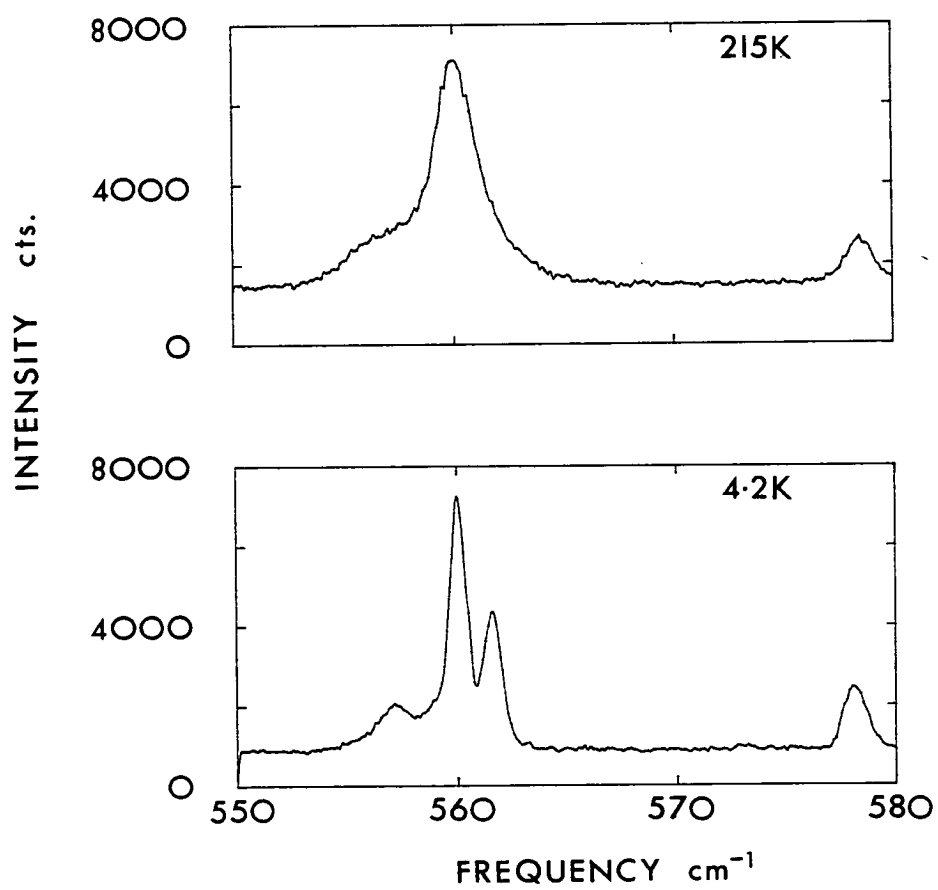
complex structure at low temperatures but this has not yet been fully elucidated.

The next section is devoted to some preliminary high pressure Raman spectra taken from a sample of $C_6D_6 \cdot C_6F_6$ at room temperature.

4.2 Preliminary high pressure Raman spectra of the $C_6D_6 \cdot C_6F_6$ system

The previous section dealt with the temperature dependence of the dynamics of the benzene-hexafluorobenzene system. A structural phase transition was found at 175K on cooling and 201K on warming for a deuterated sample of the complex.

Mention was also made of unpublished neutron powder diffraction data that has not yet been fully analysed but which shows that there are at least three phases of this system between 300K and liquid helium temperatures. It might therefore be expected that if pressure were applied to the solid phase of this system it may be possible to induce structural phase transitions.

The high pressure cell that was used has already been described in §2 and a diagram representing its essential features has also been given and in the following text we refer to Figure 2.2.

The procedure used to fill the sample chamber, S, was to cool both the 1:1 molar mixture of liquids and the anvil A2 to a temperature of about 250K. This anvil could not be cooled further since this would adversely affect its ease of movement within anvil A1. The polycrystalline sample tended to sublime rapidly when placed on the gasket G in order to fill the chamber S, so it was necessary to make an addition to the standard apparatus given in Figure 2.2 , in order to obtain a larger sample. Another gasket with a larger central bore was welded onto the top of gasket G and the resulting hole filled with sample, the calibration ruby having been inserted

first. The anvil A2 was then quickly mounted into Al and pressure applied to force the sample into the chamber S and seal this volume off so that the sample was completely enclosed. After several attempts a good sample was obtained and spectra were measured using the back scattering geometry shown in Figure 2.2.

The radiation used to excite the spectra was either the 5017Å or 4765Å line of an argon ion laser and the back scattered light was collected in the spectrometer described in §2. The laser was operated at   80 mW, and it was found necessary to reduce the laser heating in the sample by a stream of cold argon gas ($\sim$ 275K), flowing over the outer surface of diamond D1.

The spectra were measured at pressures between 2 kbar and 24 kbar, where pressures higher than 25 kbar tended to work harden and fracture the upper of the two gaskets, thereby releasing the sample from the chamber. This fracturing of the additional gasket was usually responsible for the deterioration of the sample and, as mentioned above, several attempts were necessary in order to obtain a good sample that was stable up to these high pressures. The purpose of these measurements was to observe any transitions that take place at high pressure, and no curve fitting was performed on these spectra.

These data are presented as measured and are given in Figures 2.14 and 2.15 for pressure decrease and increase respectively. The two figures do not correspond to the same sample, however, since the upper gasket fractured for the sample used for Figure 2.14 and therefore had to be replaced. However, this will not affect any qualitative conclusions drawn from the variation of the spectra with pressure. This variation is that which is expected; as the pressure decreases the sample becomes less mechanically strained

Figure 2.14:   External mode scans between 30 cm^{-1}
               and 175 cm^{-1} for pressure decrease
               from 16 kbar to 2 kbar.

Figure 2.15a,b: External (a) and internal (b)
                  mode scans for pressure increase
                  between 2 kbar and 24kbar.   Laser
                  emission lines are labelled E.
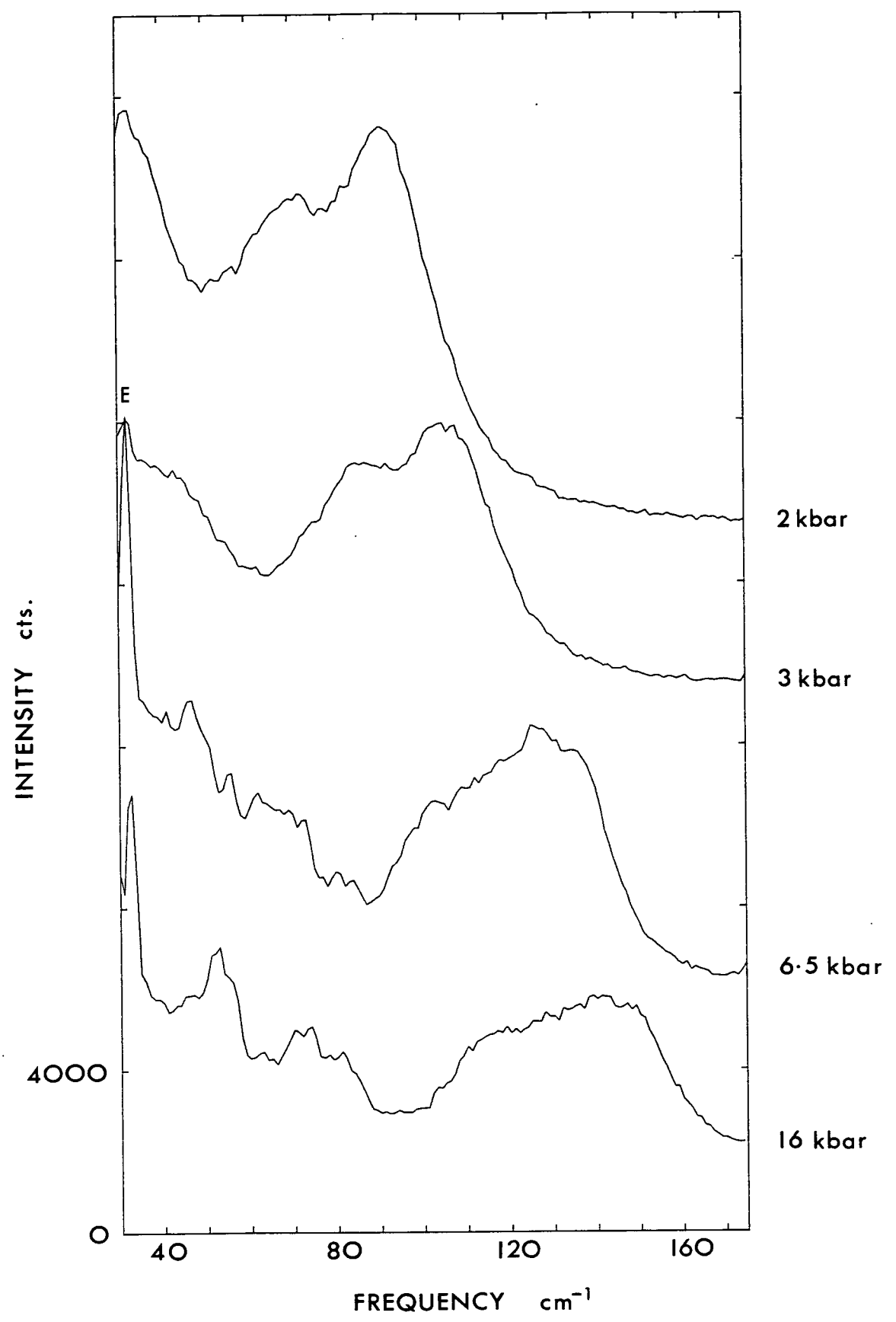
FIG. 2·14
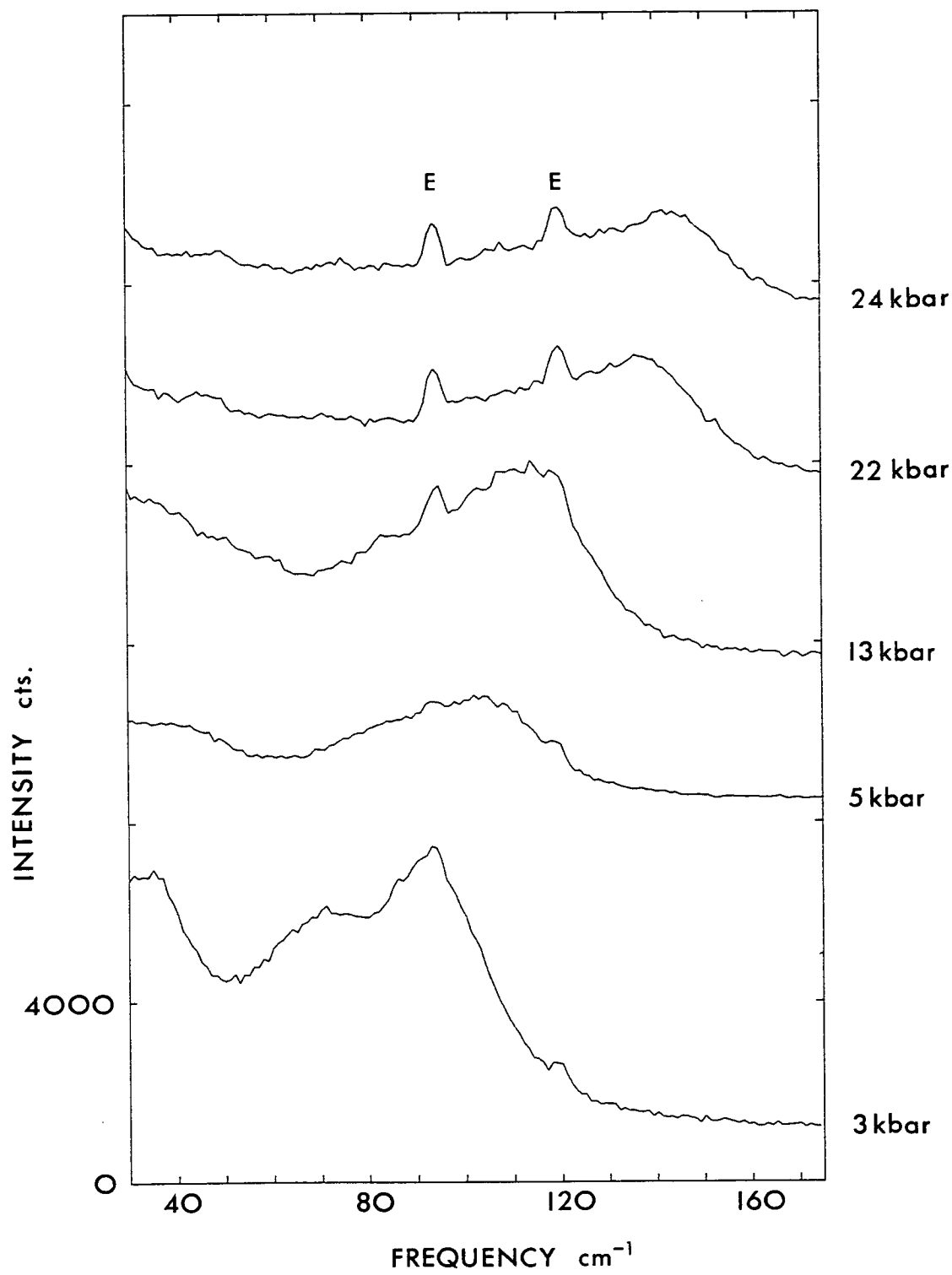
FIG. 2·15a

FIG. 2·15b
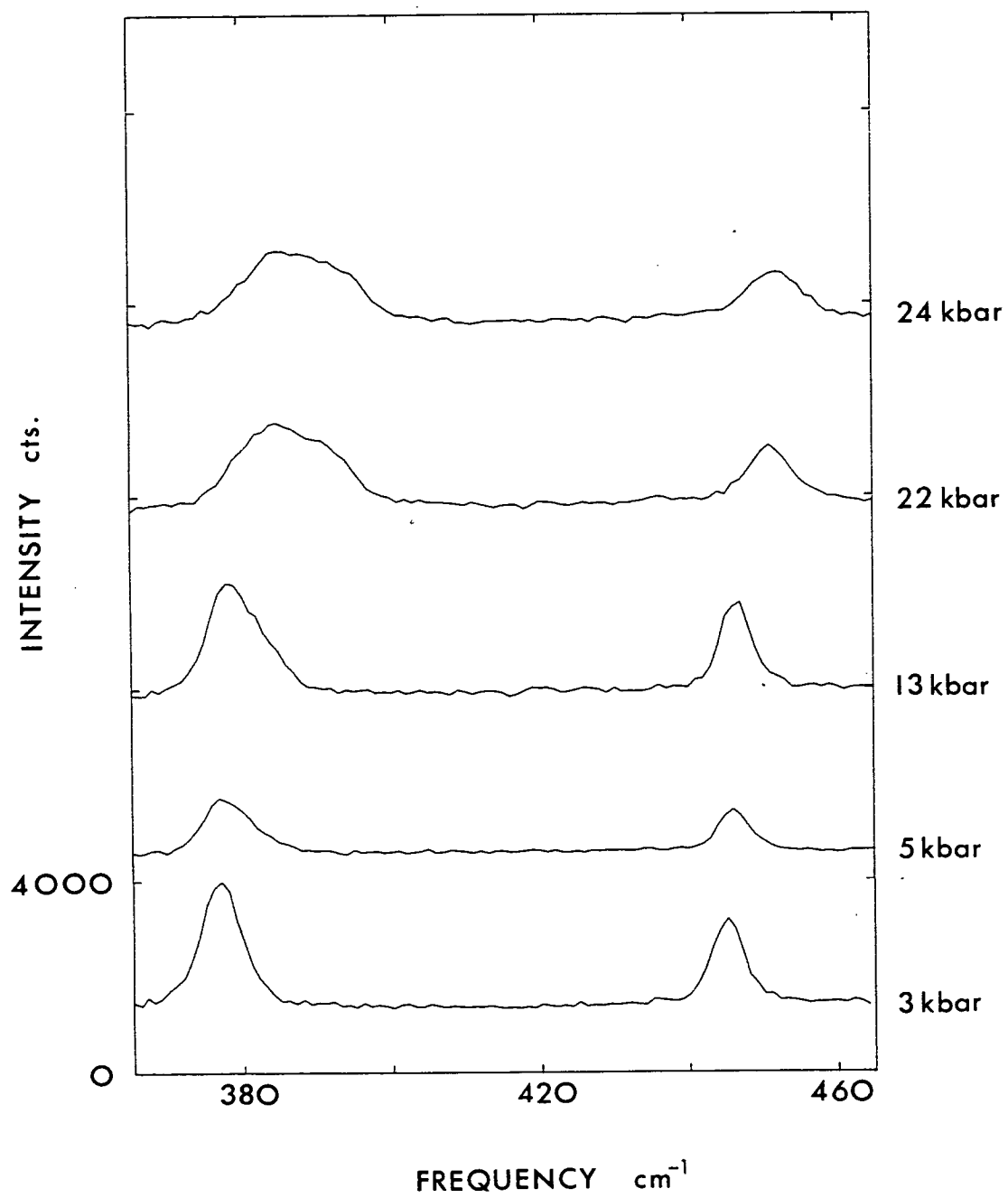
and the normal mode frequencies decrease as a result. The scan at 2 kbar shows a similar profile to the scan at 200K given in the previous section in Figure 2.11a, with a pair of peaks between 50 cm^{-1} and 90 cm^{-1}. However, the frequencies observed in the high pressure, room temperature data are different from those at atmospheric pressure and 202K. The cause of this difference may either be the pressure variation or possibly a new phase having been induced at 16 kbar which may still persist when the pressure is released. However, this is not known at present and more detailed data would be required to resolve the cause of these differences.

The spectra measured on increasing the pressure have been presented in Figure 2.15a and in Figure 2.15b part of the internal mode spectrum around ∿ 400 cm^{-1} is also given. Where laser emission lines are present in the spectra these are marked 'E'.

The pressure range in these figures is 2 kbar to 24 kbar and the behaviour of these external and internal mode spectra are also as expected. As the pressure increases the density increases and the sample has a high mechanical strain exerted upon it, thereby increasing the normal mode frequencies. The Raman lines also become broader at higher pressures and this is clearly demonstrated by the internal mode spectra in Figure 2.15b.

From the data that has been presented no abrupt change in the external mode spectrum is seen up to a pressure of 24 kbar. It is already known that this molecular system undergoes several transitions of various types when the temperature is varied. It may therefore be expected that this system would undergo a transition at low pressure since it is a soft material at room temperature. However, the cell used was designed for high pressures and it is unable to stabilise at pressures below about 1 kbar. Further studies

of this material at pressures below 1 kbar may therefore be more fruit-ful than the high pressure data presented here, where it is possible that the system has already undergone a transition to a phase different from that at room temperature and room pressure.

It is clear from the data presented in sections 3.5 and 3.6 and from previous work, that this system displays many interesting phenomena when such quantities as pressure and temperature are varied. It is therefore concluded that a great deal more research is necessary to explain the driving mechanisms that cause the transitions that have been previously mentioned.

REFERENCES FOR CHAPTER 2

(1) Ramanathan, K.R., Proc. Indian Assoc. Cult. Sci. (1923), $\underline{8}$, 18.

(2) Krishnan, K.S., Phil..Magaz. (1925), $\underline{50}$, 697.

(3) Raman, C.V., J. Opt. Soc. Am. (1927), $\underline{15}$, 185.

(4) Maiman, T.H., Nature (1960), $\underline{187}$, 493.

(5) Arthur, J.W., Ph.D. Thesis, Edinburgh University, 1974.

(6) Loudon, R., Adv. Phys. (1964), $\underline{13}$, 423.

(7) "The Raman Effect", Vols. 1-2, ed. Anderson, A.(1971) Dekker, N.Y.

(8) Leech, J.W., Newman, D.J., "How to use Groups", 1969, Methuen.

(9) McWeeny, R., "Symmetry - an Introduction to Group Theory", 1963
         Pergamon Press.

(10) Koningstein, J.A., "Introduction to the Theory of Raman
         Scattering" (1972) Reidel Publishing Co., Holland.

(11) Swamy and Samuel, "Group Theory made easy for Scientists and
         Engineers", (1979), Wiley, N.Y.

(12) "Light scattering Spectra of Solids" (1969), ed. Wright, W.B.,
         Springer-Verlag, N.Y. Inc.

(13) Born and Huang, "Dynamical Theory of Crystal Lattices", (1954)
         Clarendon, Oxford.

(14) Goldstein, H., "Classical Mechanics", (1950), Addison-Wesley.

(15) Cochran, W., Cowley, R.A., (1967), Handbuch der Physik XXV, 59.

(16) Dicke, R.H., Wittke, J.P., "Introduction to Quantum Mechanics"
         (1960), Addison-Wesley.

(17) Cowley, R.A., "Phonons in Perfect Lattices with Point Imperfections",
         (1966), Oliver and Boys.

(18) Pointon, A.J., "Introduction to Statistical Physics", (1967),
         Longman Group Ltd., London.

(19) Patrick and Prosser, Nature (1960), $\underline{187}$, 1021.

(20) Brennan, J.S., Brown, N.M.D., Swinton, F.L., J. Chem. Soc. Farad.
         (1974), $\underline{70}$, 1965.

REFERENCES FOR CHAPTER 2 (Contd.)

(21) Gilson, D.F.R., McDowell, C.A., Canad. J. Chem. (1966), 44, 945.

(22) Ripmeester, J.A., Wright, D.A., Fyfe, C.A., Boyd, R.K.,
         J. Chem. Soc. Farad. Trans. II (1978), 74(7), 1164.

CHAPTER 3   NEUTRON POWDER DIFFRACTION

§1 Introduction

The technique of neutron powder diffraction (NPD) has been extensively used in the investigations of a great variety of materials. This method is of particular use when single crystals of the size necessary for neutron diffractometry are not available, this being of the order of several mm^3. This unavailability of crystals of this size is usually because of difficulties in the growing procedure for such specimens.

A review of the literature that has used NPD would be too large to present here, since the amount of work that has been done is very great, both in its content and variety. The reader is therefore referred to several references that cover some of the main topics studied using NPD, these including crystallographic structures[37]-[40], magnetic systems[41],[42], phase transitions[43,44] and electrical properties[45] of some systems.

The content of this chapter is mainly concerned with the technique of profile refinement of NPD data and in section §2.1 the computational facet is outlined. In §2.2 the refinement parameters are described and this leads to the separation of these parameters into two categories, the structural and the profile parameters. Sections §2.3 and §2.4 deal with constrained refinement and temperature factors respectively.

Experimental conditions, of a general nature, are considered in §3, with a brief description of a high resolution diffractometer included. Experimental measurements and the relevant analyses and discussion are given in §4.

§2   The Technique of NPD

2.1 Profile analysis

An ideal powder is a collection of a large number of small crystal-
lites, each with random orientation with respect to its neighbours.
The linear size of a crystallite is approximately inversely proportional
to the diffraction peak width and therefore the diffraction conditions
limit the minimum dimension of a crystallite from which it is possible
to obtain interpretable diffraction data. This limit may be of the
order of $\sim$ 10μm. The topic of the size of powder crystallites has been
the subject of several investigations by various experimental techniques
(see, for example, references (1) - (4)).

The orientation distribution of the crystallites will usually be
almost random and therefore, whatever the sample orientation with res-
pect to the incident beam, there will always be some crystallites that
diffract the incident neutrons, but not necessarily in the beam-sample-
detector plane. This scattering results in the powder diffraction, or
Debye-Scherrer cones, whose common axis is the incident beam direction,
of semi-angle $2\theta_h$, $2\theta_h$ being the scattering angle of the reflection
of indices $h \equiv (hk\ell)$. A powder diffraction scan may therefore be
thought of as taking a section through these cones of diffracted in-
tensity in the horizontal plane containing the sample and detector.
The manner in which this section, or scan, is usually taken is to step
in the scattering angle, 2θ, and to count for a pre-determined length
of time at each point, thus forming the intensity profile as a function
of the scattering angle.

One disadvantage of using the powder diffraction technique is that
peaks in the diffraction scan may overlap, especially at high scattering
angles or for structures of low symmetry, and information is therefore

lost. This is contrary to the case of single crystal diffractometry where the Bragg peaks are usually well separated and no such loss of information occurs.

The technique of profile analysis is due to Rietveld[5,6] and involves using in the refinement, the profile intensities at each point in the scan, rather than the total integrated intensity of individual groups of overlapping reflections that was used previously[7]. This technique therefore removes some of the difficulties of the previous method, so that the maximum amount of information is now extracted from the powder diffraction scan. The program used by Rietveld proceeds in the analysis of powder diffraction data by removing from the scan a background in linear segments that are estimated graphically, after which the refinement of the background subtracted data may continue.

It is pertinent at this point to note that no realistic calculation has been done to find the contribution to a powder diffraction scan background from processes such as inelastic scattering and thermal diffuse scattering. Some work has been done in this area for the case of cubic powder diffraction patterns (see, for example, references (18) - (21)) but for lower symmetry structures there have been no results. In the refinements done by the author and described in this work, a flat background is used throughout.

The method of least squares is used to refine the structure under study and the expression that is minimised during the refinement is of the form

$$3.(1a) \quad R_W = \sum_j w_j \{y_j(\text{obs.}) - y_j(\text{calc.})\}^2 \quad ,$$

and the R factor is defined by the expression

$$3.(1b) \quad R = \frac{\sum_j w_j |y_j(\text{obs.}) - y_j(\text{calc.})|}{\sum_j y_j(\text{obs.})}$$

where y_j(obs.) and y_j(calc.) are respectively, the observed and calculated profile intensities at the jth point in the scan and w_j is the weight associated with that point. Several weighting schemes are possible and these include $(y_j(obs.))^{-1}$, $(y_j(obs.))^{-2}$ and $|y_j(obs.) - y_j(calc.)|$. However, since there is no reason to give any point in the scan more weight than any other, unit weights are used throughout the refinements of powder data described in this work.

In order to calculate the contribution of a diffraction peak at any point in the scan profile, it is necessary to know the shape of the peak as well as its integrated intensity. There are several factors that govern the observed powder diffraction peak shape and these include the thermal neutron spectral distribution, the mosaic spread of the monochromator crystal, the transmission functions of the collimator systems and the sample shape and grain size within the specimen. When all these factors are taken into account and convoluted, the result is almost exactly Gaussian. This is a somewhat surprising outcome since the above mentioned contributions need not necessarily have Gaussian forms themselves, but it is nonetheless empirically true that the shape of a neutron powder diffraction peak may be extremely well described by a normalised Gaussian distribution.

Given that this assumption is well satisfied we may write the contribution to the calculated diffraction pattern, y_j(calc.) at scattering angle $2\theta_j$, from the diffraction peak whose calculated scattering angle is $2\theta_h$, as [6]

$$3.(2) \quad y_j(\text{calc.}) = C\left\{ \frac{m_h |F_h|^2 2(\ln 2)^{\frac{1}{2}} L_h t}{(\pi)^{\frac{1}{2}} \Gamma_h} \right\} \times \exp\left[-\frac{4\ln 2(2\theta_j - 2\theta_h)^2}{\Gamma_h^2} \right]$$

which may be written as

$$3.(3) \qquad y_j(\text{calc.}) \quad = \quad g_{j,h}|F_h|^2$$

defining the peak shape function $g_{j,h}$. In the case of overlap, we sum over all the peaks that can theoretically contribute to the profile intensity at scattering angle $2\theta_j$. In order to evaluate whether or not a peak contributes to the profile intensity at $2\theta_j$, it is noted that the area under a normalised Gaussian distribution outwith the range of three standard deviations from its mean is less than 0.02%. Therefore, a negligible error results by taking the profile of a peak to be non-zero only within three standard deviations of the mean. Hence we have a way of determining the possible contributions to the profile at $2\theta_j$. Thus, in the case of overlap we have that

$$3.(4) \qquad y_j(\text{calc.}) \quad = \quad \sum_h g_{j,h}|F_h|^2 \qquad .$$

The quantities used in equation 3.(2) are described below. t is the step width of the detector and m_h, the multiplicity, represents the number of symmetry related reflections which have the same scattering angle, $2\theta_h$, and structure factor amplitude, F_h, for the structure under study. The amplitude F_h is described in more detail in §2.2. The quantity C is an overall scale factor and Γ_h and L_h are, respectively, the full width at half the diffraction peak maximum and the Lorentz polarisation factor for scattering angle $2\theta_h$. This latter is given by, in the case of neutrons, $L_h = \text{cosec}2\theta_h\text{cosec}\theta_h$, where the term in $2\theta_h$ comes from the fraction of the diffraction cone that is detected and that in θ_h is derived from the number of particles within the powder specimen and is therefore independent of the detection geometry.

The quantity Γ_h will be considered further here. The relation between Γ_h and the standard deviation, σ_h, of the Gaussian distribution given by equation 3.(2) is given by $\Gamma_h^2 = 4\sigma_h^2 \ln 2$. This substitution of Γ_h for σ_h is useful because it gives the distribution of the diffracted intensity in a peak in terms of the half width Γ_h, which is an experimentally important quantity. The half width of a neutron powder diffraction peak has been investigated experimentally by Caglioti et al.[8] and their findings may be simplified to the following expression (in $2\theta_h$) which is found to be in very good agreement with experimental results:

$$3.(5) \qquad \Gamma_h^2 = u \tan^2\theta_h + v \tan\theta_h + w \qquad .$$

The quantities u, v, and w are called the half width parameters and they must be determined initially by measuring the half widths of several observed diffraction peaks and then finding a least squares fit to equation 3.(5). The parameters u, v and w then become variables in the refinement to fit the observed diffraction data. Equation 3.(5) also takes into account the diffraction peak broadening due to the finite size of the crystallites that comprise the sample.

There are two other factors that contribute to the diffraction peak shape that have not yet been mentioned. These are the asymmetry caused by using finite vertical collimator systems and finite sample height, and the preferred orientation effect. The first of these contributions has been discussed by Cooper et al.[29]. The result is that a broadening of the diffraction peak as it becomes asymmetric occurs, coupled with a reduction in the scattering angle of the peak. Cooper et al.[29] have calculated correction factors for these effects in terms of the instrumental horizontal and vertical divergences of the incident and diffracted beams. Tables of results obtained on using

the correction factors are given in reference (29).

The preferred orientation effect may be detected by monitoring a powder diffraction peak maximum as a variable of the sample orientation with respect to the incident beam. Rietveld gives a simplified treatment of this effect[6].

Since neither of the two above effects were encountered in the analysis of neutron powder diffraction data by the author, no further discussion will be given.

There are many computer programs that have been written or adapted for use in the refinement by profile analysis of nuclear and magnetic structures. The Rietveld method[5,6] has been outlined above but it is restrictive in that, for instance, magnetic structures may be refined only if they may be described in terms of an integral multiple of the crystallographic unit cell. Also, the constraints that may be applied are restricted to be only linear or quadratic in the refinement parameters. Rietveld's[6] method has been utilised as a basis for many of the programs now used and a brief review of some of these is given here.

The program POWLS, developed by Will et al.[9] uses the integrated intensities of the powder diffraction peaks to refine a structure, either nuclear or magnetic. It is therefore less sophisticated than the Rietveld method but the authors note that it is more powerful and more general in its applications. POWLS has been extended[10] to include more complicated magnetic structure problems than the Rietveld method is capable of handling and has thus proved superior to the latter on several occasions.

The developments made by Rae Smith et al.[11] include the ability to run their set of Fortran programs, collectively named POWDER, interactively on a computer. These programs use the basic Rietveld profile

analysis technique but have advantages as these authors point out. These include the possibility of visual checking throughout the various stages of the refinement, with the consequent dispensing with manuals as a result and also the continuity of thought whilst, for instance, refining a structure that is not well known and which requires several attempts using rough parameter sets for input. These authors suggest an interactive graphics terminal for the involvement of the user in the refinements as they proceed.

More recently, the program EDINP has been described by Pawley[12] and this also uses the Rietveld technique of profile analysis. The program EDINP is based on the ORFLS version described by Busing et al.[13] and it includes the ability to apply highly non-linear constraints in the orthogonal (Å) coordinate system[14], thus making it superior to the original Rietveld program. The program described by Pawley[12] is that which is used in all powder refinements of crystal structures described in the present work.

2.2   Refinement parameters

In the previous section, we have seen how a neutron powder diffraction peak may be very well described by a normalised Gaussian distribution, given by equation 3.(2).

In order to indicate the parameters that it is necessary to take account of in a profile refinement procedure, it is instructive to expand the structure factor amplitude squared of equation 3.(2) thus:

$$3.(6) \quad |F_h|^2 = (A_h^2 + B_h^2) \exp\left(- \frac{B \sin^2 \theta_h}{\lambda^2}\right)$$

where

$$3.(7) \begin{cases} A_h = \sum_i n_i b_i \exp\left(-\frac{B_i \sin^2\theta_h}{\lambda^2}\right) \sum_r \cos 2\pi(hx_{i,r} + ky_{i,r} + \ell z_{i,r}) \\[2em] B_h = \sum_i n_i b_i \exp\left(-\frac{B_i \sin^2\theta_h}{\lambda^2}\right) \sum_r \sin 2\pi(hx_{i,r} + ky_{i,r} + \ell z_{i,r}) \end{cases}$$

The quantities used in equations 3.(6), (7) are listed below:

$\sum_i$ summation over atoms in asymmetric unit cell

$\sum_r$ "   "   equivalent positions in unit cell

n_i the occupation number of the ith lattice site

b_i coherent neutron scattering length of the ith atom

B_i individual atomic isotropic temperature parameter for the ith atom

B overall isotropic temperature parameter

h, k, ℓ Miller indices of a reflection (denoted by single suffix h)

$2\theta_h$ scattering angle of reflection of indices h

$x_{i,r}, y_{i,r}, z_{i,r}$ fractional coordinates of the ith atom in the rth equivalent position

The occupation number of the rth equivalent position is m_p/m_{pg}, where m_p is the multiplicity of the position, special or general, and m_{pg} is the multiplicity of the general position in the space group under investigation. We may divide the above parameters into two categories. Those that describe the peak shape and position, and therefore that govern the whole scan, are the profile parameters, whilst those that describe the contents of the asymmetric unit cell are the structural parameters. These are, respectively:

u, v, w the half-width parameters

$2\theta_o$ zero error of the scattering angle

$a, b, c, \alpha, \beta, \gamma$ the direct cell constants parameters

B overall isotropic temperature parameter

(we ignore the preferred orientation and diffraction peak symmetry due to instrumental collimation) for the profile parameters, and

C   overall scale factor such that

$$y_j(\text{calc.}) = C \cdot y_j(\text{obs.}) \text{ for the jth point}$$

x_i, y_i, z_i fractional coordinates of the ith atom in the asymmetric unit cell

$\left.\begin{array}{c} B_i \\ \\ n_i \end{array}\right\}$ as before

for the structural parameters. The reason for this division will be discussed shortly. In order to generate the whole unit cell, it is also necessary to provide the symmetry operations that transform the ith atom to the rth equivalent position. These are:

3.(8) $\underline{x}_{i,r} = \underline{R}_r \, \underline{x}_i + \underline{T}_r$

where $\underline{x}_{i,r}$ and $\underline{x}_i$ are the position vectors of the ith atom in the rth equivalent position and in the asymmetric unit cell respectively. $\underline{R}_r$ and $\underline{T}_r$ are the rotation (3×3) and translation (3×1) matrices describing the rth equivalent position in the particular space group.

The functional form of the calculated diffraction pattern, $y_j(\text{calc.})$, given by equation 3.(2), is highly non-linear in the refinement parameters. This non-linearity means that an initial set of parameters must be supplied and the least squares refinement procedure will then vary these in such a way as to improve the fit between the calculated profile and the observed diffraction data. Several iterative cycles will normally be required to attain a pre-specified convergence condition.

The least squares method is well documented (see, for example, references (14) to (16)), so that the derivation of the least squares

matrix equation is not given but the result is stated as

$$3.(9) \qquad \sum_m A_{nm} \, \delta p_m \;=\; V_n \quad,$$

where $\underline{A}$ and $\underline{V}$ are the least squares matrix and vector and the $\{\delta p_m\}$ are the parameter shifts. The purpose of the refinement will be to set up and invert the least squares matrix $\underline{A}$ and then to pre-multiply the least squares vector $\underline{V}$ by $\underline{A}^{-1}$ in order to find the parameter shifts $\{\delta p_m\}$ given by equation 3.(9). The standard deviations, $\{\sigma_m\}$, of the refinement variables, $\{\delta p_m\}$, are then derived using the standard equation

$$3.(10) \qquad \sigma_m^2 \;=\; (\underline{A}^{-1})_{mm} \left(\frac{R_W}{N-P}\right) \quad,$$

where $(\underline{A}^{-1})_{mm}$ is the mth diagonal element of the inverted least squares matrix, and R_W is given by equation 3.(1a). The quantities N and P are respectively the number of statistically independent points in the scan and the number of refinement parameters. In the Reitveld method, N is taken to be the number of points in the scan.

The division of the refinement parameters into two categories is connected with the statistical independence of points in the diffraction scan and this latter topic has been discussed by several authors[12],[17]. Sakata et al.[17] have analysed the Rietveld method[5,6] and they show that the standard deviations obtained from this method and the integrated intensity method are not, in general, exactly the same. These authors also note that whilst the differences in the actual refinement parameter values may not be statistically significant, the differences in the calculated standard deviations of the two methods severely limits their usefulness. The reason for the division of the refinement parameters into profile and structural parameters is also discussed by Sakata et

(17)
al. They show that observed points over the same Bragg peak are not

statistically independent but are in fact correlated. This arises be-

cause the integrated intensity of a Bragg reflection is determined

only by the structural parameters, whereas the peak shape is only

governed by the profile parameters. Therefore, the number of statis-

tically independent points in the scan is not the total number of

points in the scan. It has been argued by Pawley[12] that a more

realistic number to be used for N in equation 3.(10) is

$$\dot{N}_e = N/\bar{\Gamma} ,$$ the equivalent number of

Bragg reflections, where $\bar{\Gamma}$ is the mean full width at half height

of a well resolved peak in the scan. That this is reasonable may

be seen from equation 3.(10). Increasing the number of points in

the scan indefinitely implies that the standard deviations calculated

by the refinement procedure will become vanishingly small. This is

seen to be an incorrect result, as was shown by Sakata et al.[17] and

so the number N_e, above, is used in analyses described in §4.

2.3 Constrained refinement

The basic Rietveld program[5, 6] provides the possi-

bility of applying constraints between the parameters used in the

least squares procedure. The functional form that these constraints

must take in the above program is either linear or quadratic in some

or all of the parameters. The method of Lagrange undetermined multi-

pliers is used to solve the augmented normal equations and hence to

find the constrained parameter shifts. For a detailed reference to

the method of Lagrange multipliers, the reader is referred to

Goldstein[22].

It is apparent that the above requirement of the constraints

being either linear or quadratic in the parameters is very restrictive.
The method for solving the augmented normal equations is very cumber-
some for a large number of parameters and sometimes quite unfeasible
for certain types of constraints, for instance, highly non-linear
relationships between the parameters.   Therefore an alternative method
for applying constraints is necessary and such methods have been re-
viewed[14,23] and they will be briefly described here.

We will consider two possibilities, which are applicable in
refinements of powder as well as single crystal data. The first was
proposed by Waser[23] and these are the variable, 'slack' constraints.
The great advantage of using such slack constraints is that there is
a weighting factor that determines the degree to which the constraint
is enforced. Increasing the weight increases the 'strictness' of the
constraint and we therefore have a choice as to how slack or strict
we wish the constraint to be. The size of the least squares matrix
stays the same, since the constraint equations involve no new variables
and so the problem is much simplified from the case of the Lagrange
method, where the normal equations are augmented to their original
number plus the number of constraint equations.

The second method of applying constraints between refinement
parameters has been given by Pawley[14]. These are named strict
constraints to distinguish them from those given by Waser. Here,
there is no variable weighting scheme for the constraints and the
procedure enforces strict relationships between the parameters in the
orthogonal crystal system. This relationship may be expressed in any
relevant function form and the inverse relationship always requires a
fitting procedure.

In this latter case of strict constraints, it is quite possible
that $n_c << N_p$,   where n_c and N_p are the number of constrained

and unconstrained parameters respectively, so that a great saving in computational time is made in the case of constraints, as opposed to the unconstrained or Lagrange multiplier refinements. Therefore, it is advantageous to use constraints wherever possible. However, apart from the great savings to be made on computer time, it is also important to expand upon the philosophy underlying the use of constrained refinements in crystallography. We suppose that we analyse the results of the constrained refinement by testing statistically whether or not the difference, if any, between these results and those of the unconstrained refinement is significant and at what probability confidence level. By performing such tests on the two types of models the most beneficial aspect of constraints emerges. If the unconstrained calculation gives a set of parameters that are no better than those for the corresponding constrained case, then the latter are the better set of parameters since they are fewer. If, however, the former of the two models is found to be a better solution to the problem, then we are more certain of the quality of the result than we would have been had we only performed the unconstrained refinement.

The idea of testing different models statistically in crystallography is due to Hamilton and he has introduced the R-factor ratio test[24]. This author describes this testing technique for the case of single crystal data, but it can also be used for powder diffraction data if the value of R_W, in equation 3.(1a) is used instead of the R-factor, (3.(1b)). The reason for this is due to the problems in evaluating the contributions to a powder scan background.

Full details of this testing technique may be found in references (24) - (26).

2.4   Temperature factors

When we specify the atomic coordinates of atoms within a crystal,

these only refer to the average positions since these atoms will be

endowed with a certain amount of thermal energy.   In the section, §2.2,

the equation 3.(6) read, for the structure factor squared:

$$(3.(6)) \qquad |F_h|^2 \quad = \quad (A_h^2 + B_h^2)\exp\left(-\frac{B\sin^2\theta_h}{\lambda^2}\right) \quad ,$$

where A_h and B_h are the complex structure factor amplitudes such that

$F_h = A_h + iB_h$,   and   B   is the overall isotropic temperature parameter.

The exponential equation 3.(6) is the so called Debye-Waller factor and

for reflections that have high values of $(\sin\theta_h)/\lambda$,   this factor becomes

increasingly dominant, such that high angle reflections tend to have

their diffracted intensities severely suppressed, as well as being

broadened due to overlap in the scan.   The parameter,   B,   affects the

whole diffraction scan,   so it is a profile as opposed to a structural

parameter.

Equations 3.(7) involved the individual atomic isotropic temperature

paramters, B_i,   for the ith atom in the asymmetric unit cell.   In general

atomic thermal motion in crystals is anisotropic and this implies that the mean

square amplitudes of thermal vibration about the equilibrium position are

larger in certain directions in the crystal than in others.   It is possible

to describe the motion of a vibrating atom by a probability distribution

function, and hence surfaces of constant probability which, for anisotropic

motion (in the harmonic approximation) are ellipsoids - the familiar 'thermal

vibration' ellipsoids.   In some cases, the thermal motion may be restricted

by crystal symmetry such that the mean-square amplitude of vibration is the

same in all directions.   The surfaces of constant probability are then

spheres and the thermal motion is described as being isotropic.

The anisotropic temperature factor for a reflection with indices

$h \equiv (hk\ell)$ may be written $\exp(-B_h)$, where B_h is conveniently given by[27]

$$3.(11) \qquad B_h = \frac{1}{2\pi^2}\{\beta_{11}h^2 + \beta_{22}k^2 + \beta_{33}\ell^2 + 2\beta_{12}hk + 2\beta_{23}k\ell + 2\beta_{31}\ell h\}$$

and the $\beta_{ij} = \beta_{ji}$ are given in $\overset{\text{o}}{A}{}^2$ units in the orthogonal crystal system when using the above definition.

The crystal symmetry may restrict these anisotropic temperature parameters β_{ij} such that there are less than the maximum of six independent parameters per atom above. If, for instance, the individual atom in question is situated on a symmetry plane in the unit cell then the fact that this reduction in the number of independent β_{ij} occurs is immediately obvious. As an example, let an atom lie on a mirror plane, say the bisecting plane of the orthogonal xy- and yz-planes. It is then seen that in order to satisfy this mirror symmetry we must have $\beta_{11} = \beta_{33}$ and β_{22} not necessarily equal to β_{11}. This relatively simple example serves to indicate how the dependence of the β_{ij} may be deduced. Full symmetry considerations are contained in the International Tables for X-ray Crystallography[28].

§3 General Experimental

3.1 Typical experimental conditions

We will be concerned here with the most general experimental conditions required for a neutron powder diffraction experiment. For conditions under which specific systems were studied, the reader is referred to §4.

The sample container is usually a vertical cylindrical can of dimensions about a centimetre or less in diameter, and several centimetres in length. A spherical can[30] or a briquet shaped sample may also be used; in the latter case the mode of data collection is different, as shown in

Figure 3.1, where the geometries of scattering from a cylindrical and spherical (identical in plan view, Figure 3.1a) are also shown.

The material of which the walls of the container are made will typically be either aluminium or vanadium. The latter of these two metals has a coherent neutron scattering cross-section equal to zero, giving rise to no Bragg reflections. The aluminium, however, will give rise to coherently scattered neutrons and the resulting Bragg reflections, whose intensity depends upon the wall thickness and the dimensions of the container, must be identified and removed from the scan before data analysis may proceed.

The polycrystalline sample container is then enclosed in the appropriate cryogenics or furnace, depending upon the temperature range required. The temperatures that are available using such apparatus vary widely. The minimum temperature is usually that of liquid helium at $\sim 4.2K$, but other experimental techniques may achieve temperatures in the range of microkelvins[31]. The upper end of the temperature range is, of course, determined by the melting point of the sample (assuming atmospheric pressure). It is advisable that the sample temperature be kept well below this point because large, oriented crystallites may form by softening and partial fusing of the grains within the specimen. This would cause a preferred orientation to be created and problems would then arise in the analysis of the diffraction data, since the powder would no longer be a randomly oriented collection of crystallites.

If the polycrystalline sample is ideal then the azimuthal orientation of the whole sample with respect to the incident beam is of no consequence, since there will always be an equal number of crystallites in the correct orientation to Bragg reflect neutrons. However, this

Figures 3.1a,b: The top diagram, (a), represents a cylindrical

or spherical sample, S, and the detector D.

The incident wavevector is $\underline{k}$ and $\underline{k}'$ is that

for the diffracted beam. 2θ is the scattering

angle. The sample is rotated continuously

through $\sim 360°$.

The lower diagram, (b), represents the briquet

shaped sample, and it is necessary to use the

reflection geometry as shown. This is the

$\theta - 2\theta$, or half angling mode of data collection.

Quantities have meanings as above.

FIG. 3·1a,

a

b
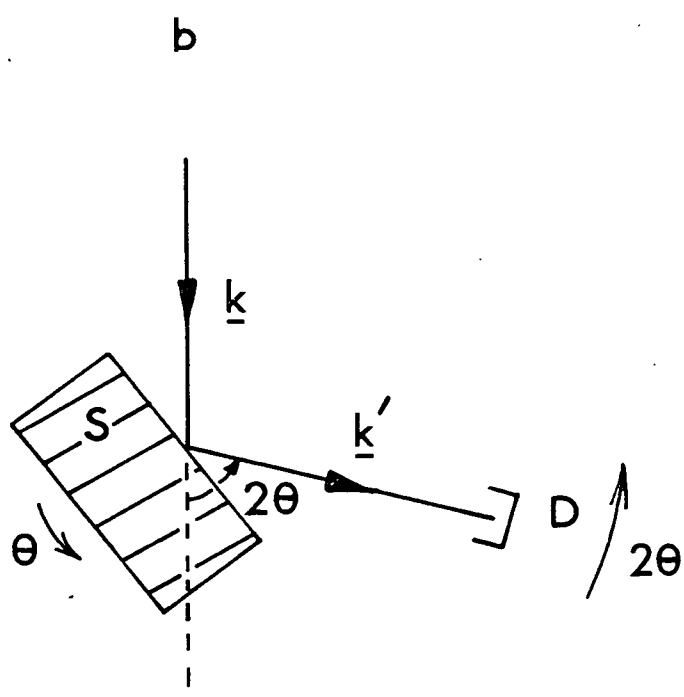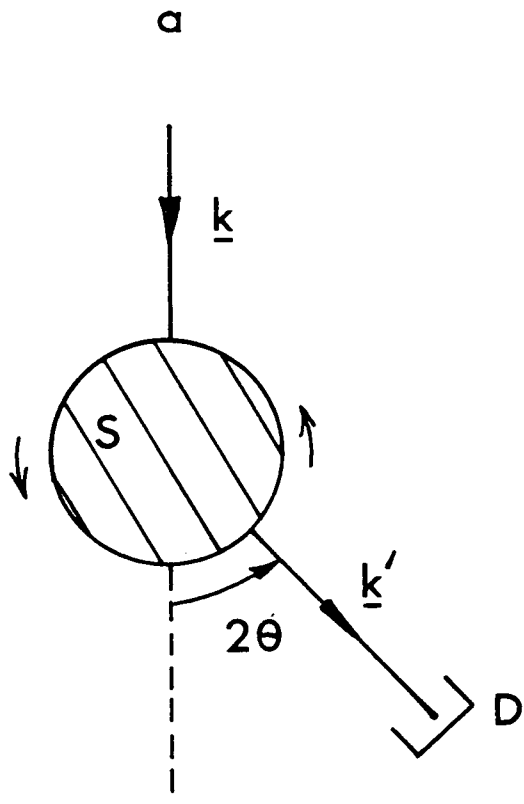
ideal case is very rarely satisfied and in this event it may be found
necessary to continuously rotate the sample through $\sim 360^{\circ}$ whilst
measurements are made. This method is called 'powder averaging',
and it allows all of the sample to give some contribution to the dif-
fracted intensity of a peak in the scan. Any larger than average
crystallites will therefore have their contribution averaged over the
whole specimen and thereby the error due to crystallinity is reduced.
This will mean that data analysis may proceed in the knowledge that
the diffracted intensities are as accurate as possible in the cir-
cumstances. Apparatus, such as in Figure 3.2, is needed to perform
an NPD experiment and this will now be discussed more fully, with
reference to the schematic representation in the figure.

The thermal neutron beam from the reactor port will be incident
upon a monochromator crystal, M. This will produce only a nominally
monochromatic beam of neutrons, since there will be some spread of
wavelength due to the mosaic of the monochromator crystal, the thermal
neutron energy distribution and the collimation that is used. Several
choices of the monochromator crystal, M, are possible and some of
these are noted in Table 3.1, along with the reflection indices of the
crystal   plane used, the monochromator take off angle and the wave-
length of radiation thus produced. Further information on this topic
is given in ref. (32).

The nominally monochromatic beam of neutrons must pass through
some reactor shielding (R) and then through a set of collimator slits
(Soller[33]), SS1 in Figure 3.2. The purpose of the collimator slits
is to reduce the horizontal angular divergence of the beam and to this
end the sides of the plates that form the slits are coated with a neutron
absorbing material, such as gadolinium oxide. Typically used angular
divergences of the Soller slits are 10 to 40 minutes of arc. The minimum

Figure 3.2:   Typical neutron powder diffraction experimental

arrangement. The components of the apparatus are

listed below.

M	monochromator crystal
R	reactor shielding
SS1,2	Soller slits [33]
MT	monitor in the incident beam
S	powder sample
D	detector
$\underline{k},\underline{k}'$	incident and scattered neutron wavevectors
2θ	scattered angle (usually in degrees).

FIG. 3·2
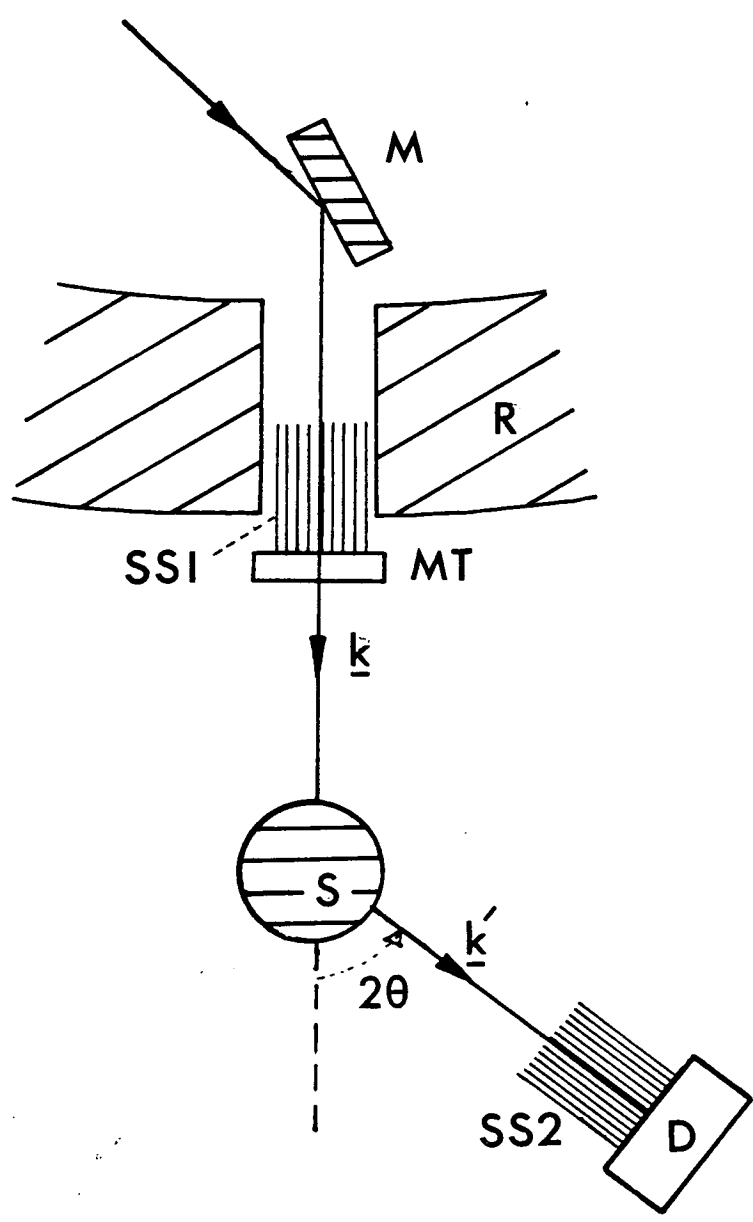
collimator angular divergence will be governed by the diffraction limit derived from the crystallite size in the specimen and this minimum is of the order of < 5 minutes of arc.

Crystal	Planes	Take off angle	$\lambda_{neutron}$
Germanium	(113)	57.045	1.629
Germanium	(220)	70.000	2.295
Germanium	(331)	50.000	1.097
Copper	(111)	76.130	2.570
Aluminium	(111)	40.000	1.60
Aluminium	(200)	40.000	1.39
Aluminium	(220)	40.000	0.98

TABLE 3.1:   The table compares several monochromators and gives the crystal, reflection indices, take off angle (in degrees) and the resulting wavelength (in $\overset{o}{A}$) of neutrons that are reflected.

In order to make a powder diffraction scan, it is necessary to count at each individual point for a given, fixed length of time. A very convenient way to do this is to monitor the incident beam. When a certain, pre-specified count is reached the diffractometer stops counting and moves automatically to the next point in the scan, where the process is repeated. The monitor, MT, is shown in Figure 3.2.

The incident beam will then impinge upon the sample and scattering will take place. The diffracted beam, characterised by wavevector $\underline{k}'$ in Figure 3.2, is then collected through a second collimation system, SS2, similar in construction to that in the incident beam, SS1. The actual value of the angular divergences of SS1 and SS2 will usually differ, that of SS1 being the larger of the two. The detector, D, is usually a beryllium fluoride or pressurised helium-3 counter,

attached to which is the appropriate electronics for relaying the diffracted counts to the computer that drives the diffractometer.

The arrangement of the detector shown need not be restricted to one single counting chain. There are in existence powder diffractometers that have multiple counter banks[34] and position sensitive detectors[35]. The high resolution diffractometer (D1A) described by Hewat et al.[34] has ten counter/collimator systems separated by 6° in the scattering angle. They move as a unit to collect diffracted intensity and the step width in 2θ is usually 0.05° or more. The individual detectors have almost identical counting efficiencies and the collimator systems have transmission functions that are nearly triangular in shape, with peak transmission of $\sim$ 97%. The collimator plates comprising each system are aluminised mylar 25 μm thick, coated with the highly neutron absorbing gadolinium oxide paint, also 25 μm thick. This arrangement results in almost no neutron reflection within the collimators, whose angular divergences are set to be 10 minutes of arc. All ten detector/collimator systems are rigidly fixed, with no realignment possible or indeed necessary, since their estimated angular error is about $\pm$ 0.02° in 2θ. Even though this error is almost half the usual step width, it causes no problem in the data analysis since it is corrected for by interpolation before summation[34].

The advantage of such a diffractometer as described by Hewat et al. is immediately apparent. For a maximum scattering angle of 160°, as is usual for this instrument, in the range $2\theta = 60^{\circ}$ to 100° the counting statistics are improved by a factor of $\sqrt{10}$ relative to the extremities of the scan. This region of the scan is usually that in which the diffraction peak overlap is severe and where a great deal of structural information is contained, so that

any improvement in the counting statistics is valuable. The resolution

of the instrument is still good even at high scattering angles and the

focussing point is $2\theta = 122^O$ for a squashed Ge monochromator reflecting

neutrons off the (551) planes, giving a neutron wavelength of $1.384\overset{o}{A}$.

Other monochromator planes are easily available. The scattering angle

zero error may be obtained by scanning an intense, well resolved Bragg

peak on both sides of the scattering angle zero. The condition of a

peak being well resolved is necessary because on one side of $2\theta = 0^O$

the diffraction pattern is defocussed, resulting in broad diffraction

peaks. Accurate wavelength determination is not described here,

rather the reader is referred to the work of Bacon et al.[56].

§4   Experimental Results

4.1   Powder refinement of carbonyl sulphide (OCS)

The crystal structure of carbonyl sulphide is reinvestigated, at

a temperature of 90K, using the NPD technique. The rhombohedral struc-

ture has already been determined by Vergard[46], who reported the unit

cell, atomic fractional coordinates and space group (R3m). The unit

cell dimensions found in the present work[47] are $a = 4.063(3)\overset{o}{A}$ and

$\alpha = 98.8_1(3)^o$, and the bond lengths are determined as $1.21(3)\overset{o}{A}$ and

$1.51(3)\overset{o}{A}$ for the oxygen-carbon and carbon-sulphur distances res-

prectively. The purpose of the present study was to refine the

crystal and molecular structures, as a preliminary to doing inelastic

neutron scattering studies on a single crystal of this system. All

the relevant experimental details may be found in a publication at the

end of this work.

The crystal structure of OCS was refined using the program EDINP[12]

for which there is a special rhombohedral section included. The results

of the isotropic temperature factor refinement for this structure are given in Table 3.2 and a plot of observed (circles) and calculated (full line) diffraction profiles is given in Figure 3.3, along with a difference plot of observed-calculated.

It will be noted that in Figure 3.3 there are regions where data is not presented. This is because there were some small impurity peaks present. An approximate estimate of the percentage present may be obtained from the ratio of the largest OCS Bragg peak to the largest impurity peak, this being of the order of one hundred to one.

The powder data was refined using the rhombohedral unit cell and the orthogonal axes were chosen such that they lay between the real space rhombohedral axes and the reciprocal lattice axes, with the orthogonal and rhombohedral [111] directions coincident.

The crystal symmetry of OCS implies that the molecules are restricted to lie with their principal axes aligned along the unique direction of the structure. The molecules were therefore restricted such that the above condition was strictly satisfied, but where the bond lengths were refinement variables. Therefore the results of refinements that are presented in this section correspond to unconstrained calculations that do not fix the molecular geometry. This is contrary to the case in Chapter 1, section 3, where single ring molecules in a similar rhombohedral structure were constrained to have a hexad symmetry axis perpendicular to the molecular planes and parallel to the unique axis of the structure, even though the crystal symmetry did not require this constraint. The philosophy of constraints has been described in §2.3 of this chapter.

The variable parameters used in the refinement were first the scale factor, after which the flat background and scattering angle zero error were added. Successive cycles included the unit cell

Parameter		Value	Standard deviation
Scale factor		305.7	2.3
Flat background		3071.7	46.7
Zero error in 2θ (degs.)		-0.073	0.005
Parameters (degs.)^2	u	2.81	0.23
	v	-1.49	0.18
	w	0.48	0.03
Cell parameters	a(Å)	4.0629	0.0005
	α (degs.)	98.814	0.006
Overall isotropic temperature parameter	B-unit	1.83	0.08
Bond lengths Å	O-C	1.205	0.006
	C-S	1.510	0.007

Scan information

	Value	
Range of 2θ (degs.)	15.0 - 100.0	-
Scan step in 2θ (degs.)	0.1	-
Wavelength (Å)	1.629	-
Mean full width at half height ($\overline{\Gamma}$, degs.)	0.744	-
Number of Bragg reflections	29	-
Equivalent number of Bragg reflections (N_e)	39	-

TABLE 3.2: The final parameters for the refinement of carbonyl sulphide at 90K. The full width at half height of a diffraction peak is given by

$$\Gamma = (u\tan^2\theta + v\tan\theta + w)^{\frac{1}{2}}, \quad 2\theta \text{ is the}$$

scattering angle.

Figure 3.3:   The neutron intensity as a function of scattering

angle, 2θ.   The observed data are the points and

the calculated profile is the full line.   The

large Bragg reflection at $2\theta \sim 30^{\circ}$ peaks at

1.1×10^{5} counts.   The data points rejected due to

impurity scattering are denoted by a dot on the

zero intensity level.   Below the main figure is a

difference plot of observed-calculated intensity.
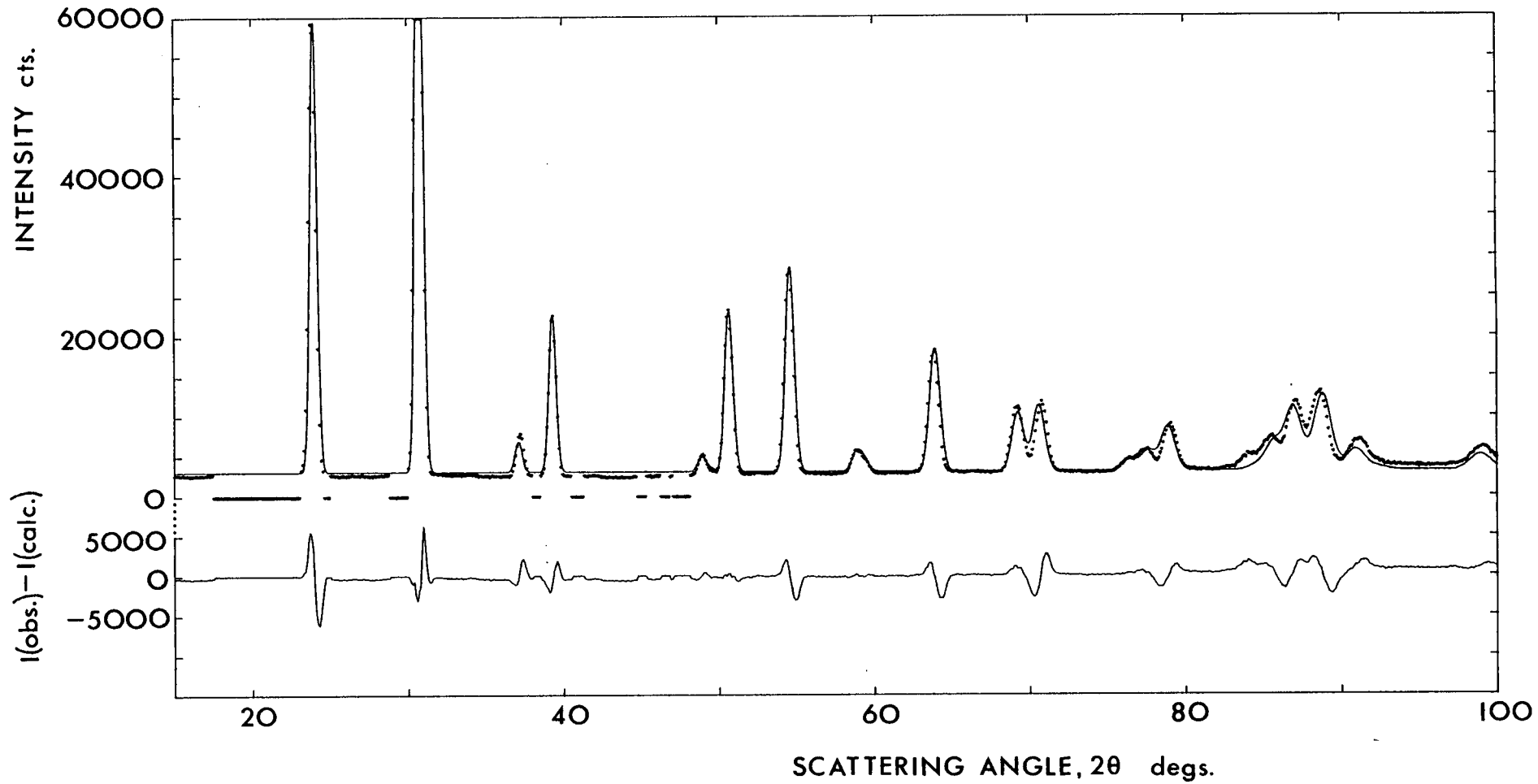
FIG. 3·3

parameters, a and α, then the two bond lengths, then the three

peak width parameters (u, v, and w) and finally the overall isotropic

temperature parameter. This made, in all, eleven parameters to be

refined in the final cycles. The impurity peak regions were not in-

cluded in the refinement. All data points had unit weights in the

refinement. The R-factor is then given by

$$3.(11) \qquad R = \frac{\sum\limits_{j=1}^{N} |y_j(\text{obs.}) - y_j(\text{calc.})|}{\sum\limits_{j=1}^{N} y_j(\text{obs.})} \quad ,$$

where $y_j(\text{obs.})$ is the observed intensity at the jth point in the scan,

$y_j(\text{calc.})$ is the calculated intensity and the sum does not include the

regions contaminated by impurity scattering. The least squares residual

is given by equation 3.(1a):

$$(3.(1a)) \qquad R_w = \sum\limits_{j=1}^{N} w_j (y_j(\text{obs.}) - y_j(\text{calc.}))^2 \qquad (\text{all } w_j = 1).$$

The standard deviations quoted in Table 3.2 are derived from the least

square matrix, $\underline{A}$, and are obtained from equation 3.(10):

$$(3.(10)) \qquad \sigma^2_m = (\underline{A}^{-1})_{mm} \frac{R_w}{N - n} \quad ,$$

where N is the number of statistically independent observations in the

scan and n the number of refinement variables. The scan information

in Table 3.2 contains a number called the equivalent number of reflections,

N_e. This number has already been discussed in section 2.2 and is

given by $N_e = N/\overline{\Gamma}$, where $\overline{\Gamma}$ is the mean full width at half height of

a well resolved diffraction peak in the scan. It was seen in section

2.2 that this is a more realistic number to use in the equation for σ^2_m,

especially for the structural parameters which are, in this case, the two bond lengths. Using N_e rather than N in equation 3.(10) gives standard deviations for these parameters as

$$\sigma(O-C) = 0.03\overset{o}{A} \quad \text{and} \quad \sigma(C-S) = 0.03\overset{o}{A}.$$

Similarly, all the standard deviations given in Table 3.2 may be increased by the factor 5.

The molecular system under discussion here presented some problems in the analysis of the data. The initial refinements, (1), were straight-forward and the results have been presented. However, on analysing the difference plot in Figure 3.3 more closely, it is seen that there are various features that remain unexplained by the results in Table 3.2. These include the rise in the diffraction background at high scattering angles and also the apparent discrepancies between the observed and calculated peak positions throughout the scan. A further refinement, (2), was done, where the scan background was subtracted in linear segments, a procedure which is identical to that used by Rietveld[5,6]. The result of this is given in Table 3.3, where the refined bond lengths (and errors) and the R factors are given for all refinements, as well as the bond length results of previous workers.

The use of the background subtraction from the observed diffraction scan does not improve the result of the refinement, as is seen from Table 3.3, and it is questionable as to whether such arbitrary cor-rections to the powder data are justified, since no realistic calcula-tion has been done to evaluate the contributions to a power diffraction scan background count. In this case it was not only observed that this correction to the data did not improve the result of the refinement, but also that the discrepancies between the calculated and observed peak positions persisted.

Therefore, these discrepancies, δ(observed 2θ – calculated 2θ),

Bond	O – C	C – S	Total length O – C – S	R-factor
Gas phase[48]	1.16(1)	1.56(1)	2.72(2)	–
Vergard [46]	1.10	1.97	3.07	–
Refinement (1)	1.21(3)	1.51(3)	2.72(4)	0.11
Refinement (2)	1.19(4)	1.54(3)	2.73(5)	0.17
Refinement (3)	1.14(2)	1.47(2)	2.61(3)	0.12

(1)   Flat background

(2)   Arbitrary segmented background removed

(3)   Sample position variable and background subtracted as in (2).

TABLE 3.3:   Comparison of gas phase and crystal diffraction results for analyses performed on the carbonyl-sulphide system.

were analysed as a function of the scattering angle (2θ) and it was found that the variation of δ could be approximated by a simple function in 2θ. This is given by

3.(12) $\delta(2\theta) = 0.1640 - 0.0032*2\theta$,

and the results of this analysis are plotted in Figure 3.4. The points on this figure represent either a single diffraction peak or a pair of peaks, and any overlap of more than two peaks is not represented in the figure. The points are reasonably well distributed about the calculated least squares line, where the first and last points have been ignored. The reason for the exclusion of these points is for simplicity, since no explanation for their not following the trend of the other points is apparent. However, the figure suggests that a systematic error may be present in the observed data. This was investigated and it was then noted that a possible misplacing of the sample on the diffracto-meter would cause some shift in the observed diffraction peak positions. This means that the sample position relative to the incident neutron beam may become a variable in the refinement. This was programmed into EDINP by adding two terms to the calculated scattering angle zero error thus:

3.(13) $2\theta_{\text{zero}}^{\text{calc.}} = P_5 - P_3 \cos 2\theta - P_4 \sin 2\theta$,

where the parameter P_5 is the refinement variable corresponding to the scattering angle zero in the absence of misplacement of the sample. The two extra parameters, P_3 and P_4, describe the sample misplace-ment parallel and perpendicular to the incident beam wavevector res-pectively.

Another refinement, (3), was done using equation 3.(13) and the

Figure 3.4 : Plot of differences between observed and
calculated diffraction peak positions as
a function of scattering angle, given as
solid squares. Both axes are in degrees
of 2Θ. The dashed line is the calculated
least squares fit (ignoring the first and
last points). The arrow indicates the
focussing angle of the monochromator used
$(2\Theta = 57.04°)$.

FIG. 3·4

$\delta = 0 \cdot 164 - 0 \cdot 0032 * 2\theta$
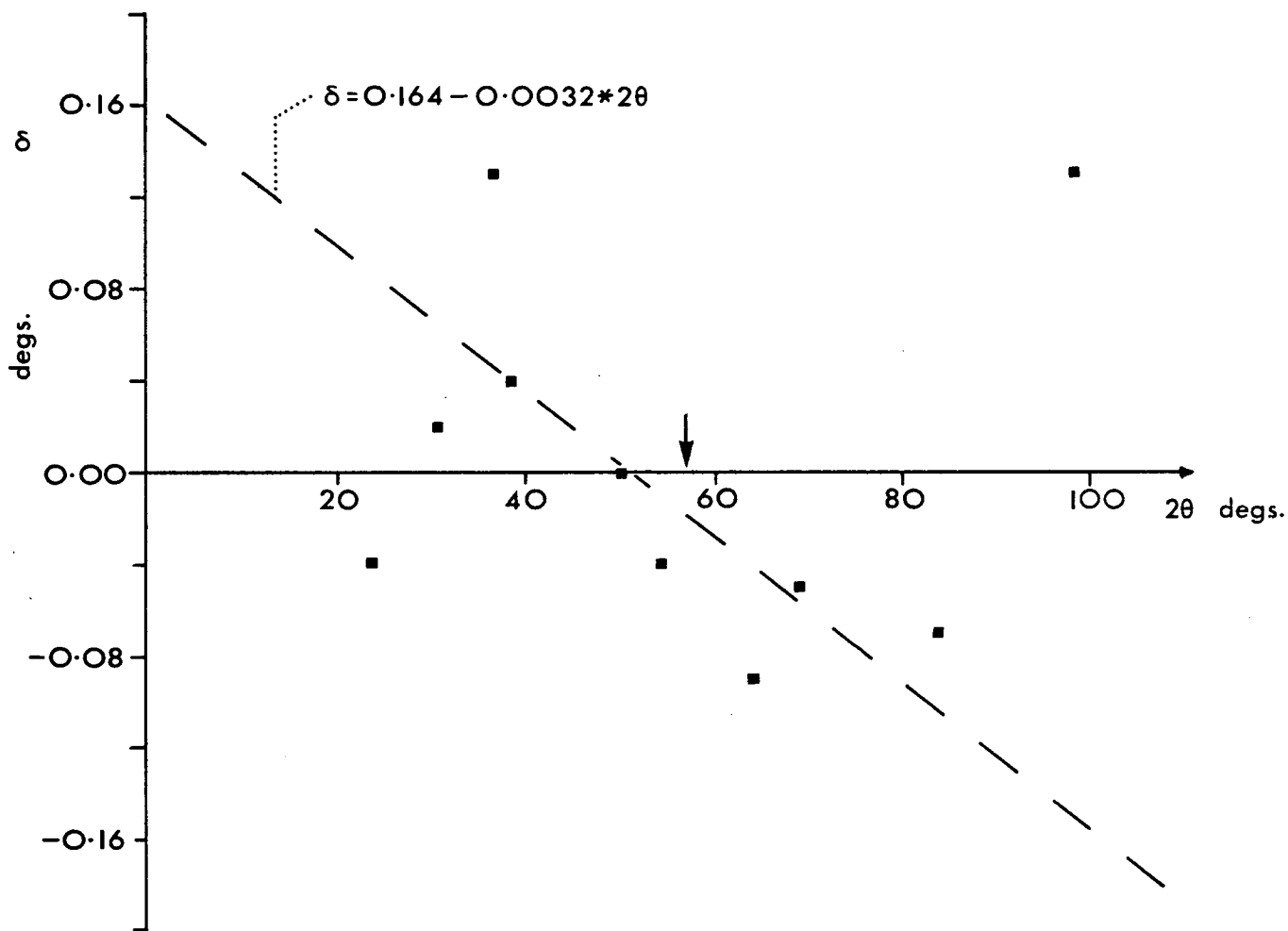
background subtraction used previously in refinement (2). The appropriate results are given in Table 3.4, and they show that the R-factor was considerably improved from that for refinement (2), indicating that the new parameters were statistically significant. The majority of the discrepancies displayed in Figure 3.4 showed an improvement as a result of refinement (3), although one or two of them in fact got slightly worse or changed sign. The overall result was an improvement in the discrepancies, δ, including those previously ignored and this is shown by the reduction in the R-factor given in Table 3.4. However, the value of the calculated scattering angle zero error had been refined to the unreasonably large value of $5.2(0.7)^{\circ}$ and these refinement results also suggested that the sample was misplaced on the diffractometer by about 75(10)mm. This is not consistent with those which we know were the actual experimental conditions under which the diffraction data were collected. Refinement (3) was therefore rejected due to the unrealistic values of the refined parameters.

The conclusion to be drawn from the analysis of the discrepancy $\delta(2\theta)$, is that the differences between observed and calculated peak positions is not easily explained, a linear relation between $\delta(2\theta)$ and 2θ giving an unrealistic result. It is possible that some instrumental misalignment, singular to the spectrometer that was used, is responsible for the observed discrepancies described above. However, a firm explanation regarding these discrepancies has not been found.

4.2 The benzene-hexafluorobenzene system

In this section we present experimental data and analyses that relate to the 1:1 molecular complex system $C_6D_6 \cdot C_6F_6$. The background and general introduction to this system has been given in Chapter 1, §3.

Experimental data that has resulted from work done by the author, using different experimental techniques to that in this chapter, have also been given in Chapters 1 and 2.

Since the introduction is given elsewhere we will not repeat it here, but refer to Chapter 1, §3 and also to the publications at the end of this work, where the first determination of the crystal structure of this system, at 279K, is described in detail and also where the Raman scattering studies are published. This latter work included the discovery of a structural phase transition at 175K on cooling, resulting in a low temperature crystal structure of considerable crystallographic complexity. The external mode spectrum at 4.2K has 12 or 13 lines, indicating as many normal modes of vibration.

We will be concerned here with the phases at lower temperatures than 279K. Specifically, data collected at temperatures of 250K and 5K are reported and analysed with a view to solving the crystal and molecular structures of these phases which, by inspection of their powder diffraction patterns (given in Figure 3.7 at the end of this section), appear to differ considerably in their complexity.

The data collected at 250K and 5K used a sample that was prepared by grinding the frozen, polycrystalline 1:1 mixture of constituents at liquid nitrogen temperature in an enclosed box with a nitrogen atmosphere. This procedure minimised the amount of moisture that might contaminate the sample and also produced excellent powder specimens. The wavelengths of neutron radiation used were 2.98Å and 5.7Å, the latter being used to resolve low angle overlap in the scans and the range in 2θ over which data was collected was 6° to $\sim 160^{\circ}$ using a step of 0.05° in 2θ. The data were measured on the high resolution powder diffractometer, D1A, at the Institute Laue-Langevin, Grenoble. This instrument was described in §3 with reference to the

original paper of Hewat et al.[34] The monitor count used for this experiment
was 50.10^3 counts, giving a counting time of approximately 25 seconds
per point in the scan.

Since the crystal structure is only known at a temperature of ∿ 280K,
we first attempt to solve the unit cell for the 250K phase. This type
of analysis may be done either by inspection for very high symmetry
structures or, as in this case where the structure is of low symmetry,
by using one of the various computer programs that have been designed
and written with this purpose in mind[49]-[51]. The program that was
used to attempt to solve the 250K unit cell for this system was that
described by Visser[49] and which is hereafter referred to as FZON. We
will briefly describe a particular method of the use of FZON that has
been discovered and which is of considerable advantage if it happens
that the scattering angle zero error of the scan is not accurately known.

Such a program as FZON relies heavily on highly accurate input
data, which is usually in the form of scattering angles of the diffrac-
tion peaks although alternative inputs such as interplanar spacings
or wavevector values, are also possible. Ordinarily, therefore, we
would require to know the scattering angle zero error very accurately,
where this is usually determined by calibration of the diffractometer.
The random error in the scattering angles input that the program FZON
may cope with is usually assumed to be about ± 0.02°, this figure being
taken from the advice given by the author of the program.[49] The minimum
assignable systematic error of a peak position is ± 0.04°, where this
is decided and then supplied by the user. This minimum value would
imply data of the highest quality, and for lower quality data this
systematic error is increased, thereby increasing the run time of the
program.

It has been found that by treating the scattering angle zero error

as a variable in the input to FZON, the chance of finding the true

indexing of the powder peaks is somewhat increased. This procedure

assumes that the zero error is not known accurately, so that a range

of values is tried, for instance, from -0.20° to $+0.20^{\circ}$ in steps of

either 0.01 or 0.02° in 2θ, whence the program FZON will calculate

the ten most probable solutions for each value of the zero error

supplied. It is then solely the responsibility of the user to decide,

by inspection of the output parameters, whether or not any of the ten

'solutions' are realistic for the system under study. The most useful

criterion by which this discrimination may be done is the volume of

the unit cells that are calculated. If a unit cell has the correct

order of volume, a high figure of merit[49] and also indexes

all the lines in the input to FZON, then the user may be reasonably

sure that the indexing is correct. The figure of merit, M_{20}, is a

number indicating the reliability of an indexing where the smaller

the value of M_{20} the less reliable is the indexing.

This method of analysis has been used with success for the dif-

fraction pattern of the $C_6D_6.C_6F_6$ system at 250K. The program FZON

found a body centred monoclinic cell, of dimensions $a = 7.28\overset{\circ}{A}$,

$b = 12.30\overset{\circ}{A}$, $c = 6.54\overset{\circ}{A}$ and $\beta = 98.5^{\circ}$, using steps of 0.02° in the

scattering angle zero error from -0.12° to $+ 0.12^{\circ}$, the zero error

that gave an indexing of the first twenty powder lines in the scan was

$+0.10^{\circ}$. The volume of this unit cell is $\sim 578\overset{\circ}{A}^3$ which is about a 3%

decrease from twice the cell volume at 280K, which is $598\overset{\circ}{A}^3$. The

cell found at 250K is therefore of the correct order of volume, and

the figure of merit for the above indexing was $M_{20} = 36.2$, which

also indicates that this body centred cell is correct. Since a body

centred monoclinic unit cell may be alternatively described by a face

centred unit cell, a transformation is necessary to find the space

group of this phase at 250K. Transforming to the new unit cell gives a c-face centred structure, which has unit cell dimensions: $a = 9.00\text{Å}$, $b = 12.30\text{Å}$, $c = 7.28\text{Å}$ and $\beta = 134.08°$. A list of observed and calculated scattering angles for the reflections are given in Table 3.4, up to $2\theta \sim 124°$. The reflection $(30\bar{4})$ will be discussed later.

In order to obtain the best possible unit cell dimensions before attempting a full structure refinement, this c-face centred unit cell was refined where the maximum peak intensities in the scan become refinement variables. The computer program, ALLHKL, used to perform this refinement is an adaptation of the EDINP program previously described by Pawley[12]. The input parameters for this type of refinement consist of the range of scattering angle and step width used in the scan, the unit cell dimensions, an overall scale factor, flat background, scan zero error in 2θ, and the diffraction peak half width parameters. Also included in the input is possible crystal symmetry, followed by the indices and maximum intensities of all the observed reflections in the range of scattering angle used. The observed profile data is supplied last along with the parameter keys to indicate which parameters are varied for each cycle of the refinement. The program ALLHKL has the facility to refine only the reflection intensities supplied, or alternatively, all those whose indices are consistent with the possible crystal symmetry supplied in input. This program is very flexible in that only rough cell parameters need be supplied, although if this type of refinement is used in conjunction with a program such as FZON, these parameters are usually reasonably well determined.

The variables in the refinement described here were the scattering angle zero error, the four cell dimensions (a, b, c, β) and all the reflection intensities in the range $2\theta = 25°$ to $128.9°$ making a total

of 37 variables in the final cycle of refinement. The result of the
final cycle of this refinement is given in Table 3.5, along with the
scan information. Where appropriate, standard deviations are given
in the column labelled 'Error' in Table 3.5. A plot of the observed
(dots) and calculated (full line) profiles is given, along with a
difference plot of observed minus calculated, in Figure 3.5. It is seen
in Table 3.5 that there is a reflection, the $(30\bar{4})$, that breaks the
c-face centring condition on the indices. This reflection is very
weak and is situated at $2\theta \sim 111.30^{\circ}$, underneath the wing of the
larger $(44\bar{2})$ reflection. The portion of the observed scan profile
at $2\theta \sim 111^{\circ}$ is shown in Figure 3.6, where it is observed that the
presence of this weak reflection is dubious. The only two reflec-
tions (ignoring crystal symmetry), that have a scattering angle of
111° given the unit cell above are the $(44\bar{2})$ and $(30\bar{4})$, so it is
not possible to reindex the peak at 111.30°. Therefore its presence
indicates evidence of this structure displaying pseudo-symmetry and
this is discussed shortly, when the space group possibilities of this
phase are considered.

From Figure 3.5 of the scan profile at 250K, it is seen that the
fit between observed and calculated intensities is very good. The
difference plot also confirms this. The R-factor of 0.125 is mainly
due to the background variation in the observed scan, and at
$2\theta \sim 54.6^{\circ}$ this appears to have a maximum underneath the large Bragg
reflection at this scattering angle. This is almost certainly due to
temperature diffuse scattering that has been mentioned in Chapter 1, §3,
for the 280K phase. No realistic calculation has been done in order
to account for such effects in a powder diffraction scan, so that it is
not possible to correct for this extra scattering which we find is

TABLE 3.4: Table of observed and calculated scattering angles

(in degrees) for reflections in the powder pattern of

the 250K phase of $C_6D_6 \cdot C_6F_6$. Those calculated are

obtained by using the result of the program FZON cited

in the text, the zero error for the observed peaks

being $+0.10^O$.

The peak at $\sim 111.30^O$ is susceptible to large

error since it is weak and under the wing of the larger

$(44\bar{2})$ reflection. Its presence is therefore dubious.

TABLE 3.5: Final unit cell refinement parameters for the calculation

corresponding to that in Figure 3.5.

$**$This reflection is mentioned above.

TABLE 3.4

h = (hkℓ)	$2\theta_h^{obs.} + 0.1°$	$2\theta_h^{calc.}$
020	28.06	28.07
110	30.20	30.19
20$\overline{2}$	48.98	48.99
130	51.06	51.02
11$\overline{2}$	54.55	54.53
22$\overline{2}$	57.44	57.41
040	58.03	58.02
220	62.75	62.79
31$\overline{1}$	66.44	66.43
13$\overline{2}$	69.73	69.82
24$\overline{1}$	72.09	72.09
131	73.53	73.50
022	76.56	76.53
33$\overline{2}$	76.96	76.96
31$\overline{3}$	78.64	78.63
24$\overline{2}$	79.30	79.30
40$\overline{2}$	83.58	83.58
42$\overline{2}$	90.33	90.33
060	93.34	93.35
15$\overline{2}$	92.19	97.20
112	98.63	98.66
330	102.75	102.77
44$\overline{2}$	110.96	111.02
30$\overline{4}$ VW	∿ 111.30	111.22
132	112.68	112.69
31$\overline{4}$	112.99	113.04
26$\overline{2}$	113.69	113.72
42$\overline{4}$	119.40	119.52
51$\overline{2}$	120.55	120.58
170	123.02	123.16
20$\overline{4}$	124.08	124.16

TABLE 3.5

PARAMETER			VALUE	ERROR
SCALE FACTOR			1.000	
BACKGROUND			460.000	
ZERO ERROR		(DEGS.)	0.147	0.020
HALF	U		0.343	
WIDTH	V	(DEGS.	−0.665	
PARAMS.	W	SQUARED)	0.492	
UNIT	A	(A)	9.000	0.004
CELL	B	(A)	12.297	0.009
PARAMS.	C	(A)	7.278	0.003
	BETA	(DEGS.)	134.076	0.022

REFLECTION
     INDICES

H	K	L		INTENSITY	ERROR
0	2	0		2364.8	113.0
−1	1	0		2239.3	112.2
−2	0	2		3540.4	105.2
−1	3	0		301.3	104.4
−1	1	2		6722.7	103.1
−2	2	2		192.5	103.3
0	4	0		432.8	102.6
−2	2	0		902.7	100.2
−3	1	1		28.1	98.9
−1	3	2		95.7	97.9
−2	4	1		25.4	97.2
1	3	1		18.3	96.8
0	2	2		71.9	102.4
−3	3	2		147.8	102.2
−3	1	3		53.9	95.7
−2	4	2		66.5	95.6
−4	0	2		63.7	94.8
−4	2	2		274.2	94.6
0	6	0		223.7	94.9
−1	5	2		213.7	95.8
1	1	2		116.8	96.3
−3	3	0		464.7	98.2
−4	4	2		234.5	134.3
−3	0	4	**	109.4	137.3
1	3	2		280.8	146.8
−3	1	4		858.9	135.7
−2	6	2		112.3	111.9
−4	2	4		141.0	114.2
−5	1	2		124.9	115.6
1	7	0		187.3	119.5
−2	0	4		614.5	121.3

CELL VOL.	(A CUBED)	578.8	1.2
TEMPERATURE (K)		250.0	
R−FACTOR		0.125	
NUMBER OF			
VARIABLES		37	

SCAN INFORMATION

RANGE OF TWO THETA	25.0−128.9
STEP IN TWO THETA	0.10
WAVELENGTH (A)	2.98
NUMBER OF BRAGG	
REFLECTIONS	28
EQUIVALENT	
NUMBER OF BRAGG	115
REFLECTIONS	

Figure 3.5:   Unit cell refinement for the 250K scan of the

                $C_6D_6.C_6F_6$ system. The observed and calculated

                profiles are the dots and full line respectively.

                The difference plot of observed minus calculated

                intensity is shown below. The range of 2θ is

                25° to 128.9^O.

Figure 3.6:   A portion of Figure 3.5 enlarged for the range

                of 2θ 110° to 112° to show the peak at $\sim$ 111°.

                The $(30\bar{4})$ reflection position is shown by the

                arrow.
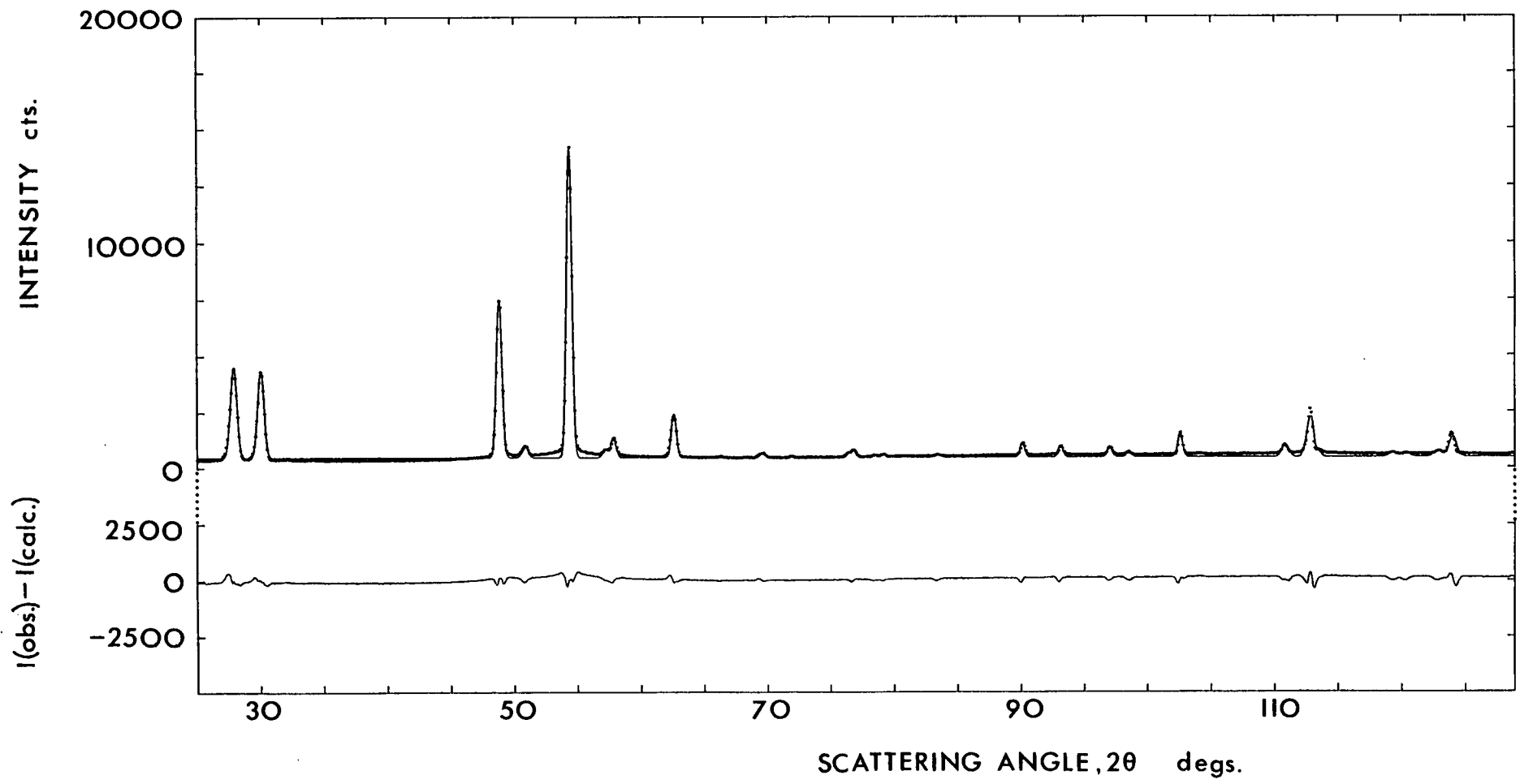
FIG.3·6
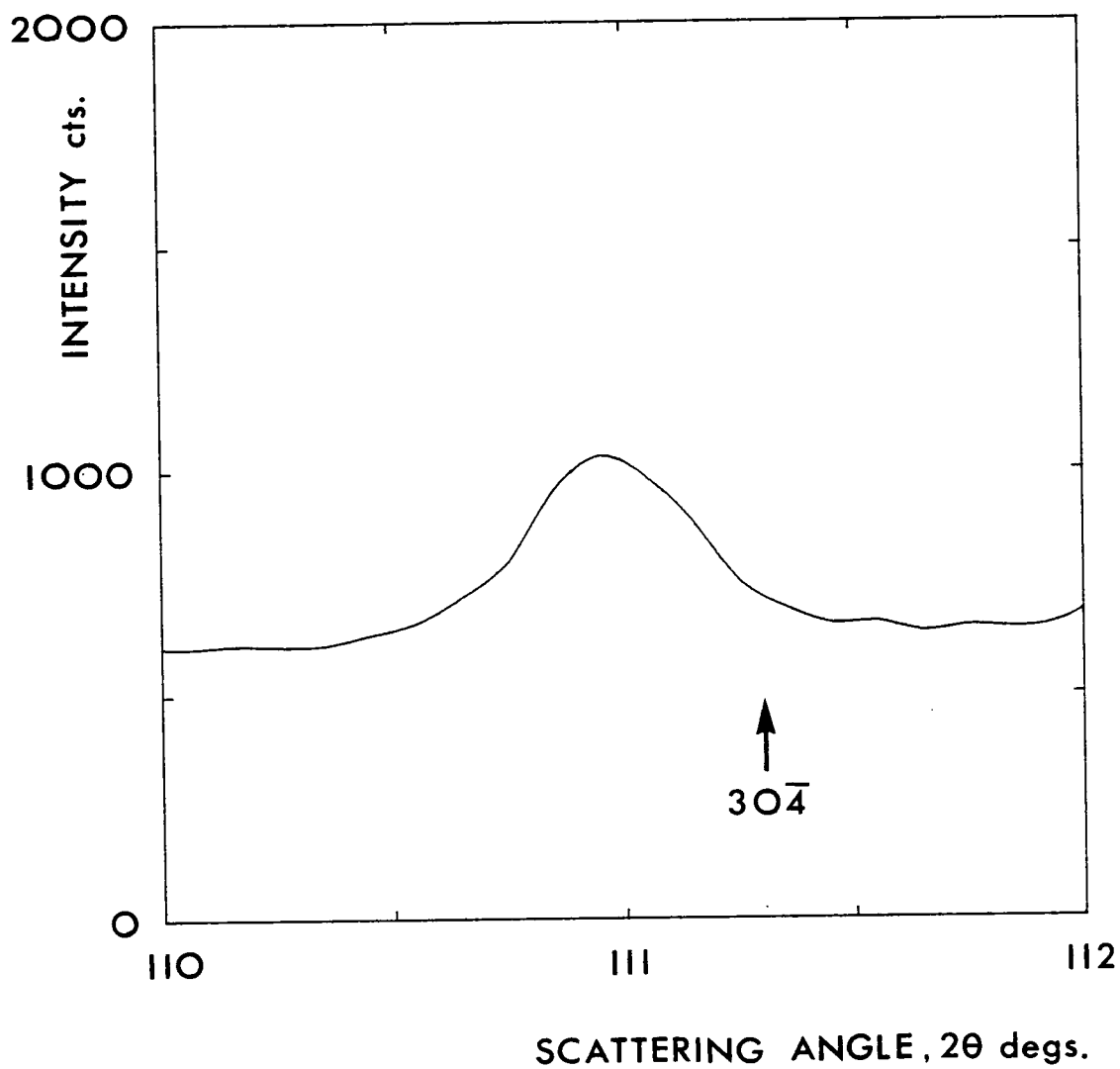
present. This R-factor might be reduced further by applying Rietveld's method of background correction[5,6], but this was not done since no further information is gained by such arbitrary corrections to powder diffraction scans.

The results of the unit cell refinement have been presented in Table 3.5 and Figure 3.5, and the refined unit cell dimensions are: $a = 9.001(4)\text{Å}$, $b = 12.303(9)\text{Å}$, $c = 7.279(3)\text{Å}$ and $\beta = 134.076(22)°$. We will next discuss the relevant space group possibilities that this unit cell and the molecular conformation allow.

There are five c-face centred monoclinic space groups, and these are, in decreasing order of symmetry, C2/c, C2/m, Cc, Cm and C2. In order to decide which of these space groups is compatible with the unit cell volume and the molecular geometry and conformation, it is instructive to refer to the crystal structure of this system at $\sim 280\text{K}$, which has already been presented earlier in this work. This structure is rhombohedral, space group R3m, and the pairs of molecules are aligned with their planes perpendicular to the unique axis, their intra- and inter-pair separations along this direction being $\sim 3.52\text{Å}$ and $\sim 3.72\text{Å}$ respectively. The volume of the cell at 280K is $299(5)\text{Å}^3$ and there is one molecular pair per cell, which indicates that the cell at 250K contains two pairs of molecules. Of the five space groups mentioned above, two are centrosymmetric, and these are C2/c and C2/m. These two space groups would therefore necessarily imply that the individual molecular centres are situated on the $\bar{1}$ symmetry points. However, if this is the case then the result is that, wherever the two pairs of molecules are placed in the unit cell, the other symmetry generated molecules are too numerous to be accommodated in the volume of 578Å^3. These two space groups are therefore rejected as possibilities for the crystal symmetry of this system at 250K. A similar argument also

rejects the space group Cc, which has high-symmetry n-glide planes perpendicular to the crystal b axis. This leaves the two space groups Cm and C2 as possibilities for the c-face centred crystal symmetry.

In the case of space group C2, the c-faced centred position is related to the origin by a screw diad that is parallel to the unique axis. The molecules must therefore be restricted in their orientation such that their molecular planes are perpendicular to the unique axis, their relative orientation about this axis being unrestricted by crystal symmetry. Taking the molecules in an individual pair to be $\sim 3.5\overset{o}{A}$ apart, as in the 280K phase and positioning the pairs on the equivalent positions in the unit cell, we find that the intermolecular atomic separation of fluorine atoms across the ac-face diagonal is $\overset{<}{\sim} 2.0\overset{o}{A}$. This is very short, compared to purely van de Waals F....F separation of $2.70\overset{o}{A}$ and is taken to be firm evidence that the space group C2 is inconsistent with the required intermolecular separations. This space group is therefore rejected as a possibility for this crystal symmetry. The only space group that is consistent with the c-face centring is therefore Cm, and this symmetry would restrict the molecules to have their molecular planes parallel to the unique axis.

However, if we consider the molecular planes to be not quite parallel to the unique axis, thereby breaking the mirror symmetry of Cm, an alternative space group, Pa, is possible. This crystal symmetry and particular molecular orientation would be equivalent to a pseudo-face centred structure, the molecular pair at the face centre being related to that at the origin by an a-glide plane. This pseudo-symmetry is not entirely unexpected, as we have seen, since there may exist a very weak reflection, the $(30\bar{4})$ at $2\theta \sim 111.30^{o}$, that breaks the face centring condition on the reflection indices. Were this

reflection to be present, it would be conclusive evidence that the c-face centred structure considered above is incorrect.

Therefore, at present, the space group of the phase at 250K of $C_6D_6 \cdot C_6F_6$ may be either Cm or Pa and this is as far as this analysis has proceeded. The powder diffraction pattern of this system at 5K has been measured in a similar manner to that at 250K. A comparison of the powder diffraction patterns at several temperatures is shown in Figure 3.7. The scans at 250K and 5K are observed profiles, whereas that at 280K is calculated using the structural parameters obtained in Chapter 1, §3. These scans show that as the temperature is reduced the rhombohedral phase, at 280K, becomes more complex at 250K, with more low angle diffraction peaks coming into existence. The associated phase transition temperature is probably about 272K, from the work of Ripmeester et al.[52] but this system has not specifically been studied by the present author with a view to finding a structural phase change at this temperature. The 280K phase was solved by using a single crystal that was grown at this temperature, above the thermal anomaly at 272K on warming found by Ripmeester et al.[52] The powder samples in the present experiment were prepared by cooling straight to liquid nitrogen temperatures and then grinding, so that the transition at ∿ 270K has been passed through. In order to obtain a powder sample at 280K, it would be necessary to cool the mixture of liquids very slowly from room temperature, but then the resulting polycrystalline sample would not necessarily be of good quality, as was the case with the sample used for the other scans. However, it may be possible to use a spherical sample chamber as described by Riekel et al.[30] and then randomising the motion of the sample using air jets, as these authors suggest. In this way a powder of poor quality would suffice for use in a diffraction experiment.

Figure 3.7:   Powder diffraction profiles for the $C_6D_6 \cdot C_6F_6$ system,

from top to bottom, at 280K (calculated) ,250K (observed)

and 5K (observed).   The wavelength of neutron

radiation used for observed scans was 2.98A, and the

range of 2θ is 15° to 120°.
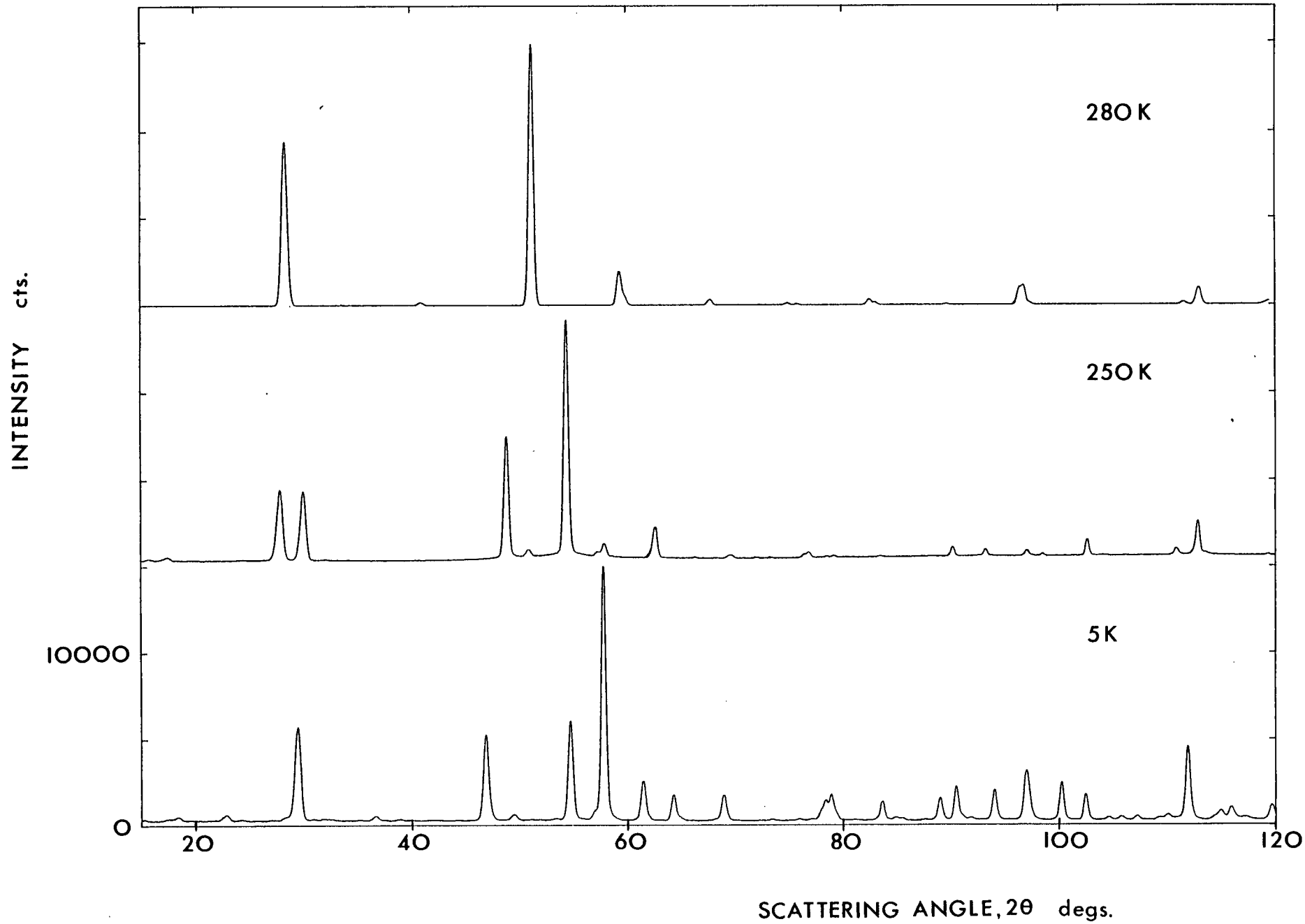
FIG. 3·7

The transition from the 280K to the 250K phase may be irrever-
sible, since no evidence of a transition on warming at 272K was observed
in the Raman measurements described in Chapter 2, §4. On cooling below
250K, this system undergoes a structural phase transition at 175K
(Chapter 2, §4). The crystal structure of the low temperature phase
is as yet unknown but it is probably of lower symmetry than that at
250K, as the observed powder diffraction pattern suggests (see
Figure 3.7).

The feature that is immediately apparent from Figure 3.7 is the
presence of a similar strong diffraction maximum in all these scans.
The factors governing the magnitude of the structure factor ampli-
tude of a Bragg reflection include the atomic positions within the
unit cell. If these atoms are positioned such that they all scatter
in phase for a particular reflection, then a large diffracted inten-
sity results. Therefore, with a knowledge of the reflection indices
and the unit cell dimensions, the approximate arrangement of atoms
and the possible orientation of molecules in the unit cell may be
deduced, since the scattering vector for the reflection is perpen-
dicular to the corresponding crystal planes. In the present case,
we have molecules that are of planar geometry (apart from thermal
motion), so that if their molecular planes lie parallel to some set
of crystal planes, then a large diffracted intensity may result if
the crystal is in the correct Bragg orientation for these planes.

The largest Bragg peak in the 280K scan is, in fact, composed of
three reflections, of which the strongest is the (110), all situated
within a small range of scattering angle of about 0.3°. At 250K
the strongest diffraction maximum is one reflection with indices
$(11\bar{2})$ and it is probable that most of the atoms are scattering in phase,
so that the approximate molecular plane orientation may be deduced as

being about 15° from the normal to the direct lattice ac-plane. This angle is not large and is consistent with the previously considered pseudo-symmetry of this phase. The phase at 280K is rhombohedral, with the molecular planes aligned perpendicular to the unique axis of the structure. In Chapter 1, §3.5 several pseudo-cells in different crystal classes were seen to be possible descriptions of the rhombohedral cell. One of these, the pseudo-monoclinic cell, is very similar to that given here for the 250K phase and the transition between these two phases probably occurs at $\sim$ 272K on warming[52]. The molecular plane orientation in the rhombohedral phase may be thought of as being perpendicular to the ab-face diagonal of the pseudo-monoclinic cell. In the 250K phase, from the deduction made in the previous paragraph, the molecular planes are $\sim$ 15° from the normal to the ac-face, therefore the transition from the 280K to the 250K phase involves a molecular reorientation in all three Euler angles where the molecules move in pairs. Hence, when the temperature is reduced the molecular pairs reorient in order to pack more favourably, resulting in a reduction of the cell volume of 3%. It may therefore be expected that on reducing the temperature further, the 5K phase may be derived from that at 250K by further molecular reorientations. The diffraction scans in Figure 3.7 indicate that the phases at 250K and 5K do not differ greatly since the number of low angle peaks is comparable in the two cases. However, the crystal structure of this system at 5K has not yet been solved and so the observed scattering angles of the diffraction peaks are tabulated in Table 3.6, the first twenty of which have been used as input for FZON. The peak intensities are also given, these having been measured graphically. The range of scattering angle zero error tried in the FZON technique described earlier was -0.20^o to + 0.20^o in steps of 0.01^o, but no complete

indexing coupled with a reasonable cell volume has resulted.

In the diffraction scan at 5K there are several groups of peaks that are not resolved, for instance, those centred on $2\theta \sim 47.1^{\circ}$, $2\theta \sim 57.8^{\circ}$ and $2\theta \sim 64.7^{\circ}$. These peaks are therefore not as accurately determined in scattering angle as they would be if they were completely resolved and since they lie within the first twenty peaks $(2\theta < 65^{\circ})$, the reliability of using the FZON technique is decreased. This may be one reason why the unit cell at 5K has not yet been found.

To conclude, this molecular complex system has been the subject of a great amount of interest and effort on the part of several authors and it is seen that this system displays a number of interesting transition phenomena. In order to be able to form descriptions of these phenomena the knowledge of the crystal structure of each phase is essential. An attempt has been made in this work to elucidate the structure of each of the three phases, at 280K, 250K and 5K. Success has been obtained with the 280K phase and a beginning has been made for that at 250K by finding the unit cell. The lowest temperature phase has so far eluded solution, but more research will probably see this crystal structure solved as well.

One possibility for such future experiments would be to make high resolution powder diffraction scans at 5K using long wavelength neutrons such as $\lambda > 5\overset{o}{A}$ with the appropriate filters to suppress wavelength contamination, in order to separate completely all the low angle peaks that exist in the scan using $2.98\overset{o}{A}$ wavelength neutrons. In this way accurate scattering angles could be determined and a unit cell may be obtained from these, assuming the cell to be not very different from that at 250K.

We have already seen that a single crystal cannot survive the phase transitions on cooling (Chapter 2, §4) and so future structural experiments on this system at low temperatures must be done using a polycrystalline specimen.

TABLE 3.6	$2\theta_{obs.}$ $(^{O})$	Peak intensity (cts.)
	22.83	650
	28.35	475
	29.47	5800
	36.66	560
	37.38	340
	38.90	370
	46.86	5300
	47.41	600
	49.45	650
	51.10	360
	51.90	350
	53.33	400
	54.72	6000
	55.92	400
	56.95	600
	57.78	15000
	58.32	1000
	61.45	2600
	64.25	1800
	64.90	450
	68.10	325
	68.88	1800
	73.37	400
	75.88	400
	77.03	400
	77.92	800
	78.35	1500
	78.95	1800
	79.42	500
	81.10	330
	83.58	1400
	84.81	450
	85.46	400
	87.55	300
	88.96	1600
	90.46	2300
	91.05	550
	91.80	450
	93.98	2100
	96.94	3200
	97.04	2500

Observed diffraction peak scattering angles and peak intensities for the 5K phase of the $C_6D_6.C_6F_6$ system. The limit of scattering angles given in $2\theta \sim 100^{O}$ for the wavelength of $\lambda = 2.98\text{Å}$ used.

REFERENCES FOR CHAPTER 3

(1)   Kalman, Z.H., Steinberger, I.T., Hasnain, S.S.,
           J. Appl. Cryst. (1979) 12, 523.

(2)   Mielcarek, W., Raczynski, J., Szklo & Ceram. (Poland) (1979) 30, 98.

(3)   Le Bail, A., Louër, D., J. Appl. Cryst. (1978) 11, 50.

(4)   Langford, J.I., Wilson, A.J.C., J. Appl. Cryst. (1978) 11, 102.

(5)   Rietveld, H.M., Acta Cryst. (1967) 22, 151.

(6)   Rietveld, H.M., J. Appl. Cryst. (1969) 2, 65.

(7)   Rietveld, H.M., Acta Cryst. (1966) 20, 508.

(8)   Caglioti, G., Paoletti, A., Ricci, F.P., Nucl. Instr. (1958) 3, 223.

(9)   Will, G., Frazer, B., Cox, D.E., Acta Cryst. (1965) 19, 854.

(10)   Will, G., J. Appl. Cryst. (1979) 12, 483.

(11)   Rae Smith, A.R., Cheetham, A.K., Skarnulis, A.J.,
           J. Appl. Cryst. (1979) 12, 485.

(12)   Pawley, G.S., J. Appl. Cryst. (1980) 13, 630.

(13)   Busing, W.R., Martin, K.O., Levy, H.A., (1962) ORFLS Report
           ORNL-TM-305, Oak Ridge National Laboratories, Tennessee.

(14)   Pawley, G.S., "Advances in Structure Research by Diffraction Methods",
           (1972), Vol. 4, p. 1-64, edited by Hoppe, W., Mason, R.,
           Pergamon Press, London.

(15)   Handscomb, D.C., "Methods of Numerical Approximation" (1965),
           p. 27 ff, Pergamon Press.

(16)   Pennington, R.M., "Introductory Computer Methods and Numerical
           Analysis" (1970) 2nd ed., p. 408 ff, Macmillan Co., Toronto.

(17)   Sakata, M., Cooper, M.J., J. Appl. Cryst. (1979) 12, 554.

(18)   Warren, B.E., Acta Cryst. (1953) 6 , 803.

(19)   Herbstein, F.H., Averbach, B.L., Acta Cryst. (1955) 8, 843.

(20)   Chipman, D.R., Paskin, A., J. Appl. Phys. (1959) 30, 1992.

(21)   Ibid , Idem, (1959) 30, 1998.

REFERENCES FOR CHAPTER 3 (Contd.)

(22) Goldstein, H., "Classical Mechanics", (1959) Addison-Wesley,
       Reading, Mass.

(23) Waser, J., Acta Cryst. (1963) 16, 1091.

(24) Hamilton, W.C., Acta Cryst. (1965) A18, 502.

(25) Hamilton, W.C., "Statistics in Physical Science; Estimation,
       Hypothesis, Testing and Least Squares", (1964), The
       Ronald Press, N.Y.

(26) Lindley, D.V., Miller, J.C.P., "Cambridge Elementary Statistical
       Tables" (1953), Cambridge Univ. Press.

(27) Levy, H.A., Acta Cryst. (1956) 9, 679.

(28) "International Tables for X-ray Crystallography" (1974),
       Vol. IV, p. 324-34, Kynoch Press.

(29) Cooper, M.J., Sayer, J.P., J. Appl. Cryst. (1975) 8, 615.

(30) Riekel, C., Convert, P., Gobert, G., Lazaro, C.,
       Nucl. Instr. & Methods (1978) 151, 201.

(31) Ono, K., Kobayasi, S., Shinohara, M., Asahi, K., Ishimoto, H.,
       Nishida, N., Imaizumi, M., Nakaizumi, A., Ray, J.,
       Iseki, Y., Takayanagi, S., Terui, K., Sugawara, T.,
       J. Low Temp. Phys. (1980) 38, 737.

(32) Turberfield, K.C., U.K.A.E.A. Research Group Report A.E.R.E. -
       R5647 (1968).

(33) Soller, W., Phys. Rev. (1924) 24, 158.

(34) Hewat, A.W., Bailey, I., Nucl. Instr. & Methods (1976) 137, 463.

(35) Eder, O.J., Kunsch, B., Nucl. Instr. & Methods (1976) 141, 533.

(36) Bacon, G.E., Cowlam, N., Acta Cryst. (1974) A30, 467.

(37) Legrand, E., Press, W., Solid State Commun. (1976) 18, 1353.

(38) Cox, D.E., Sleight, A.W., Idem (1976) 19, 969.

(39) Baharie, E., Pawley, G.S., Acta Cryst. (1979) A35, 233.

(40) Collins, B.M., Jacobson, A.J., Fender, B.E.F., J. Solid State
       Chem. (1974) 10, 29.

REFERENCES FOR CHAPTER 3 (Contd.)

(41)   Atoji, M., Tsunoda, Y., J. Chem. Phys. (1971) 54, 3510.

(42)   Wolfers, P., Fillion, G., Physica B & C (1977) 86-88,
             B & C, pt. 2, 896.

(43)   Ahtee, M., Hewat, A.W., Acta Cryst. (1978) A34, 309.

(44)   Konstantinovic, J., Babic, B., Solid State Commun. (1976) 18, 701.

(45)   Wright, A.F., Fender, B.E.F., J. Phys. C. (1977) 10, 2261.

(46)   Vergard, L., Z. Kristallogr. (1931) 77, 411.

(47)   Overell, J.S.W., Pawley, G.S., Powell, B.M., submitted to
             Acta Cryst., 1981.

(48)   Townes, C.M., Holden, A.K., Merrit, F.R., Phys. Rev. (1948) 74, 1113.

(49)   Visser, J.W., J. Appl. Cryst. (1969) 2, 89.

(50)   Taupin, D., J. Appl. Cryst. (1968) 1, 178.

(51)   de Wolff, P.M., Acta Cryst. (1957) 10, 590.

(52)   See reference (28), Chapter 1.

CHAPTER 4   <u>THE INCOMMENSURATE PHASE</u>

§1   Introduction

In this chapter we will be concerned with the quasi-crystalline state of matter, named the incommensurate phase. A great deal of scientific interest has been aroused by the discovery of this field and the topic itself is varied and extensive in its content. Much work has been done in this field and we review in this chapter only a fraction of the examples that are contained in the literature.

In §2 a general description of the phases of matter is given and this leads to an introduction to the incommensurate phase which is described in §3.   In §4 a review of several examples of systems that display incommensurate phenomena is given, these examples including several different types of systems, such as insulators and molecular organic materials.

Some conclusions are drawn from the preceding discussion and these are presented in §4.4.

Experimental data that has been collected by the author from the molecular organic system para-dibromotetra fluorobenzene is given in §5. Several different techniques of investigation have been used to probe this system, and in fact these techniques have been described in the previous chapters. Neutron powder diffraction has not been specifically used on this system by the author, but the molecular structure was previously solved using this technique.

Conclusions to be drawn from the experimental data are presented in §5.4. References are given after the chapter.

§2   The Phases of Matter

All known materials may be classified into the three phases solid, liquid and gas. It is from this that the following discussion will stem.

A gas may be defined as the 'free state' of a material, where a molecule or atom (or even an ion) may travel for very large distances, relative to its own size, before encountering a neighbour. The inter-molecular forces at work in a gas are nearly always of the van der Waals type, since the separation of the constituents is so large. However, when the atoms or molecules come into closer contact during collision processes, other forces of stronger influence are exerted, but the time spent in such collision processes is very small compared to that spent in free flight. If now the gas is compressed such that the constituents are separated by only a few times their own size, the gas condenses, under certain conditions of temperature and pressure, and one has a liquid. Of course, if the gas is a collection of ions, then obviously electrostatic forces play a larger part in determining the properties of the gas.

In the liquid phase, the intermolecular forces are still pre-dominantly of the van der Waals type, but now the possibility of electrostatic or Coulombic interaction is realised. The type of force and its range may vary depending upon whether the constituents are polar or electrically neutral with multipole moments. The form of potential functions describing such interactions is wide and varied and constitutes a separate subject, so it will not be discussed further here. Liquids may be sub-classified into two categories, pure liquids and liquid crystals.

A pure liquid may be thought of as being rotationally and trans-lationally disordered in all directions, this being isotropic. In order to distinguish this definition from a gas, the pure liquid will have surface tension, derived from a term in the free energy expressing the surface energy of the liquid.

A liquid crystal[1], however, is not a true liquid because it is not isotropically disordered. In fact, a liquid crystal has translational disorder but the molecules comprising the liquid are rotationally ordered. The general description that emerges is a phase where strong lateral intermolecular forces exist, binding molecules to form sheets, but where the sheets are allowed to slide over one another, laterally, i.e. the liquid crystal has a very low, if not zero, shear strength. The liquid crystal phase may be broken down into further types. These differing types of liquid crystals are distinguished by the manner in which molecules aggregate, these aggregations then being translationally disordered. There are other properties, such as optical activity, that are also used in classifying these types of crystals.

The last group of materials not covered by the two previous descriptions are the solids. Again, we find that we may sub-classify solids into smaller categories, the largest of these being the 'crystal' group, whereas others may come under the heading of 'amorphous'. The fundamental difference between crystals and 'the rest' is that the former possess translational symmetry whereas the latter do not. The crystal may be described by imagining an array of points, regularly situated in the three spatial directions, about which the constituents of the crystal are similarly arranged. The array of points we call a lattice, and the resulting arrangement of the atoms on this lattice is the crystal. Obviously this arrangement possesses translational symmetry in all the principal directions defining the lattice.

It is interesting to note at this point the crystalline counterpart of the liquid crystal. Remembering that a liquid crystal has rotational order but is translationally disordered, we have the

'plastic' crystal which is rotationally disordered in its constituents but which retains crystal symmetry by being translationally ordered. Thus the plastic phase of crystalline materials is pictured as a lattice of points, fixed in space, about which the constituents are, to some degree, freely rotating. The degree of rotational disorder of course depends upon the intermolecular interaction forces that are present in the crystal. For further details of plastic crystals, see for example refs. (2) - (5).

Intermediate between the true crystal, with full crystal symmetry, and the amorphous phase with no symmetry is the quasi-crystalline 'incommensurate' phase. This intermediate category will be the subject of the rest of this chapter.

This phase is more complex than the usual crystalline phase and the exact nature of it is not yet known. Far more research and study is needed to elucidate the problems that arise, both conceptual and experimental.

§3   General Description of the Incommensurate Phase

Given a regular lattice of points in (three-dimensional) space, we may characterise each point by a position vector with respect to the origin of the lattice. The components of this position vector are then integral multiples of the basis set of vectors spanning that lattice. If now we modulate the positions of the points of the lattice such that one or more of the multiplicative coefficients in the position vector expression becomes irrational, then the resulting modulated, array of points is said to be incommensurate with the original, underlying lattice. Obviously the translational symmetry contained in the original lattice is no longer present due to the irrational shift of the lattice points. It may therefore be said

that the incommensurate phase is not truly crystalline since it lacks the translational symmetry of the unmodulated lattice. In contrast to the incommensurate phase is the commensurate phase, where the shift of the lattice points is not irrational and not necessarily zero.

The mechanism causing the modulation of a crystal lattice resulting in an incommensurate phase is not simple as we shall see later. This aspect has been examined by several authors[6,7] in connection with phase transitions involving the incommensurate state. The concensus of opinion seems to be that it is inadequate to assume a single plane wave ground state for the irrational modulation of the structure, and a more detailed analysis and investigation is required.

In the preceding discussion we have only considered atoms or molecules (or indeed ions) displaced from their original positions in the lattice. We may also envisage the other types of incommensurate behaviour. These include magnetic and compositional modulations to the original crystal lattice. In the case of incommensurate magnetic structures, of which the rare earth metals are good examples[8], the magnetic moments of the atoms are modulated, whereas in the compositional case irrational modulation of the site occupancy occurs in alloys and chemically mixed phases. The theoretical background is very similar in all cases, with the magnetic moment in the rare earth crystal replaced by the site occupancy in the alloy (say) or the atomic displacement in the displacive case of incommensurate behaviour.

Having briefly described the incommensurate state we now wish to know how we might perform experiments and how to interpret the results of such investigations. The technique taken for discussion is neutron scattering, which has proved itself as a very powerful

and versatile tool for the investigation of such materials[6,9-13].

The references are representative of the variety of systems that

exhibit such phenomena, but they are by no means complete.

However, if we take as our example the displacive incommen-

surate behaviour, where the phase of each scattering centre is

changed with respect to the lattice origin, then a relatively simple

procedure will give us a qualitative result that is easily inter-

preted. If we take the modulation as harmonic, we may write, in

the case of a Bravais lattice, the component of the displacement of

the ℓth atom with position vector ℓ along the orthogonal $\underline{x}_o$ axis

in the crystal as

$$4.(1) \qquad u_{\ell x_o} = x_o \sum_i \sin(\underline{k}_i \cdot \underline{\ell}) \quad ,$$

where the $\{\underline{k}_i\}$ are the wavevectors associated with the incommen-

surate phenomenon. We now take the simplified case where only one

of the $\{\underline{k}_i\}$ is non-zero, $\underline{k}_1 \neq 0$ along $\underline{x}_o$ and then write 4.(1) as

$$4.(2) \qquad \underline{u}_\ell = \underline{x}_o \sin(\underline{k}_1 \cdot \underline{\ell}) \quad .$$

The elastic scattering amplitude, $F(\underline{Q})$, may then be written

$$4.(3) \qquad F(Q) = \sum_\ell b_\ell \exp[i\underline{Q} \cdot (\underline{\ell} + \underline{u}_\ell)] \quad ,$$

where b_ℓ is the scattering length for the atom in the ℓth unit cell

and this includes the Debye-Waller factor required to account for

thermal fluctuations. If we take $b_\ell(\underline{Q}) = b(\underline{Q})$ independent of ℓ

(true by translation symmetry in the unperturbed lattice, but not

rigorously so in the modulated structure) then we may expand equation

4.(3) in terms of the Bessel functions, $J_m(\varepsilon)$, using the relation

4.(4) $\quad e^{i\epsilon\sin\theta} \;=\; \sum_{m=-\infty}^{m=+\infty} J_m(\epsilon)\, e^{im\theta}$

giving the result

4.(5) $\quad F(\underline{Q}) \;=\; b(\underline{Q}) \sum_{\ell} \{\sum_m J_m(\underline{Q}\cdot\underline{x}_o)\exp.(i(m\underline{k}_1 + \underline{Q})\cdot\underline{\ell})\}$.

It is seen from this result that even though the modulation it-self involves only one wavevector, $\underline{k}_1$, the diffraction pattern will contain all the harmonics of $\underline{k}_1$, $m\underline{k}_1$ (m integral). These harmonics of the modulation wavevector appear as satellite reflections around the $m = 0$ peak, this being the Bragg reflection. The intensity of a satellite reflection is proportional to the squared modulus of the elastic scattering amplitude, and since $J_m(\epsilon) \sim \epsilon^m$ for small ϵ, it may be seen that the intensity of a satellite falls off as

4.(6) $\quad I(\underline{Q}) \;\propto\; (\underline{Q}\cdot\underline{x}_o)^{2m}$

for the mth satellite. This is a rapid fall off and hence higher order satellites are usually difficult to observe.

There is an important difference between the displaced and the magnetic or compositional modulations. In the former the phase of the scattering centre is modulated whereas for the latter it is the scattering amplitude that is modulated. Hence the diffraction harmonics do not appear for the latter cases as they do for the former. This means that in the latter cases only one satellite reflection will be observed, whereas the phase modulation produces many satellites, each corresponding to an harmonic of the primary wavevector of the modulation.

§4   Review of Some Incommensurate Structures

Having seen how an incommensurate phase modulation manifests it-
self in an experiment as satellite reflections, we now require more
information concerning the cause of such distortions of the lattice.
It is also interesting to note how varied the forces are that cause
the modulation, depending upon the medium in which they take place.

As we have seen there is a very wide variety of systems that
exhibit incommensurate phenomena. In order to see the differences
in the mechanisms that cause the incommensurate phase transitions,
it is instructive to examine several examples, all of which involve
some interesting aspects of physics.

4.1   Polyphenyls

In the past few years much work has been done in an attempt to
understand the temperature dependence of the structures of poly-
phenyls[12,15,16,18-23]. The aspect that makes this group of mole-
cular crystals interesting is that as the number of phenyl rings
in the molecule increases, then the balance of the competing forces
that affect the structural and dynamical properties of the crystal
changes. In the case of the polyphenyls this change of competing
forces causes a change in the type of phase transition that takes
place. In both the liquid and gaseous phases the polyphenyl molecules
are not planar[24] and there exists a double-well intramolecular
potential for the torsion angle between the phenyl rings. When the
polyphenyls crystallise the molecules become more strongly coupled
together by intermolecular forces and so a competition is set up
between the atom-atom interactions on different molecules and the
interphenyl ring interactions within one molecule. Whether any

phase transition that takes place is of the 'displacive' or 'order-disorder' type depends on the relative strength of these two competing forces compared with the double-well barrier height.

In the case of bi-phenyl, with two phenyl rings in each molecule, a soft mode has been observed at about 40K using Raman scattering[19], indicating that a displacive phase transition has taken place on warming. Contrary to this, in p-terphenyl, with three rings per molecule, critical scattering is observed similar to that found in methane[25] and an order-disorder transition takes place around 180K[20]. The soft mode in biphenyl is associated with a phase transition at 38K. It is found that biphenyl has three phases, with transitions at 38K and 21K[20]. Both the low temperature phases are incommensurate with respect to the high temperature lattice periodicity.

We define here the quantity δ, as the deviation of the component of the incommensurate wavevector from some commensurate value of one of the reciprocal lattice vectors $(\underline{a}^*, \underline{b}^*, \underline{c}^*)$, for example $\underline{k}_\delta = (1 - \delta)\underline{a}^*/3$.

The phase of biphenyl, phase II, that exists between 21 < T < 38K has an incommensurate wavevector that involves both $\underline{a}^*$ and $\underline{b}^*$, whereas that for phase III (T < 21K) only involves $\underline{b}^*$. It is noted that this behaviour is to be expected since the unit cell real b-parameter is the shortest and the molecular interactions along $\underline{b}$ are stronger than along the other directions. Hence as the temperature is lowered through 21K the incommensurate $\underline{a}^*$ behaviour becomes less energetically favourable and disappears, whereas the $\underline{b}^*$ component of the incommensurate wavevector is still favoured due to the stronger coupling forces and so it persists into the phase III below 21K. The transition at 38K is observed through clear discontinuities

in the satellite wavevector deviation, δ.

Cailleau et al.[12] also point out that the occurrence of strong coupling and incommensurate behaviour is consistent with their observations of the satellite deviations, δ_a, δ_b along a^* and b^* respectively. The deviation δ_a varies little with temperature except at the transition at 21K. These authors also discuss the symmetry requirements of any soft mode that occurs in this structure. At the (monoclinic) b^* zone boundary there is a doubly degenerate mode, so that the dispersion surface is continuous and has non-zero gradient. The soft mode has a wavevector that is not quite equal to $\frac{1}{2}b^*$, as Cailleau et al.[12] point out. Biphenyl is thus an example of a material whose structure is driven to a phase transition at low temperatures by a lattice instability.

4.2   Metal dichalcogenides

A completely different category of material that exhibits incommensurate behaviour is the metal dichalcogenide series. These materials have the general formula AB_2 where A is a transition metal element and B is a chalcogen non-metal element. (S, Se, Te or Po). This group of materials is of particular interest since the number of packing arrangements of the AB_2 units is large and varied[14]. These materials are good examples of incommensurate structures that undergo transitions to a commensurate state. This type of transition is called a 'lock-in' transition and represents a situation where the incommensurate lattice is no longer energetically favourable for the crystal and the free energy is thereby lowered in transforming to a commensurate structure.

As an example of the metal dichalcogenides we shall study results

obtained from the hexagonal crystals $2H-NbSe_2$ and $2H-TaSe_2$ more closely. The prefix denotes the packing arrangement of the AB_2 unit in the crystal[14]. In both these crystals anomalous changes in their electronic properties show that the transitions that occur on lowering the temperature involve the conduction electrons to a large extent. From electron diffraction experiments Wilson et al.[14] have observed that superlattice reflections develop at the same temperatures that electronic properties show changes. Similar experiments on the closely related crystal structure $1T-TaSe_2$ show that the wavevector of the incommensurate distortion is changed by doping with titanium.

Therefore it has been deduced that the incommensurate behaviour in these dichalcogenide materials is derived from a charge density wave instability of the kind first suggested by Overhauser[26]. Moncton et al.[6] observed that superlattice reflections develop in a (nearly) second order manner in both $2H-NbSe_2$ and $2H-TaSe_2$. For the latter of these two crystals three novel features were observed in the development of the superlattice. Firstly, the superlattice is found to be incommensurate with the high temperature ($T \gtrsim 150K$) lattice and is characterised by a wavevector $\underline{k}_\delta = \frac{1}{3}(1 - \delta)\underline{a}^*$ with $\delta \sim 0.02$ and temperature dependent. Secondly, there exists a first order (lock-in) transition at 90K and below this temperature the structure is commensurate with the underlying lattice periodicity. Finally, in addition to the primary distortion, characterised by $\underline{k}_\delta$, there is observed a secondary, weaker, distortion with wavevector $\underline{k}_{2\delta} = \frac{1}{3}(1 + 2\delta)\underline{a}^*$.

Similar behaviour was found for the $2H-NbSe_2$ superlattice but unfortunately the sample used was too small (of the order of a few mm^3) to observe the secondary distortion if it occurred.

Following the discussion of Moncton et al.[6] it is possible to

understand the behaviour of the superlattices mentioned above by using
a simple theory similar to a Landau free energy expansion. The free
energy is expanded in terms of the order parameters, which are de-
fined as the amplitudes of the plane wave distortions with well
defined symmetry. For the incommensurate phase this becomes

$$4.(7) \quad F_{inc.} = A(\underline{k}_{-\delta}, T)\eta_\delta^2 + A(\underline{k}_{-2\delta}, T)\eta_{2\delta}^2 - B\eta_\delta^2\eta_{2\delta} + \tfrac{1}{4}C\eta_\delta^4 ,$$

whereas for the low temperature commensurate phase it is

$$4.(8) \quad F_{com.} = A(\underline{k}_{-c}, T)\eta_c^2 - \tfrac{1}{3}B\eta_c^3 + \tfrac{1}{4}C\eta_c^4 ,$$

where η_δ, $\eta_{2\delta}$, η_c are the real amplitudes of the distortions at
wavevectors $\underline{k}_\delta$, $\underline{k}_{2\delta}$, and $\underline{k}_c = \tfrac{1}{3}\underline{a}^*$ respectively. B and C are
assumed constant. The coefficient $A(\underline{k}, T)$ is given by

$$4.(9) \quad A(\underline{k}, T) = \alpha(T - T_o) + |\underline{k} - \underline{k}_o|^2 ,$$

which is the simplest form of $A(\underline{k}, T)$ that will produce a lattice
susceptibility diverging at $T = T_o$ for $\underline{k} = \underline{k}_o = \tfrac{1}{3}(1 - \delta_o)\underline{a}^*$.
For brevity Moncton et al.[6] take into account only terms coupling order
parameters having wavevectors along the same $<\xi 00>$ directions. The
temperature dependence of the order parameters and δ are obtained
by minimisation of the free energy with respect to these parameters.

The results of such minimisations indicated two distinct cases
to be considered:

(i) if $B^2/C \geqslant 9\delta_o^2$ then a first order transition occurs at $T_{com.} \geqslant T_o$
with a wavevector $\underline{k} = \underline{k}_c$ commensurate with the underlying lattice.

(ii) However, if $B^2/C < 9\delta_o^2$, a second order transition to the
incommensurate phase, with wavevector $\underline{k} = \underline{k}_o = \tfrac{1}{3}(1 - \delta_o)\underline{a}^*$, occurs
at T_o.

The coupled term in the free energy expansion, namely, $-B\eta_\delta^2\eta_{2\delta}$, is the origin of the temperature dependence of δ and, of course, it ensures that the secondary distortion $\underline{k}_{2\delta} = \frac{1}{3}(1 + 2\delta)\underline{a}^*$ is possible.

For values of B^2/C close to $9\delta_o^2$, $F_{com.}$ becomes less than $F_{inc.}$ at some temperature below T_o, and the lock-in transition to the commensurate phase occurs.

The quantitative agreement of this simple model with the experimental results was good, but a more realistic model would include additional $\underline{k}$-dependence of the coefficients A, B, C in the free energy expansion. These authors[6] then describe a study of some dynamical aspects of these transitions through observing some phonon modes in the principal $[\xi 00]$ and $[00\zeta]$ directions. They found that as the temperature was lowered towards 130K (where 2H-TaSe$_2$ becomes incommensurate) one of the acoustic longitudinal modes softened, but clearly did not reach zero frequency as the transition temperature was approached. This softening is likened to a Kohn anomaly[27] where the conduction electrons partly screen a vibrational mode of the lattice in a metal and this screening varies rapidly on the Fermi surface. This leads to abrupt changes in the phonon frequencies as a function of wavevector and is indicative of strong electron-phonon interaction. The fact that Kohn-like anomalies occur can be taken as evidence of charge density wave instabilities in both 2H-TaSe$_2$ and 2H-NbSe$_2$.

We see that for these examples the incommensurate ground state is not simply a plane wave distortion since a weaker secondary peak was observed. It may have been concluded that this weaker component was a diffraction harmonic of the primary distortion, but this interpretation is excluded because the intensity observed was far too large to be accounted for in this way.

4.3   Insulators

As final examples of incommensurate structures to be considered here, we shall discuss some insulator materials. The specific crystals chosen for review are deuterated thiourea $(CS(ND_2)_2)$[13], potassium selenate (K_2SeO_4)[11] and deuterated ammonium fluoroberyllate $((ND_4)_2BeF_4)$[10]. They shall be taken in this order.

Thiourea has an orthorhombic structure, space group Pnma, at room temperature and it is an anti-ferroelectric. On lowering the temperature this crystal shows successive dielectric anomalies and it is believed that five phases exist[28], of which two are ferro-electric. In a protonated sample these two ferroelectric phases occur below 169K and between 176 and 180K. This latter phase III is sandwiched between two non-ferroelectric phases (II and IV) and phases III and IV are incommensurate with respect to the lattice periodicity of the antiferroelectric phase (V). The low temperature phase which is ferroelectric is denoted by I ; see Figure 4.1 for a schematic representation of these phases. The temperatures of the dielectric anomalies are higher by some 10-20K for a deuterated sample.

Recently, neutron scattering results published by Moudden et al.[13] for a deuterated sample of thiourea, revealed that on lowering the temperature, several structural phase transitions take place. The high temperature, antiferroelectric phase V persists until at 220K an antiferroelectric transition takes place and the structure be-comes incommensurate, having a wavevector of $\underline{k} = 0.14\underline{b}^*$. This wave-vector steadily decreases and at about 200K it has a value of $\underline{k} = 0.127\underline{b}^*$ and the temperature dependence of this satellite wave-vector exhibits a small anomaly which probably marks, though none too

Figures 4.1a, b: The successive phase transitions of deuterated
(a) and protonated (b) thiourea. The Roman
numerals denote the different phases cited in
the text, the temperatures are in K. Symbols
used as superscripts in the figure are:

*   incommensurate   □   high temperature
                                  cell of phase V

†   antiferroelectric   ⊠   cell with 9b of
                                  phase V.

o   ferroelectric

Phase II has a unit cell whose b-axis is nine
times that of phase V.

FIG. 4·1a

a

$I^{o\square}$ $II^{\boxtimes}$ III^{*o} IV^{*} $V^{\dagger\square}$

190   192   200   220

b

$I^{o\square}$ $II^{\boxtimes}$ III^{*o} IV^{*} $V^{\dagger\square}$

169   176   180   ~200
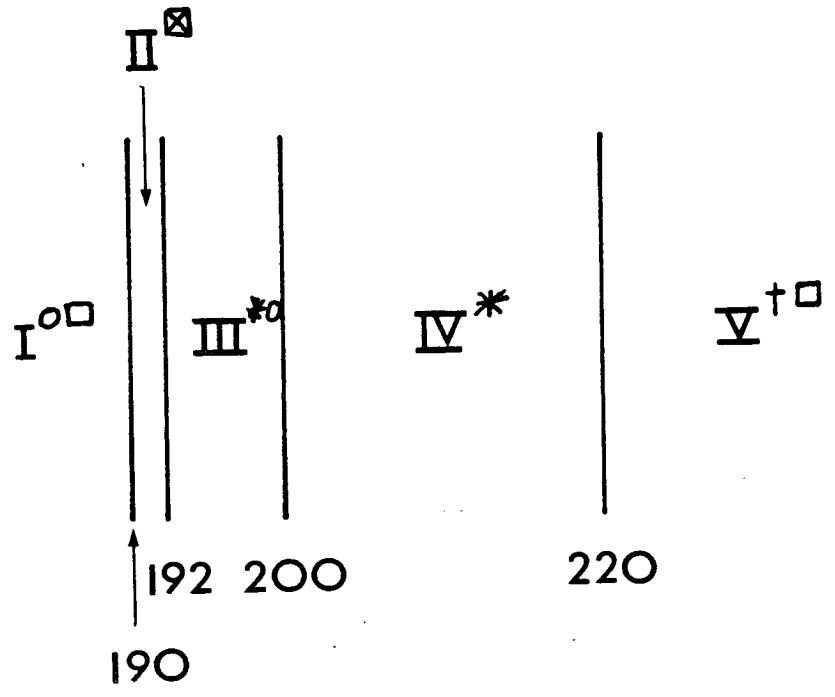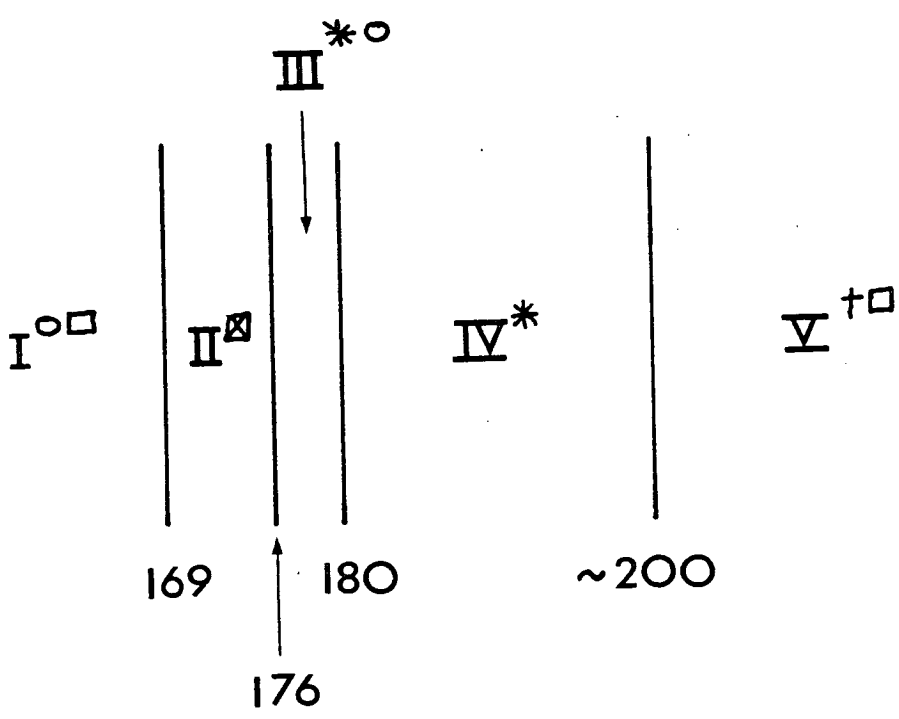
clearly, the transition believed to separate the phases IV and III. Phase III is ferroelectric whereas phase IV is not. More data is required to elucidate the character of these two phases more fully. However, on lowering the temperature still further the satellite wavevector varies smoothly until at just above 193K its value is $0.116\underline{b}^*$. At 192K a lock-in transition takes place and the structure becomes commensurate, with a $9\underline{b}$-superstructure with respect to the antiferroelectric phase. The wavevector of the satellites is therefore $0.111\underline{b}^*$. This lock-in wavevector is known very accurately since measurements were taken successively with orders of satellites 2, 3 and 4 at different reciprocal lattice points and the results were consistently $0.222\underline{b}^*$, $0.333\underline{b}^*$ and $0.444\underline{b}^*$ respectively. These satellites, because of their relative intensities, not only correspond to diffraction harmonics of the distortion $\underline{k}_1 = 0.111\underline{b}^*$, but are also harmonics of the distortion itself, so that $\underline{k}_m = m\underline{k}_1$. Hence the accuracy of the determination of $\underline{k}_1$ increases as m[32].

This commensurate superstructure persists for about 2K until at 190K another transition takes place whence the high temperature crystallographic cell is regained, the wavevector of the satellites having jumped discontinuously to zero. Thus the low temperature ferroelectric phase I is established. Also observed around this transition from phases II to I is a thermal hysterisis of the transition temperature of about 2K. This is found to be consistent with the predictions made by Aubry[30] for this type of system, which are not discussed further here. The high and low temperature phases, V and I respectively, differ in that the latter is ferroelectric rather than antiferroelectric but more importantly it has lost the n-glide symmetry element of the Pnma space group of V.

The high temperature structure may be viewed as parallel planes,

perpendicular to $\underline{b}$, of polar molecules having the same orientation on the same plane but opposite orientations to molecules on neighbouring planes. Neighbouring planes are related by the n-glide symmetry element so the structure may be thought of as two symmetry related sub-lattices. The transition at 220K may therefore be expected to be of the incommensurate type as a result of the competition between the polarisation modulations in each sub-lattice.

This is similar to the case of TTF-TCNQ[33] where there exist two sets of parallel 1-dimensional chains of molecules both of which are disordered at temperatures above 54K. One set of chains orders at 54K whilst the other chain becomes ordered at 47K. Here the similarity between TTF-TCNQ and thiourea is evident, because now the two modulations of the chains in TTF-TCNQ are in competition, giving rise to an incommensurate phase. This phase persists until 38K where a lock-in transition to a 4$\underline{a}$-superstructure is induced by Umklapp terms in the free energy. In the case of thiourea the incommensurate wavevector variation is caused by the modulation of the polarisation vectors in the two sub-lattices competing one against the other.

Thiourea is an interesting specimen not only for its varied structural changes but also with regard to its unique lock-in transition. The high order of commensurability, $p = 9$, in the 9$\underline{b}$-superstructure was observed for the first time by Moudden et al.[13] This parameter, p, plays an important role in the continuous theories of lock-in transitions[29] and is in fact the order of the Umklapp energy that induces the transition. Such values of $p > 5$ have previously been considered as too high for a structurally stable crystal with the argument that the value of $\underline{k}_\delta$, the incommensurate satellite wavevector of the distortion, becomes more and more restricted in the values that it may take and is therefore less likely

to occur.

The transitions in thiourea seem to stem from the interaction of the polarisations of the molecules and in this way it differs from the previous examples of biphenyl and the metal dichalcogenides. However, more work is required to characterise the other phases, especially III and IV and their transition, in order that the driving mechanisms of the structural changes may be known more fully.

In sharp contrast to the previous example, thiourea is the insulating compound potassium selenate (K_2SeO_4). We shall see that this crystal follows the more usual pattern of high and low temperature phases (P and F, respectively), with one intermediate incommensurate phase (I) [11].

Potassium selenate has three phases, the high temperature phase being paraelectric and existing from room temperature down to a temperature of 130K where the first of the two transitions takes place. The paraelectric phase is orthorhombic, with space group Pnam . As the temperature is lowered from 300K it was observed by Terauchi et al. [31], using X-ray scattering techniques, that at a wavevector of $\underline{k}_{\frac{1}{3}} = \frac{1}{3} a^*$ critical scattering appears that condenses into superlattice reflections at $T_i = 130K$. These observations led these authors to conclude that the phase below T_i was commensurate with respect to that above T_i. However, when Iizumi et al. [11] studied the same phenomena with high resolution apparatus, using cold neutrons, it was found that at round 145K the scattering consisted of phonon side bands centred on zero energy. As the temperature was lowered to 130K critical scattering appeared, whose intensity diverged as the transition at 130K was approached. On closer analysis of this critical scattering, it was observed that

the peak of this anomalous intensity was precisely located along $\underline{c}^*$, but that it took an incommensurate value along $\underline{a}^*$. The width of the critical scattering was resolution limited. Moreover, in the same temperature range, about 250K to 130K, a soft phonon mode was observed whose frequency tended to zero as the transition was approached. The wavevector at which this soft mode was least stable was found to be incommensurate, taking a value of $0.31\underline{a}^*$. This lattice instability above 130K was then analysed by expanding the dispersion relation in terms of a Fourier series and then fitting this to the observed soft mode. This analysis showed that the observed dynamical instability above 130K of the phonon optic branch, designated as of Σ_2 symmetry by a normal mode analysis, was caused by a temperature dependent decrease of interlayer forces of range $^a/2$ and a in the presence of strongly persistent forces of range $\frac{3}{2}a$ ('a' being the unit cell parameter along the real space $\underline{a}$-axis). A further analysis of the intensity of the soft mode scattering around several reciprocal lattice points suggested that the soft mode was a result of coupled translations of the potassium ions and vibrations of the selenate groups.

When, on cooling, the first transition temperature is reached, at $T_i = 130K$, the structure becomes incommensurate with respect to the paraelectric phase and it is characterised by the wavevector $\underline{k}_\delta = \frac{1}{3}(1 - \delta)\underline{a}^*$, with $\delta = 0.07$ at 130K. As the temperature is lowered, δ varies smoothly until at just above 93K it takes the value 0.02. This observation of incommensurability corrects the less highly resolved X-ray data of Terauchi et al. who concluded that this phase was commensurate. As well as the primary distortion of wavevector $\underline{k}_\delta$, secondary peaks characterised by $\underline{k}_{2\delta} = \frac{1}{3}(1 + 2\delta)\underline{a}^*$

were also observed with intensity about two orders of magnitude less than the primary distortion. Whether these were diffraction harmonics of the primary distortion or a secondary lattice distortion was not concluded since the data was not sufficient to resolve the point.

At T_c = 93K a unique type of transition takes place in potassium selenate. Firstly, it is a lock-in transition and the parameter δ jumps discontinuously to zero. However, simultaneously with the lock-in transition another type of transition also takes place with spontaneous macroscopic polarisation appearing along the c-axis and the crystal becomes ferroelectric, as well as commensurate. The order of commensurability is p = 3 since $\underline{k}_c = \frac{1}{3}\underline{a}^*$ and a superlattice of 3$\underline{a}$, with respect to the paraelectric unit cell, appears at the lock-in transition. This combination of two types of transition occurring simultaneously is unusual and makes the study of K_2SeO_4 of interest since the two mechanisms are simultaneously at work and may well be intimately related.

These transition phenomena as a whole have been treated by Iizumi et al.[11] using a Landau type free energy expansion, where the term $Q^3(\underline{k}_\delta)P(\underline{k}_{3\delta})$ plays an important role in driving the transitions, where $\underline{k}_{3\delta} = 3\delta\frac{1}{3}\underline{a}^*$. This term represents a coupling between the real amplitude of the primary distortion, $Q(\underline{k}_\delta)$ and the polarisation wave propagating along the c axis in the incommensurate phase, $P_z(\underline{k}_{3\delta})$. Since the order of commensurability is three, then $Q(\underline{k}_\delta)$ is raised to that power. The polarisation wave freezes to the lattice at 93K and the crystal becomes ferroelectric.

In summary, the treatment of K_2SeO_4 by Iizumi et al.[11] suggests that coupled motions of the potassium ions and selenate groups are responsible for the soft mode observed above T_i = 130K. They also propose an interaction term in the free energy expansion that causes

ferroelectricity at the low temperature transition. The fact that this transition is both of the lock-in as well as the ferroelectric type suggests that the polarisation wave propagating along the c-axis in the incommensurate phase is coupled to the lattice distortion characterising that phase. The polarisation wave is hidden until the distortion wavevector takes a commensurate value, when it becomes the macroscopic polarisation of the crystal.

The final example of the incommensurate phase to be reviewed here is the ferroelectric, ammonium fluoroberyllate, $(ND_4)_2BeF_4$ [10]. This system is very similar in its behaviour as the previous example, K_2SeO_4, so that the details will be discussed only briefly.

Ammonium fluoroberyllate undergoes two transitions, the first at 173K where the orthorhombic Pnam structure becomes incommensurate, being characterised by the wavevector $\underline{k}_\delta = (\frac{1}{2} - \delta)\underline{a}^*$, where $\delta \sim 0.02$ at 173K. δ follows the behaviour of decreasing as the temperature is lowered, becoming zero discontinuously at 164K, where the lock-in transition occurs. In this case the low temperature structure has a $2\underline{a}$-superlattice with respect to the high temperature unit cell. The same driving mechanism for these transitions is postulated as for K_2SeO_4, viz. that a polarisation wave modulation is induced by a high order coupling term in the free energy expansion of the crystal. Since the distortion wavevector in the incommensurate phase is given by $\underline{k}_\delta \sim \frac{1}{2}\underline{a}^*$ in this crystal, then the real amplitude of the atomic displacements, $Q(\underline{k}_\delta)$, appears to second order in the free energy. Hence the relevant term in the free energy is $BQ^2(\underline{k}_\delta)P(\underline{k}_{2\delta})$ where B is a constant and $P(\underline{k}_{2\delta})$ is the polarisation wave associated with the wavevector $\underline{k}_{2\delta} = 2\underline{a}^*\delta$ polarised in the b-direction. At 164K, the lock-in transition, the quantity $P(\underline{k}_{2\delta})$ becomes $P_b(0)$ the

macroscopic polarisation along b, consistent with observations made experimentally.

4.4   Conclusions drawn from the reviewed examples

We have seen from the previously discussed examples how the incommensurate modulations manifest themselves in a variety of materials, the choice of which is only representative of the many materials that exhibit such phenomena.

Incommensurate phenomena result from the competition of forces of interaction of varying range within the crystal structure. The case of biphenyl revealed that the long range atom-atom intermolecular potential competes with the shorter range forces generated by the interaction of the phenyl rings, an intramolecular force field. However, there are always forces present in a crystal attempting to restore lattice periodicity once the incommensurate phase has been established. In the case of biphenyl, these restoring forces are the long range intermolecular interactions. The free energy is thereby lowered when translational symmetry is restored and the crystal returns to a commensurate phase.

On the other hand we have electron-phonon interactions and charge density wave instabilities that cause crystal symmetry to be lost. These interactions involve the Fermi surface and the conduction electrons in metallic crystals, such as the metal dichalcogenides and Nb_3Sn, niobium stannate[34]. Kohn anomalies manifest themselves in the dynamical properties of crystals and are themselves related to the geometry of the Fermi surface. These anomalies are usually observed through soft phonon scattering in crystals.

Furthermore, we have systems, such as the insulators discussed, in which the incommensurate behaviour is intimately involved with the

electrical properties of the crystal, such as the electrical polarisation and dipole moments of the molecules.

The field of incommensurate phenomena is wide and varied as well as vast, and a great deal is probably, as yet uncovered, in which case far more work is needed before we may fully comprehend all the results gathered to date.

§5   Experimental Data on the $p-C_6F_4Br_2$ System

5.1   Introduction

In this section we present various experimental data that have been obtained from measurements on the organic molecular system para-dibromotetrafluorobenzene. The techniques used were neutron quasi-elastic and Raman scattering, as well as single crystal X-ray diffraction.

The neutron and Raman scattering data, for various temperatures, are given in §5.2 and the room temperature X-ray diffraction experiment is described in §5.3. The data that are presented have not yet been analysed but they suggest that this system gives rise to quasi-elastic and diffuse scattered intensity with neutron and X-radiation respectively.

When the neutron scattering data were collected it was suggested that this system may have an incommensurate phase[9], but the more recently obtained room temperature X-ray diffraction measurements show the presence of weak diffuse scattered intensity, which is extensively distributed throughout reciprocal space. It is therefore possible that the thermally agitated lattice of this system is partly responsible for this X-ray diffuse scattering. The question of the source of the extra neutron and X-ray scattering at various temperatures is discussed in more detail in §5.4, where possible conclusions

are drawn from the data presented in §5.2 and §5.3

As far as the author is aware, the amount of literature concerning the $p-C_6F_4Br_2$ system in its crystalline state is limited. The Raman scattering data may be the first light scattering study of the temperature dependence of the external lattice vibrations in this system. Therefore, the normal mode frequencies obtained from this study are tabulated as variables of the absolute temperature. Previous Raman and infra-red measurements have been done on solutions of this system in various organic solvents[39], but these data give information about the internal vibrations of the molecules and are therefore of no immediate relevance here. Some nuclear magnetic resonance studies have also been done[40], but these have not been available for study.

The remainder of this introduction will be concerned with a brief description of the structure of this system. This structure was determined[35] using the technique of profile refinement[41] of neutron powder diffraction data . The monoclinic unit cell and crystal symmetry were deduced from single crystal X-ray diffraction photographs and the neutron powder diffraction data was refined to solve the molecular and crystal structure. The refined cell parameters had values $a = 6.089(1)Å$, $b = 11.414(2)Å$, $c = 5.403(1)Å$ and $\beta = 93.11(1)°$, where there are two molecules contained within this unit cell.

The molecular conformation is such that the individual molecules are stacked along the unique axis of the structure, with refined Euler angles (ϕ, θ, ψ) (after Goldstein[36]) given by $(-0.124(4)^c, 0.757(1)^c, 2.446(2)^c)$[35]. There is one molecule at the origin and the other at the bc-face centre position is related to the former by a screw diad parallel to the unique axis of the

structure. The atomic thermal motion was described using an overall isotropic temperature parameter, which was refined to the value 0.12(1)$\overset{o}{A}^2$. A full discussion of the structure refinement is given in reference (35).

5.2   Quasi-elastic neutron scattering in $p-C_6F_4Br_2$

We present here a quasi-elastic neutron scattering study of the $p-C_6F_4Br_2$ system. Two single crystals, cut from the same original specimen, were used. One of these was cooled to 4.2K and then warmed to 300K and the other was not cooled, so that the latter represented a crystal in its 'as grown' state.

A single crystal of $p-C_6F_4Br_2$, of dimensions approximately 6×4×10 mm, was mounted with the a^* and b^* reciprocal axes in the horizontal scattering plane and enclosed in a standard helium cryostat. The measurements were taken on the IN3 triple axis spectrometer at the I.L.L., Grenoble. The monochromator was a pyrolytic graphite crystal scattering from the (002) planes giving neutrons of wavelength 2.36$\overset{o}{A}$, second order contamination being removed by an appropriately oriented graphite filter.

The structural work[35] preceding the present experiment had shown no evidence of a phase transition. The initial aim of the present measurements was therefore to establish the phonon dispersion curves at a temperature of 4.2K. However, when the b^* reciprocal lattice direction was investigated it was found that strong quasi-elastic intensity, about 2% of the (020) Bragg reflection intensity, was present near to the zone boundary. Therefore, further measurements were made at several equivalent b^* zone boundary points in reciprocal space, these points being the $(4,-\frac{1}{2},0)$, $(4,-\frac{3}{2},0)$ and $(2,-\frac{1}{2},0)$. The neutron intensity was monitored on a

Figure 4,2:   Intensity contours for the quasi-elastic scattering

in $p-C_6F_4Br_2$ at 4.2K for three positions in reciprocal

space: $(4,-\frac{1}{2},0)$, $(4,-\frac{3}{2},0)$ and $(2,-\frac{1}{2},0)$. These points

are marked on the diagrams with a cross and the neutron

intensity contour values are marked in thousands of

neutron counts. All three figures have the same monitor

count time.

Figure 4.3a,b,c: Intensity contours around the reciprocal point

$(4,-\frac{1}{2},0)$ for (a) 300K before cooling, (b) at 4.2K and

(c) after warming to 300K from 4.2K. Neutron counts

are marked on the contours in thousands and all ·

figures have the same monitor counts as in Figure

4.2. The axes for (a) and (b) are the same as those

in (c).

Figure 4.4:   Quasi-elastic neutron intensity plotted against the

fractional b^* coordinate for the main peaks in

Figure 4.3b. The two peaks given in Figure 4.3b

(A,B) are marked on this figure also. The monitor

count count for this figure is $\frac{1}{5}$th of that for

Figure 4.3b.

FIG.4·2

FIG.4·4

$(3·97, \eta, 0)$
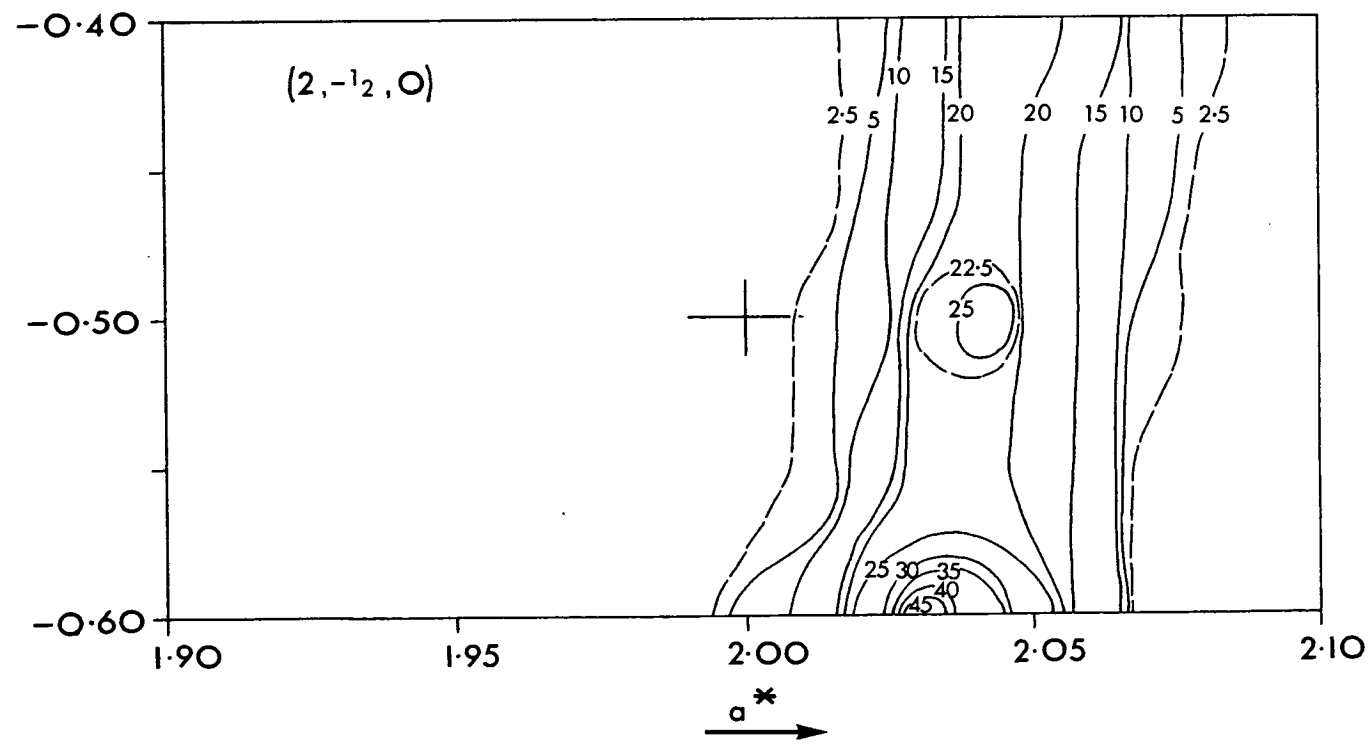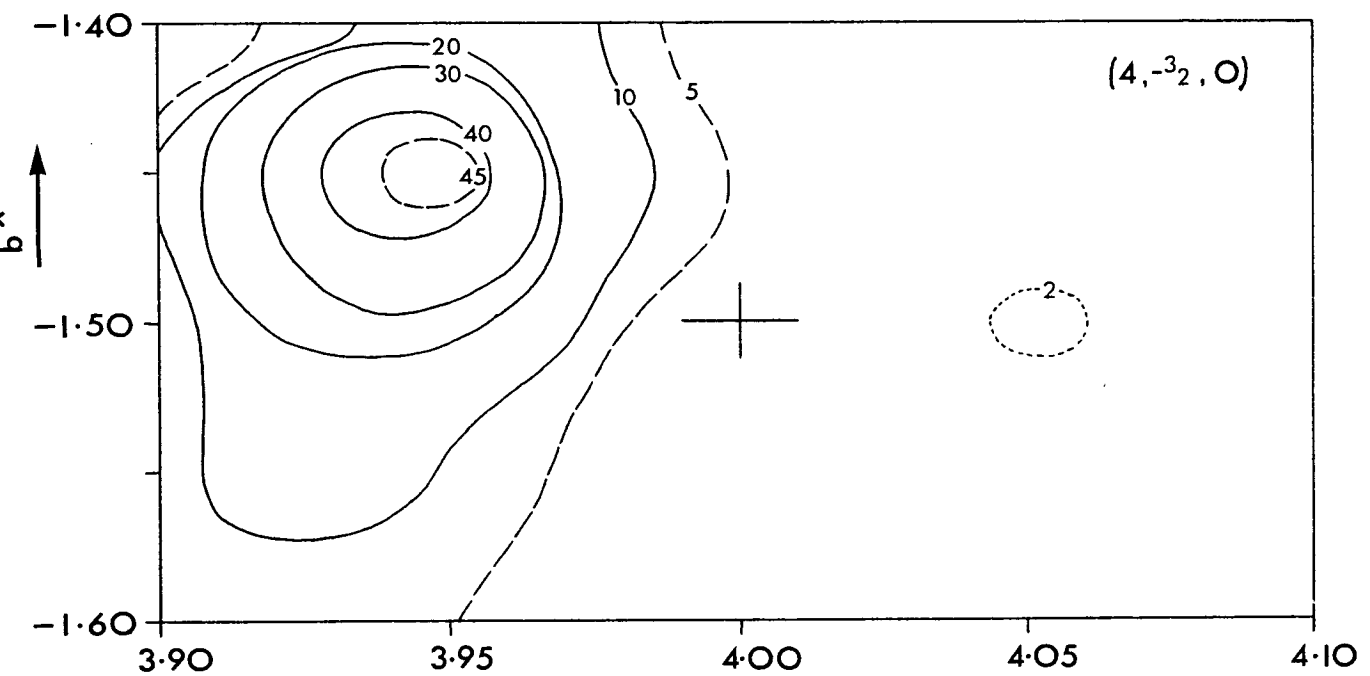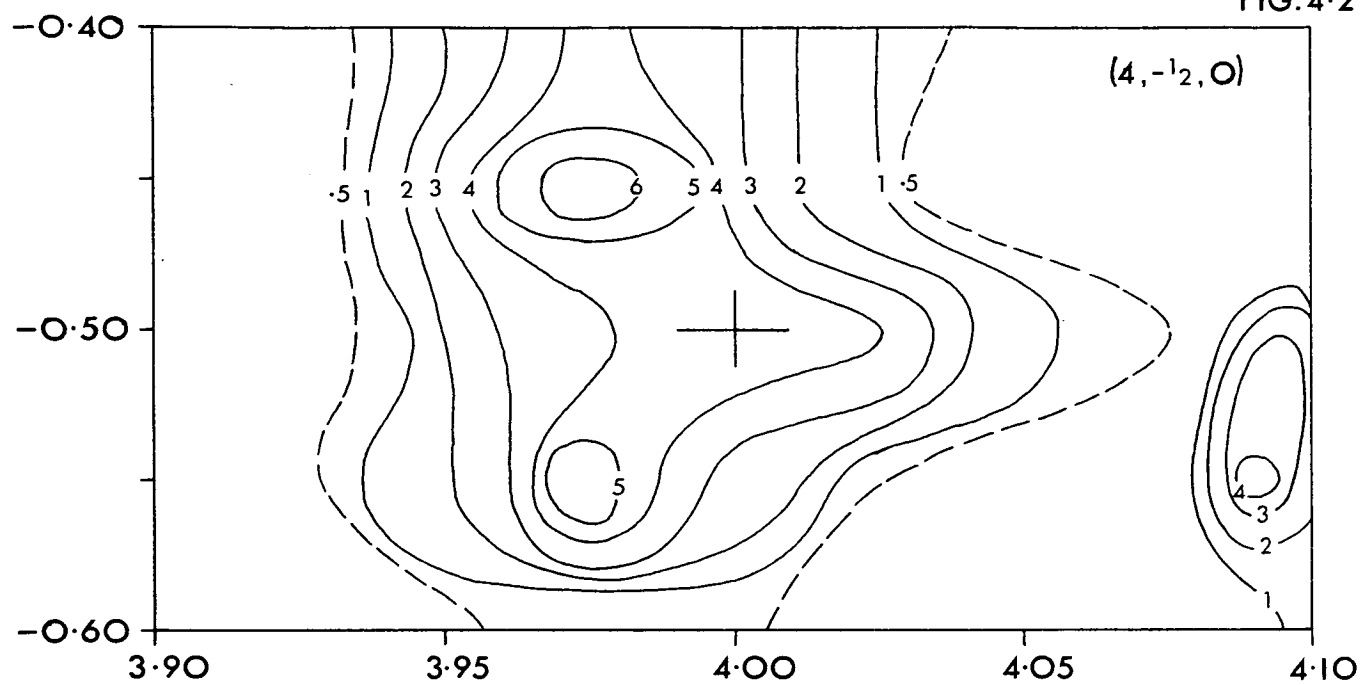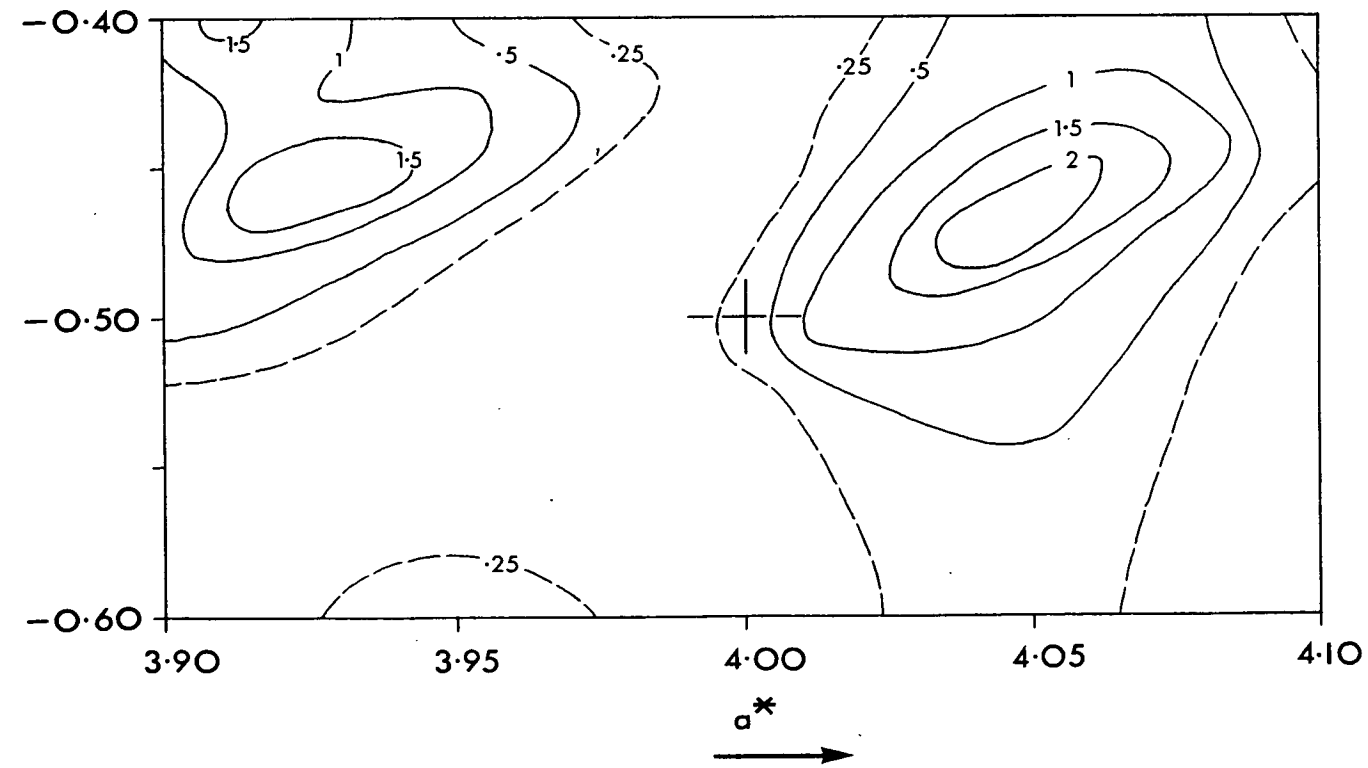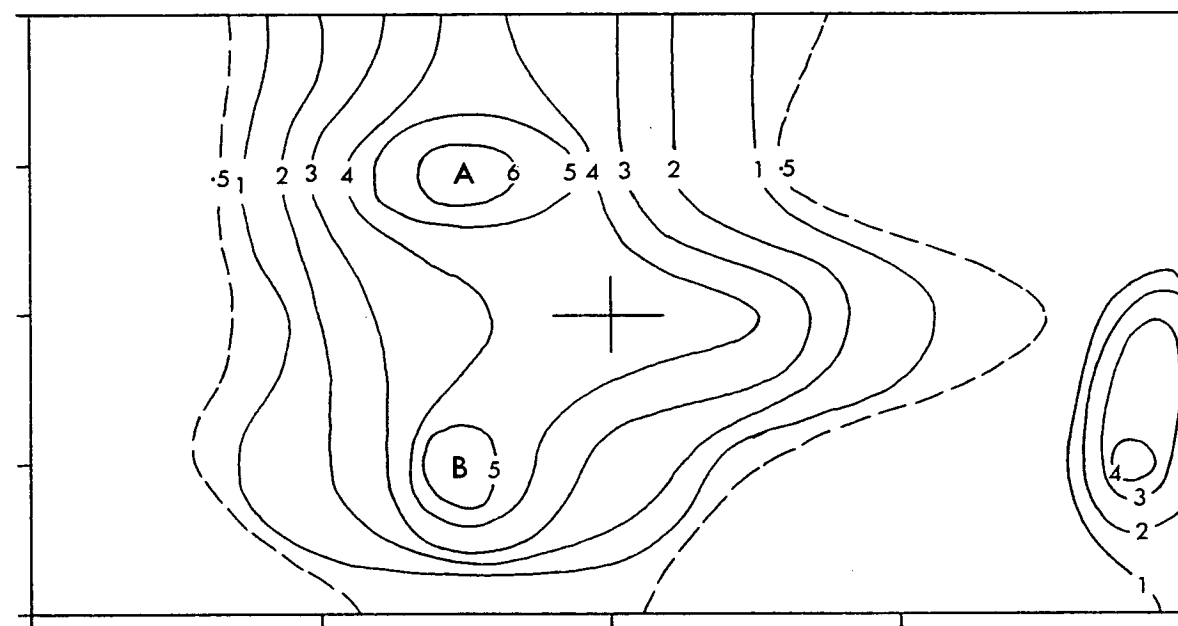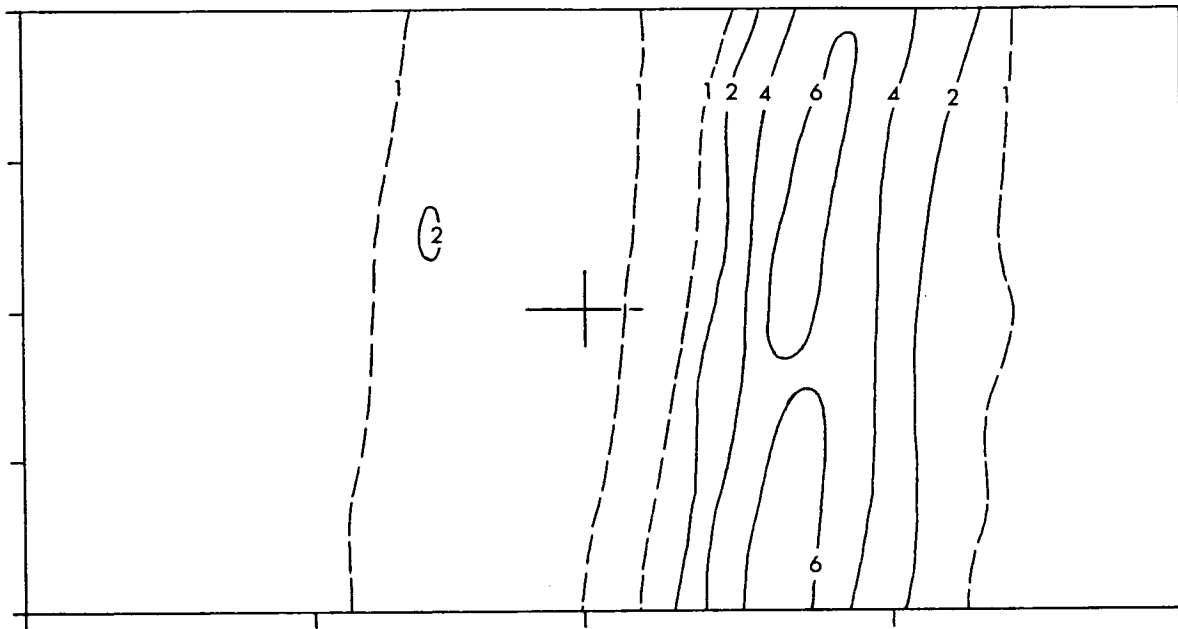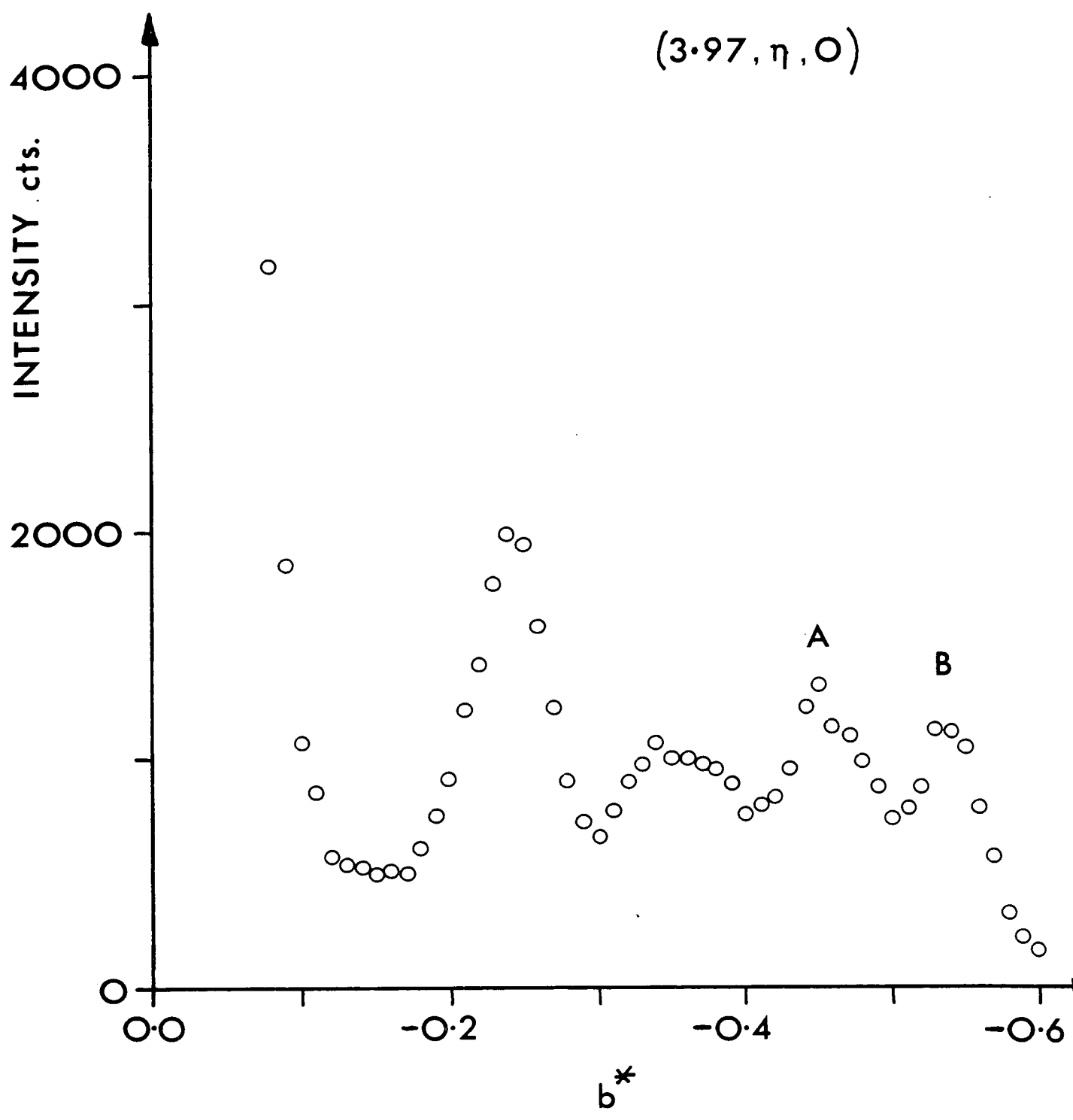
grid of points around these positions. The procedure used for the neutron intensity measurement was first to vary the fractional coordinate along b^* in increments of 0.05, then to step in 0.01 fractional units along a^*, thus forming the grid in the a^*b^* plane. The results of these measurements are given in Figure 4.2 and they show that there is considerable quasi-elastic scattering at 4.2K in the a^*b^* plane. The structure of the scattering appears to be very sharply peaked around the points ($\sim$3.95, -1.45, 0) and ($\sim$2.03, -0.6, 0) and where the scattering around the $(4, -\frac{1}{2}, 0)$ is also peaked but is very much weaker. The temperature variation of this scattering was also studied, but since time was limited only temperatures of 4.2K and 300K were used. This was done for the $(4, -\frac{1}{2}, 0)$ point only and the result of this study is given in Figures 4.3a, b, c, where (a) used the as grown crystal, (b) was the scattering from a crystal at 4.2K and (c) used the crystal in (b) that had then been warmed to 300K.

All the contour maps in Figures 4.2 and 4.3 were made for zero energy transfer and with an energy resolution of 0.17 MeV. Figure 4.4 shows a scan that was made at 4.2K through the main peaks of Figure 4.3b, these having been labelled A, B.

The scattering from the as grown crystal at 300K in Figure 4.3a shows a well defined ridge of intensity parallel to b^*, but this ridge does not contain the point $(4, -\frac{1}{2}, 0)$ exactly. This point is marked in Figures 4.3a, b, c as a cross. There is also in evidence another, weaker ridge, again parallel to b^*, but on the other side of the point $(4, -\frac{1}{2}, 0)$. There is no clear evidence of peaks on this weaker ridge as there is on the other, stronger intensity ridge.

The structure of the quasi-elastic scattering in the a^*b^* plane

changes considerably on cooling, resulting in Figure 4.3b. This
figure suggests that a superstructure has been established and that
the temperature is below that of the phase transition. The measure-
ments displayed in Figure 4.4 show several peaks in the neutron in-
tensity, the first of which occurs at a value equal to $\sim$ 0.24 b^*
and this suggests an incommensurate wavevector of the same value.
The other peaks occur at approximately 0.35, 0.45 and 0.54 b^*. However,
since the point $(4,-\frac{1}{2},0)$ does not lie exactly between the two
peaks in Figure 4.3b and therefore does not lie in the line con-
taining the peaks of Figure 4.4, the superstructure periodicity at
4.2K must involve the a and perhaps the c directions as well.

On warming the specimen from 4.2K to 300K the structure of the
scattering changes again, with the result shown in Figure 4.3c.
This figure is distinctly different from that obtained from a
crystal before cooling. This implies that a superlattice that
may be present at 4.2K is still in evidence at 300K, but its
structure has changed quite substantially, unless such changes
are caused by the thermal expansion of the lattice. Therefore,
the transition to a possible incommensurate structure on cooling
is irreversible, although there may be a change from one super-
lattice to another when the sample is warmed from 4.2K to 300K.

Further evidence for the superlattice at 300K suggested
above is furnished by the existence of a very weak but non-zero
(010) Bragg reflection intensity. This reflection is prohibited
in the accepted $P2_1/c$ structure[35] and considerable care was
taken to ensure that this intensity was not spurious, because it
is strong evidence of a structure where the screw diad symmetry
has been broken. The existence of the weak (010) reflection
means that the crystal symmetry has been changed by varying the

temperature of this system. In order to collect more evidence of a possible phase transition on lowering the temperature, some Raman light scattering measurements have been collected and these are described presently.

The experimental data presented above has been interpreted in terms of an irreversible phase transition to an incommensurate structure on lowering the temperature. It is usual in any phase transition that the intermolecular forces may change and if these forces are of varying range then an incommensurate structure may result. This has been seen to be the case in the examples reviewed in §3, so that such competing forces may not be unlikely to occur in this system. Hence, if the competition between different inter-molecular forces changes on cooling, then we might expect a corresponding change in the external Raman mode spectrum of this system as the temperature is reduced.

The Raman spectra were excited using the 5145Å line of an argon ion laser and measured using the spectrometer arrangement described in Chapter 2, §2. A standard Thor cryostat and temperature controller were also used. The sample used in this Raman experiment was a single crystal cut from the as grown specimen described previously and was of approximate dimensions $2 \times 3 \times 4$ mm. The orientation of the crystal with respect to the incident laser beam was unknown, making a polarisation analysis uninterpretable. The external mode spectra that were measured at several temperatures on cooling are shown in Figure 4.5, the range of frequency shift being 10 cm^{-1} to 120 cm^{-1}. The external mode frequencies are listed for the different temperatures in Table 4.1.

It is clear from these spectra that no unusual external mode

Figure 4.5:   External Raman mode spectra for $p\text{-}C_6F_4Br_2$ at

several temperatures (shown in degrees K) on

cooling. The range of frequency shift is

$10\ cm^{-1}$ to $120\ cm^{-1}$ and each scan is raised by

40×10^3 counts from the preceding one.

Table 4.1:   External mode frequencies (ω_c) for the system

$p\text{-}C_6F_4Br_2$ at the temperatures shown for the

scans in Figure 4.5.

Figure 4.6:   Internal Raman mode spectra for $p\text{-}C_6F_4Br_2$ at

262K and 30K from $120\ cm^{-1}$ to $600\ cm^{-1}$. The

scan at 30K (top) is raised from that at 262K

by 15×10^3 counts.

FIG. 4·5
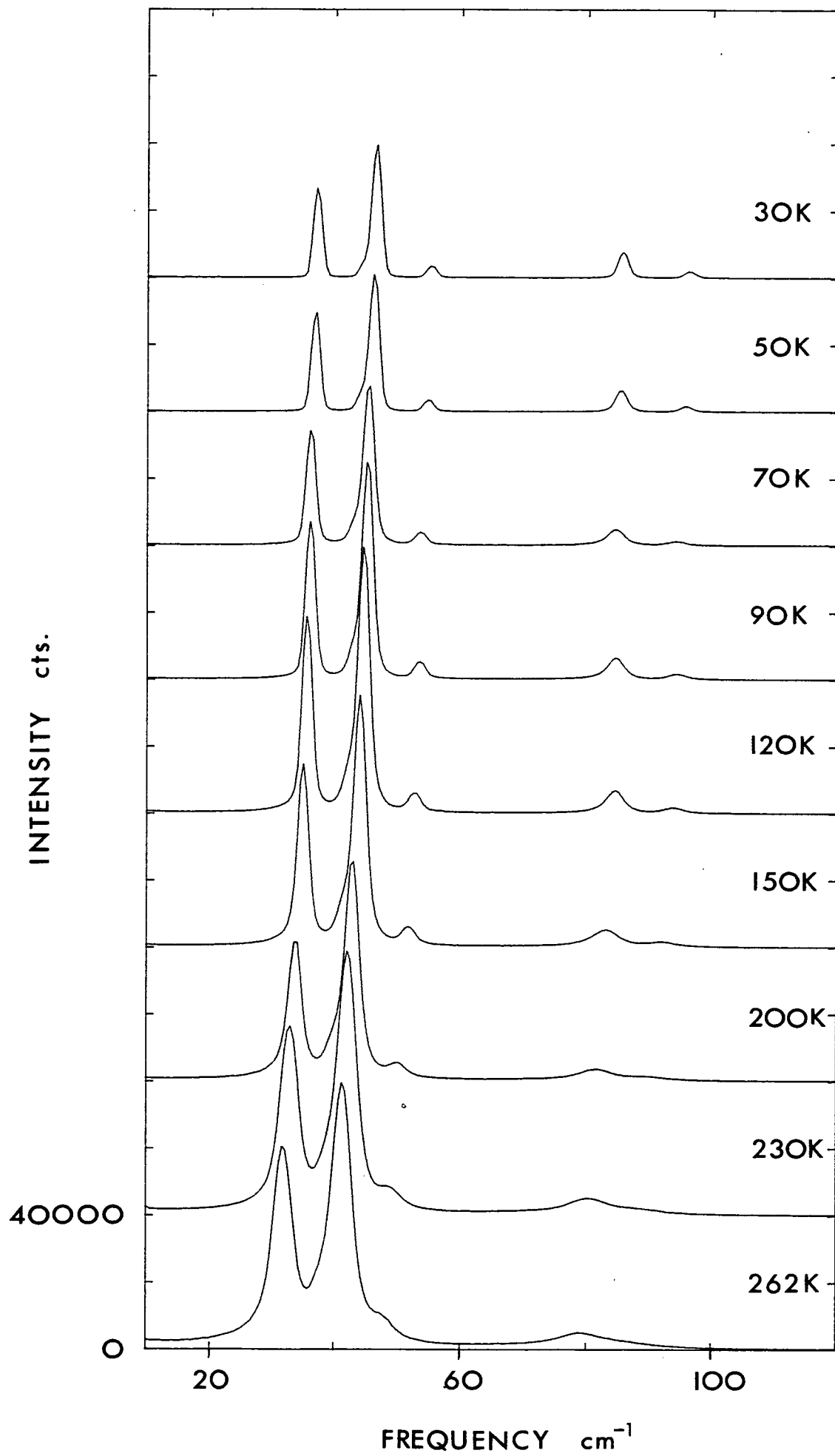
TABLE 4.1

T(K)	ω_c (cm^{-1})	T (K)	ω_c (cm^{-1})
262	31.7	90	35.9
	41.1		45.1
	78.9		53.3
230	32.8		84.4
	42.0		94.4
	∿48.6	70	36.4
	80.3		∿45.7
	∿88.7		54.2
200	33.6		84.9
	42.6		95.2
	∿50.0	50	36.7
	81.3		∿43.4
	∿88.2		∿46.0
150	34.9		54.5
	44.0		85.2
	51.6		95.6
	82.9	30	36.7
	91.7		∿43.5
120	35.4		∿46.0
	44.5		54.5
	52.6		85.2
	84.3		95.6
	93.7		
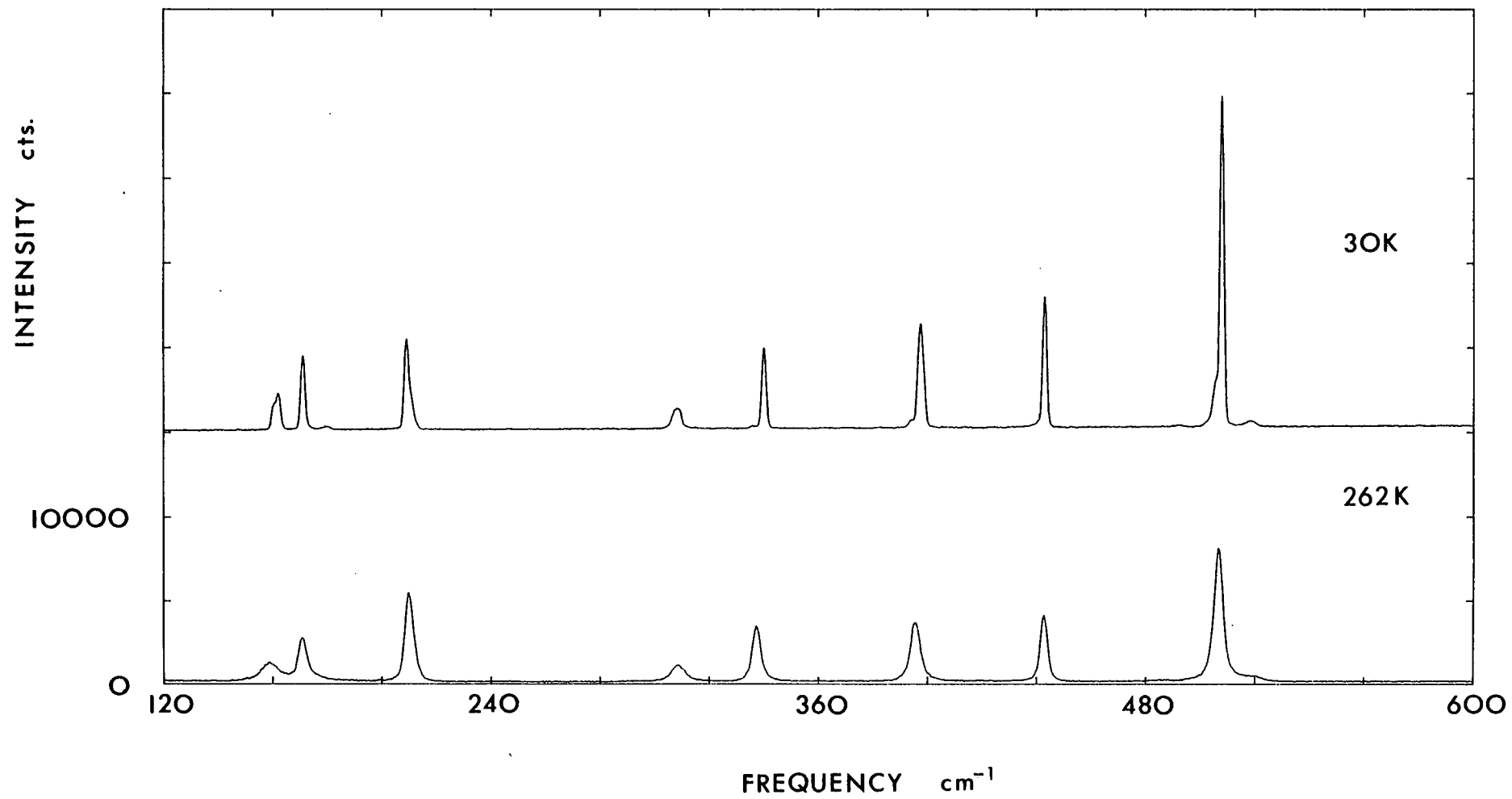
behaviour occurs between 262K and 30K on cooling. The internal mode
spectrum between 120 cm^{-1} and 600 cm^{-1} was also measured on cooling
from 262K and this becomes better resolved at 30K, as is shown by
Figure 4.6, but no dramatic change is evident.

The Raman data that has been described above does not show any
evidence of a phase transition that may have been expected from the
interpretation of the neutron scattering data. Therefore, the change
in the molecular conformation that results in the crystal symmetry
change does not have an appreciable effect on the lattice vibrations
in this system, so that the transition temperature cannot be
estimated from the Raman data given above.

It is interesting to note that the isomorphous crystal structure
of para-diiodotetrafluorobenzene undergoes a phase transition at
about 358K[35] and the closely related crystal structure of para-
dichlorobenzene also has a phase change[37,38]. It may therefore be
expected that $p-C_6F_4Br_2$ may exhibit similar phenomena but the data
presented above does not support this conjecture conclusively.

In order to probe this system further with a view to finding
the source of the quasi-elastic scattering described above, it would
be necessary to use an instrument capable of investigation in three
dimensions, such as a four circle neutron diffractometer. An attempt
at such a three-dimensional investigation has been made by using
X-ray photographic techniques and the results of these studies are
presented next in §5.3.

5.3   X-ray diffuse scattering in $p-C_6F_4Br_2$

Several X-ray photographic techniques have been used in an attempt
to explore reciprocal space with a view to finding the extent of the
extra scattering that was found in the experimental study described

in §5.2. These techniques included the Weissenberg and Precession methods[42] and it is the results of the former that are the clearest and therefore only these are presented. Unfortunately, the quasi-elastic scattering in this system is very weak with X-rays and so the data that are presented are not of the best quality. However, they are sufficiently clear that some qualitative conclusions may be drawn.

One possible reason for the very weak diffuse X-ray intensity observed in this system may be due to the linear absorption coefficient, which has the large value of $\sim$ 155 cm^{-1} for CuK$\bar{\alpha}$ X-radiation. This gives an attenuation of the beam of $\sim$ 79% on passing through crystal of thickness 0.1 mm. (For a crystal 0.5 mm. thick the corresponding attenuation of the incident beam would be 99.96%). A 0.1 mm. diameter crystal, of approximate length 0.2 mm. was used and the method of crystal growth was similar to that described in Chapter 1, §3.3.

The crystal was mounted on an Enraf-Nonius CAD 4 4-circle diffractometer for rapid orientation and the refined unit cell parameters obtained from the resulting orientation matrix were a = 6.097(3)Å, b = 11.352(10)Å, c = 5.514(2)Å and β = 91.88(4)°. The crystal was then mounted on a Weissenberg camera with the direct lattice b-direction as the oscillation axis so that the reciprocal a*c* planes could be photographed. The incident radiation was filtered CuK$\bar{\alpha}$ of wavelength 1.5405Å and the incident beam divergence was 1.5°. The slit width used to separate the layer line screens was 1 mm.

Consecutive half-layer upper level equi-inclination Weissenberg photographs, of exposure times 4 to 9 days, were taken for fractional values of the direct lattice b-parameter equal to $\frac{1}{2}$, $\frac{3}{2}$ and $\frac{5}{2}$.

Orientation control photographs were taken before each reciprocal layer photograph and these indicated that the orientation of the crystal was satisfactorily stable over the very long exposure times used. The results of these photographs have been copied and enlarged and are shown as Figures 4.7 to 4.9. The experimental details for each photograph were the same and each had a long developing time of 12 minutes, 3 to 4 minutes being the normal allowance for this process. The brand of film paper used was Kodak NS-59T crystallographic X-ray film.

The diffuse scattering that is sought is shown as lightly coloured areas (their approximate positions being marked on the overlay of each figure) with diffuse edges, these edges merging with the grey background of the figure. The areas of diffuse scattering are distinguishable by the manner in which they follow definite curves, these being the festoons of the Weissenberg net corresponding to the reciprocal lattice rows. The white, linear streaks on the right hand side of the figures are Bragg scattering from other reciprocal layers that are being intercepted by the sphere of reflection during the exposure. However, there are certain features on the photographs that are not connected with the scattering that is sought. These are described assuming the figures to have their longest dimension vertical and the figure number at the top right corner. There are vertical striations on all of the photographs and having investigated this, it was found that it could be explained by scattering from the capillary tube. Specific features on each photograph include a dark over-exposed spot on the top of the $\frac{1}{2}$-layer photograph, and a similar dark spot on the upper right quarter of the $\frac{3}{2}$ - layer photograph. Both were due to pinholes in the pieces of film used. Also on the $\frac{3}{2}$ - layer photograph is a horizontal white band, this was due to an accidental over-exposure

Figures 4.7 to 4.9:   X-ray diffuse scattering in p-$C_6F_4Br_2$.

The figures 4.7 to 4.9 show, respectively,

the a^*c^* reciprocal planes with direct

lattice parameter values of $\frac{1}{2}$, $\frac{3}{2}$, $\frac{5}{2}$.

They therefore show reciprocal planes

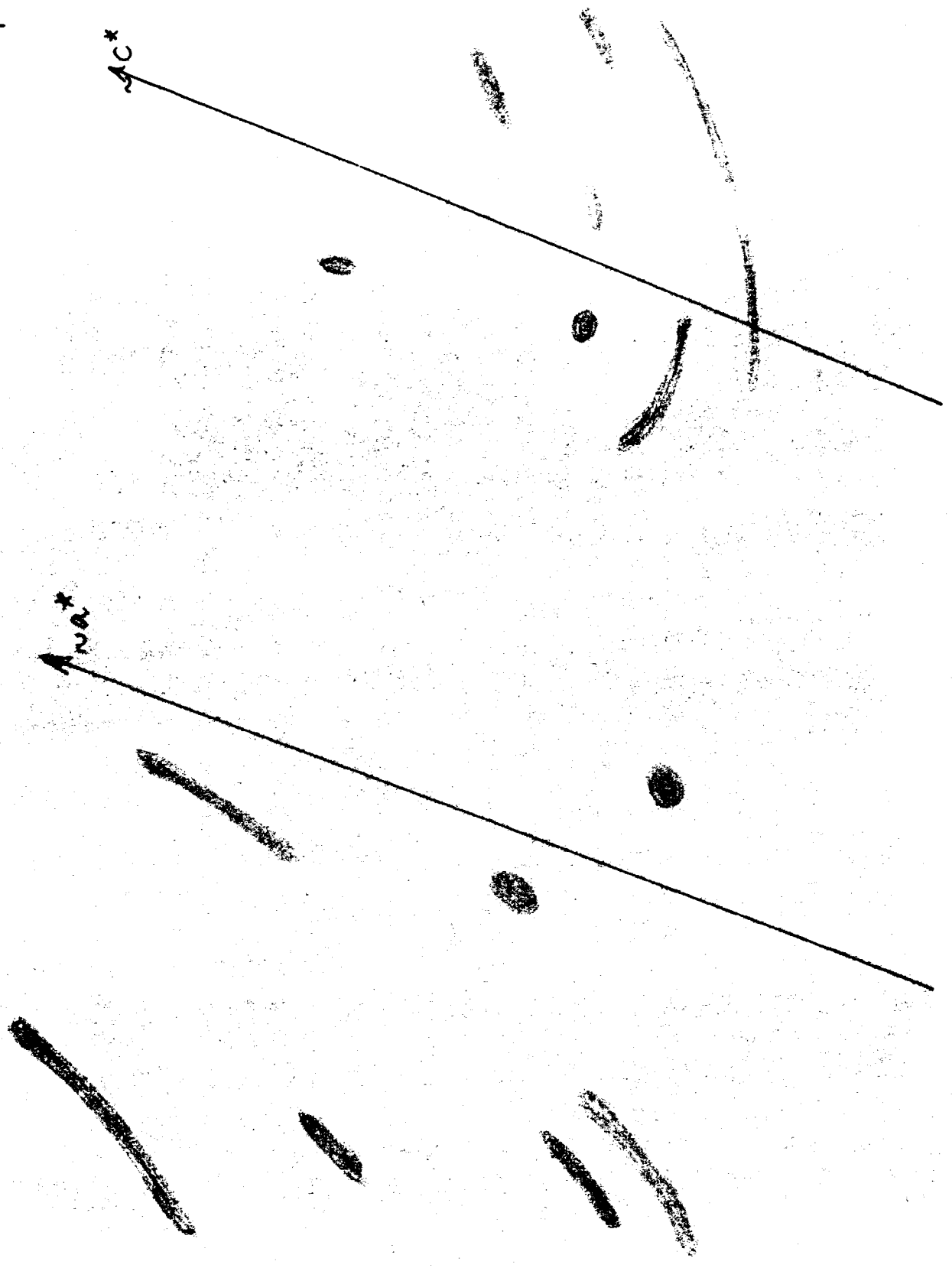with indices $(h,\frac{1}{2},\ell)$, $(h,\frac{3}{2},\ell)$ and
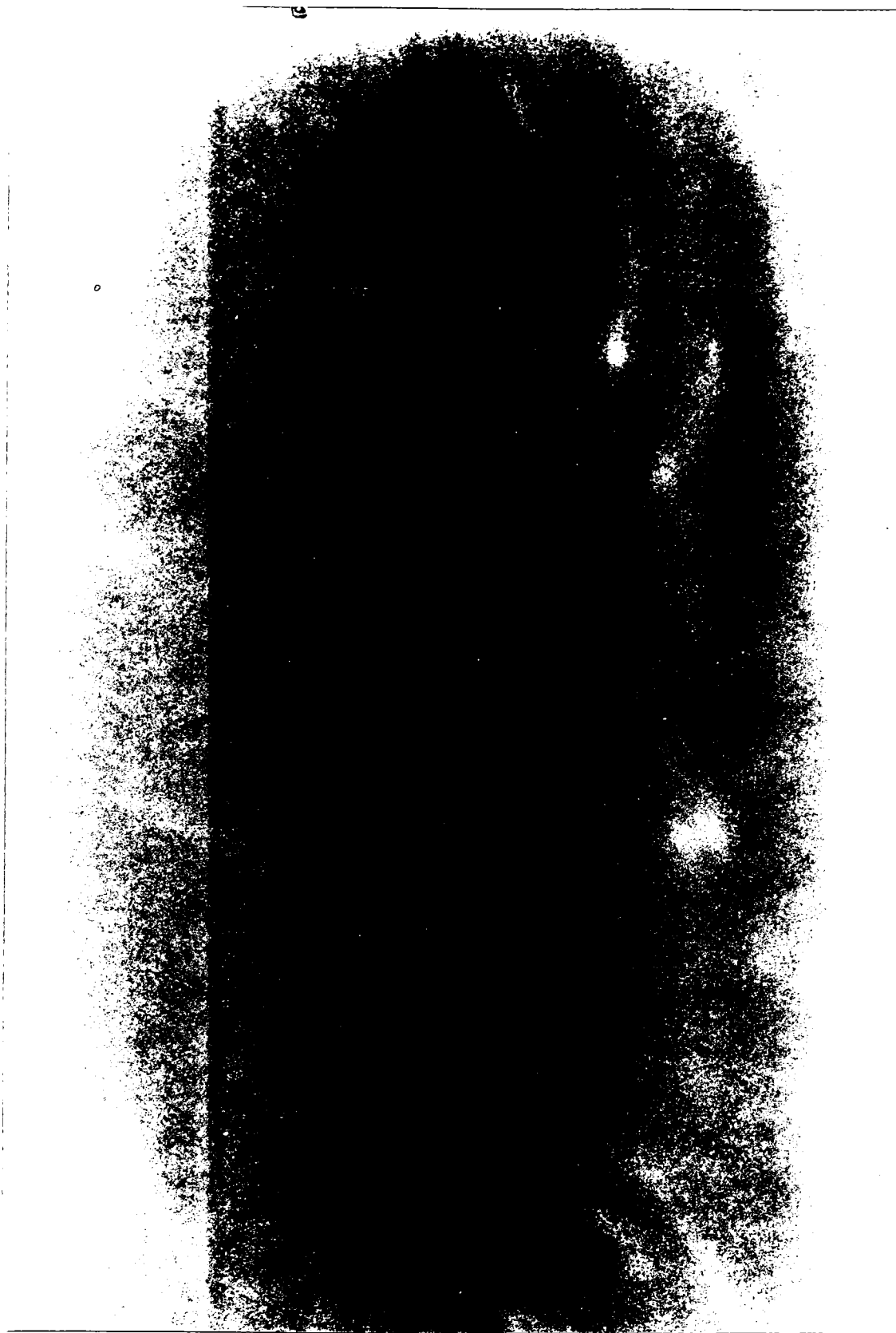
$(h,\frac{5}{2},\ell)$ respectively.
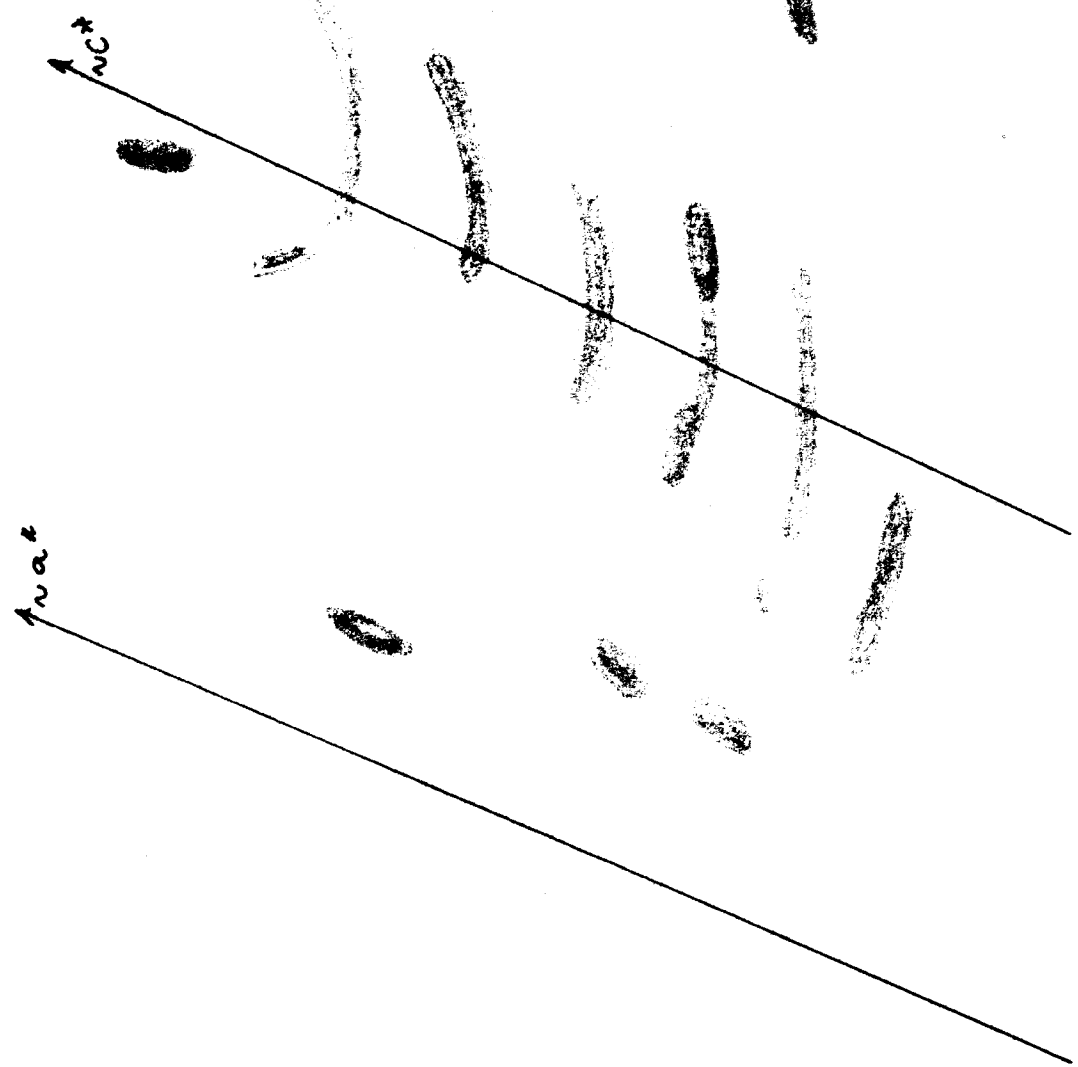
The scattering is very weak and is shown
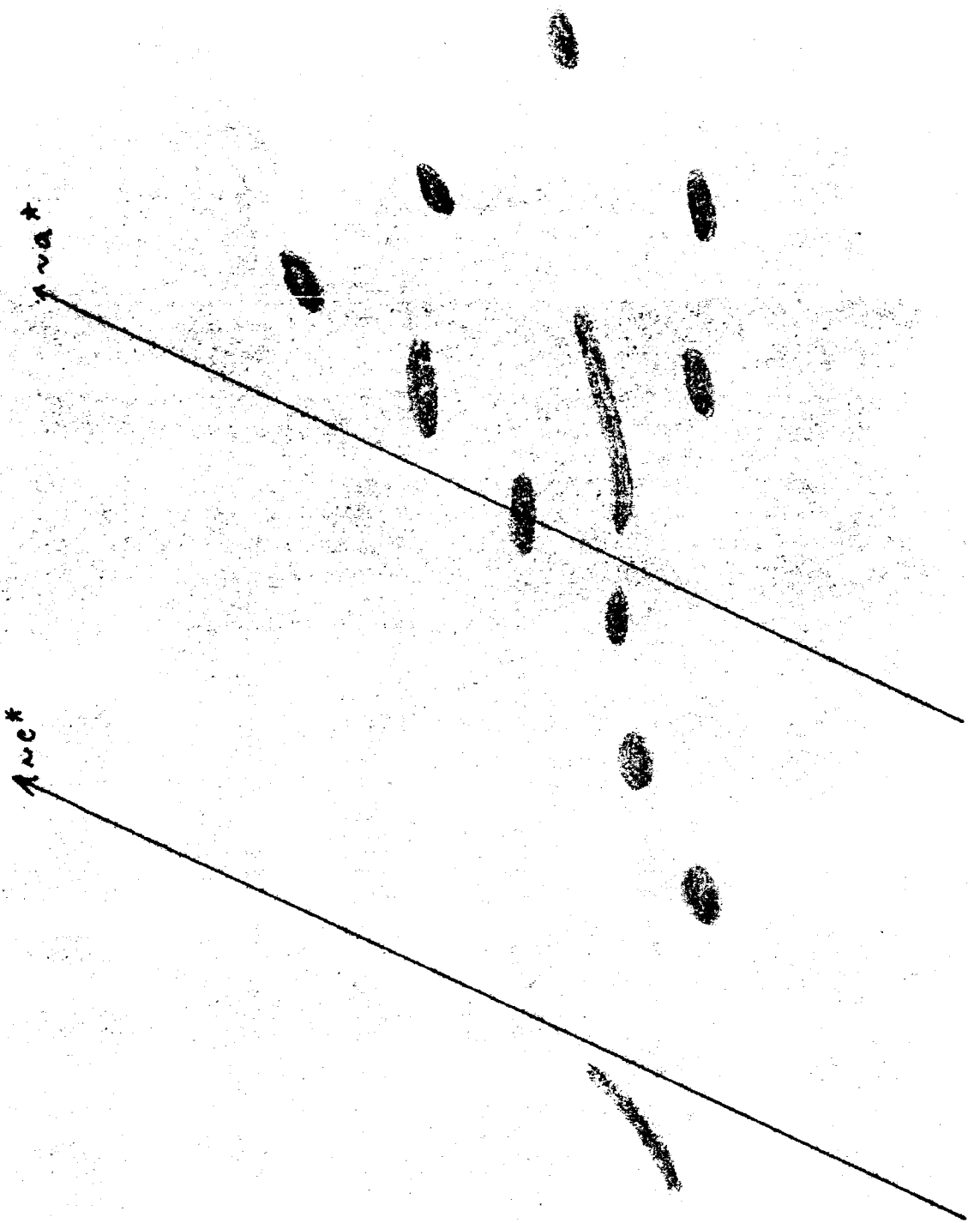
as diffuse white areas on the photographs.

Fig. 4.7

Fig.

Fig. 4.9

of the film whilst the casette was stationary. The $\frac{5}{2}$ - layer photograph shows feint horizontal bands of light colour in the upper half of Figure 4.9, the cause of this is not known. However, despite the poor quality of the photographs the diffuse scattering is visible on all of those shown.

The diffuse scattering of the X-rays is seen to be extensive throughout reciprocal space. From the figures, there is no obvious fine structure to the scattering other than the general trend of lying along the festoons of the Weissenberg net, indicating that the diffuse scattering tends to be parallel to reciprocal lattice rows, as was the case with the neutron scattering data.

5.4   Conclusions

The neutron scattering data presented in §5.2 shows the presence of strong quasi-elastic intensity whose structure changes both on cooling and on subsequent warming. At 4.2K an incommensurate wave-vector of $\sim 0.24b^*$ is suggested, although this may involve the other reciprocal directions as well. No lock-in transition is observed but the incommensurate transition is seen to be irreversible because the strong quasi-elastic scattering persists on warming to 300K, although the superlattice may have changed.

The structure of the scattering due to an incommensurate lattice distortion is usually in the form of satellite reflections, as we have seen in §3 where several examples were reviewed. In the case of thiourea the high order of incommensurability enabled the authors[13] to measure satellite reflections up to fourth order, giving a very accurate measure of the incommensurate wavevector and also of the commensurate wavevector at the lock-in transition. In the present case from Figure 4.4, it is seen that several peaks are visible at

different wavevectors but their relative intensities suggest that they are not simply harmonics of the primary lattice distortion. Also, the wavevectors of the peaks in Figure 4.4 are not simple multiples of some fundamental wavevector, so that it is difficult to come to a firm conclusion about the nature of these peaks.

Further evidence for structural changes is indicated by the presence of the prohibited (010) reflection on warming from 4.2K. This observation suggests that the structure of this system has lost the screw diad symmetry that is present in the as grown structure. Since the Raman data collected on cooling from 262K to 30K has shown no evidence of a phase transition, it may be possible to determine the transition temperature by monitoring the (010) reflection intensity on cooling and warming. This intensity will indicate the degree to which the molecular conformation departs from the accepted $P2_1/c$ structure[35], such that the space group may become $P2/c$, for instance, when this system is warmed after cooling to low temperatures.

The X-ray photographs that have been displayed in Figures 4.7 to 4.9 have had abnormally long exposure times using very sensitive X-ray film. Therefore, spurious photographic processes, called edge effects, may cause distortions and non-uniformities when very weak images are photographed. In the present work, the X-ray diffuse scattering is seen to be very weak, even with the exposure times used, so that these spurious effects may become important. However, the diffuse areas sought on the photographs appear to lie on the festoons of the Weissenberg net and it is therefore believed that these areas represent real scattering. This is evidence that the structure of the scattering lies parallel to the reciprocal lattice rows, a similar result to that found with the neutron scattering data. However, the X-ray diffuse scattering is too faint to be able to

identify positions where the intensity peaks, as was possible with the neutron data.

Concerning the source of the data given in §5.3, temperature diffuse scattering is not uncommon in organic molecular crystals (see, for example, references (43) to (46)) and so the diffuse scattering observed at room temperature in the $p-C_6F_4Br_2$ system may be partly due to temperature effects. Certainly, for low temperatures any thermal motion would be expected to be very small and so that mechanisms other than temperature effects become important contributors to the quasi-elastic scattering observed at 4.2K with neutrons.

In order to find whether there are large atomic mean square displacements in this system at 300K further experiments are necessary. The structural work[35] preceding the measurements described in §5.3 used isotropic thermal parameters in the refinements using neutron powder data. However, it is doubtful whether the data used was of sufficient accuracy to allow the refinement of anisotropic thermal parameters. Single crystal diffractometry will usually give sufficiently accurate integrated intensity data in order that anisotropic thermal parameters may be refined, contrary to the case of powder diffraction data that usually has a more limited amount of information to be extracted.

Therefore, in order to determine which of an anisotropic or isotropic temperature factor model will give a realistically better fit to diffraction data from the $p-C_6F_4Br_2$ system, a single crystal X-ray experiment could be done at 300K to measure very accurate integrated intensities. Thus, we would have an accurate measure of the thermal motion in this system at 300K and therefore the source of the X-ray diffuse scattering may become clearer.

The experimental data presented in this chapter suggests an

incommensurate phase, of wavevector $\sim 0.24b^*$, for the $p\text{-}C_6F_4Br_2$
system using neutron quasi-elastic scattering. The transition is
irreversible on cooling and the extra scattering persists to room
temperature, although its structure has changed. X-ray diffraction
data shows the presence of extensive diffuse scattering in reciprocal
space at 300K, which may be due, in part, to temperature effects.
Suggestions for future experiments have been made in order to eluci-
date the sources of the extra scattering, as well as the transition
temperature on cooling and warming. It is believed that this system
needs more time and research to be able to come to firm conclusions
concerning the extra scattering that is observed at various tempera-
tures.

REFERENCES FOR CHAPTER 4

(1)   See for example, Chandrasekhar: "Liquid Crystals".
            Ed. Woolfson, M.M., Ziman, J.M.; Cambridge Univ. Press.

(2)   Timmermans, J., J. Chem. Phys., 18 1 (1961.

(3)   Andrew, E.R., idem, 18, 9 (1961)

(4)   Powles, J.G., idem, 18, 17 (1961).

(5)   Dunning, W.J., idem, 18, 21 (1961).

(6)   Moncton, D.E., Axe, J.D., Shirane, G., Phys. Rev. Letters,
            34(12), 734 (1975).

(7)   Axe, J.D., Conference on Neutron Scattering, Gatlinburg (1976),
            pp. 362-367.

(8)   See for example; Koehler, W.C.: "Magnetic Properties of Rare
            Earth Metals", Elliot, R.J. editor. Plenum, New York,
            1972, pp. 81-128.

(9)   Overell, J.S.W., Mackenzie, G.A., Pawley, G.S., Fitzgerald, W.J.,
            Kirin, D., Chem. Phys. Letts. (1980) 74(2), 373.

(10)   Iizumi, M., Gesi, K., Sol. State Comm., 32, 37 (1977).

(11)   Iizumi, M., Axe, J.D., Shirane, G., Shimaoka, K.,
            Phys. Rev. B15, 4392 (1977).

(12)   Cailleau, M., Moussa, F., Mons, J., Sol. State Comm. 31, 521 (1979).

(13)   Moudden, A.H., Denoyer, F., Lambert, M., Fitzgerald, W.J.,
            Solid State Comm. 32, 933 (1979).

(14)   Wilson, J.A., DiSalvo, F.J., Mahajan, S., Adv. in Phys. 24, 117 (1975).

(15)   Cailleau, H., Moussa, F., Zeyen, C.M.E., Bouillot, J.,
            Solid State Comm. 33(4), 407 (1980).

(16)   Cailleau, H., Baudour, J.L., Meinnel, J., Dworkin, A., Moussa, F.,
            Zeyen, C.M.E., Farad. Gen. Disc., 69 (1980).

(17)   Iizumi, M., Axe, J.D., Shirane, G., Shimaoka, K., Bull. Am. Phys.
            Soc. 21, 292 (1976).

(18)   Charbonneau, G.P., Delugard, Y., Acta Cryst. B33, 1586 (1977).

(19)   Bree, A., Edelson, M., Chem. Phys. Letts., 46, 500 (1977).

REFERENCES FOR CHAPTER 4 (Contd.)

(20) Baudour, J.L., Delugard, Y., Caillean, H., Acta Cryst. B32, 150 (1976).

(21) Baudour, J.L., Cailleau, H., Yelan, W.B., Acta Cryst. B33, 1773 (1977).

(22) Cailleau, H., Baudour, J.L., Zeyen, C.M.E., Acta Cryst. B35, 426 (1979).

(23) Cailleau, H., Girard, A. Moussa, F., Zeyen, C.M.E.,
          Solid State Comm. 28, 259 (1979).

(24) Bastiansen, O., Acta Chem. Scand. 3, 408 (1949).

(25) Hüller, A., Press, W., Phys. Rev. Lett. 26, 266 (1972).

     Press, W., Hüller, A., Phys. Rev. Lett. 30, 1207 (1973).

     Press, W., Hüller, A., Stiller, H., Stirling, W., Currat, R.,
          Phys. Rev. Lett. 32, 1354 (1974).

(26) Overhauser, A.W., Phys. Rev., 167, 691 (1968).

(27) Kohn, W., Phys. Lett. 2, 393 (1959).

(28) Goldsmith, G.J., While, J.G., J. Chem. Phys. 31, 1175 (1959).

(29) Cowley, R.A., Bruce, A.D., Murray, A.F., J. Chem. Phys. 11, 3591 (1978)

(30) Aubry, S., Proc. of the Symposium on "Non-Linear Structure and
          Dynamics in Condensed Matter", Oxford, England,
          27-29 June, 1978. Springer Verlag.

(31) Terauchi, H., Takenaka, H., Shimaoka, K., J. Phys. Soc. Japan,
          39, 435 (1975).

(32) Moudden, A.H., Denoyer, F., Lambert, M., J. Phys. 39 (12), 1323 (1978)

(33) Bak, P., Emery, V.J., Phys. Rev. Letts. 36 (16), 978 (1976).

(34) Shirane, G., Axe, J.D., Phys. Rev. Letts. 27, 1803 (1971).

(35) Pawley, G.S., Mackenzie, G.A., Dietrich, O.W.,
          Acta Cryst. (1977), A33, 142.

(36) Goldstein, H., "Classical Mechanics" (1959), Reading,
          Massachusetts: Addison-Wesley.

(37) Housty, J., Clastre, J., Acta Cryst. (1957) 10, 695.

(38) Reynolds, P.A., Kjems, J.K., White, J.W., J. Chem. Phys.
          (1972), 56, 2928.

REFERENCES FOR CHAPTER 4 (Contd.)

(39) Green, J.H.S., Harrison, D.J., Spectroehim Acta (1977), $\underline{33A}$, 193.

(40) Gerritsen, Koopmans, Roltema, Maclean, J. Mag. Res. (1972)
      $\underline{8}$(1), 20.

(41) See Chapter 3, references (7, 8).

(42) See for example: Henry, N.F.M., Lipson, H., Wooster, W.A.
      "The Interpretation of X-ray Diffraction Photographs"
      (1961) MacMillan and Co. Ltd., N.Y.

(43) Lonsdale, K., Smith, H., Proc. Roy. Soc. (1942), $\underline{54}$, 314.

(44) Lonsdale, K., Robertson, J.M., Woodward, I., Proc. Roy. Soc.
      (1941), A$\underline{178}$, 43.

(45) Lonsdale, K., Rep. Phys. Soc. Progr. Phys. (1942-3), $\underline{9}$, 256.

(46) Lonsdale, K., Proc. Phys. Soc. (1942), $\underline{54}$, 314.

LIST OF PUBLICATIONS

"Transitions in the benzene-fluorobenzene system";

   Mackenzie, G.A., Overell, J.S.W., Pawley, G.S.,

   Solid State Commun. (1979) 31, 431.

"Incommensurate phase of the molecular crystal p-$C_6F_4Br_2$";

   Overell, J.S.W., Pawley, G.S., Mackenzie, G.A., Fitzgerald, W.J.

   Kirin, D.,

   Chem. Phys. Letts. (1980) 74, 373.

"Powder refinement of carbonyl sulphide";

   Overell, J.S.W., Pawley, G.S., Powell, B.M.

   Submitted to Acta Cryst., 1981. *(now accepted, 23/9/81)*

"An X-ray single crystal study of the system $C_6F_6 \cdot C_6D_6$";

   Overell, J.S.W., Pawley, G.S.

   Submitted to Acta Cryst., 1981.

TRANSITIONS IN THE BENZENE–FLUOROBENZENE SYSTEM

G.A. Mackenzie, J.S.W. Overell and G.S. Pawley

Physics Department, University of Edinburgh, King's Buildings, Mayfield Road, Edinburgh EH9 3JZ, Scotland, U.K.

The Raman spectra of $C_6H_6 \cdot C_6F_6$ and $C_6D_6 \cdot C_6F_6$ between helium temperature and melting are analysed for evidence of phase transitions. Such evidence appears about 170 K on cooling and 200 K on warming, and indicates a transition in a temperature range that shows no thermal or NMR anomaly. No spectral changes occur where these two techniques give anomalies. Future structural experiments are suggested.

BENZENE AND FLUOROBENZENE are both liquids above about 6°C but when they are mixed together in equal molecular proportions, a solid is formed. This solid has a texture very similar to cyclohexane in its plastic phase, and a plastic to crystalline transition is therefore expected at reduced temperatures. The structure of the mixture is not known at any temperature, and the X-ray investigation made near room temperature by Small [6] showed virtually no diffraction pattern. This is consistent with this phase being "very plastic", having a small entropy of fusion like cyclohexane rather than having a larger entropy of fusion like adamantane [7].

Differential scanning calorimetry measurements on $C_6H_6 \cdot C_6F_6$ have already been done by Brennan et al. [3]. The standard procedure of their work was to warm the material up from a low temperature and record the thermal anomalies. No anomaly was observed from 90 K upwards until 249 K was reached. At this temperature an anomaly was found with all the samples they used, and two more anomalies were found before the melting point at 297 K. These other two anomalies were not reliably reproducible and were attributed to melting of small pockets of the two eutectic mixtures which occur at approximately 14/86 and 86/14 molecular ratios. Brennan et al. give accurate values for concentrations and temperatures, leaving no doubt that a transition was observed at 249 K on warming and 246 K on cooling.

Nuclear magnetic resonance measurements by Gilson and McDowell [4] on the same material show no effects in the temperature range of the thermal anomaly. However NMR line broadening takes place on cooling between 150 and 90 K, but it is not uncommon for NMR linewidths to change at temperatures where no thermal anomaly exists.

Other techniques must be brought to bear on this subject. The present work is the study of the Raman scattering spectra and in the future we hope to study the structure by diffraction methods.

1. RAMAN SPECTRUM MEASUREMENTS

The samples of $C_6H_6 \cdot C_6F_6$ and $C_6D_6 \cdot C_6F_6$ were prepared by mixing equal molar quantities of the two constituents. The resulting mixtures were sealed in glass tubes 11 mm long and 0.9 mm in diameter which could be mounted in a Thor Cryogenics cryostat. Cooling was achieved by the flow of helium or nitrogen gas depending on which temperature range was being investigated. The temperature of the sample was measured by a GaAs diode and controlled by a Thor 3010 temperature controller which was connected to a heater close to the sample.

The spectra were excited using the 676.6 nm line of a krypton ion laser and measured on a Coderg T-800 triple grating monochromator with on-line computer control and data acquisition [1]. The laser beam was focussed on the sample and the light scattered at 90° was collected in the spectrometer. Since the sample was a powder, the scattered light was completely depolarised so that it was impossible to separate the modes of different symmetry by polarisation analysis.

The powder formed by freezing the liquid sample does not necessarily have a random distribution of crystallite orientations. Preferred orientation in the powder can cause spectra of some polarisations to be scattered more intensely than others, although the light emerging from the sample is depolarised. This is similar to the problem of preferred orientation in powder diffraction [2].

We have found that the same sample can give different relative intensities in the Raman spectrum at a particular temperature if the powder is melted then re-frozen causing a different arrangement of crystallites.

In the present work we have compared relative intensities of Raman peaks at different temperatures. The spectra were recorded using the same powder in each case so that the polarisation effects described above may be assumed to be the same for each spectrum.
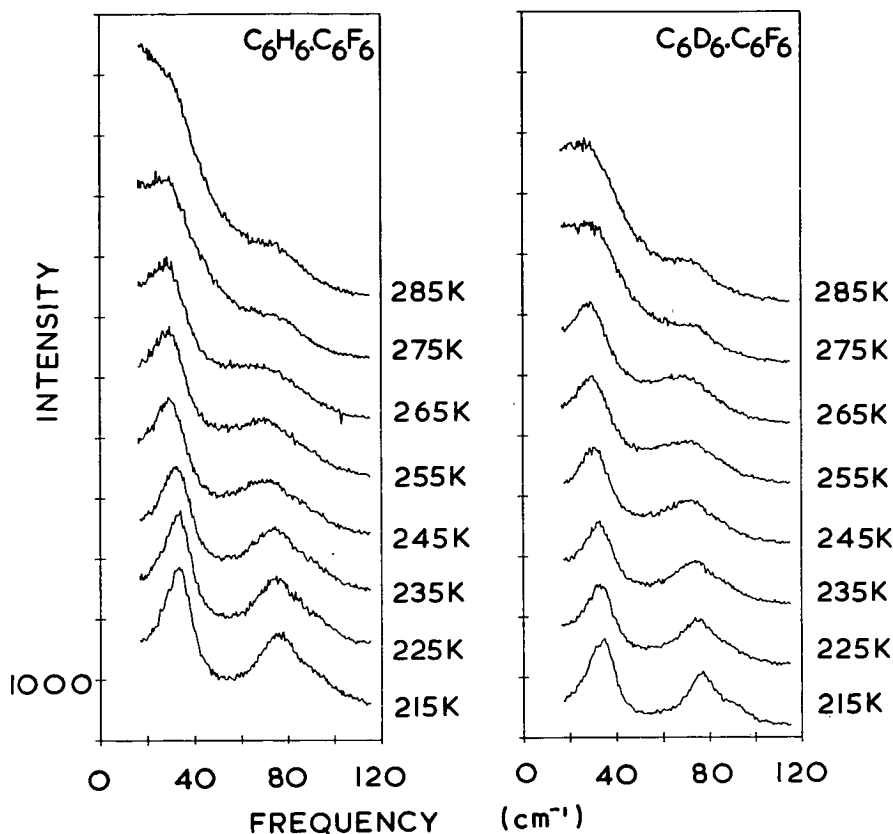
Fig. 1. The external mode spectrum in $C_6H_6 \cdot C_6F_6$ and $C_6D_6 \cdot C_6F_6$ on warming from 215 K (bottom scan) to 285 K (top scan) in 10° intervals. Each set of scans are on the same scale, with the zero level raised by 1000 counts between each scan.
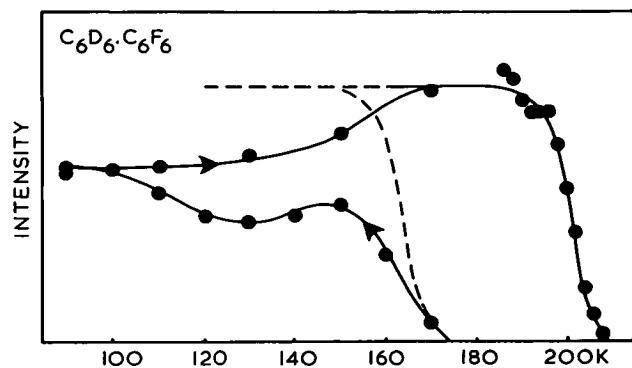

Fig. 2. The intensity of the peak at 59.5 cm^{-1} for $C_6D_6 \cdot C_6F_6$ as a function of temperature, measured on cooling to 90 K followed by warming. The sequence is indicated by the arrows.

First we look for evidence of the transition at 249 K. Figure 1 shows the Raman scattering from 16 cm^{-1} (just above the plasma line) to 120 cm^{-1} in the temperature range 215–285 K. The samples were first cooled, and measurements were made on warming. Two specimens were used, (a) $C_6H_6 \cdot C_6F_6$ and (b)

$C_6D_6 \cdot C_6F_6$. From the figure it is clear that no sharp transition is observable, the peaks at 34 and 77 cm^{-1} gradually decrease in intensity as they shift slightly to lower frequencies and broaden while the scattering about the exciting line increases in intensity and also broadens. No evidence of these two peaks occurs in the scattering from the liquids. These scans are featureless and have been omitted.

Dramatic changes do take place at lower temperatures. On cooling the $C_6D_6 \cdot C_6F_6$ sample to 170 K a new peak appears on the spectrum — in fact the spectrum changes in more ways than one, but the new peak at 59.5 cm^{-1} can be used as an indication of the change. The area under this peak as a function of temperature has been measured with a planimeter, and the intensity thus measured was found to increase as the temperature was reduced. This area has been plotted against temperature in Fig. 2, where the solid line with the arrow indicator shows the time sequence of the measurements. At the lower temperatures it became increasingly difficult to decide on what background to subtract from under this peak. Furthermore some structure developed in the peak, making a reliable area measurement
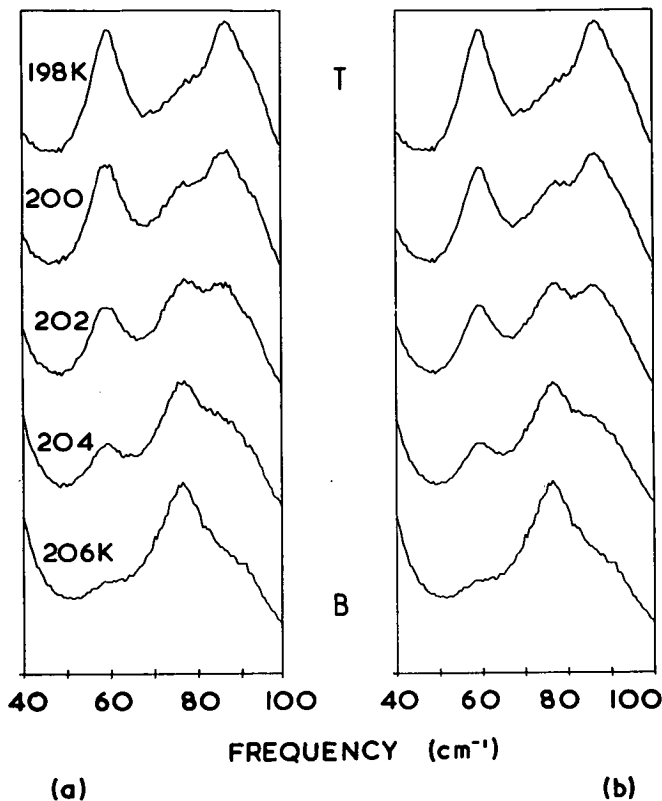
Fig. 3. External mode scans for $C_6D_6 . C_6F_6$ obtained on warming. (a) Top scan (T) at 198 K, next three scans at 200, 202 and 204 K, bottom scan (B) at 206 K. (b) Scans made from T and B, from top to bottom: T, (3T + B)/4, (T + B)/2, (T + 3B)/4, B.

Fig. 4. The external mode spectra at 6 K for $C_6H_6 . C_6F_6$ and $C_6D_6 . C_6F_6$. This shows a complexity not consistent with a simple crystal structure.

impossible. However a pattern of results emerged indicating that completion of the transition did not take place until about 100 K.

Each measurement in Fig. 2 was taken about 5 min after the thermocouple near to the sample indicated stability. The change in intensity was very rapid following the temperature change, and in a few cases where the scan was repeated after an extra 10 min of equilibration time, no significant subsequent changes were apparent. Clearly the state of the sample was not equilibrium on cooling, as a comparison with measurements taken at the same temperatures on warming demonstrate, but, following comparison with measurements made on warming from 6 K, we think that saturation of the transition occurs on cooling to about 100 K. A similar but not so clear result was obtained for $C_6H_6 . C_6F_6$.

The upper curve of Fig. 2 was obtained by warming, showing a transition centred on 201 K. We are satisfied that this shows a complete change in the spectrum between 190 and 210 K, as Fig. 3 demonstrates. This figure shows scans made after the measurements of Fig. 2, as the sample was warmed from 6 K. From top
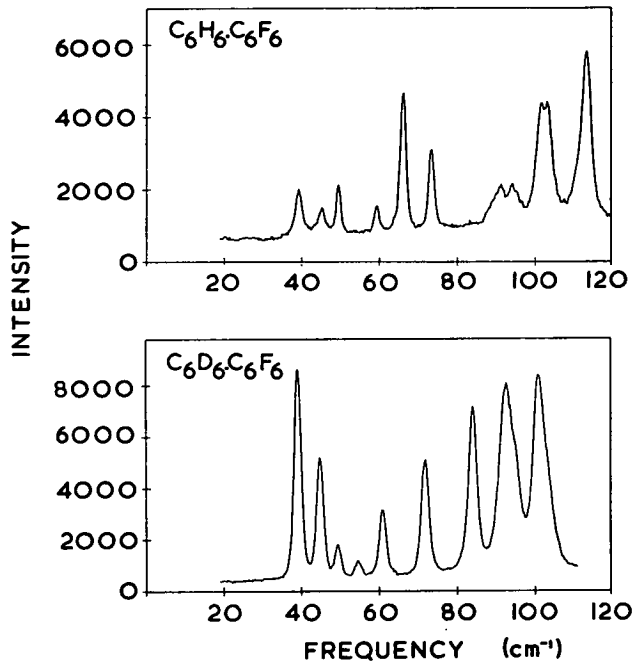
to bottom of Fig. 3(a) the scan temperatures were 198, 200, 202, 204 and 206 K. Figure 3(b) has been constructed from the top scan (T) and the bottom scan (B) of Fig. 3(a). From top to bottom the scans are T, (3T + B)/4, (T + B)/2, (T + 3B)/4, and B. These correspond so closely to the scans of Fig. 3(a) that the proportions of each phase present at these temperatures can be deduced.

The hysteresis of about 29° in this transition is so much greater than that found by the thermodynamic measurements at 249 K that we must deduce that the different techniques are sensing different phenomena. One would hope to observe a curve in Fig. 2 similar to the broken line, which suggests a hysteresis of as much as 36°. Part of the deviation of the measurements from this line is due to the difficulty of interpreting the scans, but some other reason must be sought for the discrepancy between the measurements on warming and on cooling between 150 and 110 K. This may well be due to the continued existence of frozen pockets of eutectics which eventually transform by 100 K. There is a small deuteration effect in these measurements, the results on using samples of $C_6H_6 . C_6F_6$ gave temperatures for the transition about 4° higher, with a very similar hysteresis effect.

No major change in the Raman scattering occurs between 150 and 90 K, the region of the NMR linewidth change, though it should be pointed out that this is the range in which the transition probably saturates on
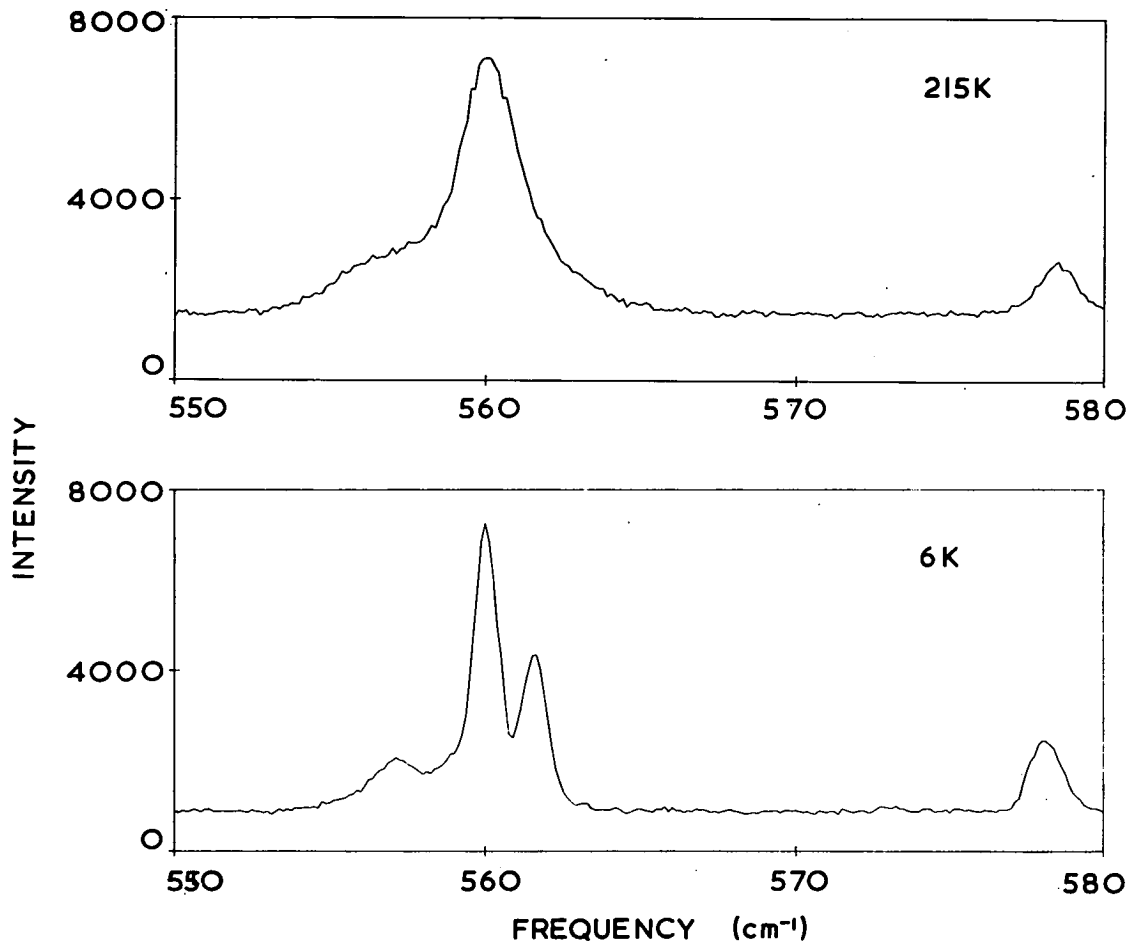
Fig. 5. The internal mode spectra around $560\,cm^{-1}$ for $C_6D_6 \cdot C_6F_6$ at 215 and at 6 K.

cooling. It is doubtful however whether this indicates a relationship between the Raman and NMR measurements, as the NMR line width has narrowed on warming by 150 K, whereas we see no evidence of transition until above 198 K, after Fig. 3(T).

The Raman spectrum changes continuously on cooling to helium temperatures, the lines for the external modes become sharper, giving very detailed spectra at 6 K. Figure 4 shows these spectra for both specimens used. On a peak and shoulder count these spectra display about 13 peaks, indicative of a crystalline material of considerable crystallographic complexity.

Further evidence for this complexity was sought by taking high resolution scans over the internal mode peaks. It was our expectation that these peaks would show a change in structure over the transition, as this is caused by the Davydov splitting which should change in a phase change. In all cases the structure in these peaks became better resolved at the lower temperature, as Fig. 5 shows, but no change in the structure was apparent. The only deduction we can make from this experiment is that if there is a transition to a phase with

a more complex structure, the intermolecular forces are so weak that they do not noticeably alter the Davydov splitting.

2. FUTURE EXPERIMENTS

Our measurements indicate that there are a number of fascinating transitional phenomena taking place in these systems on cooling. We plan to make powder diffraction measurements on both systems using neutron and X-ray techniques, especially at low temperatures. It is however tempting to speculate on the possible nature of the structures that will be found — such speculation is necessary for powder work as the diffraction data is considerably limited. It is well accepted that the molecules either tend to form pairs, as in a charge transfer complex, or form stacks in which the different species alternate. If the molecules form pairs, as in Fig. 6(a), then one pair may move as a roughly spherical unit, these spheres being arranged in cubic close packing. Binding a pair together is a force which may not be sufficient to prevent frequent relative
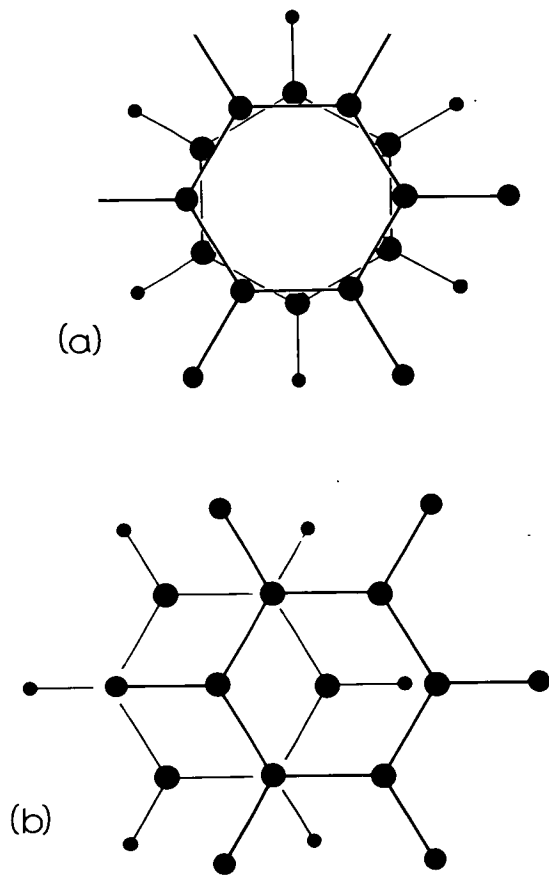
(a)

(b)

Fig. 6. Possible pairings of the two species (a) high temperature, (b) low temperature.

reorientations, in which rotation of multiples of $\pi/3$ take place about the common symmetry axis. This form of motion is effectively one-dimensional plastic-crystalline, and may persist even when the sphere reorientation is frozen out. At this point the crystal symmetry may be $Pa3$ or $P2_13$.

For the lowest phase structure we might have to look at related work such as that of Potenza and Mastropaolo [5] on $C_{10}H_8 . C_{10}F_8$, where the two molecules are laterally displaced relatively by about 1.4 Å. If similar behaviour occurs in the benzene–fluorobenzene system, then the molecular arrangement at 4.2 K might resemble Fig. 6(b). The molecule pair will then not approximate to a sphere, and a cubic phase is unlikely. It is clear from the variety of these possibilities that there may indeed be a number of transition phenomena.

REFERENCES

1. J.W. Arthur, Ph.D. thesis, University of Edinburgh (1974).
2. E. Baharie & G.S. Pawley, *J. Appl. Cryst.* **10**, 465 (1977).
3. J.S. Brennan, N.M.D. Brown & F.L. Swinton, *J. Chem. Soc. Faraday I* **70**, 1965 (1974).
4. D.F.R. Gilson & C.A. McDowell, *Canad. J. Chem.* **44**, 945 (1966).
5. J. Potenza & D. Mastropaolo, *Acta Cryst.* **B31**, 2527 (1975).
6. R.W.H. Small, Private communication (1979).
7. J. Timmermans, *J. Phys. Chem. Solids* **18**, 1 (1961).

INCOMMENSURATE PHASE OF THE MOLECULAR CRYSTAL $p\text{-}C_6F_4Br_2$

J.S.W. OVERELL, G.S. PAWLEY

Department of Physics, University of Edinburgh, Edinburgh, EH9 3JZ, UK

G.A. MACKENZIE

Physics Department, Risö National Laboratory, Roskilde, Denmark 4000

W.J. FITZGERALD

Institut Laue–Langevin, Grenoble Cedex 38042, France

and

D. KIRIN

Ruder Boškovič Institute, 41001 Zagreb, Croatia, Yugoslavia

Received 21 May 1980

A quasi-elastic neutron scattering study of $p\text{-}C_6F_4Br_2$ crystals is presented. Evidence is given for a low-lying phonon branch near the Brillouin zone boundary in the b^* direction for a sample at 300 K. The associated incommensurate phase at 4.2 K has a wavevector of about 0.24 b^*, and although there are distinct changes in the superlattice structure on cooling and warming, the transition is irreversible and no lock-in is evident.

1. Introduction

In the past few years interest in the incommensurate phases of crystalline matter has grown rapidly. The associated phase transitions have, in some cases, been described through the mechanism of soft modes [1]. Similar studies of molecular systems have not been so numerous [2], but include thiourea [3] and biphenyl [4]. The high-temperature phase of thiourea is para-electric and the low-temperature phase is ferroelectric, and so it is reasonable to assume that the three intermediate phases which show incommensurate behaviour are associated with this change. The Coulomb interaction is clearly of major importance in these transitions, but this is unlikely to be so in the case of the two transitions in biphenyl. It is this system which is physically most similar to the system studied in this work, namely p-dibromo-tetrafluorobenzene, for which neutron scattering data suggests an irreversible incommensurate transition.

2. Experimental

A single crystal of $p\text{-}C_6F_4Br_2$, of dimensions 6 × 4 × 10 mm, was mounted with the a^* and b^* reciprocal axes in the scattering plane and enclosed in a standard helium cryostat. Measurements were taken on the IN3 triple axis spectrometer at I.L.L., Grenoble. The monochromator was a pyrolytic graphite crystal scattering from (002), giving 2.36 Å neutrons, and second-order contamination was removed by an oriented graphite filter.

The initial aim of the experiment was to measure the phonon dispersion curves at low temperature, there being no evidence in the structural work [5] of any phase transition. When the b^* direction was investigated it was found that there existed strong quasi-elastic intensity, equal to about 2% of the largest Bragg reflection, near to the zone boundary. Measurements were therefore made at a number of equivalent points in reciprocal space, of which only one is chosen for presentation in
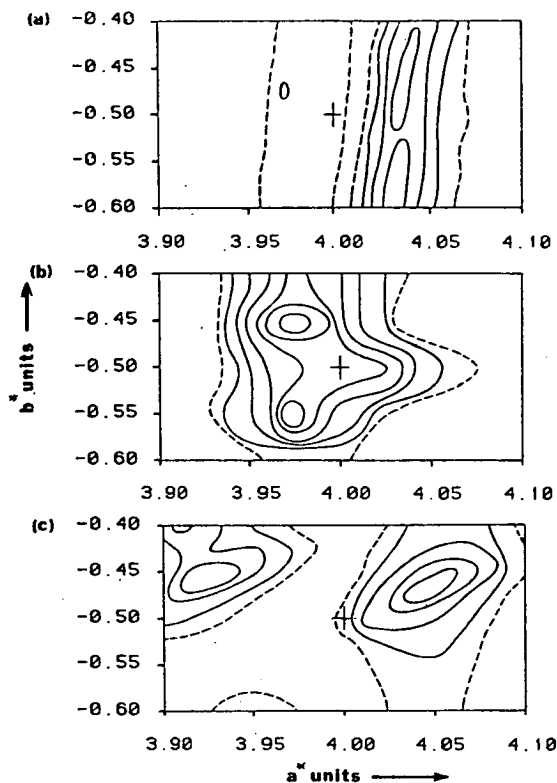
Fig. 1. Neutron quasi-elastic scattering about the point (4, −0.5, 0) at (a) 300 K on crystal 2 before cooling, at (b) 4.2 K on crystal 1 and at (c) 300 K on crystal 1 after being cooled. The contours are evenly spaced but arbitrary, and the broken contour is equal to half the value of the first full contour.

fig. 1, this being about the point (4, −0.5, 0). The temperature variation of this scattering was also studied, but as time was limited, only two temperatures, 4.2 K and 300 K, were used, and the results are in figs. 1b and 1c. As structure in the scattering persisted at 300 K, a second sample, cut from the original specimen, was studied on the assumption that the scattering from it at 300 K would be typical of the "as-grown" material. The result is in fig. 1a.

All the contour maps of fig. 1 were made for a zero energy transfer with energy resolution 0.17 meV. The procedure used was to vary the b^* coordinate in steps of 0.05 (fractional units) and then the a^* coordinate in steps of 0.01, thus forming a grid in the a^*b^* plane. A further measurement at 4.2 K is shown in fig. 2, which is a scan parallel to b^* through the main peaks of fig. 1b.
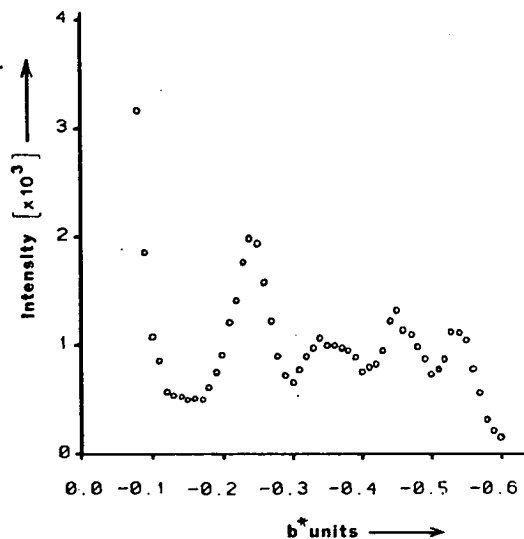

Fig. 2. The neutron scattering intensity along (3.97, η, 0), in steps of $0.01\,b^*$, taken from the first sample at 4.2 K. The incommensurate wavevector is shown to be approximately $0.24b^*$.

3. Discussion

The scattering from the sample at 300 K before cooling (fig. 1a) shows a well defined ridge of intensity along the b^* direction which does not contain the point (4, −0.5, 0) exactly. This point is marked with a cross on the diagrams, and there is a minor ridge of intensity parallel with the first situated on the other side of this point. There are no clear peaks along the length of this ridge. This scattering is consistent with a low-lying region of dispersion surface, this being the soft mode associated with an incommensurate phase above the temperature of the transition.

On cooling to 4.2 K (fig. 1b), structure appears in the soft mode scattering near (4, −0.5, 0), suggesting that a superstructure has been established and that the temperature is below that of the phase transition. The measurements of fig. 2 show that the peaks in the intensity suggest an incommensurate wavevector of about $0.24b^*$, but as the point (4, −0.5, 0) does not lie between two peaks the superstructure periodicity must involve a and perhaps c directions as well.

After warming to 300 K (fig. 1c), a certain structure remained in the quasi-elastic scattering, a result quite distinct from that obtained before cooling. A superlattice is still in evidence, though there is clearly a fun-

damental change in the structure, unless such a result can be caused by expansion of the lattice. The transition which occurs is therefore irreversible, though there might be a phase change from one superlattice structure to another on warming.

Further evidence for a superstructure in the sample after warming to 300 K is furnished by the existence of a very weak but non-zero Bragg intensity at (010), which is prohibited in the accepted $P2_1/c$ structure [5]. Considerable care was taken to ensure that this intensity was not spurious, as it is strong evidence of a superlattice in which the screw diad symmetry is lost.

Some preliminary Raman scattering measurements were made in the hope of finding further support for the proposed transition. But between 300 and 20 K no extraordinary lattice vibrational behaviour was observed. However we believe that the neutron scattering evidence is so strong that further investigation is justified, and we plan an extensive study of the quasi-elastic scattering on an instrument that permits investigation in three dimensions.

References

[1] A.D. Bruce and R.A. Cowley, J. Phys. C11 (1978) 3577.
[2] I.F. Shchegolev, Phys. Stat. Sol. 12a (1972) 9;
    J.A. Wilson, F.J. DiSalvo and S. Mahajan, Advan. Phys. 24 (1975) 117;
    K. Shimaoka, N. Tsuda and Y. Yoshimura, Acta Cryst. A28 (1972) 187.
[3] Y. Shiozaki, Ferroelectrics 2 (1971) 745.
[4] H. Cailleau, F. Moussa and J. Mons, Solid State Commun. 31 (1979) 521.
[5] G.S. Pawley, G.A. Mackenzie and O.W. Dietrich, Acta Cryst. A33 (1977) 142.

Powder refinement of Carbonyl Sulphide

J.S.W. Overell and G.S. Pawley

Department of Physics, Edinburgh University,
Mayfield Road, Edinburgh EH9 3JZ, Scotland, U.K.

and

B.M. Powell

Neutron and Solid State Physics Branch, Atomic Energy of Canada Ltd.,
Chalk River, Ontario, K0J 1J0, Canada.

Abstract: The crystal structure of carbonyl sulphide (OCS) at 90 K has been reinvestigated using neutron powder diffraction. The structure is rhombohedral, space group, R3m, with unit cell parameters $a = 4.063(3)$Å and $\alpha = 98.81(3)°$. There is one molecule per unit cell, aligned along the [111] crystallographic axis. The bond lengths have been determined as 1.21(3)Å and 1.51(3)Å for the oxygen-carbon and carbon-sulphur distances respectively.

Introduction

The structure of solid carbonyl sulphide was first determined by Vergard (1931), who reported the unit cell parameters, atomic positions and space group. The present work is aimed at improving the accuracy of the early work, as a preliminary to doing phonon studies.

Experimental

The sample of carbonyl sulphide was condensed in a vanadium can of dimensions 15 mm diameter and 70 mm length. This was quenched by immersion in liquid nitrogen producing a polycrystalline sample. A powder diffraction scan was made using the C5 triple axis spectrometer, in the two axis mode, on the reactor NRU at the Atomic Energy of Canada Ltd. at Chalk River. Neutrons of wavelength 1.629 Å scattered at 57.05° from a germanium (113) monochromator were used. The flux on the monochromator was approximately 10^5 neutrons $cm^{-2}s^{-1}$. The width of the beam at the sample was about 25 mm. Soller slits were placed before and after the sample. No analyser was used and the intensity was measured by a helium-3 detector. The zero scattering angle position and wavelength were determined by calibrating the spectrometer with several aluminium powder diffraction peaks.

The diffraction scan was made between the scattering

angles $2\theta = 15°$ and $2\theta = 100°$ at steps of $0.1°$, counting for
70 seconds at each point. Independent measurements of the
largest Bragg peak intensity were made at a number of
sample orientations taken at 10° intervals. These
individual measurements were distributed with a standard
deviation of 8% from the mean intensity, indicating that
continuous rotation of the sample was necessary to
reduce the error due to crystallinity to less than 1%.

Results

The results are presented in Figure 1, and are shown
as points in the scan, and the final calculated spectrum
is given by the full line. The sample contained about 1%
of impurities, giving rise to some small diffraction peaks.
These peaks have been removed from the data as used in the
refinement, and the regions so affected can be seen from the
difference plot (observed-calculated) in Figure 1.

The structure was refined using the program EDINP
(Pawley, 1980). The variable parameters used in the refinement
were introduced in stages. First the scale factor was
refined by itself, after which the flat background and
zero angle were added. Successive cycles included the
unit cell parameters, a and α, then the two bond lengths,
then the three peak width parameters and finally the overall
isotropic temperature factor. This made a total of eleven
parameters to be refined in the final cycles.

The final values of the parameters with their errors,
and the scan information are given in Table 1. All data

points had unit weights in the refinement. The R-factor
is given by

$$R = \frac{\sum_{i=1}^{N} \left| y_i(\text{obs}) - y_i(\text{calc}) \right|}{\sum_{i=1}^{N} y_i(\text{obs})}$$

where $y_i(\text{obs})$ is the observed intensity at the ith point in
the scan, and $y_i(\text{calc})$ is the calculated intensity, and the
sum does not include the regions contaminated by impurity
scattering. The R-factor for this refinement was 0.11. The
least squares residual is

$$R_w = \sum_{i=1}^{N} w_i \{y_i(\text{obs}) - y_i(\text{calc})\}^2 \qquad (\text{all } w_i = 1) \quad .$$

The standard deviations quoted in Table 1 are derived
from the least squares matrix, A, and are defined thus:

$$\sigma_i^2 = (A^{-1})_{ii} \frac{R_w}{N - n} \quad ,$$

where N is the number of statistically independent observations
in the scan and n is the number of refinement variables. The
scan information in Table 1 contains a number called "the
equivalent number of reflections", N_e. This is given by

$$N_e = N/\Delta$$

where Δ is the mean width at half height of a diffraction peak

in the scan. It can be argued, (Pawley, 1980) that this is a more realistic number to use for N in the equation for σ_i^2 , especially for the structural parameters which are, in this case, the two bond lengths. Using N_e, the standard deviations for these parameters become

$$\sigma(O-C) = 0.03 \text{ Å} \quad \text{and} \quad \sigma(C-S) = 0.03 \text{ Å}$$

These are the errors presented in Table 2. Similarly all the standard deviations in Table 1 could be increased by the factor 5.

It will be noted that at high scattering angles the background increases by about 10% from that at low angles. As there is at present no satisfactory function for the background which can be refined, except the flat background already used, an arbitrary background of straight line sections was subtracted in an attempt to get a better agreement in the high angle region (Rietveld, 1969). The R-factor achieved with refinement (2), 0.17, cannot be directly compared with that obtained when the background was not subtracted from the scan intensities. Although the agreement at high scattering angles was improved, the parameters of importance, namely the unit cell and atomic position parameters did not differ from those of refinement (1) by more than one standard deviation, where the standard deviation was based on N_e rather than N. The new bond lengths are given in Table 2.

Thus although the structural parameters do not change significantly in using arbitrary corrections, the use of such corrections to observed powder data does not improve the final result.

It may also be noted that the difference plot shows discrepancies between the calculated diffraction peak positions and those observed. In refinement (2) these discrepancies persisted. When the variation of the discrepancy, $\Delta = 2\Theta_{obs} - 2\Theta_{calc}$, was analysed as a function of scattering angle it was found that it could be approximately described by a straight line of equation $\Delta = (0.164 - 0.0032(2\Theta))$, degrees, giving $\Delta = 0$ for $2\Theta \sim 51°$. This is near to the focussing angle of 57.05° for the monochromator used. This would suggest that a systematic error is present, therefore another refinement, (3), was done with the background subtracted as in refinement (2), but including new parameters to describe a possible misplacement of the sample on the instrument. This was done by adding two terms to the scattering angle zero, $2\Theta_{zero}^{calc}$, giving

$$2\Theta_{zero}^{calc} = + P_5 - P_3\cos 2\Theta - P_4\sin 2\Theta$$

and P_5 is the refinement variable corresponding to the scattering angle zero error in the absence of misorientation. The new parameters, P_3 and P_4, describe the possible shift of the sample parallel and perpendicular to the incident beam in the

plane in which the measurements were made. The effect
of this refinement was to decrease the R-factor from 0.17
to 0.12, indicating that the new parameters were
statistically significant. The resulting parameters
in the final cycle of refinement (3) implied that the
scattering angle zero error had increased to the unreasonable
value of 5.2(0.7)° and the unit cell side and total OCS
molecular length decreased by ~5%, with standard deviations
of the order of 1%. Refinement (3) also suggested that
the sample was misplaced on the instrument by 75(10) mm.
This shift of the sample is not consistent with what we
know were the experimental conditions and therefore the
result of refinement (3) is rejected due to the unreal
values of the final parameters.

Thus we cannot find any plausible cause for the
peak position discrepancies, but believe that they are no
more extensive than that found in data taken on other
instruments.

Conclusion

This analysis constitutes the first determination of the
bond lengths in solid carbonyl sulphide by elastic neutron
scattering. They are found to be 1.21(3)Å for the O-C distance
and 1.51(3)Å for the C-S distance. Those reported by Townes
et al. (1948), using electron diffraction in the gaseous
phase, were 1.16(2)Å and 1.56(2)Å respectively. Although
the bond lengths in these analyses differ, it must be
remembered that there is a high unavoidable correlation
between the two bond length parameters. The total molecular
length is not affected in this way and we see that the
gaseous phase and solid phase measurements both yield a value
of 2.72 Å.

References

Pawley, G.S., (1972), "Advances in Structure Research by
Diffraction Methods", vol. 4, ch. 1, edited by
W. Hoppe and R. Mason, Oxford: Pergamon Press.

Pawley, G.S., (1980), J. Appl. Cryst., $\underline{13}$(6), 630.

Pawley, G.S., Mackenzie G.A., Dietrich, O.W., (1977),
Acta Cryst., $\underline{A33}$, 142.

Rietveld, H.M., (1979), J. Appl. Cryst., $\underline{2}$, 65.

Townes, C.N., Holden, A.K., Merritt, F.R., (1948),
Phys. Rev., $\underline{74}$, 1113.

Vergard, L., (1931), Z. Kristall. (Strukturbericht)
Vol. II, 373.

Table 1

The final parameters for the constrained refinement, (1)

		parameter value	standard deviation
scale factor		305.7	2.3
flat background		3071.7	46.7
zero error in $2\Theta(°)$		-0.073	0.005
peak shape	u	2.81	0.23
parameters	v	-1.49	0.18
(degs.^{2})	w	0.48	0.03
cell parameters	a(Å)	4.0629	0.0005
	$\alpha(°)$	98.814	0.006
overall isotropic temperature factor	B-unit	1.83	0.08
bond lengths (Å)	O - C	1.205	0.006
	C - S	1.510	0.007

scan information

range of $2\Theta(°)$	15.0 - 100.0
scan step in $2\Theta(°)$	0.1
wavelength (Å)	1.629
mean full width at half height	19.0
number of Bragg reflections in scan	29
equivalent number of Bragg reflections	39

The peak shape at full width at half height in degrees is $[u\tan^2\Theta + v\tan\Theta + w]^{\frac{1}{2}}$,

2Θ is the scattering angle.

Table 2
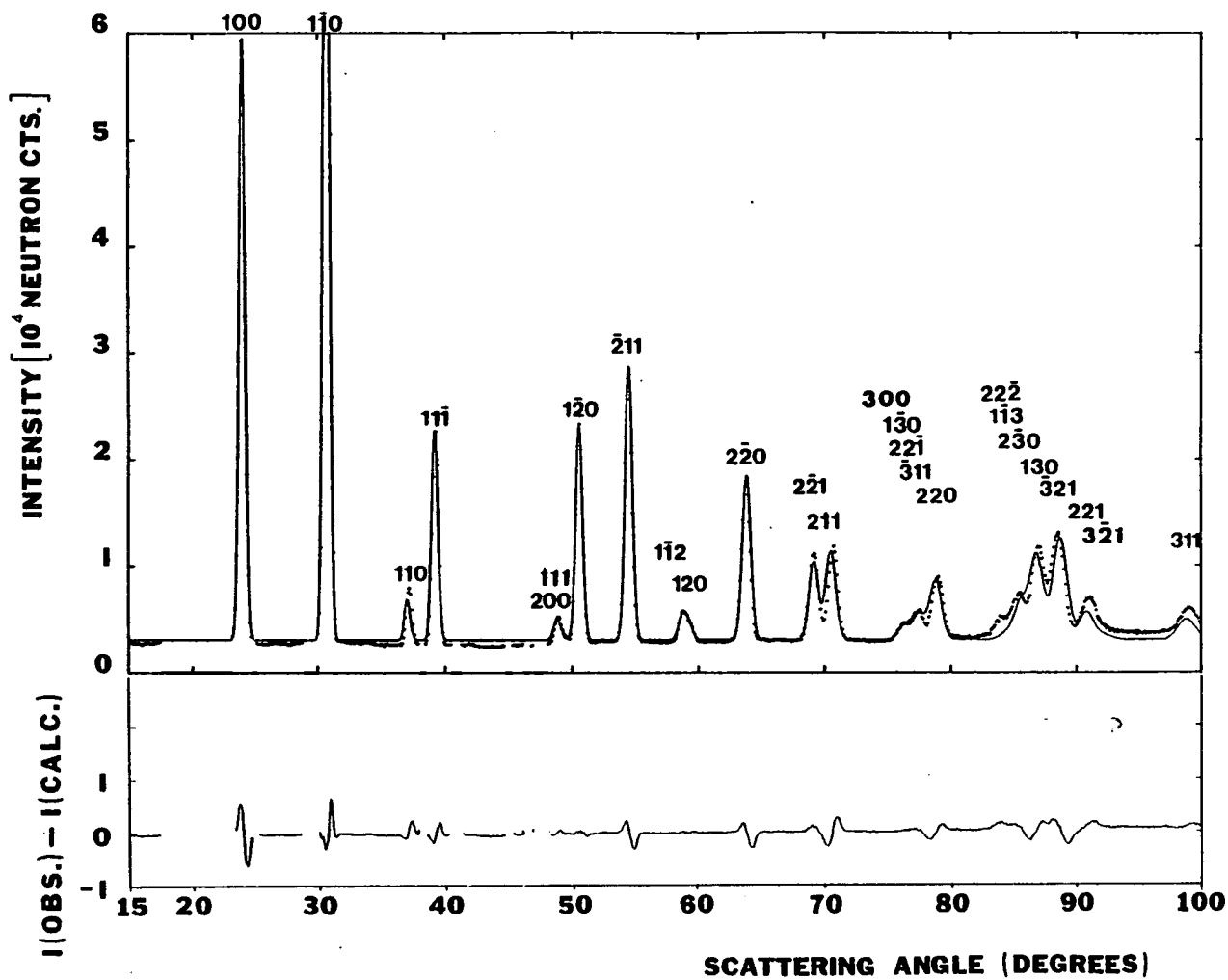
Comparison of gas phase and crystal diffraction results.

Bond	O - C	C - S	Total length O - C - S	R-factor
Gas phase	1.16(1)	1.56(1)	2.72(2)	
Vergard	1.10	1.97	3.07	
Refinement (1)	1.21(3)	1.51(3)	2.72(4)	0.11
Refinement (2)	1.19(4)	1.54(3)	2.73(5)	0.17
Refinement (3)	1.14(2)	1.47(2)	2.61(3)	0.12

(1) Flat background

(2) Arbitrary segmented background removed

(3) Sample position variable

OCS POWDER AT 90 K.

Caption for figure 1

Neutron intensity as a function of scattering angle, 2Θ. The large Bragg reflection at $2\Theta \sim 30°$ peaks at 1.1×10^5 neutron counts. Below the scan is the difference intensity, observed-calculated. The gaps in this plot show the regions removed due to impurity scattering.

An X-ray single crystal study of

the molecular system $C_6F_6 \cdot C_6D_6$

by

J.S.W. Overell and G.S. Pawley

Department of Physics

Edinburgh University

Mayfield Road

Edinburgh EH9 3JZ

Scotland, U.K.

ABSTRACT

An X-ray diffraction study of the molecular complex system hexafluorobenzene-deuterobenzene at 279K is reported. The structure has been determined for the first time as rhombohedral, space group R3m, and of unit cell dimensions a = 7.310(19)$\AA$ and α = 109.67(43)^{o}, giving a unit cell volume of 299(5)$\AA^3$. There is one molecule of each species within the unit cell and they are alternately arranged in infinite stacks along the unique [111] crystallographic direction, the molecular planes being perpendicular to this direction.

Both constrained and unconstrained refinements have been done and the results of both are presented. The constraints consisted of rigidly fixing the bond lengths and geometry of the molecules such that the resulting molecular hexad symmetry axis was coincident with the unique axis of the structure. The unconstrained model relaxes the fixed bond lengths but the hexad symmetry is retained.

The crystal structure and molecular packing are discussed with respect to the constrained refinement results, which suggest that the different molecular species are rotationally staggered by 30° about the unique axis, and that the structure is in fact pairs of molecules along the stack direction. The inter- and intra-pair separations are found to be $\sim$ 3.72$\AA$ and $\sim$3.52$\AA$ respectively.

INTRODUCTION

Considerable interest was generated by the report by Patrick et al.[1] of the existence of several molecular complexes between hexafluorobenzene (HFB) and various aromatic hydrocarbons. A great variety of studies of these complex systems using different experimental techniques have been performed and a brief account of that work is given here.

Thermodynamic measurements by Duncan et al[2,3] were done in order to establish the phase diagrams, amongst other properties, of several complexes involving HFB, including HFB-benzene. Gilson et al[4] have made nuclear magnetic resonance (NMR) measurements on the HFB-benzene system, and reported line width and second moment transitions at about 90K on cooling. They conclude that these transitions are probably caused by reorientations about the six-fold axis of the molecules. Spectroscopic[5] and dipole[6] measurements of complexes containing HFB do not show any evidence of charge transfer between the different species of molecules as was first assumed by Patrick et al. This led to the X-ray diffraction studies of Dahl[7,8,9] performed to gain information concerning the intermolecular forces present in the two complexes HFB-mesitylene and HFB-hexamethylbenzene. Dahl concludes that the possibility of forces stronger than the van de Waals type should not be ignored in these systems.

The differential scanning calorimetry measurements done by Brennan et al [10] on the HFB-benzene system demonstrated a thermal anomaly at 249 K on warming and at 246 K on cooling. However, the work done by Gilson et al showed no unusual NMR behaviour at $\sim$ 250 K.

More recently Potenza et al[11] have determined the crystal structure of the closely related complex system naphthalene-octafluoronaphthalene. The molecules were found to be arranged in infinite stacks, alternating in the two species but unpaired, and where the differing species are laterally displaced, relative to each other, by about 1.4 $\AA$.

Further calorimetric and NMR experiments on the HFB-benzene-d_6 system have been done by Ripmeester et al[12] and they observed a number of transition phenomena on warming at temperatures of 199 K, 247.5 K and 272K .   They also propose that the HFB molecule is rotationally disordered to some extent in the temperature range 100K to 300K in accord with the observations of Gilson et al.[4] The transition at 247.5K is in agreement with the calorimetric work of Brennan et al[10]. Recently the Raman light scattering technique was used in order to probe the temperature dependence of the dynamics of the HFB-benzene system[13]. Polycrystalline samples, both protonated and deuterated, were studied in this work in the temperature range 4.2K to 300K, and a structural phase transition was reported at ~ 170K on cooling and ~ 200K on warming. This will be related to the thermal anomaly reported by Ripmeester et al.[12]. Since the crystal structure was unknown at any temperature, this prompted the present X-ray diffraction study of a small single crystal of the 1:1 molar complex HFB-benzene-d_6 at just below room temperature. Previously, Small[14] had reported a very weak X-ray diffraction pattern for this system at room temperature.

EXPERIMENTAL

Constituent chemicals were obtained from the Imperial Smelting C^{o} (C_6F_6, stated purity 99.95% at.) and Fluka Chemicals (C_6D_6, stated purity 99.6% at.) and were used without further purification. The mixture used was equimolar in the two constituents to ~ 0.3%.

A sample was prepared by sealing some of the frozen, polycrystalline, mixture in a Lindemann capillary tube of diameter 0.5 mm and approximate length 4 mm. To avoid any combustion, and hence contamination from the combustion products that would result by sealing the ends of the tube by melting the glass, the sample tube was sealed with epoxy-glue, and then attached directly to the goniometer head. This goniometer arrangement was then mounted on an Enraf-Nonius CAD-4 4-circle diffractometer.

The zone refining technique was used to grow the crystal on the diffractometer, using a fine wire as the heater. Since the materials used were impure before mixing, this crystal growing technique would aid in the partial purification of the mixture. The result of this process was a single crystal ~ 2 mm in length, and nitrogen gas cooling apparatus was used to maintain the crystal at a temperature of about 280K, well below its melting point of about 297K. Great care had to be taken when growing the crystal to ensure that the temperature of the cold nitrogen stream was above 272K, where the constituent chemicals tended to supercool and then solidify below their natural, individual freezing points of about 279K. If a crystal was grown below 273K then it was found to be a mixed crystal of the required complex and one of the constituents.

The crystal gave a distinct diffraction pattern and it was also observed that considerable diffuse scattering was present underneath the Bragg reflections, but this has not been measured and analysed. It is probable that this diffuse scattering is related to the dynamical disorder reported by Ripmeester et al[12].

The data were collected using a CAD4 diffractometer operating with filtered CuKα radiation of wavelength $\lambda = 1.5405\text{Å}$. 1487 reflections were measured in concentric shells out to $(\sin\theta)/\lambda = 0.532\text{Å}^{-1}$ in reciprocal space (corresponding to a maximum scattering angle of $2\theta = 110^{o}$). The average sample temperature throughout the experiment was 279(1)K. The beam width used was 0.4 mm at the sample, this value being taken from the collimator specifications. The shape of the crystal relative to the incident beam is not the optimum spherical shape that would normally be chosen, had the choice been available. This problem was partially overcome in the analysis by applying a rudimentary volume correction to the measured integrated intensities, the form of which

will be given later.

RESULTS AND ANALYSIS

The raw data consisted of 1487 integrated intensities grouped over 150 symmetry independent reflections, both the reflection and its Friedel pair having been measured. The variation of the integrated intensities of the three control reflections as a function of time throughout the experiment was less than 4% from the corresponding mean integrated intensities, showing that the experimental conditions were satisfactorily stable. The linear absorption coefficient was calculated as 14.14 cm^{-1}, but no corrections were applied to account for any possible variation in the diffracted intensity caused by the absorption process. This was justified in terms of the asymmetrical crystal shape relative to the incident and diffracted beams. The process of extinction becomes important only when crystals of very high perfection are used, and therefore in the present study this process is ignored. Hereon we use the word intensity to imply integrated intensity.

From an initial analysis of the reflection intensities it was seen that about 30 were spuriously high in intensity relative to the other reflections in the same proposed symmetry related group. The Miller indices of these reflections were analysed with the knowledge of the indices of the 9 reflections whose intensity exceeded 5×10^5 counts, and it was found that all of the spurious intensities could be explained as being double Bragg scattering processes. The most pronounced case of this double scattering process was the $(\bar{5}13)$ reflection (and its' Friedel pair), whose intensity was approximately twenty times that of the average intensity taken over the other reflections in the same group. The $(\bar{5}13)$ reflection indices are equivalent to the $(\bar{3}03) + (\bar{2}10)$ indices. These 30 spurious intensities were therefore removed from the data set, making a reduced total of 1457 reflections.

The correction to be applied that accounts approximately for the volume variation of the crystal in the incident beam is of the form $I = I_o \csc \delta$, where I_o and I are the measured and corrected intensities respectively. The angle δ is that between the incident beam direction and the axis of the cylindrical tube in which the crystal is contained. With knowledge of the four orientation angles the angle δ was calculated for each individual reflection. It is convenient at this point to introduce an overall consistency factor in order to test whether or not the above correction makes an improvement on the data. This quantity will be defined as

$$R_{overall} = \left| \frac{\sum_j (\sum_i |\bar{I}_j - I_{ij}|)}{\sum_j (\sum_i I_{ij})} \right|$$

where the sum over i is for a proposed individual symmetry group of reflections of intensities I_{ij} and mean intensity $\bar{I}_j$, and the sum over j runs over the 150 symmetry independent groups. $R_{overall}$ had the value ~ 12.0 for the raw data and ~ 8.5 for the volume corrected intensities. This indicates a considerable overall improvement in the data, and therefore the corrected intensities were used in the refinements

A similar consistency factor defined by

$$R_{internal}^j = \frac{\sum_i |\bar{I}_j - I_{ij}|}{\sum_i I_{ij}}$$

was calculated for each symmetry independent group of reflections. For the most intense 51 groups, the average of this internal consistency factor was 0.055, which gives an indication of the quality of the data. In this case, the value of the consistency factor means that the data i not of the highest quality, but it must be remembered that the shape of the crystal is non-uniform with respect to the incident and diffracted beams and that no account has been made for the absorption

or extinction processes.

Of the different rhombohedral space groups only two, R$\bar{3}$m and R3m, were found to be consistent with the groupings of the indices of the reflections. There are statistical ways of determining whether or not a centre of symmetry is present, such as Wilson's test[15], but it is not possible to determine this given only a reflection and its' Friedel pair.

The molecular planes are necessarily aligned perpendicular to the unique axis of the structure but there are four possible relative orientations of the two species of molecule about this axis. In the space group R$\bar{3}$m we choose to set the benzene molecule at the origin and the HFB at the body centre position. These four distinct possibilities arise since an atom must either lie on a mirror plane or midway between a pair of such planes. In order to distinguish easily between these various structural models in the text that follows, abbreviations are introduced where 'D' indicates the carbon-deuterium pair in the benzene molecule and 'F' the carbon - fluorine pair in the HFB molecule. The abbreviations used are:

DOM   only 'D' on mirror planes

FOM   "   'F' "   "   "

AOM   all atoms on mirror planes

NOM   no   "   "   "   "

For atoms that lie on a symmetry plane in this structure the possibility of 'puckering' of the molecules is allowed as there is no crystalline hexad symmetry axis. This has not been included in the calculations but the structural models that would allow this molecular distortion, along with the relations between the fractional coordinates and the anisotropic temperature parameters, are indicated in Table 1. Also given in table 1 for each model is an indication of the possibility of one of the molecules being displaced from its' centre of symmetry,

thereby reducing the space group symmetry from R$\bar{3}$m to R3m. This last aspect of th[e] analysis is given in greater depth later, the purpose of table 1 is merely to give a clear indication of the molecular distortions and translations allowed by each structural model within the space groups considered in the absence of any constraint on the molecular geometry.

The constraints that are used fix the molecular geometry to be planar, and to have a hexad symmetry axis that is parallel to the unique axis of the structure. Hence the puckering of the molecules mentioned above is not allowed in this regime of constraints. The bond lengths are also fixed and their values are C-C = 1.38A[19], C-F = 1.34A[20] and C-D = 1.08A. The unconstrained models retain the hexad molecular symmetry but relax the fixed bond lengths, with the exception of the C-D bond, and the initial values for these bonds in the unconstrained refinements are taken from those of the constrained results.

The data comprising the symmetry related groups of reflections was then reduced by statistical averaging to a single value of the intensity for each group. There were 19 groups that were considered unobserved and they were left in the data set.

The refinement program is based on the familiar ORFLS[16] programe but differs in that it has the facility of adding constraints in the orthogonal coordinate system[17]. The structure refinements were started using an overall scale factor and an overall isotropic temperature parameter, with extra isotropic thermal motion allowed for the fluorine atoms. Both the constrained and unconstrained calculations were done and the philosophical justification for performing the constrained refinements is given later in the discussion of the analyses. The molecules are forced to have a hexad symmetry axis and so in the case of the unconstrained refinements one molecule is specified by only two atom coordinates. Therefore the number of parameters in the initial refinements is three in the constrained case and six in the unconstrained case.

The results of the initial refinements are given in tables 2a and 2b for the constrained and unconstrained cases respectively, and are labelled as rows I. These tables give, in the first two columns, the model abbreviation and the R factor defined by

$$R = \frac{\sum_j w_j |I_j^{calc.} - I_j^{obs.}|}{\sum_j I_j^{obs.}}$$

where the j labels the intensity of the jth observed $(I_j^{obs.})$ and calculated $(I_j^{calc.})$ symmetry independent reflection. The weight associated with the jth reflection is w_j, and unit weights were used throughout. The function that is minimised in all refinements is

$$R_W = \sum_j w_j (I_j^{calc.} - I_j^{obs.})^2$$

and the value of this is given in column 3 of tables 2a and 2b. The corresponding refined parameters are given in the other columns, along with their respective standard deviations in parentheses and, where appropriate, isotropic temperature parameters are given.

It is apparent on studying table 2a that the structural models that place the fluorine atoms on the symmetry planes (models FOM and AOM) give a considerably poorer fit to the data than do the models that put these atoms midway between these planes. This means that the structural models that would allow a puckering distortion of the HFB molecule in the absence of any molecular constraint give the poorest fit to the data, and for this reason the constraints on the bond lengths are not lifted for models FOM and AOM.

The above refinements have been done for the space group R$\bar{3}$m, the highest symmetry consistent with the data. However, the other possibility, R3m, must also be considered. In order to reduce the symmetry we must introduce a further parameter into the refinement in the form of a shift of one of the molecules, chosen arbitrarily to be the HFB, along the unique axis of the unit cell. This corresponds to a dimerisation of the molecules and we call this the shift parameter hereon, the variation of which alters the separation of the molecules along the unique axis.

Further refinements were done using the overall scale factor and the overall isotropic temperature parameter for the constrained molecules, with the addition of atomic coordinates in the unconstrained case, as well as the shift parameter described above. The shift parameter was found to be very highly correlated with the extra thermal motion parameter for the fluorine atoms. The latter was therefore fixed in these refinements. The sense of the shift parameters is unimportant since the reflection intensities are invariant under a change of sign of this new parameter. As a result of this invariance, if the refinement is initiated with zero shift then the parameter changes calculated by the refinement will be arbitrary and the result indeterminate, and so the refinement cannot converge to the minimum in parameter space. Therefore, it is necessary to initiate the refinement with a small non-zero shift in order to obtain an interpretable result. Several such starting values were tried, with the initial values of the other parameters the same for each refinement, and all parameters were refined. This was done for both the constrained and unconstrained cases for models NOM and DOM and some of the results are given in table 2a, 2b rows II. The results for all four models in the constrained case are presented, but for the unconstrained case the models AOM and FOM were unstable and so their results are not tabulated. That this instability exists is probably because these unconstrained models are far enough from the minimum that the refinement cannot converge.

The constrained models that give the best results for the above refinements are DOM and NOM, and a diagram for each model illustrating all of these results is displayed as figures 1a and 1b respectively. These figures show the R factor for the initial conditions described above versus the initial shift and the inset shows the final R factor to which the refinement converges when all parameters are refined, such that a parameter set describing a point on the initial R factor curve refines to a corresponding parameter set in the inset. These points are labelled 1,2,3..... . Also given in these figures are points corresponding to parameter sets to which the refinement converges if the shift parameter is held fixed at non-zero values whilst all other parameters are refined.

The discussion and interpretation of these results and figures is postponed until later, the purpose at present being to give the results of the analyses.

We now introduce anisotropic thermal parameters, β_{ij}, for the best models NOM and DOM, for both constrained and unconstrained cases. The definition of these parameters is given in Table 3. The justification for introducing more parameters into the refinement is based upon the value calculated for the internal consistency factor. Experience shows that the expected best R factor is somewhat greater than this internal consistency factor, but possibly as low as 0.08. The best R factors obtained have been 0.174 and 0.133 for the constrained and unconstrained refinements, so that it should be possible to reduce this value further, and the only course open is to introduce the β_{ij}.

Mention must be made at this point of the correlation between the β_{ij} and the shift parameter. The use of anisotropic thermal parameters implies that the atoms move in such a way that the so-called surfaces of constant probability are ellipsoids. Consider, then, the HFB molecule at the body centre of the unit cell undergoing isotropic thermal motion. The shift parameter is then varied, and since the sign of the shift is either positive or negative with equal weight, we may think of the isotropic, spherical surface of constant probability being elongated along the direction of shift. If now the isotropic thermal motion is replaced by anisotropic parameters and the shift parameter is again varied, the latter variable elongates the already ellipsoid shape of the constant probability surface. This leads to two sets of parameters performing much the same role in the refinement and hence ill-conditioning of the least squares matrix results. We therefore set the shift parameter to zero and fix it throughout the remainder of the calculations described. The crystal symmetry is therefore increased to $\overline{R3m}$ again, the symmetry of the structure of the initial isotropic refinements.

It has already been pointed out that the atomic coordinates, and also the β_{ij}'s, are interrelated and these relationships have been given in table 1. The result is that one coordinate and four independent β_{ij}'s are necessary to describe an atom. Some of the β_{ij}'s for different atoms were found to be highly correlated and were therefore removed from the variable list. Therefore, in the case of constraints, of the 13 possible parameters only 12 for DOM and NOM were varied, whereas in the unconstrained case, of the 16 possible parameters only 13 for NOM and 14 for DOM were varied. Where a parameter is held fixed, the tabulated standard deviation is left blank. These results are given in tables 2a, 2b in rows III. From these tables it is seen that the constrained and unconstrained 'best fits' occur for

different structural models. The value of R_w is least for constrained model DOM, whereas it is least for unconstrained model NOM and the implications of this are discussed shortly. The final R factor for the constrained and unconstrained cases are 0.167 and 0.098 respectively and the final parameter set values are given for the constrained model DOM in table 3, with standard deviations where applicable. The R factor was further reduced to 0.138 and 0.080, for the respective constrained and unconstrained refinements, by repeating the above anisotropic thermal parameter calculation but using a reduced data set consisting of the strongest 51 reflections whose intensities exceeded 4000 counts. The unconstrained refinement R factor of 0.080 is consistent with the expected limit set by the previously calculated internal consistency factor. No further reduction of the R factor is expected and the results of these refinements are given in the final rows (IV) in tables 2a and 2b.

DISCUSSION

The isotropic refinements give values of the temperature parameters that are large, especially for the C-F pair in HFB. This is in accord with the observation of Ripmeester et al[12] that the HFB molecule is to some extent dynamically disordered in the temperature range 100 K to 300 K. These large amplitudes of thermal motion are undoubtedly connected with the presence of strong thermal diffuse scattering observed in unpublished X-ray photographic work, done by one of the authors, on single crystals of the same complex system.

The introduction of anisotropic thermal parameters into the refinement procedure was justified in terms of the internal consistency factor. Their subsequent refinement shows that the principal temperature parameters (β_{ii}) have large values, and this is again in qualitative agreement with the observations of disorder by

Ripmeester et al.[12]. A structural model for the possible disorder of the HFB molecule was not explicitly included in the refinements presented here, but the values of the thermal vibration parameters do suggest that large amplitudes of thermal motion are present in this structure, in fact far larger than those present in the benzene crystal where the largest anisotropic mean square displacement has a value ~0.09 $\overset{o2}{A}$ [19]. In the present structure we have a largest value of ~1.1 $\overset{o}{A}^2$.

The results for the unconstrained models, given in table 2b, give a refined C-C bond length of ~1.20 $\overset{o}{A}$ in all cases, and this is not a satisfactory result. This is an example of where the unconstrained model gives a better R-factor and fit to the data than does the constrained model, but where certain refined parameter values do not correspond to those which are generally accepted. In this case, it is known that a C-C bond value of ~1.20 $\overset{o}{A}$ is too short by about 13% so any comparison between the structural models DOM, NOM, ... etc. must be made using the constrained model results. The philosophy of constraints is that it is always better to include parameter values that are known more accurately than the measured data could possibly determine, thereby increasing the reliability of the other variables that are refined. Therefore, the comparison of the different structural models, NOM and DOM, with respect to the shift parameter will be based upon the constrained results obtained for these models.

The introduction of the shift parameter reduced the symmetry of the structure used in the initial refinements to R3m by removing the $\bar{1}$ centre. Refinements were done with the shift parameter varied and the results have been given in Figures 1a, 1b for the best constrained models. These results indicate that for model DOM

the refined shift parameter is confined to values of 0.096 Å with standard deviations approximately 0.02 Å, giving a distribution of values between 0.08 Å and 0.12 Å. However, it is seen from figure 1b that model NOM gives results that suggest that the refined shift parameter has a value of ~0.03 Å with error ~0.05Å, so that it is not possible to say whether or not the shift is non-zero in model NOM. The results of model DOM are therefore tentatively taken as evidence that the HFB molecule is not situated at the body centre of the unit cell, and that therefore the space group symmetry is R3m. This distortion that breaks the centre of symmetry in R$\bar{3}$m will not alter the intensity distribution by an amount that would make statistical tests, such as that due to Wilson[15], effective. It is therefore believed that such tests cannot be used in cases where crystal pseudo-symmetry exists.

The differences between models DOM and NOM are twofold. The former model has the molecules eclipsed as viewed down the unique axis, whereas in the latter the molecules are staggered. Therefore in the absence of molecular hexad symmetry, in model DOM the possibility of puckering of the benzene-d_6 molecule is realised whereas in model NOM this is prohibited by crystal symmetry. Secondly, and probably most importantly, model DOM gives a small shift of the HFB molecule, and this gives rise to the structure being made up of pairs of molecules rather than the molecules of different species being equally spaced along the unique axis. This molecular pairing means that there are a great variety of possible stacking faults that would cause the calculated structure (with no faults) to be only a moderately good fit to the true, faulted structure. This would partially account for the seemingly poor quality of the data and the relatively high R factor obtained in the final cycles of the constrained refinement.

The work of Dahl[7,8,9] has shown that in some HFB complexes, forces stronger than van de Waals may be present and in the present case the intermolecular separations are calculated to see whether or not this is true in this system. These results are tabulated in table 4, along with the relevant van de Waals radii and separations. For Model DOM with a shift of ~0.10 Å the nearest neighbour, intra-stack C....F separation observed in this sytem is ~3.90 Å and this is about 1 Å larger than that expected from purely van de Waals interactions. Part of the rhombohedral structure is shown in figure 2, and the nearest neighbour, interstack F....D separations are shown as 2.72 Å and 2.80 Å. Again, these intermolecular separations are somewhat larger than those expected from van de Waals interactions alone. These observations are not inconsistent with the evidence[5,6] that this complex does not display any charge transfer characteristics. Also, theoretical work concerning molecular complexes[21,22] indicates that even in strongly charge transferred systems, the stability of the complex may involve forces other than those of charge transfer. The pairing of the molecules found in the present work is therefore not inconsistent with the fact that this system is not of the charge transfer type.

Following the proposal, given by Ripmeester et al.[12], of a degree of dynamic rotational disorder of the HFB molecule, the closest interstack F....D approach when the benzene-d_6 molecule is stationary whilst the HFB is rotationally disordered about the unique axis is found to be 2.04 Å. This value is considerably less than the van de Waals separation of 2.55 Å, so it is possible that forces of a different type may be involved if the HFB molecule is disordered in the manner considered above.

Further evidence for disorder of the HFB molecule is furnished by the unit cell volume, which is observed to be $299(5)\text{Å}^3$, about $13(2)\%$ larger than that given by the sum of the two molecular volumes, $\sim265\ \text{Å}^3$, calculated from the separate structures.

CONCLUSION

The organic molecular complex in the present work is of particular interest since it consists of two species of molecule that are of the simplest aromatic form. The analyses were performed with and without constraints on the bond lengths, which, in the case of one of the $C-C$ bonds, showed that the comparison of the structural models had to be based upon the constrained refinement results.

These results have been fully discussed and it is believed that the data, although not of the highest quality, is good enough to be able to draw a conclusion relating to the pairing of the different species of molecules in model DOM. In order to be able to arrive at a more conclusive result it would be necessary to collect intensities of higher angle reflections than was done in the present study. This may be achieved by using a shorter wavelength of radiation, preferably neutrons. The preference for using neutron radiation rather than X-radiation is that the Bragg scattering of neutrons is governed by the relevant coherent scattering length which is angle independent. However, the X-ray scattering factors are heavily suppressed at high scattering angles which means that the Bragg reflections with large indices would be more readily observed with neutrons than with X-rays. Therefore, if greater resolution is required, then a shorter wavelength must be used, of the order of $\lambda \leq 0.5\ \text{Å}$, in order to probe out to $\sim2\ \text{Å}^{-1}$ in reciprocal space, for a maximum scattering angle of $2\Theta \sim 110^{\circ}$ as we have in the present work. Neutron wavelengths of this order are not easily available on conventional diffractometers, but the spallation neutron source (SNS) which is in construction will be able to produce such wavelength with ease. Therefore, it would be worthwhile to use the SNS for investigating system further. Neutron powder diffraction could be used initially in order to see if the high angle reflections needed are observable, and then single crystal diffractometry would follow. In the present case, of the highest angle reflections, for which $2\Theta \geq 100^{\circ}$, there are several that have intensities of several hundred counts. These reflections would therefore be more intense with neutrons and thus more easily measurable.

The brief discussion of packing considerations indicated that the interstack F....D separations are larger than the van de Waals separations, but if rotational disorder of the HFB is allowed then this separation may become much less, as little as $2.04\ \text{Å}$. This latter distance is smaller than the separation required for hydrogen bond formation, which is $\sim2.35\ \text{Å}$, but this type of bond has not been discussed with respect to this system before and it is not known whether or not hydrogen bonds occur. Since the complex is not of the charge transfer type it seems unlikely that hydrogen bonds would form.

We therefore conclude that the intermolecular forces acting within a stack have a lesser effect on the molecular binding to form the crystal, than do the corresponding forces between molecules in different stacks. This leads us to believe that the interstack F....D interaction plays a relatively important role in the formation of the crystal.

Finally we note that the transition phenomenon observed
by Ripmeester et al.[12] at 272 K is probably related to a structural
phase transition, since unpublished neutron powder diffraction
data taken by the authors indicates that at 250 K the structure
is possibly monoclinic, different from the rhombohedral structure
presented here. Furthermore, when the present experiment was completed
the single crystal was cooled by several degrees, whereupon it
shattered. This is indicative of a phase transition which is probably
related to that observed by Ripmeester et al.[12] at 272 K. It is already
known that a structural phase transition takes place at ~200 K[13] on
warming, and other neutron powder diffraction scans at 5 K suggest an
even more complicated crystal structure than at 250 K.

Figure 3 shows the neutron powder diffraction scans of this
system at 280 K, 250 K and 5 K. The first of these is a calculated
profile using the structural parameters reported here and the other
two are the observed data mentioned above. It is clear that the
crystal structures at these various temperatures are distinctly different.

It is clear therefore, that a great deal more work must be done
in order to elucidate the various structural transitions that take
place in this system.

ACKNOWLEDGEMENT

1. Patrick, C.R. and Prosser, G.S., Nature (1960), 187, 1021.

2. Duncan, W.A., Swinton, F.L., Trans. Farad. Soc. (1966), 62, 1082-9.

3. Duncan, W.A., Sheridan, J.P., Swinton, F.L., Trans. Farad. Soc. (1966),
   62, 1090-96.

4. Gilson, D.F.R., McDowell, C.A., Canad. J. Chem. (1966), 44, 945-52.

5. Beaumont, T.G., David, K.M.C., J. Chem. Soc. (B) (1967), 1131-3.

6. Bauer, M.E., Knobler, C.M., Horsma, D.A., Perez, P., J. Phys. Chem. (1970),
   74, 4594-6.

7. Dahl, T., Acta Chem. Scand. (1971), 25, 1031-39.

8. Dahl, T., Acta Chem. Scand. (1972), 26, 1569-75.

9. Dahl, T., Acta Chem. Scand. (1973), 27, 995-1003.

10. Brennan, J.S., Brown, N.M.D., Swinton, F.L., J. Chem. Soc. Farad. I (1974),
    70, 1965-70.

11. Potenza, J., Mastropaolo, D., Acta Cryst. (1975), B31, 2527-9.

12. Ripmeester, J.A., Wright, D.A., Fyfe, C.A., Boyd R.K.,
    J. Chem. Soc. Farad. Trans. II (1978), 74 (7), 1164-78.

13. Mackenzie, G.A., Overell, J.S.W., Pawley, G.S., Solid State Commun. (1979),
    31, 431-5.

14. Small, R.W.H., Private Communication, (1979)

15. Wilson, A.J.C., Acta Cryst. (1949), 2, 318-21.

16. Busing, W.R., Martin, K.O., Levy, H.A., (1962) ORFLS Report ORNL-TM-305,
    Oak Ridge Nat. Labs., Tennessee.

17. Pawley, G.S., (1972), "Advances in Structure Research by Diffraction Methods
    p.1-64, ed. Hope W., Mason, R.; Pergamon Press, London.

18. International Tables for X-ray Crystallography, (1952), vol. 1, p.272,
    vol. 4, p.327-8 and 323.

19. Cox, E.G., Cruickshank, D.W.J., Smith, J.A.S., Proc. Roy. Soc. (1958),
    247, 1-21.

20. Boden, N., Davis, P.P., Stam, C.H., Wesselink, G.A., Molecular Physics (1973
    25, 81-86.

21. Hanna, M.W., J. Amer. Chem. Soc. (1968), 90, 285-91.

22. Lippert, J.C., Hanna, M.W., Trotter, P.J., ibid, (1969), 91, 4035-44.

Table 1.   Molecular distortions and translations allowed by the various structural models cited in the text within the space groups considered in the absence of constrained hexad symmetry of the molecules. Also given are the relationships[18] of the fractional coordinates and anisotropic temperature parameters for atoms on (1) and midway (2) between symmetry planes.

Space group : $R\bar{3}m$

Model	Puckering allowed in absence of hexad axis	Translation along unique axis
DOM	C—D only	
FOM	C—F only	Not allowed in $R\bar{3}m$.
AOM	C—D , C—F	
NOM	None	

Space group :   R3m

	Puckering allowed in absence of hexad axis	Translation along unique axis
DOM	C—D only	
FOM	C—F only	Allowed for all models in R3m.
AOM	C—D, C—F	
NOM	None	

	x_f	y_f	z_f	β_{11}	β_{22}	β_{33}	β_{23}	β_{31}	β_{12}
(1)	x	x	-2x	A	A	C	D	D	E
(2)	x	-x	z	A	A	C	D	-D	E

Table 2a. Salient results from the constrained refinements cited in the text. The bonds are given in $\mathring{A}$ and the isotropic temperature parameters ($TO_{C,D}$, that for carbons and deuteriums, TO_F for fluorines) in genuine $\mathring{A}^2$ units. Rows labelled as I, II, III, IV are as follows:

I   Isotropic refinements in $R\bar{3}m$,

II Isotropic refinements in $R3m$ with the shift parameter refined,

III Anisotropic refinements in $R\bar{3}M$,

IV As III but using the strongest 51 reflections.

Model	R	R_W $(\times 10^{12})$	$TO_{C,D}$	TO_F	SHIFT	
NOM	0.174	1.40	0.19(4)	0.27(5)	-	
DOM	0.182	1.36	0.18(4)	0.28(5)	-	I
AOM	0.442	5.57	0.20(8)	0.36(14)	-	
FOM	0.393	5.12	0.17(7)	0.40(15)	-	
NOM††	0.174	1.40	0.19(3)	0.27(-)	0.034(46)	
DOM††	0.179	1.32	0.18(3)	0.28(-)	0.096(22)	II
AOM*	0.443	5.51	0.18(7)	0.35(-)	0.155(32)	
FOM*	0.397	4.88	0.16(6)	0.38(-)	0.215(21)	
NOM	0.184	0.684	-	-	-	III
DOM†	.0.167	0.676	-	-	-	
NOM	0.160	0.628	-	-	-	IV
DOM	0.138	0.624	-	-	-	

*These refinements had an initial shift of 0.01 $\mathring{A}$.

†A full parameter set is given in table 3.

††These refinements had an initial shift of ~ 1.02 $\mathring{A}$.

Table 2b. Salient results from the unconstrained refinements cited in the text. All bonds and the shift parameter are given in $\mathring{A}$ and the temperature parameters (isotropic $TO_{C,D}$ for the carbons and deuteriums, isotropic TO_F for the fluorines) are given in genuine $\mathring{A}^2$ units.

Rows labelled I, II, III, IV are as in table 2a.

Model	R	R_W $(\times 10^{12})$	C—C	C—C	C—F	$TO_{C,D}$	TO_F	SHIFT	
NOM	0.134	0.611	1.20(4)	1.33(3)	1.35(3)	0.19(3)	0.23(3)	-	
DOM	0.133	0.643	1.21(3)	1.34(3)	1.33(3)	0.18(3)	0.24(4)	-	I
NOM††	0.135	0.614	1.21(5)	1.33(4)	1.34(4)	0.19(2)	0.23(-)	0.015(22)	
DOM††	0.133	0.643	1.21(4)	1.34(4)	1.32(4)	0.18(3)	0.23(-)	0.015(32)	II
NOM	0.098	0.154	1.20(3)	1.38(3)	1.33(3)	-	-	-	III
DOM	0.104	0.159	1.16(3)	1.31(4)	1.42(3)	-	-	-	
NOM	0.080	0.137	1.19(5)	1.39(6)	1.31(5)	-	-	-	IV

†† These refinements had an initial shift of ~ 1.02 $\mathring{A}$

Table 3. Full parameter set for the anisotropic constrained refinements of DOM model. The temperature parameters, B_{ij}, are defined by $\exp -[B_{ij}.h_i.h_j]$ $i,j = 1, 2, 3$ using the summation convention. All coordinates and bond lengths in orthogonal Å units, temperature parameters in genuine Å² units.

par. atom	x	y	z	B_{11}	B_{22}	B_{33}	B_{23}	B_{31}	B_{12}
C	0.5636	0.5636	-1.1272	0.232(95)	0.232(95)	0.445(153)	-0.041(55)	-0.041(55)	-0.025(69)
D	1.0048	1.0048	-2.0096	0.232(95)	0.232(95)	0.445(153)	-0.041(55)	-0.041(55)	-0.025(69)
C	1.1149	3.0651	2.0900	1.092(280)	1.092(280)	0.588(223)	-0.182(-)	0.182(-)	0.417(185)
F	0.1705	4.0095	2.0900	0.487(57)	0.487(57)	0.211(33)	0.018(58)	-0.018(58)	-0.327(25)

Table 4. Intermolecular distances for models NOM and DOM with a shift of 0.10 Å. Van de Waals radii and separations are also shown. All values in Å units.

van de Waals

radii		separations	
C	1.55	C—F	2.90
F	1.35	F—D	2.55
D	1.20	C—D	2.75

Observed separations

Model		Shift	C—C	C—F	F—D	C—D
NOM	intra-stack	0	3.62	3.86	3.63	3.78
NOM	inter-stack	0	-	-	2.69	-
DOM	intra-stack	0	3.69	3.99	3.87	3.90
DOM	intra-stack	0.10	3.60	3.91	3.78	3.81
DOM	inter-stack	0	-	-	2.76	-
DOM	inter-stack	0.10	-	-	2.72	-

FIG.1a

Figure 1a, 1b

Plots for constrained models DOM and NOM (respectively 1a, 1b) showing the variation of:

(i)   initial R factor against initial shift (●)

(ii) final R factor against the initial shift when all parameters
      except the shift are refined (○).

The inset shows the variation of the final R factor against the refined

shift, when all parameters are refined (▲).
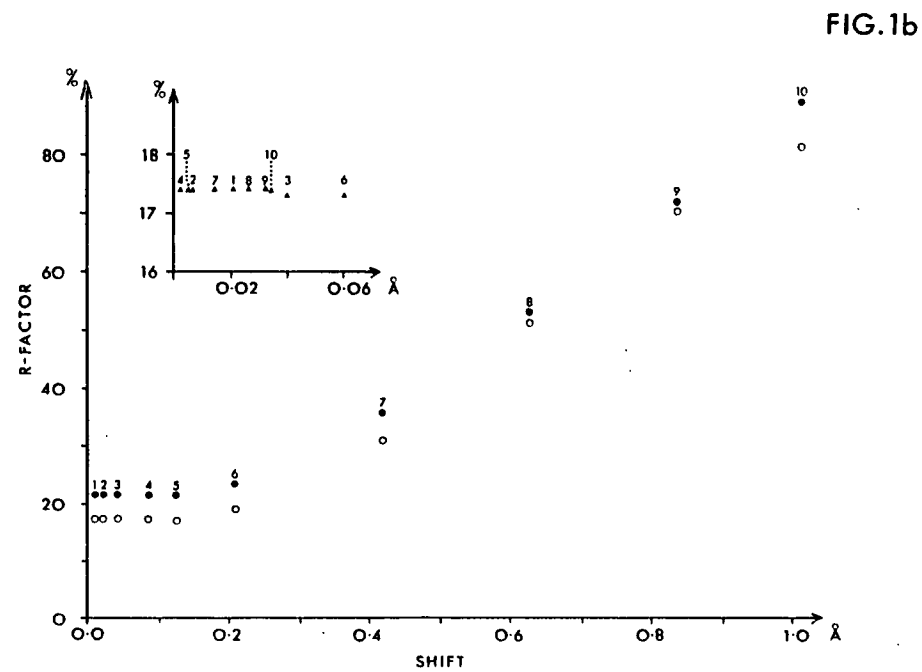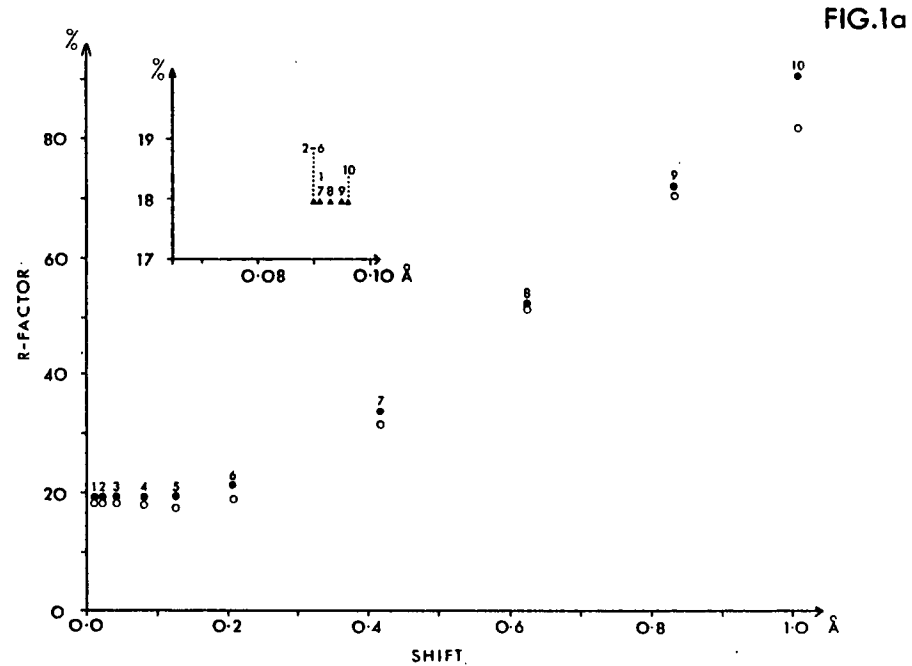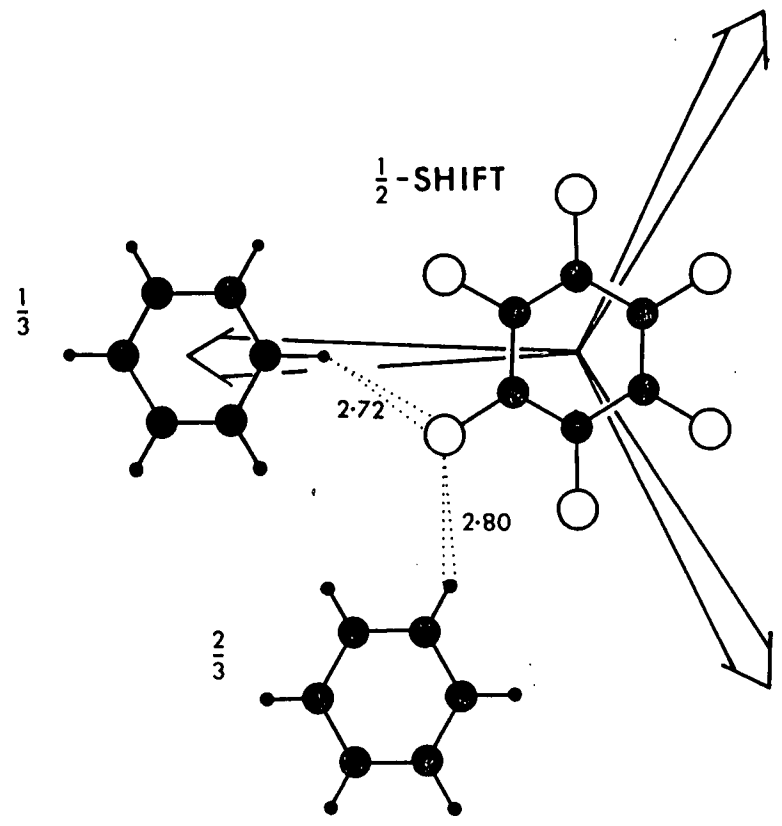
R factors are given in % and shifts in Å.

FIG.1b

FIG.2

Figure 2

Projection of part of the structure in space group R3m, along the unique axis. Heights of molecules are given in fractions of the body diagonal. The symmetry planes are vertical and coincident with the rhombohedral axes shown. Some separations are also shown (in Å).
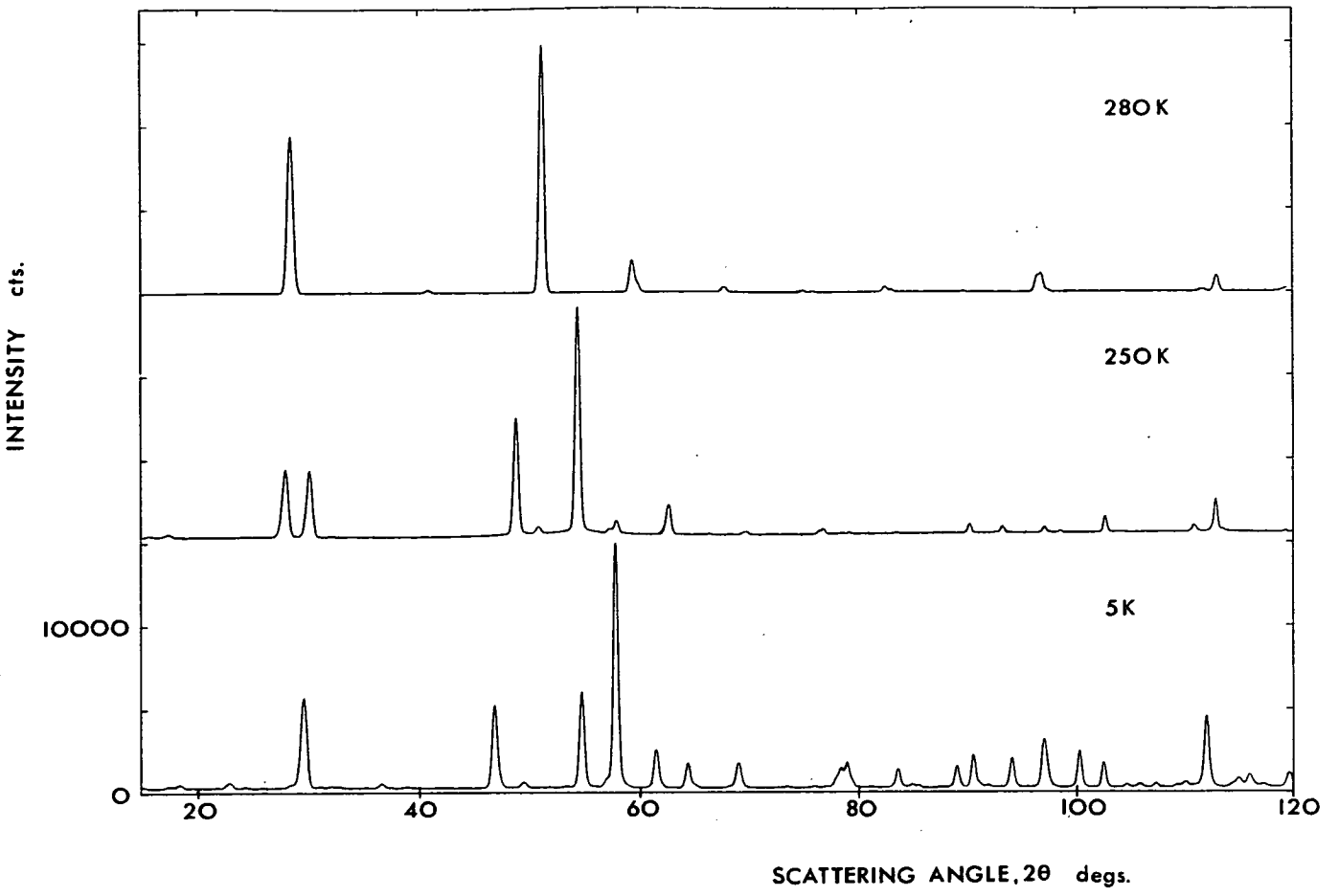

○ ········· fluorine atom

● ········· carbon atom

● ········· deuterium atom .

FIG.3